Ministry of Education and Science of the Russian Federation
Saint Petersburg National Research University of Information Technologies, Mechanics, and Optics

NANOSYSTEMS:

PHYSICS, CHEMISTRY, MATHEMATICS

2014, volume 5(4)

Наносистемы: физика, химия, математика

2014, том 5, № 4

NANOSYSTEMS:

PHYSICS, CHEMISTRY, MATHEMATICS

ADVISORY BOARD MEMBERS

Chairman: V.N. Vasiliev *(St. Petersburg, Russia)*,
V.M. Ievlev *(Voronezh)*, P.S. Kop'ev*(St. Petersburg, Russia)*,
V.N. Parmon *(Novosibirsk)*, A.I. Rusanov *(St. Petersburg, Russia)*.

EDITORIAL BOARD

Editor-in-Chief: N.F. Morozov *(St. Petersburg, Russia)*
Deputy Editor-in-Chief: I.Yu. Popov *(St. Petersburg, Russia)*

Section Co-Editors:
Physics – V.M. Uzdin *(St. Petersburg, Russia)*,
Chemistry, material science –V.V. Gusarov *(St. Petersburg, Russia)*,
Mechanics – A.K. Belyaev *(St. Petersburg, Russia)*,
Mathematics – I.Yu. Popov *(St. Petersburg, Russia)*.

Editorial Board Members:
V.M. Adamyan *(Odessa, Ukraine)*; O.V. Al'myasheva *(St. Petersburg, Russia)*; S. Bechta *(Stockholm, Sweden)*; V.G. Bespalov *(St. Petersburg, Russia)*; A. Chatterjee (*Hyderabad, India)*; S.A. Chivilikhin *(St. Petersburg, Russia)*; A.V. Chizhov *(Dubna, Russia)*; P.P. Fedorov *(Moscow, Russia)*; E.A. Gudilin *(Moscow, Russia)*; D.A. Indeitsev *(St. Petersburg, Russia)*; H. Jónsson *(Reykjavik, Iceland)*; A.A. Kiselev *(Madison, USA)*; Yu.S. Kivshar *(Canberra, Australia)*; S.A. Kozlov *(St. Petersburg, Russia)*; Yu.B. Kudasov *(Sarov, Russia)*; S.E. Kul'kova *(Tomsk, Russia)*; P.A. Kurasov *(Stockholm, Sweden)*; A.V. Lukashin *(Moscow, Russia)*; V.A. Margulis *(Saransk, Russia)*; I.V. Melikhov *(Moscow, Russia)*; G.P. Miroshnichenko *(St. Petersburg, Russia)*; H. Neidhardt *(Berlin, Germany)*; K. Pankrashkin *(Orsay, France)*; B.S. Pavlov *(Auckland, New Zealand)*; A.V. Ragulya *(Kiev, Ukraine)*; V. Rajendran *(Tamil Nadu, India)*; A.A. Rempel *(Ekaterinburg, Russia)*; V.P. Romanov *(St. Petersburg, Russia)*; V.Ya. Rudyak *(Novosibirsk, Russia)*; V.M. Talanov *(Novocherkassk, Russia)*; A.Ya. Vul' *(St. Petersburg, Russia)*.

Editors:
I.V. Blinova; A.I. Popov; M.A. Skryabin; A.I. Trifanov; E.S. Trifanova *(St. Petersburg, Russia)*, R. Simoneaux *(USA)*.

Address: University ITMO, Kronverkskiy pr., 49, St. Petersburg 197101, Russia.
Phone: +7(812)232-67-65, **Journal site:** http://nanojournal.ifmo.ru/,
E-mail: popov1955@gmail.com

AIM AND SCOPE

The scope of the journal includes all areas of nano-sciences. Papers devoted to basic problems of physics, chemistry, material science and mathematics inspired by nanosystems investigations are welcomed. Both theoretical and experimental works concerning the properties and behavior of nanosystems, problems of its creation and application, mathematical methods of nanosystem studies are considered.

The journal publishes scientific reviews (up to 30 journal pages), research papers (up to 15 pages) and letters (up to 5 pages). All manuscripts are peer-reviewed. Authors are informed about the referee opinion and the Editorial decision.

Content

NANOSYSTEMS: PHYSICS, CHEMISTRY, MATHEMATICS, 2014, 5 (4), P. 457–466

IN MEMORIAM: ALEXANDER IVANOVSKII, INNOVATIVE RESEARCHER AND SCIENCE MANAGER IN COMPUTATIONAL MATERIALS SCIENCE OF ADVANCED INORGANIC MATERIALS

V. V. Bannikov, T. A. Denisova, A. N. Enyashin, N. I. Medvedeva,
I. R. Shein, D. V. Suetin, V. P. Zhukov, M. V. Kuznetsov

Institute of Solid State Chemistry UB RAS, Ekaterinburg, Russia

kuznetsov@ihim.uran.ru

PACS 01.60.+q

The paper is written to pay a tribute to Prof. Alexander Leonidovich Ivanovskii, Head of the Quantum Chemistry and Spectroscopy Laboratory at the Institute of Solid State Chemistry, Ural Branch of the Russian Academy of Sciences (RAS), and is devoted to recalling the most significant landmarks in his scientific career. A broad-minded man of great erudition, A. L. Ivanovskii made invaluable contributions in the field of computational materials science — a new field of research covering computational modeling for properties of existing substances and for compounds yet to be synthesized, including nanostructured materials. Under his leadership, a group of young, talented researchers have grown to become specialists in the electronic structure simulation and computational modeling to predict the properties of solids, which formed a unique school of thought in the field of quantum chemistry and spectroscopy research in the Urals.

Keywords: Superconductors, nanostructures, carbon allotropes, MAX phases, refractory materials, magnetic materials, computational chemistry.

Received: 16 June 2014
Revised: 30 June 2014

A well-bred intellectual, a man of noble principles and genuine culture, always pursuing an initiative, living positively with venture and verve — these are the attributes by which a leading scientist Alexander Leonidovich Ivanovskii will always be commemorated by his colleagues and friends.

A. L. Ivanovskii passed away on February 28, 2014, in his 62nd year of life, thus ending a remarkable career filled with scientific accomplishments: Doctor of Chemistry, Professor, Honored Scientist of the Russian Federation, National Prize Winner in Science and Engineering, and a remarkably creative leader of the Laboratory of Quantum Chemistry and Spectroscopy at the Institute of Solid State Chemistry, Ural Branch of the Russian Academy of Sciences. The scientific activity after Alexander Ivanovskii and his school of thought cover a broad spectrum of issues [1-20]: advanced solid solutions, alloys and intermetallic compounds, superconductors and superconducting magnets, antiperovskite-structured compounds, MAX phases, refractory interstitial phases, nanomaterials, just to mention a few. A. L. Ivanovskii has authored and co-authored more than 860 papers published in national

Fig. 1. Alexander Leonidovich Ivanovskii

and international science journals; he is the author of 14 monographs and more than 20 reviews on the scientific issues related to computational materials research in inorganic chemistry. The scientific accomplishments earned him wide respect in the scientific community, of which over six thousands of citations to his works is a convincing proof.

Over fifteen years, Alexander Ivanovskii gave lectures on the structure of matter to students at the Ural Federal University. Many of the students trained by Alexander can now be found in laboratories actively involved in quantum chemical modeling research.

Alexander Leonidovich Ivanovskii was born in Sverdlovsk on February 2, 1953. In 1976, he graduated from the Physical Engineering Department of the Ural Polytechnical Institute (currently, Ural Federal University named after B.N. Yeltsyn), and early upon graduation, he joined a group of researchers headed by Prof. V. A. Gubanov and by Academician-to-be, Prof. G. P. Shveikin at the Lab of Physical Methods of Investigations of Solids at the Chemistry Institute, Ural Branch of RAS. Starting from those days and over his entire career to the end of his days, one of the most significant directions of his research was devoted to refractory compounds and interstitial phases. In 1980, Alexander Ivanovskii received his Candidate of Science degree; and in 1988, at the age of 35, he earned his Doctor of Science degree, having defended his thesis titled “Electronic Structure and Chemical Bond in Refractory Compounds of $d-$Elements of IVA, VA Subgroups”. In 1994, he was elected a corresponding-member of the Natural Science Academy and was appointed Head of the Quantum Chemistry and Spectroscopy Laboratory at the Institute of Solid State Chemistry, Russian Academy of Sciences. In 1995, Alexander Ivanovskii received the Russian Federation State Prize for a series of works "Quantum-Chemical and Radio-Frequency Spectroscopy Methods for Solid Chemistry Applications".

Contemporary solid state research is striking in its variety, bringing to the forefront such systems and objects as micro and nano-porous solids, low-dimensional crystals, nanosized and nano-structured objects. Nanomaterials came to be one of the topics most favored by Prof. Ivanovskii: a giant leap was made by him and his team in understanding the field of nanostructure design for both existing materials as well as newly synthesized substances, in studying their stability and investigating their physical and chemical properties, using a great diversity of computational techniques. The breadth of his research interests encompassed a great number of nanostructures: diversified forms of carbon allotropy (diamond-like modifications, nanotubes, fullerenes, graphene and its analogs) and various inorganic nanomaterials, such as nanofibers, nanotubes and fullerene-like particles of boron nitrides, carbides, borides, silicides, oxides, halogenides and chalcogenides. Prof. Ivanovskii had an in-depth and critical view of these science developments in the world, which was reflected in the number of his reviews published in international journals and monographs, with some of the publications having pioneered in this field of materials research on the national scale. The following results deserve special notice.

A. L. Ivanovskii became interested in nano-objects in the 1990's, when a surge of interest was generated by the experimental evidence for a new class of nanostructured titanium carbides, observed in gaseous phase as ultrasmall cubic 27-atom clusters. Nanosized titanium carbide clusters were found to transform into nonstoichiometric dodecahedral clusters, referred to as metalocarbohedrenes Ti_8C_{12} (or metcars for short). Combining his many years' experience of studying the chemical bonding of binary carbide systems with the then-available software and hardware capabilities made these nanoclusters an apt research endeavor. Along with his research group, he issued several fundamental publications related to the stability and reactivity of nano-systems. Furthermore, this direction of research evolved towards the computational design and study of structures, both theoretical and experimentally observed, and towards studying compounds plotted on a metal-carbon phase diagram: endohedral complexes of carbon and boron-nitrogen nanotubes with metcars, endofullerenes with d- and f-element atoms, and nanopeapods based thereon [1,2,3].

While studying metalocarbohedrenes, which, in fact, were regarded as heteroatomic analogs to ultra-small carbon fullerenes, Alexander Ivanovskii could not but get involved in studying other, then-new low-dimensional nanostructures, such as fullerenes and carbon nanotubes. He wrote a review and was the first Russian author to have written a monograph on the state-of-the-art production, characterization and modeling of carbon nanostructures [4]. Alexander Ivanovskii's enthusiasm and research interest was stimulating his team in pursuing the modeling of these low-dimensional objects and structurally related nanotubes based on hexagonal boron nitride and magnesium boride. Later, that triggered explosive growth of inventive research projects looking for new compounds as candidates for making hollow nanostructures. Under Ivanovskii's leadership, atomistic models were proposed and, for the first time in Russia and even in the world, quantum chemical computations were performed for the properties of inorganic nanotubes based on the oxides of titanium, vanadium, magnesium, on poly(titanic) acids, aluminum hydroxides, sulfides and selenides of molybdenum, niobium and zirconium. These computational results, along with the analysis of experimental data worldwide, were summarized by his team in a series of unique reviews and books, which were the first publications on this kind of research in the national scientific literature [5,6,7]. Along with inorganic nanotubular systems, hollow polyhedral nanoparticles — layered chalcogenides and halogenides-based inorganic fullerenes — were also of special interest to A. L. Ivanovskii. Their structure must have differed significantly from the carbon fullerene structure. Under Ivanovskii's leadership, the laboratory researchers were the first in the world to have performed quantum chemical computations of electronic and magnetic properties for some of these structures [8].

Fig. 2. Young scientists in the group of quantum chemistry in 1980: in the first row from left to right (sitting): Andrei Postnikov (now – Professor, Université de Lorraine Laboratoire de Chimie et Physique-Approche Multi-Echelles des Milieux Complexes, Metz, France;) and Alexander Ivanovskii (from 1994 to 2014 – Head of Laboratory of Quantum Chemistry and Spectroscopy, Institute of Solid State Chemistry, Ekaterinburg); in the second row from left to right: Alexander Lichtenstein (now – Professor, Institute of Theoretical Physics University of Hamburg; Germany, Max-Born-Preis, 2014), Sergei Freidman (now – Head of Software Department, Vidisco Ltd, Israel) and Michail Ryzhkov (now – Leading researcher, Institute of Solid State Chemistry, Ekaterinburg)

It is worth noting that early into this research, the experience gained by Ivanovskii and his laboratory had already drawn great attention from scientists abroad, involving both theoretical and applied aspects of materials science. That opened up an opportunity to establish fruitful and enduring collaboration between the Quantum Chemistry and Spectroscopy Laboratory and the Theoretical Chemistry Group headed by Prof. G. Seifert at TU Dresden, Germany, and the Materials Synthesis Group headed by Prof. R. Tenne, Weizmann Institute of Science, Israel. Numerous collaborative projects performed by Ivanovskii's lab jointly with these two research groups resulted not only in atomistic models being developed for carbon fibers, nano-diamonds, nanotubes and nanoparticles of layered chalcogenides, exo- and endohedral molecular complexes of carbon nanotubes, but also in the mechanisms underlying their formation having been verifiably established, in the correlation to have been proposed between their structure and thermodynamic stability, strength characteristics, electronic and magnetic properties.

As early as the beginning of 2000's, being completely immersed in his studies on carbon nanotubes and fullerenes, Alexander Ivanovskii was also making research efforts towards the design of new allotropes of carbon and boron nitride. He was very keen on sp^2- and sp-hybridized atom-based nanostructures, which could form layers. He was also eager to study the structures designed from sp^3-hybridized atoms, which tended to form "monolithic" diamond-like modifications. The former nanostructures, in his opinion, could demonstrate a set of nontrivial electronic properties that could be modified using chemi- or physisorption [9]. The latter family of compounds, however, showed promise as superhard refractory materials that could compete with transition metal carbides and nitrides [10]. Long before the graphene boom, following the world trends in the field of computational design, Alexander Ivanovskii and his colleagues had studied a great number of potential allotropic modifications of carbon and boron nitrides and carbonitrides, including layered graphene-like materials: graphynes, graphdiynes, nanotubes and fullerenes based thereon, icosahedral nanodiamonds and diamond nanofibers, having pioneered in the design of so-called interpenetrated fullerite structures.

Even with the strong competition in the field of computational materials science relating to carbon materials, Alexander Ivanovskii maintained warm relations with several researchers, which was, for example, reflected in collaborative projects with Prof. E.A. Belenkov from Chelyabinsk State University and with Prof. V.V. Porkropivny from the Institute for Problems in Materials Science, National Academy of Sciences, Ukraine [11, 12]. Ironically, despite being performed at a world class level of research excellence in this field, Alexander Ivanovskii's series of early papers had met some skepticism from his scientific opponents, who had labeled this kind of basic studies as "nano-centaurs research". However, the discovery of grapheme, and the technology boom that followed, gave an extra impetus to the research by Prof. Ivanovskii and his group in the field of modeling layered carbon and inorganic analogs of grapheme, graphene-based and graphene-like materials. [13,14]. In a wondrous fashion, the topic of his most recent review overlaps with the research objects of his earlier thesis for Candidate's degree and covers the problems of materials science and prospects of the intensely shaping research direction: the so-called MAX phases – a family of transition metal layered carbides [15].

It is noteworthy that A. L. Ivanovskii was one of the leading authorities in the world for studying the electronic structure, chemical bonding, stability and mechanical properties of binary and ternary refractory phases. This research allowed the prediction of homogeneity regions, which were caused by the presence of vacancies and 2, 3d- element impurities in a wide spectrum of refractory compounds. These results were published in a large number of scientific papers and monographs [16-18]. Scientific achievements gained by the group were welcomed in the scientific community and were held in great esteem by the Russian Government, which awarded A. L. Ivanovskii the State Prize in Science and Engineering in 1995, and with the title of Honored Scientist of the Russian Federation in 2007.

The obtained knowledge about binary transition metal carbides and nitrides had formed the basis for research into an advanced novel family of ternary layered MAX phases which exhibited a unique combination of properties, intrinsic to both ceramic and metal materials. Such nanolaminates of $M_{n+1}AX_n$ (n=1,2,3...) are composed of layers of transition d-element carbides or nitrides, M_{n+1}, sandwiched by layers of p-elements designated as : (Si, Ge, Al, S, Sn, etc.); and carbon or nitrogen (X_n). The phases exhibit totally reversible plasticity, excellent shockwave resistance, high thermal and electrical conductivity, corrosion resistance, and show promise for industrial application as refractory materials that call for further investigation into their properties. Theoretical studies of the electronic structure and properties of $M_{n+1}AX_n$ phases using *ab initio* techniques were initiated by A. L. Ivanovskii in the mid 1990's, and are still intensely ongoing. In particular, specifics for the electronic properties and chemical bonding in Ti_3SiC_2 were established for the first time, and non-stoichiometry and doping effects were studied in different sub-lattices [19,20]. A significant experimental contribution was made by A. L. Ivanovskii into the studies of MAX phases, predicting new nanolaminates and modeling the properties using the state-of-the-art *ab initio* quantum chemistry methods. The superconducting transition, experimentally detected in a number of MAX phases, set forth a series of theoretical studies exploring the fundamentals of this phenomenon in nanolaminates.

In 2011, an original method was proposed for the synthesis of a new family of MAX phase-based graphene-like (quasi-two-dimensional) nanocarbides and nanonitrides of d-metals, which were named MXenes. These materials possessed a nontrivial combination of properties, and showed promise for various technology applications. Under the leadership of A. L. Ivanovskii, modeling new 2D nanostructures was carried out, their stability factors were determined, and directional modifications were proposed for their electronic, cohesion, mechanical and magnetic properties [21,22]. Models were developed and systematic studies were performed for structural and electronic properties and for relative stability of 2D graphene-like carbide structures of $Ti_{n+1}Al_{0.5}C_n$ and $Ti_{n+1}C_n$ (n = 1 and 2), which could be obtained from the corresponding MAX phases. The possibility of obtaining new 2D graphene-like carbides and nitrides, which had electronic and magnetic properties, such as semiconductors, nonmagnetic and magnetic materials controllable by altering the type and degree of atomic coverage of the 2D carbides and nitrides with various ad-atoms and molecules was shown. Structural, cohesion and electronic characteristics for graphene-like carbide nanotubes were predicted.

One of the most significant directions of A. L. Ivanovskii's research was the theoretical modeling of properties for tungsten carbides and nitrides and for multicomponent phases based upon those materials. His interest in this was piqued by the unique physical and chemical properties of tungsten carbide (WC), which is characterized with a small thermal expansion coefficient and improved hardness over a wide temperature range and which is now widely used as a basic component for making wear-resistant, hard alloys and high-strength coatings. Besides, from the theoretical point of view, tungsten carbides and nitrides could be considered as "transitional" phases between the series of new crystalline carbides and nitrides of platinum-group elements (Ru, Rh, Pd, Os, Ir, Pt) and the "classical" carbides and nitrides of d-metals of IV and V groups [23]. Alexander Ivanovskii was the first in Russia to have published a review on computational materials science exploring these materials [18]. Under his direct guidance, a series of studies were carried out to predict the electronic structure, chemical bonding, phase stability and mechanical properties of binary carbides and nitrides of tungsten (WC, W_2C, WN, W_2N) and ternary solid solutions and individual phases.

In particular, the energy stability and a number of physical and chemical characteristics were established for all known polymorphous modifications of tungsten sub-carbide W_2C (α, β, γ, ε), which differ one from another in the type of carbon atom distribution over octahedral interstices of the crystal lattice and which, when added as doping elements, cause an effect on the performances of carbide-metal WC/M composites and coatings. Structural and electronic properties were determined, and the role played by carbon vacancies was established for the synthesized solid solutions — tungsten aluminocarbides $W_{1-x}Al_xC_z$, which were formed by nonstandard substitution, when *d*-element (W) is replaced by a *p*-element (Al) in the nodes of the metallic sublattice of the hexagonal tungsten carbide WC. As a result, introducing aluminum into tungsten carbide reduced the carbide density considerably, while maintaining its strength properties. Other remarkable results of his research include the prediction of electronic and magnetic properties of the so-called η-phases (M_3W_3C, M_6W_6C), which appear in composite materials in the region between the WC grains and transition metals or their alloys, and which cause a significant impact on the functional (e.g., mechanical) properties of tungsten-containing materials [24,25].

Predicting new doped and non-stoichiometric semiconducting phase-based magnetic materials was another direction of his research that Alexander Ivanovskii eagerly pursued, thus developing quantum chemical materials science for spintronics applications. Along with the traditional approach, which comprised doping nonmagnetic semiconductors with atoms of magnetic 3*d*- and 4*f*-metals, Alexander Ivanovskii was engaged in developing a new research direction, which is referred to as d^0-magnetism and involves inducing the magnetic state of a system by doping the system with the atoms of *sp*-elements (B, C, N) in the anion sub-lattice or by vacancy-induced spin polarization of the states near the Fermi level. Alexander Ivanovskii was the first Russian author to have published such an in-depth review of science literature on this issue [26]. Under his direct guidance, a number of research projects were performed devoted to the theoretical prediction of d^0-magnetism for a wide range of crystalline systems and nano-objects. In particular, a vacancy-induced mechanism was predicted for non-stoichiometric oxide of BeO_{1-x},; it was demonstrated that doping wide-band oxides (such as MgO, La_2O_3, $SrTiO_3$ and related perovskites) with *sp*-elements allows a magnetic semimetal state to be realized in some cases, resulting in a material with 100% spin polarization of current carriers – which, without a doubt, is of great practical significance for various applications. Modeling the magnetic properties of nanotubes was also carried out for carbon-, BN-, AlN- and MgO- nanotubes doped with nonmagnetic *sp*-impurities.

In the same context, another intriguing direction of modeling new magnetic materials is remarkable, which was initiated and supervised by Alexander Ivanovskii in the Quantum Chemistry and Spectroscopy Laboratory at the Institute of Solid State Chemistry, UB RAS. This research direction is called “fine tuning” the electronic and magnetic properties of layered semiconducting phases, for instance, having the structure of ZrCuSiAs or $ThCr_2Si_2$, and involves co-doping of the phases in various structural domains, when varying the type and content of each dopant is instrumental in making flexible adjustment in the electronic and magnetic properties of such compounds. His efforts in this direction resulted in the prediction of the first realization of a bipolar magnetic semiconductor (a material with external electric field “switchable” spin polarization carriers). This bipolar magnetic semiconductor was realized among crystalline systems and comprised a manganese and iron-doped layered semiconductor YZnAsO [27]. Further, experimental data on the magnetic properties of LaZnAsO and LaCuSeO phases, co-doped with the atoms of 3*d*− and alkali-earth metals, were also clarified [28]. There is hardly a common opinion on whether a theorist should avoid abstracting far off from the experimentally observed reality or if it is better to be daring enough to go ahead. However, to do justice to the Alexander Ivanovskii's nontrivial intuition, which was amplified by his phenomenal ability to find his bearing among the colossal volumes of science literature, he was surely well balanced in resolving this dilemma.

A. L. Ivanovskii made a significant contribution in the quantum chemistry research of new superconducting materials. Hence, of the vast variety of the research projects, two stand out — the pioneering research endeavors directed and contributed by Alexander Ivanovskii most appreciably. Firstly, a series of works was devoted to studying the properties of superconducting compound MgB_2 and its structural analogs [29-33]. Ivanovskii's laboratory has taken a leading position in the field of diboride research. Note that the article [30] on MgB_2 had once been the only non-empirical study available at the moment of discovery that had investigated the electronic structure and chemical bonding parameters of the compound. Under Ivanovskii's leadership, a large series of modeling works was performed dealing with the analysis of the effect caused by band occupation and crystalline parameters on the band structure, Fermi surface; and major criteria were established for superconductivity in diborides. Secondly, the basic research works on a large family of compounds related to the so-called Fe-As superconductors were devoted to studying their electronic, magnetic, spectroscopic and mechanical properties [34-38].

Analyzing the scientific activity of Alexander Ivanovskii, one cannot overestimate his outstanding qualities as a scientific manager. Throughout his carrier, he pursued collaborations with scientists from Ekaterinburg, Novosibirsk, Saint Petersburg, Moscow, and his contacts were sustaining and fruitful. To honor Ivanovskii's outstanding scientific accomplishments, the State Prize was awarded to him for the research work, which was performed in cooperation with scientists from the Institute of Solid State Chemistry and with a research group headed by Prof. S.P. Gabuda from the Institute of Inorganic Chemistry, Novosibirsk. Most appreciably, his remarkable organizing skills and managerial competence were manifested in his role as Scientific Secretary, Head of Laboratory and Deputy Director at the Institute of Solid State Chemistry. His graciousness to those around him, his democratic approach and most considerate attitude to people, when combined with his ardent zeal and excellence in understanding science mechanisms and research functionality, contributed to a great extent to the efficient work of the Institute and the laboratory that he was leading. His laboratory was a regular winner of scientific grants from the Russian Foundation for Basic Research and other science-oriented foundations (INTAS, CRDF). Alexander Ivanovskii's scientific and managerial competence was a significant contribution that had helped to establish strong links with scientific organizations in Germany, France, USA, and Spain.

In the memory of so many people, Alexander Ivanovskii made a long-lasting impression as a prominent scientist and decent man, truly dedicated to science, education and culture. Being genuinely talented, his creativity extended far beyond his occupational interests: he loved and understood music deeply, relished the beauties of art and literature. In 1982, he received a university degree in art history (from Ural State University after A.M. Gorky). A genuine Russian intellectual, a man of great culture and wisdom, living on drive and determination, with creative excitement and verve — these are his qualities by which he will always be remembered. He was a fascinating researcher, a valuable colleague and a good friend. It is so hard to think of him gone, and words, once written by a Russian poet Nikolay Nekrasov in his 'In Memory of Dobrolyubov' verse, are drumming in our memory as a refrain: "What a torch of reason ceased to burn, What heart has ceased to beat!"

Acknowledgments

The authors thank N. Yu. Pomortseva for their help with materials for publication.

References

[1] Ivanovskii A.L. Modeling of the nanotubular form of the matter. *Russian Chemical Reviews*, **67**, P. 357–374 (1998).

[2] Ivanovskii A.L. Fullerenes and related nanoparticles incapsulated within nanotubes: synthesis, properties and modeling of new hybrid nanostructures. *Journal of Inorganic Chemistry*, **48**, P. 1–15 (2003).

[3] Ivanovskii A.L. Titanium nanocarbides: synthesis and modeling. Theoretical and Experimental Chemistry, 2007, 43, 1-23.

[4] Ivanovskii A.L. *Nanotubular Forms of Matter.* Ekaterinburg: ISSC UB RAS, 172 p. (1999). (in Russian)

[5] Ivanovskii A.L. Non-carbon nanotubes: Synthesis and simulation. *Russian Chemical Reviews*, **71**, P. 175–194 (2002).

[6] Zakharova G.S., Volkov V.L., Ivanovskaya V.V., Ivanovskii A.L. Nanotubes and related nanostructures of d-metal oxides: Synthesis and computer design. *Russian Chemical Reviews*, **74**, P. 587–618 (2005).

[7] Zakharova G.S., Volkov V.L., Ivanovskaya V.V., Ivanovskii A.L. *Nanotubes and Related Nanostructures of Metal Oxides.* Ekaterinburg: ISSC UB RAS, 240 p. (2005). (in Russian)

[8] Enyashin A.N. Theoretical studies of inorganic fullerenes and fullerene-like particles. *Israel Journal of Chemistry*, **50**, P. 468–483 (2010).

[9] Ivanovskii A.L. New layered carbon allotropes and their nanostructures: modeling of atomic structure, chemical bonding and electronic properties. *Journal of Inorganic Chemistry*, **50**, P. 1408–1422 (2005).

[10] Ivanovskii A.L. Search for superhard carbon: between graphite and diamond. *Journal of Superhard Materials*, **35**, P. 1–14 (2013).

[11] Pokropivny V.V., Ivanovskii A.L. New nanoforms of carbon and boron nitride. *Russian Chemical Reviews*, **77**, P. 837–873 (2008).

[12] Belenkov E.A., Ivanovskaya V.V., Ivanovskii A.L. *Nanodiamonds and Related Carbon Nanomaterials.* Ekaterinburg: ISSC UB RAS, 169 p. (2008).(in Russian)

[13] Ivanovskii A.L. Graphene-based and graphene-like materials. *Russian Chemical Reviews*, **81**, P. 571–605 (2012).

[14] Ivanovskii A.L. Graphynes and graphdyines. *Progress in Solid State Chemistry*, **41**, P. 1–19 (2013).

[15] Ivanovskii A.L., Enyashin A.N. Graphene-like transition-metal nanocarbides and nanonitrides. *Russian Chemical Reviews*, **82**, P. 735–746 (2013).

[16] Gubanov V.A., Ivanovskii A.L., Zhukov V.P. *Electronic structure of refractory carbides and nitrides.* Cambridge, University Press, 250 p. (1995).

[17] Ivanovskii A.L. Gubanov V.A., Kurmaev E.Z., Shveikin G.P. Electronic structure and the chemical bond in non-stoichimetric refractory compounds of transition metals in sub-groups IVA and Va. *Russian Chemical Reviews*, **52**, P. 395–412 (1983).

[18] Suetin D.V., Shein I.R., Ivanovskii A.L. Tungsten carbides and nitrides and ternary systems based on them: the electronic structure, chemical bonding and properties. *Russian Chemical Reviews*, **79**, P. 611–634 (2010).

[19] Medvedeva N.I, Ivanovskij A.L, Novikov D.L, Freeman A.J. Electronic properties of Ti_3SiC_2-based solid solutions. *Physical Review B*, **58**, P. 16042–16049 (1998).

[20] Ivanovskii A.L., Medvedeva N.I., Enyashin A.N. Ab initio prediction of structural, electronic and mechanical properties of Ti_3SiC_2, Chapter in book: “MAX Phases: Microstructure, Properties and Applications” (Eds. J. Low, Y. Zhou), Nova Sci. Publ., N.Y., pp. 183–203 (2012).

[21] Shein I.R., Ivanovskii A.L. Graphene-like titanium carbides and nitrides $Ti_{n+1}C_n$, $Ti_{n+1}N_n$ (n=1, 2, and 3) from de-intercalated MAX phases: First-principles probing of their structural, electronic properties and relative stability. *Cmputational Materials Science*, **65**, P. 104–114 (2012).

[22] Shein I.R., Ivanovskii A.L. Planar nano-block structures $Ti_{n+1}Al_{0.5}C_n$ and $Ti_{n+1}C_n$ (n=1, and 2) from MAX phases: Structural, electronic properties and relative stability from first principles calculations Superlattices and Microstructures, **52**, P. 147–157 (2012).

[23] Ivanovskii A.L. Platinum group metal nitrides and carbides: synthesis, properties and simulation. *Russian Chemical Reviews*, **78**, P. 303–318 (2009).

[24] Suetin D.V., Shein I.R, Ivanovskii A.L. Structural, electronic and magnetic properties of eta carbides (Fe_3W_3C, Fe_6W_6C, Co_3W_3C and Co_6W_6C) from first principles calculations. *Physica B*, **404**, P. 3544–3549 (2009).

[25] Suetin D.V., Shein I.R, Ivanovskii A.L. Structural, elastic, electronic and magnetic properties of perovskite-like Co_3WC, Rh_3WC and Ir_3WC from first principles calculations. *Solid State Science*, **12**, P. 814–817 (2010).

[26] Ivanovskii A.L. Magnetic effects induced by sp impurities and defects in nonmagnetic sp materials. *Physics-Uspekhi* (Advances in Physical Sciences), **50**, P. 1031–1052 (2007).

[27] Bannikov V.V., Ivanovskii A.L. Ab initio search of novel bipolar magnetic semiconductors: layered YZnAsO doped with Fe and Mn. *JETP Letters*, **96**, P. 735–738 (2013).

[28] Bannikov V. V., Ivanovskii A.L. Electronic and magnetic properties of a new 2D diluted magnetic semiconductor $La_{1-x}Ba_xZn_{1-x}Mn_xAsO$ from ab initio calculations. *JETP Letters*, **98**, P. 393–396 (2013).

[29] Medvedeva N.I., Ivanovskii A.L., Medvedeva J.E., Freeman A.J. Electronic structure of superconducting MgB_2 and related binary and ternary borides. *Physical Review B*, **64**, P. 020502-4(R) (2001).

[30] Ivanovskii A.L., Medvedeva N.I. Interatomic interactions and electronic structure of hexagonal magnesium, aluminum, and silicon diborides: ab initio full-potential LMTO calculations. *Russian Journal of Inorganic Chemistry*, **45**, P. 1234–1240 (2000).

[31] Shein I.R., Ivanovskii A.L. Elastic properties of mono- and polycrystalline hexagonal AlB_2-like diborides of s, p and d metals from first-principles calculations. *Journal of Physics*, **20**, P. 415218 (2008).

[32] Ivanovskii A.L. Mechanical and electronic properties of diborides of transition 3d-5d metals from first principles: Toward search of novel ultra-incompressible and superhard materials. *Progress in Materials Science*, **57**, P. 184–228 (2012).

[33] Ivanovskii A.L. Band structure and properties of superconducting MgB_2 and related compounds (a review). *Physics of Solid State*, **45**, P. 1829–1859 (2003).

[34] Ivanovskii A.L. New high-temperature superconductors based on rare-earth and transition metal oxyarsenides and related phases: synthesis, properties, and simulations. *Physics-Uspekhi* (Advances in Physical Sciences), **51**, P. 1229–1260 (2008).

[35] Ivanovskii A.L. New superconductors based on five-component transition metal oxypnictides. *Russian Chemical Reviews*, **79**, P. 1–11 (2010).

[36] Shein I.R., Ivanovskii A.L. Structural and electronic properties of the 17 K superconductor $Sr_2ScFePO_3$ in comparison to $Sr_2ScFeAsO_3$ from first principles calculations. *Physical Review B*, **79**, P. 245115 (2009).

[37] Ivanovskii A.L. New ternary $ThCr_2Si_2$-type iron-selenide superconducting materials: Synthesis, properties and simulations. *Physica C*, **471**, P. 409–427 (2011).

[38] Shein I.R., Ivanovskii A.L. Electronic band structure, Fermi surface, and elastic properties of polymorphs of the 5.2 K iron-free superconductor $SrPt_2As_2$ from first-principles calculations. *Physical Review B*, **83**, P. 104501 (2011).

NANOSYSTEMS: PHYSICS, CHEMISTRY, MATHEMATICS, 2014, 5 (4), P. 467–476

SCIENTIFIC ACTIVITIES OF PROFESSOR A. L. IVANOVSKII IN BIBLIOMETRIC INDICES

A. V. Deryabina, A. S. Vorokh
Institute of Solid State Chemistry UB RAS, Ekaterinburg, Russia
vorokh@ihim.uran.ru

PACS 01.60.+q

The publication activity dynamics of Prof. A. L. Ivanovskii has been examined and the bibliometric indices of his scientific work have been analyzed.

Keywords: Scientometrics, Bibliometrics, Ivanovskii A.L.

Received: 16 June 2014
Revised: 30 June 2014

Alexander Leonidovich Ivanovskii (1953–2014), Professor, Doctor of Chemistry, was known in the scientific community as a leading specialist in the application of quantum-chemical computational methods for the modeling of physicochemical properties of novel compounds and materials. For almost forty years of his scientific career (1976–2014), he, personally and with co-authors, published more than 860 scientific works in domestic and foreign journals, 14 monographs and more than 20 reviews devoted to computational studies of materials science and inorganic systems. The research findings obtained by A. L. Ivanovskii are highly valued in the scientific community. His papers have high citation indices in international scientific and technical information resources.

The investigation of personal bibliographies of scientists is of theoretical and applied importance because it allows one to obtain individual and comparative quantitative characteristics of publication activity and efficiency of scientific work of a scientist. This also allows one to determine the place of the scientists' effort in the developed domains of science as well as to study the processes of formation and change in research trends in one or several scientific fields [1].

In this work, we analyze the dynamics of bibliometric indices of the scientific heritage of A. L. Ivanovskii from 1978 to 2013. In 2014, several articles by A. L. Ivanovskii have been already published and perhaps other works will appear later; that is why the quantitative indicators of the scientific heritage of A. L. Ivanovskii will change slightly in the future. The electronic database search was carried out in May 2014 with consideration of different spelling variants of the surname (Table 1). Figure 1 presents the general dynamics of publication activity of .L. Ivanovskii in the considered period. The global scientific and technical information resources — Web of Science (WoS) [2], Scopus [3], Chemical Abstracts Plus (CAPlus) [4] and the Russian Science Citation Index (RSCI) [5] have been used. The experience in the bibliometric analysis of chemists' works earned after I.V. Zibareva et al. reveals that, the application of different electronic databases provides more complete volume of examined material since each database has its own peculiarities (different time periods, primary sources, functional capabilities, thematic scope) [6, 7, 8].

Analysis of the data in Fig. 1 allows one to distinguish three stages in the scientific work of A. L. Ivanovskii depending on his publication activity. In turn, each stage can be

TABLE 1. The main bibliometric indices of scientific activities of A. L. Ivanovskii

Index	**RSCI**	**WoS**	**Scopus**
Total number of publications	828	541	531
Total number of citations	5830	4022	3646
Average number of citations per 1 publication	5.6	7.4	6.8
Hirsch index	28	27	27

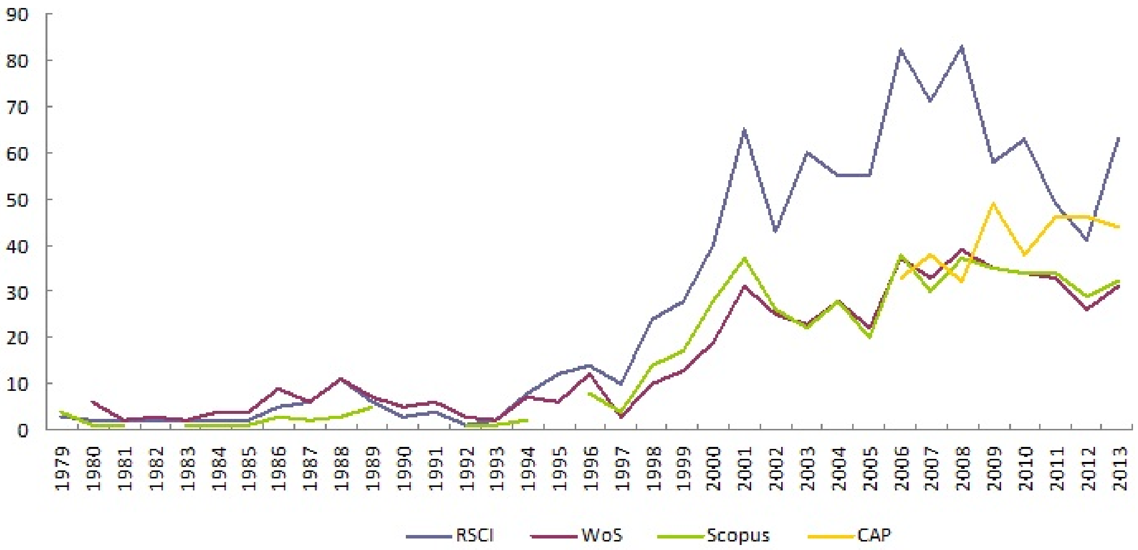

FIG. 1. The general dynamics of publication activity of A. L. Ivanovskii. The number of published items on the year is depicted concerning to different electronic databases

subdivided into separate phases. The first stage, from 1979 to 1987, reflects his formation as a scientist. The activity of young researcher is related to the investigations of the electronic structure, chemical bonding and interatomic interactions in transition metal compounds. This period can be characterized by low publication activity: about 30 papers are published in total. The activity peaks in 1986, when two monographs of A. L. Ivanovskii (in co-authorship with V. A. Gubanov, M. V. Ryzhkov, G. P. Shveikin) devoted to the evaluation of quantum chemical research methods have been published. As a result of this stage, the main approaches in the quantum chemical simulation of the properties of complex multi-component compounds and in the search of their optimal compositions have been formulated.

The second stage of the scientific activity begins in 1988, after the defense of his doctoral thesis. At that time, A. L. Ivanovskii is 36 years old, and everything promises the beginning of the most fruitful creative period. However, judging by the number of published articles, a decline begins, which continues from 1991 to 1993. This slowdown is typical for the majority of Russian scientists and is related to the general situation in the country. The Soviet system was disorganized, the support for research and development was drastically reduced, and science teetered on the brink of extinction.

In 1994, the third stage in the academic career of A. L. Ivanovskii begins, which can be characterized as a research and organization period. He got elected among other candidates to the position of the Head of Laboratory of Solid State Chemistry and Spectroscopy at ISSC UB RAS. At that time, new forms of financing of the Russian science emerge: the support of scientists from the Russian Foundation of Basic Research was actively undertaken, the International Soros Science Education Program was created. Thanks to these and other foundations, Russian scientists were once again actively involved in R&D work. Besides, A. L. Ivanovskii directs the theoretical group and these reasons can explain the fact that more than fivefold increase in the publication activities of A. L. Ivanovskii takes place in the next 7 years. Under his leadership, investigations of chemical bonding, electronic structure and physicochemical properties of carbides, nitrides, silicides, hydrides, oxides, multicomponent solid solutions and alloys were carried out in the laboratory. Together with his team, A. L. Ivanovskii elaborated original methods, performed research work and developed general theoretical models for the targeted control over the functional properties of inorganic compounds by modified structural defects. The organized teamwork provided a purposeful search for novel materials with pre-assigned characteristics (cermets, heat-resisting coatings, superconductors, nano-systems).

The phase of the highest creative productivity of the scientist falls on the first decade of the 21^{st} century. The research team of A. L. Ivanovskii was reinvigorated by young scientists. About 80% of his publications are written in the last 13 years. On average, A. L. Ivanovskii published about 30 papers per year (or about 60 papers according to RSCI, which is probably due to the peculiarities of the Russian database, which takes into account both the original works in Russian and their English versions [8]). Obviously, such high productivity is due to the active participation in the rise of a new research area – computational materials science for inorganic nanostructures (nanotubes and fullerene-like clusters) and nanomaterials based thereon.

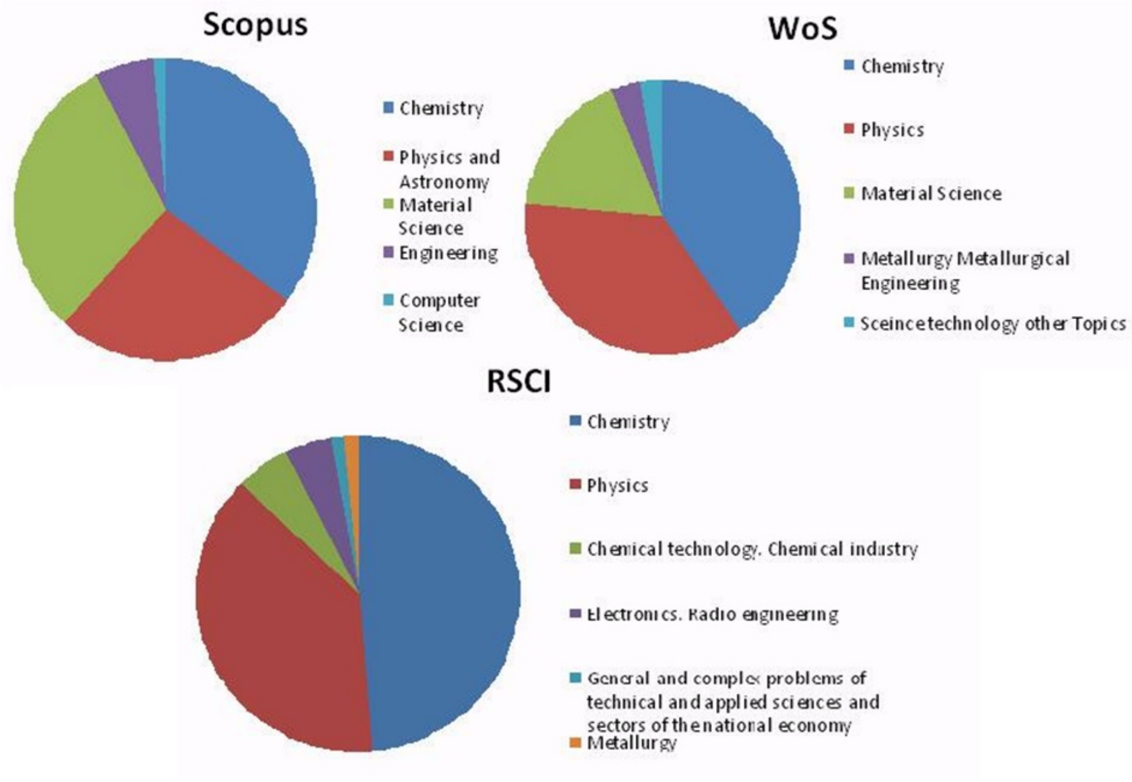

FIG. 2. The object domains of research in the publications of A. L. Ivanovskii

TABLE 2. Key words from the publications of A. L. Ivanovskii (Scopus)

Key word	**Quantity**
Electronic properties	89
Electronic structure / Band structure	67 / 19
Chemical structure	39
Calculations/ Ab initio calculations/ First-principles calculation/ First-principles	39 / 37 / 31 / 24
Chemical bond / Chemical bonds	28 / 24
Superconductivity / Superconducting materials	28 / 19
Structure / Structure analysis	26 / 19
Elastic properties / Elasticity / Elastic moduli	25 /19 /18
Density functional theory	24
Nanotubes / Fullerene	22 / 13
Magnetic properties	21
Carbon	19
Stoichiometry	18
Inter-atomic bonding / Molecular interaction	16 / 16
Unclassified drug	16

The works of A. L. Ivanovskii are at the intersection of three distinct domains, among which the major areas are Chemistry and Physics (Physics and Astronomy in Scopus) (see Fig. 2). Materials science is a separate research field in Scopus and WoS and also constitutes a significant part of his research. This is indicative of clearly defined scientific interest at the junction of three scientific disciplines. The use of keywords determined by Scopus show that the works of A. L. Ivanovskii deal mainly with electronic properties, electronic structure, chemical structure, first-principles calculations, chemical bond and stoichiometry (Table 2). These keywords allow one to single out from general articles the works where the properties of a substance (superconductivity, elasticity, magnetic properties) and the forms of a substance (nanotubes, fullerenes) play decisive roles.

The types of publication items are analyzed in Table 3. The main body of the creative heritage of A. L. Ivanovskii consists of the journal articles. In the foreign databases, review articles are classified in a separate category (review). According to CAPlus, data this type of publication possesses more than 10% of the total number of articles; in other databases, this index is smaller. It is worth noting that, among the 10 most frequently cited papers of A. L. Ivanovskii, three are reviews. Although A. L. Ivanovskii is known primarily as a theoretician, he is listed as an inventor on several patents (e.g. a device for ultrasound transmission, a method for producing ceramics etc.).

The list of journals, in which A. L. Ivanovskii publishes his works, includes more than one hundred titles, which confirms the multidisciplinary character of his research. At the same time, there are several journals, to which he contributes on a regular basis, in particular, *Zhurnal strukturnoy khimii*, *Zhurnal neorganicheskoy khimii* and *Fizika tvyordogo tela* among the Russian periodicals and *Physica Status Solidi B Basic Research* (Germany) occupying the leading place among foreign journals (Table 4).

Table 3. The distribution of the works of A. L. Ivanovskii by the types of publications

	APlus*	**RSCI**	**WoS**	**Scopus**
Article in journal / review	271/27	661	474/32	471/17
Article in conference proceedings	1	7	8	5
Patent	1	6		
Report		4		
Book or collection of articles		3		1

* In CAPlus, the authors considered the data for a period from 2006 to 2013.

Table 4. The distribution of the publications of A. L. Ivanovskii by the journals

Journal	**RSCI**	**WoS**	**Scopus**
Zhurnal strukturnoy khimii	51		
Journal of Structural Chemistry	20	54	54
Zhurnal neorganicheskoy khimii	40		
Russian Journal of Inorganic Chemistry	27	34	38
Fizika tvyordogo tela	39		
Physics of the Solid State	17	30	18
DOKLADY AKADEMII NAUK	36	3	
Doklady Chemistry	3		
Doklady Earth Sciences	2		
Doklady Physical Chemistry		21	22
Uspekhi khimii	30	9	
Russian Chemical Reviews		6	
Pisma v Zhurnal eksperimentalnoy i teoreticheskoy fiziki	28		
Journal of Experimental and Theoretical Physics Letters (JETP Letters)	17	24	19
Physica Status Solidi B Basic Research		13	21
Inorganic Materials		30	20
Mendeleev Communications	17	10	

The greatest number of works, reflected in the scientific and technical information resources, is published in English, the difference in the indices being small (see Fig. 3). The RSCI data are different: 82% of the articles are published in the Russian journals and 40% — in the Russian journals in translation.

The scientific activity of Prof. A. L. Ivanovskii is connected to a single institution — the Institute of Solid State Chemistry of the Ural Branch of the Russian Academy of Sciences (before 1991, the Institute of Chemistry UB USSR AS). The most of his articles is represented by this institute. In the foreign automatic search systems, the name of the Institute goes as the Institute of Solid State Chemistry, but more general names should be also taken into consideration during the search: Russian Academy of Sciences, Ural Branch Russian Academy of Sciences. For a long period of time, A. L. Ivanovskii cooperated with the Ural Federal University named after the First President of Russia B. N. Yeltsin (Ural

Table 5. The scientific cooperation of A. L. Ivanovskii

Co-author	**Years of cooperation**	**RSCI**	**WoS**	**Scopus**
Shein I.R.	2001 – 2013*	288	193	179
Enyashin A.N.	2003 – 2013	137	87	89
Medvedeva N.I.	1994 – 2013	121	66	68
Makurin Yu.N.	1999 – 2010	109	53	62
Ivanovskaya V.V.	2001 – 2011	80	38	42
Sofronov A.A.	1999 – 2006	69	33	46
Shveikin G.P.	1979 – 2006	62	34	28
Bannikov V.V.	2007 – 2013	49	40	39
Gubanov V.A.	1979 – 1992	38	41	22
Suetin D.V.	2008 – 2013	33	26	25
Okatov S.V.	1999 – 2005	32	18	21
Bamburov V.G.	1998 – 2012	30	13	15
Kiyko V.S.	2001 – 2011	30	20	21
Gorbunova V.M.	2006 – 2010	25	13	12
Kuznetsov M.V.	1995 – 2012	25	11	15
Anisimov V.I.	1979 – 2013	19	11	7
Novikov D.L.	1986 – 2002	19	13	7
Kozhevnikov V.L.	2005 – 2008	18	11	9
Moiseyev G.K.	2005 – 2008	18	8	8
Ryzhkov M.V.	1999 – 2013	18	12	-
Shein K.I.	2004 – 2007	17	13	-
Yuryeva E.I.	2000 – 2006	16	7	7
Medvedeva Yu.E.	1998 – 2005	13	5	4
Kurmayev E.Z.	1979 – 2004	12	16	12
Cherkashenko V.M.	1984 – 2001	12	5	5
Votyakov S.L.	2002 – 2013	11	6	5
Shchapova Yu.V.	2002 – 2013	11	6	5
Shalaeva E.V.	1995 – 2012	11	3	-
Gusev A.I.	2001 – 2008	10	3	5

* The first three papers co-authored by A.L. Ivanovskii and I.R. Shein were published as early as in 1990; however then there was a 10-year interval in this creative tandem.

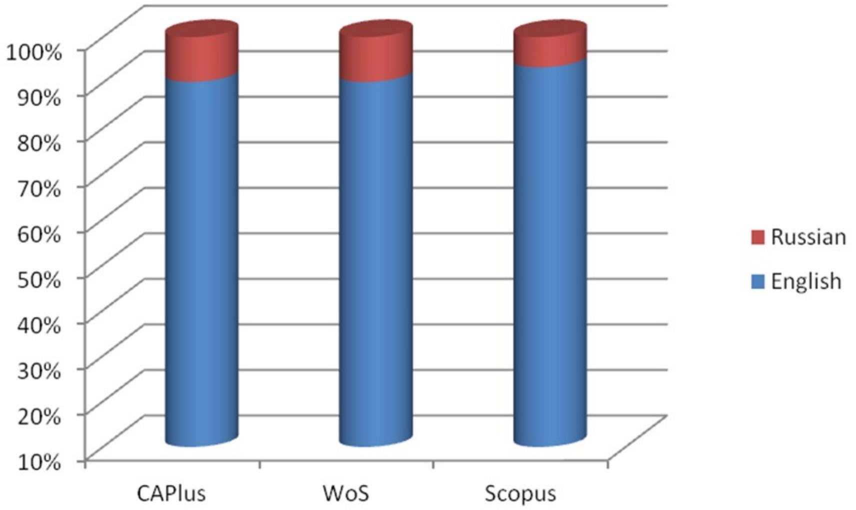

Fig. 3. The ratio of the articles of A. L. Ivanovskii published in Russian and English

Federal University), giving lectures on quantum and general chemistry at the Department of Chemistry and about 10% of his publications are affiliated with this University.

A characteristic feature of the research work of A. L. Ivanovskii is productive scientific co-authorship. The number of all co-authors of A. L. Ivanovskii exceeds one hundred. Table 5 lists the names of scientists who are the co-authors of more than 10 papers. According to this data several groups of co-authors can be distinguished. The first group can be tentatively called *tutors*. They are characterized by long-term and fruitful cooperation limited in time (G. P. Shveikin, V. A. Gubanov). The second group — *colleagues* — is represented by long-standing co-authorship of different intensity (N. I. Medvedeva, V. I. Anisimov). The third group — *pupils* — is characterized by temporary fruitful cooperation (V. V. Ivanovskaya, A. A. Sofronov, S. V. Okatov). It is noteworthy that some pupils later become the most productive co-authors (I. R. Shein, A. N. Enyashin).

In view of the aforementioned, the geography of cooperation of A. L. Ivanovskii covers primarily the Russian Federation. Among foreign countries, the most intensive cooperation took place with German scientific groups and to a lesser degree — with scientists from Switzerland, France and the US (Table 6).

Table 6. The geography of co-authors of A. L. Ivanovskii

Country	**WoS**	**Scopus**
Russian Federation	507	446
Germany	19	18
Switzerland	4	5
France	3	3
USA	6	3

Three of the ten most cited papers are reviews written by A. L. Ivanovskii as the sole author (Table 7). This is indicative of his tremendous working capacity and a wide scientific range of investigations. The current decade is marked by the most fruitful collaboration with the scientists of the Institute. A strong research team has been formed, which is regularly

Table 7. The most frequently cited articles (times cited)

Article	**RSCI**	**WoS**	**Scopus**
Ivanovskii A.L. Non-carbon nanotubes: synthesis and simulation. *Russ.Chem.Rev.*, 71, 3, P. 175–194 (2002)	121	60	41
Medvedeva N.I., Ivanovskii A.L., Medvedeva J.E., Freeman A.J. Electronic structure of superconducting MgB_2 and related binary and ternary borides. *Phys. Rev. B*, 64, 2, P. 205021–205024 (2001)	119	92	119
Medvedeva N.I., Novikov D.L., Ivanovskii A.L., Kuznetsov M.V., Freeman A.J. Electronic properties of Ti_3SiC_2-based solid solutions. *Phys. Rev. B*, 58, 24, P. 16042–16050 (1998)	99	89	98
Ivanovskii A.L. New high-temperature superconductors based on rare-earth and transition metal oxyarsenides and related phases: synthesis, properties and simulations. *Phys.Uspekhi*, 51, 12, P. 1229–1260 (2008).	115	87	90
Shein I.R., Ivanovskii A.L. Elastic properties of mono-and polycrystalline hexagonal AlB_2-like diborides of s, p and d metals from first-principles calculations. *J. Phys. Condens. Matter.* 20, 41, 415218 (2008).	81	90	74
Enyashin A.N., Ivanovskii A.L. Graphene allotropes. *Phys. Status Solidi (B)*, 248, 8, P. 1879–1883 (2011).	39	53	55
Makurin Yu.N., Sofronov A.A., Gusev A.I., Ivanovskii A.L. Electronic structure and chemical stabilization of C_{28} fullerene. *Chem. Phys.*, 270, 2, P. 293–308 (2001).	53	–	51
Shein I.R., Medvedeva N.I., Ivanovskii A.L. Electronic and structural properties of cementite-type M_3X (M=Fe, Co, Ni; X=C or B) by first principles calculations. *Physica B: Cond.Matter*, 371, 1, P. 126–132 (2006).	48	49	50
Ivanovskii A.L. Band Structure and Properties of Superconducting MgB_2 and Related Compounds (a Review). *PlaceNameplacePhys. PlaceNameSolid PlaceTypeState*, 45, 10, P. 1829–1859 (2003).	63	51	47
Zakharova G.S., Volkov V.L., Ivanovskaya V.V., Ivanovskii A.L. Nanotubes and related nanostructures of d-metal oxides: Synthesis and computer design. *Uspekhi Khimii*, 74, 7, P. 651–685 (2005).	74	33	45

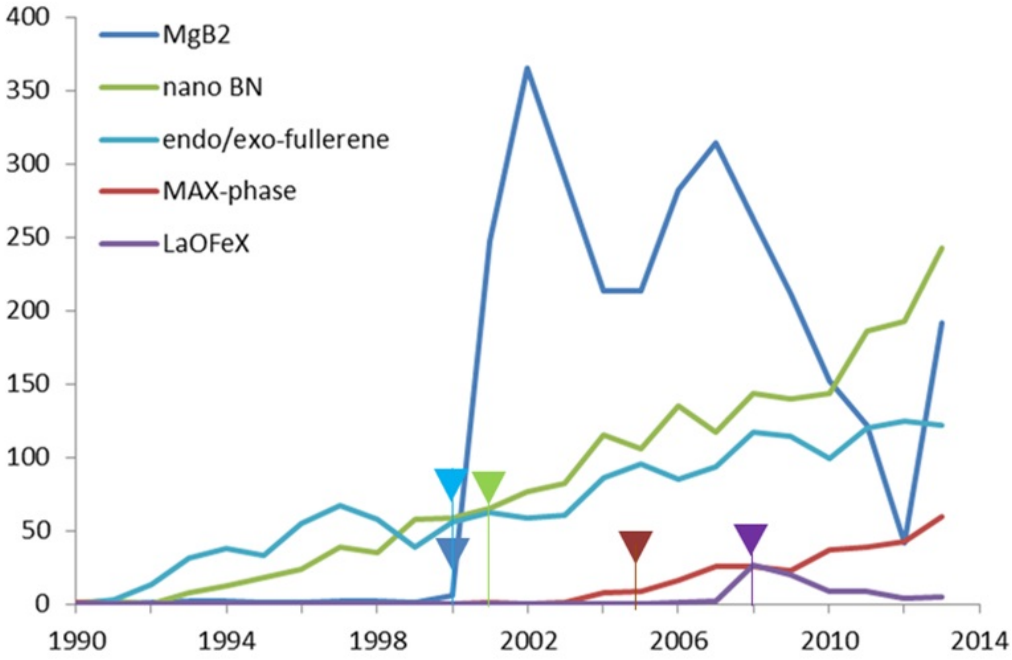

FIG. 4. The number of articles and review papers published in the world during one year on various topics (Scopus). The first works of A. L. Ivanovskii devoted to these topics are marked by arrows with vertical lines

reinforced with post-graduates. This period is a peak of publication activity with maxima of 37 and 39 publications in 2006 and 2008 according to WoS, 37 and 38 publications according to Scopus and 83 publications according to RSCI. The main drawings up of scientific work are considered by A. L. Ivanovskii as a paper published in a scientific journal. It should be noted again that most of his articles are written by two or three co-authors. The review papers hold a special place, and here, A. L. Ivanovskii often acts as the sole author. Although the majority of his papers are published in the Russian journals, the works of A. L. Ivanovskii are recognized and known worldwide in the scientific community.

It is significant that A. L. Ivanovskii often anticipated the growth of interest in new hot topics. Figure 4 demonstrates the number of the world publications (Scopus) in the main areas, where A. L. Ivanovskii investigated. As is seen, his papers represent avant-garde studies. This is most visually illustrated both by the abrupt boom in the investigations of magnesium diboride (MgB_2 curve) and by the growing interest in MAX phases (MAX-phase). The works of A. L. Ivanovskii devoted to nano-dimensional boron nitride (nano BN) and special endo- and exohedral forms of fullerenes (endo/exo-fullerene) are at the very beginning of the uprising trend. Naturally, the preliminaary searches do not always end successfully. So, a growth in the interest to the oxypnictides (LaOFeX) as new promising superconducting materials is almost gone today. On the one hand, such analysis reveals a large insight of the scientist and his ability to foresee, if the interest in a topic in the world scientific community grows. On the other hand, with the erosion of interest in the topic, it illustrates the relevance of search and high complexity of potential topicality assessment. However, such work requires supreme organization since all resources in this direction should be mobilized over a short period of time. Besides, personal volitional powers of scientist are of much importance, since the already explored research areas have to be sacrificed for the development of a new topic. In the judgment of his colleagues, it is exactly these qualities that were exemplified by A. L. Ivanovskii.

The presented bibliometric indices analysis of A. L. Ivanovskii's research activities is preliminary and is based only on the examination of statistical data from the global scientific and technical information resources. Undoubtedly, comprehensive evaluation of activities of a scientist calls for a more thorough and profound examination, compilation of a detailed bibliographic index of works, as well as analysis of scientific and organizational activities, involvement in grants (projects) and teaching experience. On the whole, the performed analysis reveals the pronounced characteristic features of Prof. A. L. Ivanovskii as a scientist – the ability to generate new ideas, to arrange team work and to organize effective cooperation. The publication activity of A. L. Ivanovskii shows that he was at the peak of possible work capacity and reached the maximum efficiency of his work as a scientist and an organizer. Unfortunately, many other problems of computational materials science will not be addressed by the researcher: his sudden and untimely death ended this important scientific activity.

References

[1] Rybachuk V.P., Videnina N.G. Scientometric measurement of scientific activities of G. M. Dobrov. *Science and Science of Science*, **1**, P. 24–43 (2009). [in Russian]

[2] URL: http://apps.webofknowledge.com

[3] URL: http://www.scopus.com

[4] URL: https://chemabs.cas.org

[5] URL: http://elibrary.ru/defaultx.asp

[6] Buznik V.M., Zibareva I.V. Bibliometric analysis of scientific publications of Academician Yu.D. Tretyakov. *Nanosistemy: fizika, khimiya, matematika*, **4**(1), P. 14–23 (2013). [in Russian]

[7] Zibareva I.V. Scientific publications of Academician N.N. Vorozhtsova – bibliometric essay. *Khimiya v interesakh ustoichivogo razvitiya*, **15**(5), P. 549–555 (2007). [in Russian]

[8] Zibareva I.V., Parmon V.N. The examination of institutes of the Russian Academy of sciences with the use of the Russian citation index. *Vestnik rossiiskoy akademii nauk*, **82**(9), P. 779–789 (2012). [in Russian]

NANOSYSTEMS: PHYSICS, CHEMISTRY, MATHEMATICS, 2014, 5 (4), P. 477–485

CHLORGRAPHYNES: FORMATION PATH, STRUCTURE AND ELECTRONIC PROPERTIES

A. L. Ivanovskii, A. N. Enyashin

Institute of Solid State Chemistry UB RAS, Ekaterinburg, Russia

enyashin@ihim.uran.ru

PACS 61.48.Gh, 68.43.-h, 73.22.Pr, 81.05.ue

The presence in graphyne sheets of a variable amount of sp^2 and sp^1 carbon atoms suggests a high ability of these nanostructures for saturation. E.g., covalent binding of chlorine atoms would lead to sp^3- and new sp^2 hybridized carbon atoms, and the emergence of chlorgraphynes (chlorinated graphynes) with variable Cl/C stoichiometry may be expected. Here, employing DFT band structure calculations, a series of new graphyne derivatives — layered chlorgraphynes — is examined on example of α-graphyne. The possible formation path of chlorgraphynes as a set of consecutive free-radical additions of Cl atoms is established. From examples of a few representative compounds, the trends in the structural and electronic properties are discussed, depending on their stoichiometry.

Keywords: Graphynes, carbon allotropes, graphene derivatives, DFT calculations.

Received: 16 June 2014
Revised: 30 June 2014

1. Introduction

Graphene, a two-dimensional (2D) mono-atomic-thick sheet of sp^2 hybridized carbon, exhibits a unique combination of structural, mechanical, electronic and thermal properties [1,2]. It is viewed today as an advanced material for use in a vast range of nanotechnology applications [3-5]. However, “graphene is not the end of the road”; and numerous efforts have been focused recently on the search for graphene-based materials with novel functionalities [6], particularly, through adsorption of various atoms or molecules onto the surface of graphene [7,8]. For example such atoms as fluorine, oxygen, or hydrogen adsorbed on graphene can form covalent bonds with the carbon atoms, which lead to a change in the hybridization state of C atoms from sp^2 to sp^3 and may provoke the opening of a band gap. In this manner, fluorination of graphene gives rise to the wide-band-gap 2D crystals, which were termed *fluorographenes* [9]. A set of outstanding chemical and physical properties for single-layered fluorographenes has been already found experimentally and predicted theoretically [8-17]. These materials, with a variable F/C content (up to the stoichiometry CF), may be considered as a promising platform for further applications.

At the same time, the versatile flexibility of carbon to form a few competing hybridization states allows one to design numerous types of flat single-atom-thick carbon networks: so-called graphene allotropes [18]. One of interesting families of these allotropes is represented by so-called *graphynes*, which can be described as graphene lattices, where some or all aromatic =C=C= bonds are modified by the insertion of acetylenic linkages (–C≡C–) [19]. These carbon (sp^2+sp^1) sheets with a high level of π-conjunction, with uniformly distributed pores, and with density much less than that of graphene, possess unusual electronic properties, nonlinear optical susceptibility, thermal resistance, conductivity, and through-sheet transport of ions [20-23]. Currently, they are considered as promising materials for nanoelectronics, for hydrogen storage, as membranes (for example, for hydrogen separation from syngas — as an alternative of the graphene nanomesh), for energy storage applications or as candidates for the anode materials in batteries [24-26]. Tuning of these materials' properties should be critical for their further application. Analogously to graphene, it might be achieved using surface chemisorption of hydrogen or fluorine atoms [13,14,16,17]. Quantum-chemical calculations demonstrate that the electronic and transport properties of modified carbon layers should be very sensitive to the surface arrangement of adsorbed atoms. Yet, both experimental and theoretical work show that the formation of a desired configuration of ad-atoms on the layers cannot be released in the large scales and has mainly casual character.

While the hydrogen, fluorine and oxygen derivatives of graphene and graphyne layers are profoundly studied, the information about other possible types of derivatives is lacking. In contrast to H or F atoms, Cl atoms have larger atomic radii. The latter magnifies the role of steric factors and may lead to a more selective chemisorption of ad-atoms, i.e. to a narrower family of possible types of modified layers. Herein, we theoretically explore the structural, electronic properties and stability for the consequence of hypothetical chlorinated graphynes (*chlorgraphynes*), which could be fabricated by chlorination of a graphyne layer and could become likely candidates for the engineering of novel electronics materials.

2. Computational details

All calculations were performed by means of the density functional theory (DFT) [27] using the SIESTA 2.0 code [28,29] within the local-density approximation (LDA) with the exchange–correlation potential in the Perdew-Zunger form [30]. The core electrons were treated within the frozen core approximation using norm-conserving Troullier–Martins pseudopotentials [31]. The valence electrons were taken to be $2s^2 2p^2$ for C and $3s^2 3p^5$ for Cl. The pseudopotential core radii were chosen as suggested by Martins and equal to 1.50 and 1.54 bohr for s- and p-states of C, and 1.75 bohr for both $s-$ and p-states of Cl. In all calculations, only single-ζ basis set was used for all atoms. For k-point sampling, a cutoff of 10 Å was used [32]. The k-point mesh was generated by the method of Monkhorst and Pack [33]. A cutoff of 350 Ry for the real-space grid integration was utilized. All calculations were performed using variable-cell and atomic position relaxation, with convergence criteria set to correspond to the maximum residual stress of 0.1 GPa for each component of the stress tensor, and the maximum residual force component of 0.01 eV/Å. Initial interlayer spacing along c-direction of a hexagonal or an oblique lattice was set to 50 Å.

As a representative of graphyne layers, the layer of α-graphyne (so-called *supergraphene*) was selected (Fig. 1). This hexagonal carbon network consists of sp^2-hybridized C atoms interlinked via dimers of sp-hybridized C atoms and contains 8 atoms per unit cell. A possible reaction path for the full chlorination of α-graphyne was established as a set of consecutive free-radical additions of single Cl atoms. At every step of the reaction path all possible variants of Cl atom anchoring to the carbon atoms were analyzed. Afterwards, the most stable isomer found served as the ancestor for the next step. In total, the chlorgraphynes with stoichiometric compositions C_8Cl_n (n = 1 – 14) and different ordering of Cl atoms were taken into consideration, which required calculations for 78 compounds.

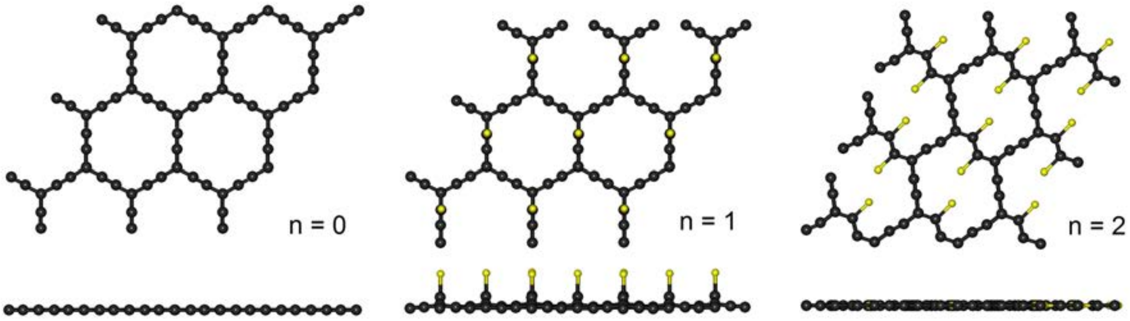

FIG. 1. Optimized atomic structures for the layers of pure α-graphyne (n=0) and the most stable isomers of chlorgraphynes C_8Cl_n with low Cl content (top and side views are depicted)

3. Results and Discussion

3.1. Electronic structure of pure α-Graphyne

The first clue about the reactivity of α-graphyne can be found from the analysis of the band structure. In terms of electronic structure, lattice symmetry and chemical bonding, pure α-graphyne is the closest relative of graphene. Hexagonal network of α-graphyne possesses the picture of band structure with characteristic crossing of the bands at the Fermi level in K-point (Dirac cones) (Fig. 2). The near-Fermi bands are composed of states from the broadly conjugated π-system of $2p_z$C-orbitals from both sp^2- and sp-hybridized C atoms. Both features should provide semimetallic type of conductivity and superior mobility of electrons in α-graphyne similar to those in the graphene [18].

However, in contrast to the graphene, the band structure of α-graphyne is characterized by bands with clearly low dispersion at 2.5 eV below the Fermi level. These bands are associated exclusively with $2p_y$C-orbitals from the dimers of sp-hybridized C atoms and are responsible for the formation of second π-bond network within the carbyne groups. $2p_y$C-orbitals are united in couples and are fairly localized in the plane of layer, barely overlapping with orthogonal $2p_z$C-orbitals.

The presence of two types of π-bonding suggests the different reactivity of sp^2- and sp-hybridized C atoms in α-graphyne. The formation of chemical bonding between an ad-atom and carbon layer by means of a $2p_z$C-orbital should imply an essential interference into the aromatic-like π-system due to the appearance of sp^3-hybridized C atom and cannot be favorable in framework of this classical concept. In turn, the chemical bonding to the orthogonal π-bond consisting of $2p_y$C-orbitals between two sp-hybridized C atoms does not perturb the conjugation of this π-system and is accompanied only by the rupture of one π-bond. The preliminary comparison of the total energies for α-graphyne with single Cl atom bounded covalently either to sp^2- or to sp-hybridized C atoms (C_8Cl chlorgraphyne) confirms this conjecture: the second type of chemisorbate is more stable on 0.545 eV per Cl-atom.

3.2. Electronic structure and stability of lower Chlorgraphynes (C_8Cl and C_8Cl_2)

In order to elucidate the stability of different chlorgraphynes in more detail, the theoretical energies of formation ΔE_n were estimated assuming formal reactions: C_8(graphyne)

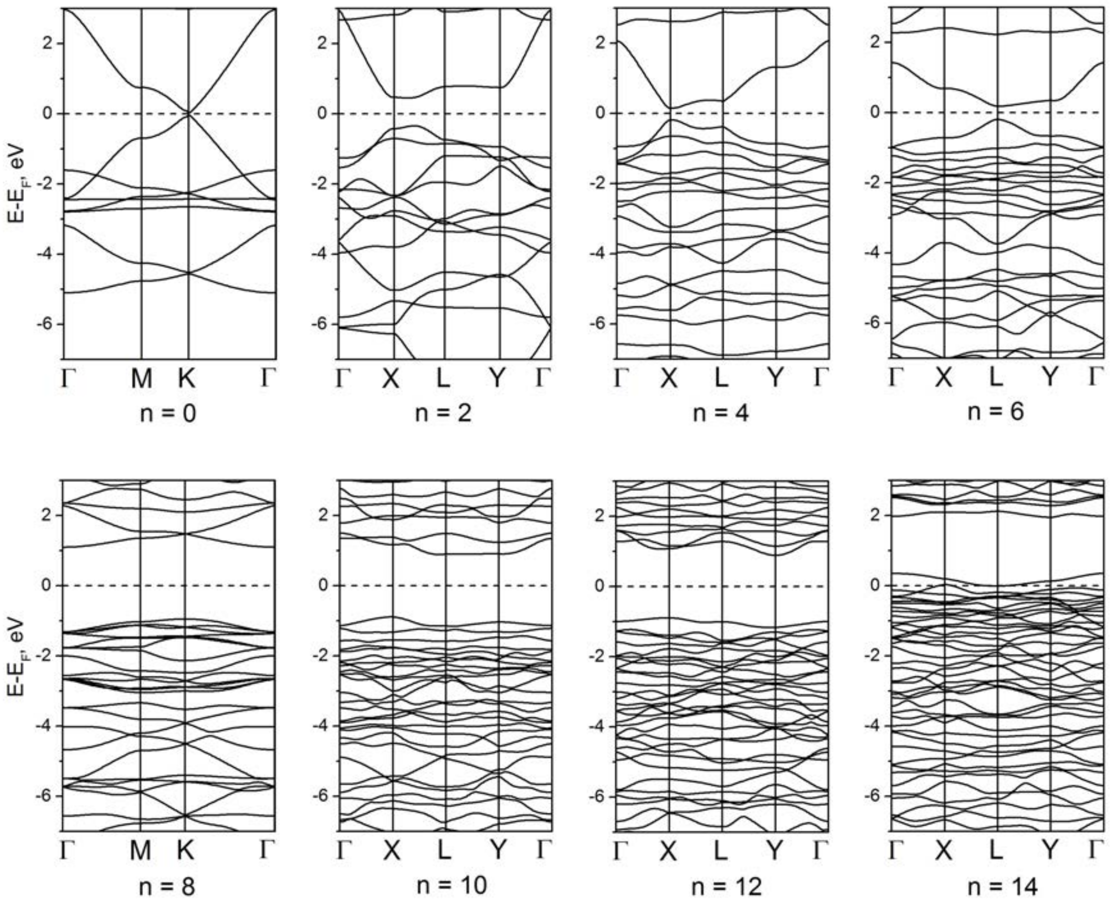

n = 0 n = 2 n = 4 n = 6

n = 8 n = 10 n = 12 n = 14

FIG. 2. Band structures of pure α-graphyne (n = 0) and the most stable isomers of chlorgraphynes C_8Cl_n

+ $(n/2)Cl_2 = C_8Cl_n$, and the values of E_{form} were calculated as: $\Delta E_n(C_8Cl_n) = [E_{tot}(C_8Cl_n) - (n/2)E_{tot}(Cl_2) - E_{tot}(C_8(\text{graphyne}))]/n$, where E_{tot} are the total energies of the corresponding substances as obtained in our calculations. Within this definition, a negative value of ΔE_n indicates that it is energetically favorable for given reagents to form stable phases, and *vice versa.* The calculations of ΔE_n performed for more than 70 structures of different composition depending on their constitutional and conformational isomerism reveal a quite strong influence of both electronic and steric factors on the stability of chlorgraphynes' series.

All the stablest chlographynes of different stoichiometry are characterized by the negative values of the formation energy ΔE_n, i.e. the saturation of graphyne network with the formation of covalent C–Cl bonds is an exothermic process favored by electronic factors (Fig. 3). E.g., the value ΔE_n for the stablest isomer of aforementioned C_8Cl chlorgraphyne with anchoring of Cl atom to *sp*-hybridized C atom is about –0.35 eV/Cl-atom, while anchoring to sp^2-hybridized C atom is endothermic and requires at least +0.20 eV/Cl-atom.

The chemisorption of additional Cl atoms with the formation of C_8Cl_2 chlorgraphyne may be highly favorable, when it is released in the structure shown in Fig. 1 (n = 2). This isomer of C_8Cl_2 chlorgraphyne possesses a unique structural motif. Like graphene or α-graphyne layers it is a single-atom thick layer. All Cl atoms of this structure are lodged in the trans-position at ethylidene bridges and within the plane of C atoms. In this manner, the structure preserves as much as possible the system of conjugated π-bonds formed by

$2p_z$C-orbitals, as in the parent graphyne and consists of planar 18-membered rings, yet, in an oblique conformation. Despite the hexagonal nature of α-graphyne, the electronic structure of C_8Cl_2 chlorgraphyne is characterized by a band gap opening of about 0.78 eV and a greater dispersion of the bands (Fig. 2, n = 2). Meanwhile, the new peak of $3p$Cl states arises at 3.5 eV below the Fermi level, while the top of valence band and the bottom of conduction band are still composed of $2p$C states (Fig. 4).

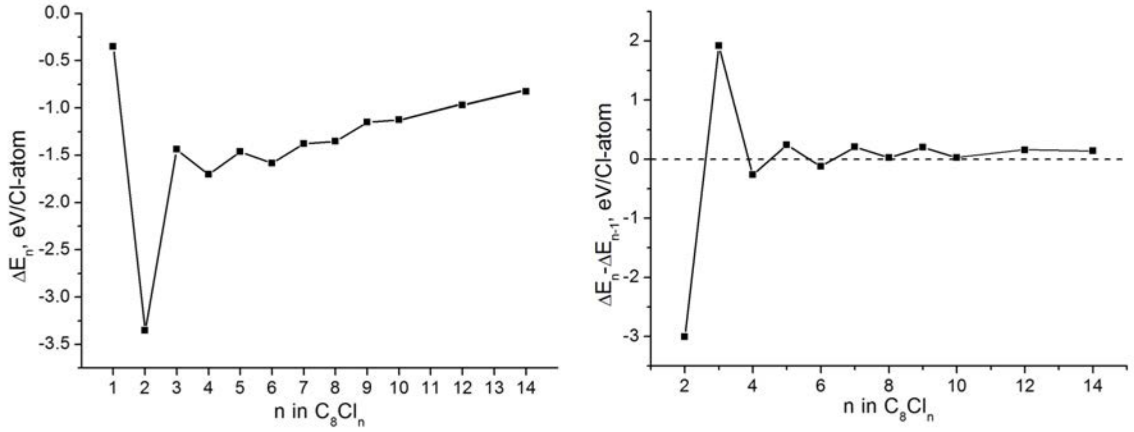

FIG. 3. Formation energies ΔE_n for the most stable isomers of chlorgraphynes C_8Cl_n and their relative difference depending on the stoichiometry

3.3. Electronic structure and stability of higher Chlorgraphynes ($C_8Cl_{3\text{-}14}$)

In fact, further saturation of graphyne network follows the same trends as for the formation of lower chlorgraphynes. Any next addition of Cl atoms with the formation of covalent C-Cl bond proceeds with the least possible violation of the conjugation between $2p_z$C-orbitals (Fig. 5). In the first steps, the consecutive anchoring of Cl atoms to the sp-hybridized C atoms should be obtained by means of bonding with $2p_y$C-orbitals in trans-position, which releases chlorgraphynes with the compositions up to C_8Cl_6. It is noteworthy that at this stage, the chlorination process is already considerably affected by steric factors. A major part of added Cl atoms cannot be placed into the hole of the 18-membered ring. Rotational displacement of planar bridging groups of C=C bonds can be observed, when the Cl atoms come out of the plane of graphyne. Yet, the π-conjugation of $2p_z$C-orbitals still remains. Even-numbered chlorgraphynes are semiconductors with relatively narrow band gaps (0.34 eV for C_8Cl_4 and 0.37 eV for C_8Cl_6, Fig. 2). The near Fermi states are represented by $2p_z$C states like in the parent phases. The relative intensity of the $3p$Cl states on the DOS profile increases in strength (Fig. 4, n = 4 and 6). They demonstrate splitting and have higher energies, than those in planar C_8Cl_2, which is evidence for a weaker overlap between the $3p$Cl states and the conjugated system of π-bonds.

Subsequently, calculations have proven that the anchoring of Cl atoms would likely proceed by means of $2p_z$C-orbitals of initially sp^2-hybridized C atoms with emergence of sp^3-hybridized C atoms, which breaks π-conjugation in the network of double C=C bonds (formerly, carbyne dimers) (Fig. 5, n = 8). Obviously, this process is driven mainly by steric factors and Cl atoms settle on the C atoms with a larger available space. A comparison of relative formation energies between the conformers of the C_8Cl_7 and C_8Cl_8 chlorgraphynes corroborates, that the steric effects should play also a major role in the conformer stability of these molecular networks. The most stable conformers should possess minimal strain energy of the layers due to symmetric structure and the ratio of Cl atoms chemisorbed from different sides as close as to 1:1. The occurrence of new type of sp^3-hybridized C atoms in the chlorgraphyne layer and complete destruction of the π-conjugation are accompanied by the emerging of new band of $3p$Cl states near the top of valence band and a considerable increase of the band gap to 2.2 eV (Fig. 4, n = 6).

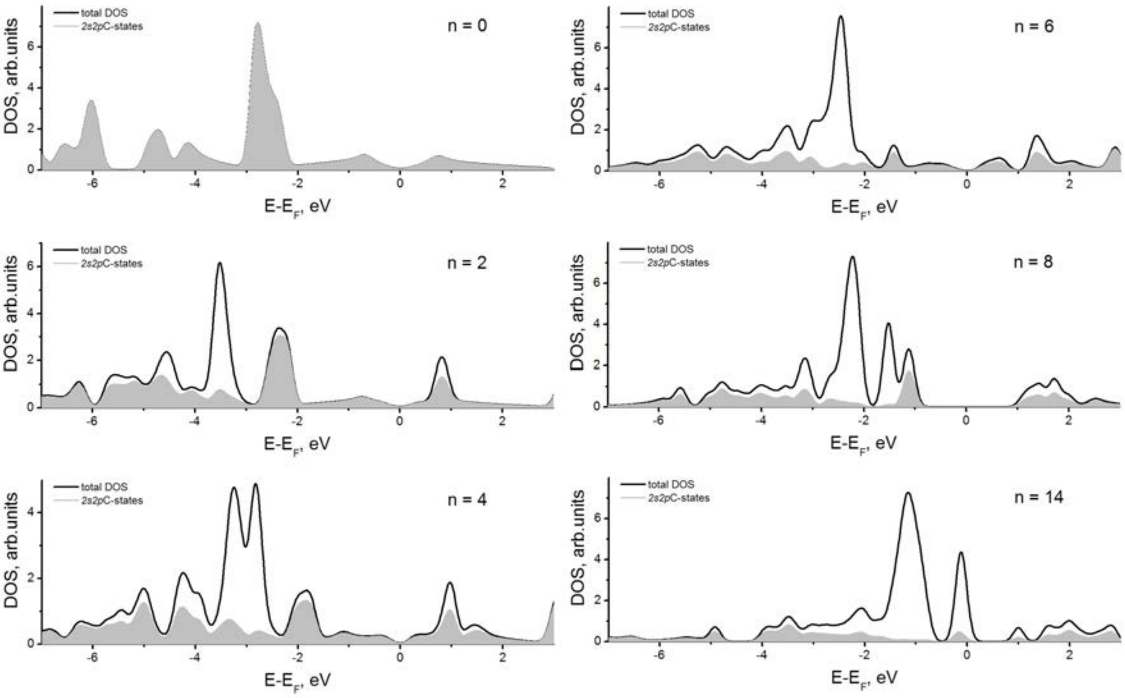

FIG. 4. Total and partial spC densities of states for a few of the most stable isomers of chlorgraphynes C_8Cl_n depending on the Cl content

The formation of higher chlorgraphynes C_8Cl_n with n up to 14 is possible only by the anchoring of Cl atoms to the rest of C=C bonds of former carbyne bridges (Fig. 5). The arrangement of Cl atoms within these structures can be characterized as strongly staggered at all carbon atoms fragments and as always *anti*-conformic at forming $-CCl_2-CCl_2-$ bridges, which provides the minimal energy of the steric stress. Despite the negative formation energy values, these chlorgraphynes demonstrate an essential stretch of the carbon network with an essential increases in the C–C bond lengths, which cannot be attributed to kinetically stable systems. The C–C bond lengths increase gradually from α-graphyne to C_8C_8 chlorgraphyne, but do not exceed the values for classical C–C bonds of different order in hydrocarbon compounds. For example, the bond lengths between atoms of different hybridization in α-graphyne are equal to 1.44 and 1.27 Å for sp^2C–spC and spC–spC bonds, respectively. After chlorination and change of hybridization, these bond lengths become 1.46 and 1.45 Å in C_8Cl_2, 1.50 and 1.42 Å in C_8Cl_6 and 1.56 and 1.40 Å in C_8Cl_8, respectively. In the fully chlorinated α-graphyne, C_8Cl_{14} chlorgraphyne, these bond lengths are 1.72 and 1.66 Å, which is much greater than the 1.55 Å for sp^3C– sp^3C in alkanes. Indeed, the geometry optimization of C_8Cl_{14} chlorgraphyne never was finished with a pure covalently bounded structure and a part of Cl atoms always can be found as physisorbed at the C_8Cl_{12} layer (Fig. 5, n = 14). The latter can be proven by the picture of DOS distribution: the Fermi

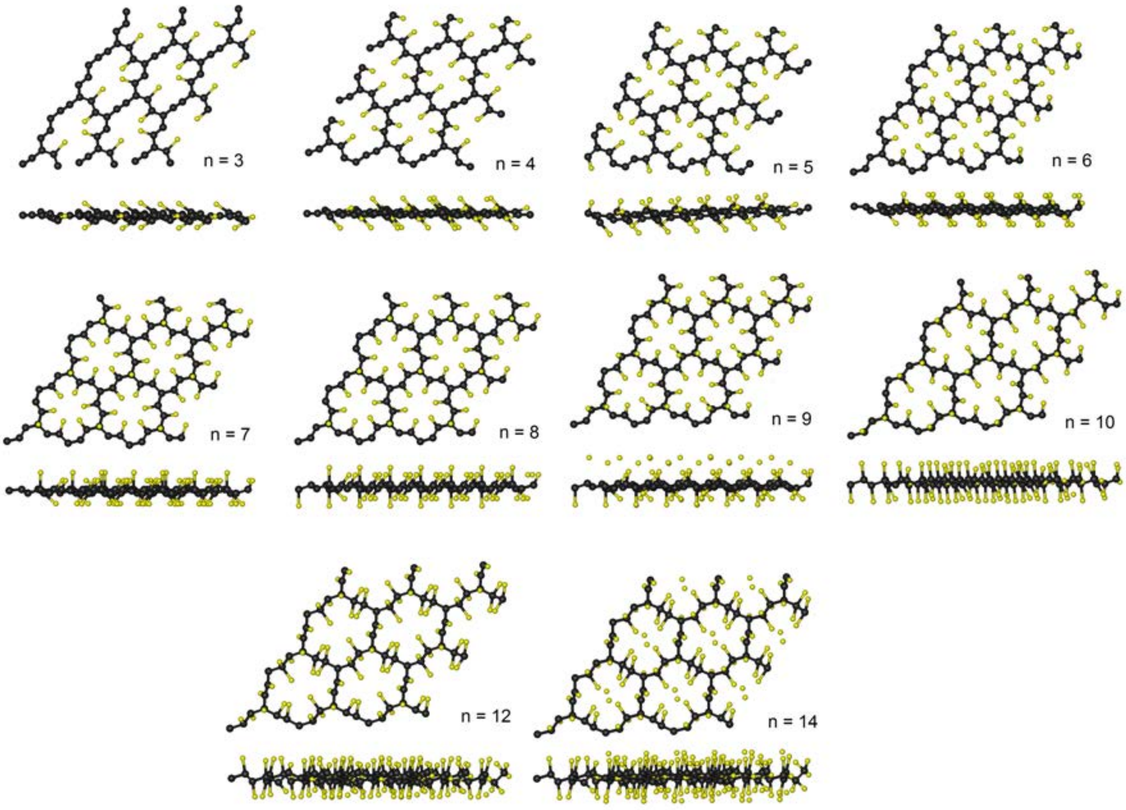

Fig. 5. Optimized atomic structures for the layers of the most stable isomers of chlorgraphynes C_8Cl_n with different Cl content (top and side views are depicted)

level is hosted at the band of Cl states, i.e. the system contains the free Cl radicals (Fig. 4, n = 14).

In addition, the low kinetic stability of the highly numbered C_8Cl_n chlorgraphynes may be traced using the relative difference in the formation energies between parent and daughter structures $\Delta E_n - \Delta E_{n-1}$ (Fig. 3). As it might be expected, the formation of compounds with open-shell electronic structure (the case of odd-numbered chlorgraphynes) is hindered and the difference in ΔE_n is always positive. Though, even-numbered chlorgraphynes with closed-shell electronic structure have negative values only up to the stoichiometry C/Cl = 8/6, the formation of chlorgraphynes with a higher Cl may be prohibited despite negative values for the calculated formation energies.

4. Summary

In summary, we have investigated the trends in stability, structural, and electronic properties of the proposed chlorinated graphynes (chlorgraphynes) with variable C/Cl stoichiometry up to composition C_8Cl_{14}, which is much higher than C/F ratio for “classical” fluorographene (C/F = 1) and could give an opportunity for the larger modulation of the properties and the engineering of a rich family of novel 2D materials.

Our DFT calculations have revealed the phenomena, which could occur during saturation of graphyne sheets by Cl atoms. We have considered a limited number of stoichiometries, isomers and conformers among the family of chlorinated α-graphynes and established a possible path for the formation of these compounds. The joint analysis of the structure, stability and electronic properties for a given stoichiometry uncovers the competition between electronic and steric factors. In contrast to the fluorine and hydrogen derivatives of graphene or graphynes [14,34], the maximal chemical saturation of graphyne layers by chlorine atoms should be prohibited due to the larger atomic radius of Cl. The maximal degree of chlorination would be likely possible only up to the composition C_8Cl_8 instead of nominal C_8Cl_{14}.

The most stable chlorgraphynes were found to be semiconductors, irrespective of their stoichiometry. The near Fermi level bands in C_8Cl_n monolayers are composed mainly of the $2p_z$C states, which can be assembled into a π-conjugated system in different manner. The found significance of steric factor in the formation of chlorgraphynes suggests also that the variety of the possible ad-atom arrangements would be much impoverished, than for their F- and H-substituted counterparts, and a more precise regulation of the structure may be achieved. Thus, the chlorination could be a more attractive route for the fabrication of graphyne layers with specific arrangement of ad-atoms and, consequently, tuned electronic and transport properties, than fluorination or hydrogenation.

Acknowledgments

The support of the RFBR project 13-03-00272- is gratefully acknowledged.

References

[1] Geim A.K., Novoselov K.S. The rise of graphene. *Nature Materials*, **6**, P. 183–191 (2007).

[2] Castro Neto A.H., Guinea N.M., Peres N.M.R., Novoselov K.S., Geim A.K. The electronic properties of graphene. *Reviews of Modern Physics*, **81**, P. 109–162 (2009).

[3] Castro Neto A.H. The carbon new age. *Materials Today*, **13**, P. 12–17 (2010).

[4] Soldano C., Mahmood A., Dujardin E. Production, properties and potential of graphene. *Carbon*, **48**, P. 2127–2150 (2010).

[5] Rozkov A.V., Giavaras G., Bliokh Y.P., Freilikher V., Nori F. Electronic properties of mesoscopic graphene structures: Charge confinement and control of spin and charge transport. *Physics Reports*, **503**, P. 77–114 (2011).

[6] Castro Neto A.H., Novoselov K.S. New directions in science and technology: two-dimensional crystals. *Reports on Progress in Physics*, **74**, P. 082501 (2011).

[7] Huang X., Yin Z., Wu S., Qi X., He Q., Zhang Q., Yan Q., Boey F., Zhang H. Graphene-based materials: synthesis, characterization, properties, and applications. *Small*, **7**, P. 1876–1902 (2011).

[8] Singh V., Joung D., Zhai L., Das S., Khondaker S.I., Seal S. Graphene based materials: past, present and future. *Progress in Materials Science*, **56**, P. 1178–1271 (2011).

[9] Nair R.R., Ren W.C., Jalil R., Riaz I., Kravets V.G., Britnell L., Blake P., Schedin F., Mayorov A.S., Yuan S., Cheng H.M., Strupinski W., Bulusheva L.G., Okotrub A.V., Grigorieva I.V., Grigorenko A.N., Novoselov K.S., Geim A.K. Fluorographene: a two-dimensional counterpart of teflon. *Small*, **6**, P. 2877–2884 (2010).

[10] Robinson J.T., Burgess J.S., Junkermeier C.E., Badescu S.C., Reinecke T.L., Perkins F.K., Zalalutdinov M.K., Baldwin J.W., Culbertson J.C., Sheehan P.E., Snow E.S. Properties of fluorinated graphene films. *Nano Letters*, **10**, P. 3001–3005 (2010).

[11] Zboril R., Karlicky F., Bourlinos A.B., Steriotis T.A., Stubos A.K., Georgakilas V., Safarova K., Jancik D., Trapalis C., Otyepka M. Graphene fluoride: a stable stoichiometric graphene derivative and its chemical conversion to graphene. *Small*, **6**, P. 2885–2891 (2010).

[12] Jeon K., Lee Z., Pollak E., Moreschini L., Bostwick A., Park C.M., Mendelsberg R., Radmilovic V., Kostecki R., Richardson T.J., Rotenberg E. Fluorographene: a wide bandgap semiconductor with ultraviolet luminescence. *ACS Nano*, **5**, P. 1042–1046 (2011).

[13] Withers F., Russo S., Dubois M., Craciun M.F. Tuning the electronic transport properties of graphene through functionalisation with fluorine. *Nanoscale Research Letters*, **6**, P. 526 (2011).

[14] Leenaerts O., Peelaers H., Hernandez-Nieves A.D., Partoens B., Peeters F.M. First-principles investigation of graphene fluoride and graphane. *Physical Review B*, **82**, P. 195436 (2010).

[15] Withers F., Dubois M., Savchenko A.K. Electron properties of fluorinated single-layer graphene transistors. *Physical review B*, **82**, P. 073403 (2010).

[16] Samarakoon D.K., Chen Z., Nicolas C., Wang X.Q. Structural and Electronic Properties of Fluorographene. *Small*, **7**, P. 965–969 (2011).

[17] Artyukhov V.I., Chernozatonskii L.A. Structure and Layer Interaction in Carbon Monofluoride and Graphane: A Comparative Computational Study. *The Journal of Physical Chemistry A*, **114**, P. 5389–5396 (2010).

[18] Enyashin A.N., Ivanovskii A.L. Graphene allotropes. *Physica Status Solidi (b)*, **248**, P. 1879–1883 (2011).

[19] Baughman R.H., Eckhardt H., Kertesz V. Structure-property predictions for new planar forms of carbon: layer phases containing sp^2 and sp atoms. *Journal of Chemical Physics*, **87**, P. 6687–6699 (1987).

[20] Narita N., Nagai S., Suzuki S., Nakao K. Electronic structure of three-dimensional graphyne. *Physical Review B*, **62**, P. 11146–11151 (2000).

[21] Coluci V.R., Braga S.F., Legoas S.B., Galvao D.S., Baughman R.H. Families of carbon nanotubes: graphyne-based nanotubes. *Physical Review B*, **68**, P. 035430 (2003).

[22] Kang J., Li J., Wu F., Li S.S., Xia J.B. Elastic, Electronic, and optical properties of two-dimensional graphyne sheet. *The Journal of Physical Chemistry C*, **115**, P. 20466–20470 (2011).

[23] Srinivasu K., Ghosh S.K. Graphyne and graphdiyne: promising materials for nanoelectronics and energy storage applications. *The Journal of Physical Chemistry C*, **116**, P. 5951–5956 (2012).

[24] Zhang H., Zhao M., He X., Wang Z., Zhang X., Liu X. High mobility and high storage capacity of lithium in sp–sp^2 hybridized carbon network: the case of graphyne. *The Journal of Physical Chemistry C*, **115**, P. 8845–8850 (2011).

[25] Pan L.D., Zhang L.Z., Song B.Q., Du S.X., Gao H.J. Graphyne- and graphdiyne-based nanoribbons: Density functional theory calculations of electronic structures. *Applied Physics Letters*, **98**, P. 173102 (2011).

[26] Malko D., Neiss C., Vines F., Gorling A. Competition for graphene: graphynes with direction-dependent dirac cones. *Physical Review Letters*, **108**, P. 086804 (2012).

[27] Hohenberg P., Kohn W. Inhomogeneous electron gas. *Physical Review B*, **136**, P. 864–871 (1964).

[28] Ordejon P., Artacho E., Soler J.M. Self-consistent order-N density-functional calculations for very large systems. *Physical Review B*, **53**, P. R10441 (1996).

[29] Soler J., Artacho E., Gale J.D., Garcia A., Junquera J., Ordejon P., Sanchez-Portal D. The SIESTA method for ab initio order-N materials simulation. *Journal of Physics: Condensed Matter*, **14**, P. 2745–2779 (2002).

[30] Perdew J.P., Zunger A. Self-interaction correction to density-functional approximations for many-electron systems. *Physical Review B*, **23**, P. 5048–5079 (1981).

[31] Troullier N., Martins J.L. Efficient pseudopotentials for plane-wave calculations. *Physical Review B*, **43**, P. 1993–2006 (1991).

[32] Moreno J., Soler J.M. Optimal meshes for integrals in real- and reciprocal-space unit cells. *Physical Review B*, **45**, P. 13891–13898 (1982).

[33] Monkhorst H., Pack J.D. Special points for Brillouin-zone integrations. *Physical Review B*, **13**, P. 5188–5192 (1976).

[34] Enyashin A.N., Ivanovskii A.L. Fluorinated derivatives of sp^2 carbon allotropes: Structure, stability and electronic properties. *Chemical Physics Letters*, **545**, P. 78–82 (2012).

NANOSYSTEMS: PHYSICS, CHEMISTRY, MATHEMATICS, 2014, 5 (4), P. 486–493

AB-INITIO STUDY OF Re AND Ru EFFECT ON STABILITY OF TCP NANOPARTICLES IN Ni-BASED SUPERALLOYS

N. I. Medvedeva, A. L. Ivanovskii

Institute of Solid State Chemistry UB RAS, Ekaterinburg, Russia

medvedeva@ihim.uran.ru

PACS 71.15.Mb 71.15.Nc 71.20.Be

Modern nickel-based superalloys contain high concentrations of rhenium that allows the improvement of their creep strength. The high levels of rhenium, however, results in the formation of topologically close-packed phases (TCP) which have a negative influence on its properties. The addition of ruthenium was found to reduce the precipitation of nano-sized TCP phases, but the reasons have not been established. In this paper, by using an ab-initio approach, we studied the effect of rhenium and ruthenium on the structural properties of Ni matrix as well as the TCP phases. We demonstrate that Cr, Mo and W are the most effective additions to provoke the formation of TCP phases, whereas ruthenium has a destabilizing effect.

Keywords: Ab initio calculations, rhenium effect, superalloys.

Received: 16 June 2014
Revised: 30 June 2014

1. Introduction

The high-temperature strength of Ni-based superalloys is achieved by adding refractory elements, such as molybdenum, tungsten, tantalum and rhenium [1-3]. Rhenium is the most effective solid solution strengthener and superalloys normally contain 3-6% of rhenium [1-4]. The addition of 6 %Re increases the creep and thermomechanical fatigue strength to 46% and 59% at 950°C. The third-generation of heat-resistant nickel alloys contain a high concentration of rhenium up to 9-12 % [5-7]. However, the higher level of rhenium results in the formation of topologically close-packed phases (TCP), which have a negative influence on the mechanical properties, since these particles serve as sites for crack initiation and cause embrittlement. The effects of solid-solution and precipitation strengthening are reduced due to the lower concentration of rhenium and other useful impurities in the γ and γ' matrices. The 4^{th}- and 5^{th}- generation superalloys contain lower Re concentrations up to 6% and addition of 3-6 % Ru which hinders formation of the undesirable TCP phases [7-12]. The mechanism by which ruthenium improves the microstructural stability is still under discussion [10-12] and thus, understanding the stability of TCP phases is crucial for the further development of superalloys.

The close-packed nanoparticles of different structural types (σ, μ, χ and A15 with space groups P42/mnm, R3m, Pnma and Pm3n, respectively) were observed in the rhenium-containing alloys [1-3]. It should be noted that the A15 structure is competitive with bcc and σ phases, and considered as a prototype of TCP phases [13-17]. The particles or thin films of A15 structure, known as β-W (Cr_3Si-type), were observed in the Cr, Mo and W alloys, as well as in the Fe–Cr, Ni–Cr and Co–Cr alloys. Nickel does not form ordered phases with rhenium or ruthenium, and the appearance of TCP particles is facilitated by the alloying elements, which can change phase stability, diffusion of atoms and misfit of lattice parameters of γ and γ' phases. Group VI (W, Cr, Mo) impurities were observed to favor TCP formation and thus, the reduction of TCP phases may be achieved by their controlled concentration. Metastable particles of A15-type were predicted in the Cr–Re alloys from first-principles calculations [18,19]. Furthermore, *ab-initio* calculations [20] for Mo–Re and Mo–Ru demonstrated that the A15 phase has the greatest stability among other TCP binary phases (χ, σ, μ, C14, C36) within a small volume difference ΔV/V with bcc Mo.

The effect of impurities depends on their partitioning as well as their influence on the lattice parameters and elastic moduli of these phases (size and elastic misfit). The complexity of the eutectic ($\gamma + \gamma$') system makes it difficult to experimentally determine these changes under alloying. Empirical approaches [5] could not predict the mechanism of rhenium's effect on structural parameters and elastic moduli as well as the effect of interaction with other additives.

In this work, we present *ab-initio* study of the effects which rhenium and ruthenium have on the electronic structure, lattice parameters and elastic moduli of fcc Ni, as ascertained that rhenium and ruthenium is mainly distributed in the γ phase (the concentration of these impurities in the γ' phase is known to be more than an order of magnitude less). We also investigate the electronic structure and stability for the A15 elemental phases (Ni, Re, Ru, Cr, Mo, W) as well as binary M_3Re and M_3Ru phases (M=Ni, Cr, Mo, W). To elucidate the simultaneous presence of Ru and Re, we performed calculations for $M_3Re_{0.5}Ru_{0.5}$ (M=Ni, Cr, Mo, W). These simulations provide the reasons for the influence of d-impurities on the stability of topologically close-packed phases in Ni alloys.

2. Computational details

The calculations were performed by using the projector-augmented wave (PAW) method, as implemented in the Vienna *ab initio* simulation package (VASP) [21,22]. The generalized gradient approximation (GGA) in the Perdew–Burke–Ernzerhof (PBE) form [23] was employed for the exchange-correlation functional. Energy cutoff for plane-wave expansion of 400 eV and the k sampling with 8×8×8 k-points in the Brillouin zone were used for A15 structure, while elemental metals were calculated with 16×16×16 k-points. To study the effect of rhenium and ruthenium on the electronic structure and elastic properties of fcc Ni, we used 32-atom supercell, where one impurity atom (Re or Ru) was substituted for Ni atom that corresponds to the impurity concentration of 3 at.%. The A15 structure of M_3X consists of six equivalent M atoms in c site (0.25,0.25,0) which compose the pairs on each cube face and two X atoms in bcc positions with coordinates (0, 0, 0). To model A15 M_3X (X= Re,Ru) we followed to experimental findings [24] which established that transition metal atoms such as Cr occupy the twinned c positions and X atoms are in bcc a sites. The structural optimization was performed for the lattice parameters and atomic coordinates which were relaxed to their ground state by minimizing their Hellman–Feynman forces, using the conjugate gradient algorithm, until all interatomic forces were less than 0.1 eV/A°.

3. Results and discussion

3.1. Rhenium and ruthenium in fcc Ni

The calculated lattice parameters and elastic moduli for pure fcc Ni and Ni-3at.% Re (Ru) are listed in Table 1. First, the comparison of our results with experimental and theoretical data available for fcc Ni showed that these calculations provide reliable results. Furthermore, our calculations are in better agreement with the experimental data, especially for elastic constants. Rhenium and ruthenium at 3at.% concentration increase the lattice parameter of fcc Ni by 0.34% and 0.30%, respectively, and the distances between the nearest Ni and Re (Ru) atoms increases to 2.50 Å in accordance with a smaller atomic size of Ni.

Re and Ru substitutions decrease both C_{11} and C_{12}, and as a result, the bulk modulus B=$(C_{11} + 2C_{12})/3$ is significantly reduced. However, the tetragonal shear modulus $G'=(C_{11} - C_{12})/2$ increases slightly with these impurities. Comparison of changes in volume (increases of 10% and 9% for Re and Ru, respectively) and in bulk modulus B (decreases of 13% and 18% for Re and Ru, respectively) shows that not only lattice expansion is responsible for the reduction of B. As can be seen from the calculated charge density maps, ruthenium leads to a weakening of chemical bonds in the first coordination sphere (Fig. 1). The calculated densities of states (DOS) for fcc Ni, Ni-3at.% Re, Ni-3at.% Ru (Fig. 2) demonstrate the changes in electronic structure are due to impurities. The Fermi level E_F in fcc Ni is located on the slope almost of the completely filled Ni3d band. The large density of states at the Fermi level N(E_F) favors a metallic conductivity and a high specific heat in fcc Ni. For Ni-3at.% Re, the Fermi level E_F falls into a pseudogap between the filled bonding and empty antibonding 5d-states of rhenium. The contribution of Re5d states near E_F is small and rhenium impurity leads to a decrease in N(E_F), (Table 1, Figure 2).

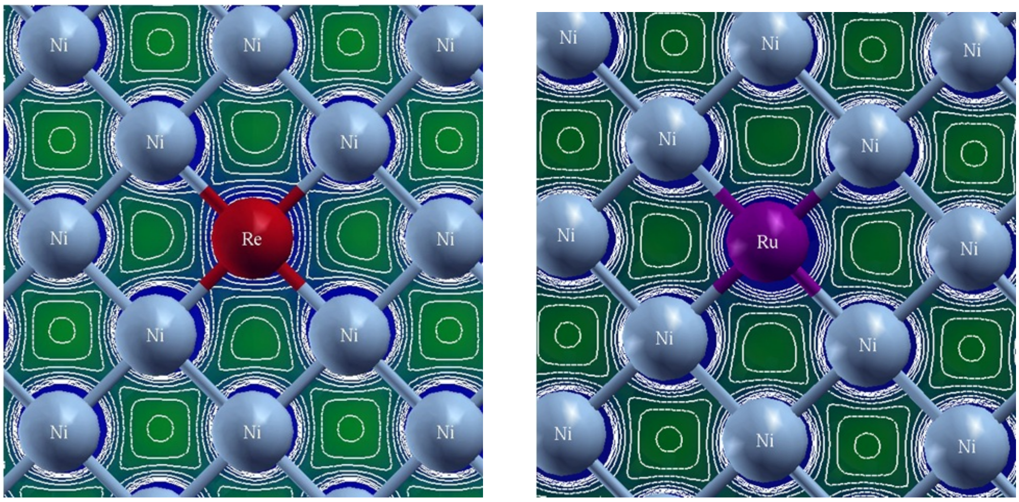

(a) (b)

FIG. 1. Charge density plot for Ni-3at.%Re (a) and Ni-3at.%Ru (b)

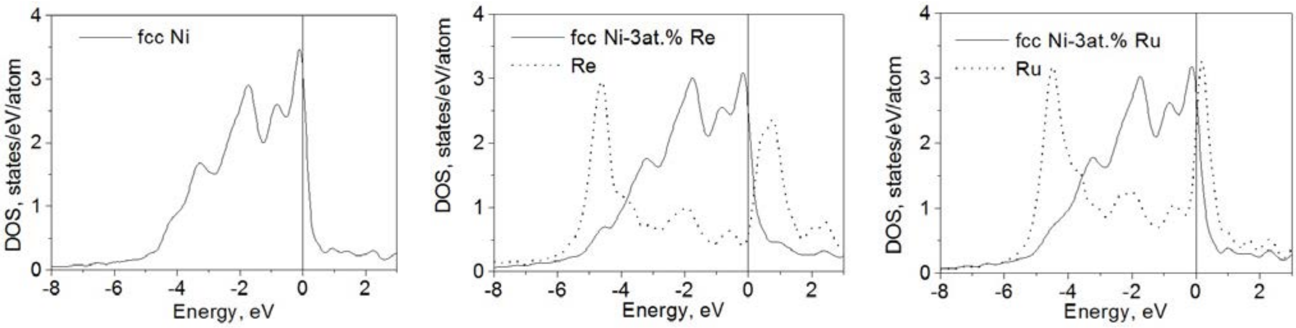

(a) (b) (c)

FIG. 2. Density of d-states for fcc Ni (a), Ni-3at.%Re (b) and Ni-3at.%Ru (c)

TABLE 1. Lattice parameters and elastic parameters for fcc Ni and Ni-3%(Re,Ru)

	Ni	Ni-3at.%Re	Ni-3at.%Ru
a, Å	3.518 3.520 [14] 3.540 [25]	3.5299	3.5286
C_{11}, GPa	239 248 [14] 323 [25]	218	213
C_{12}, GPa	152 155 [14] 162 [25]	126	117
C_{44}, GPa	127 124 [14] 39 [25]	131	126
B, GPa	181 186 [14] 207 [25]	157	149
G, GPa	44 54 [14] 83 [25]	46	48

For Ni-3at.% Ru, the increase in the number of valence electrons due to ruthenium leads to a shift of E_F to a high peak of Ru4*d* antibonding states (Fig. 2). Contributions from Ru4*d* and Ni3*d* states are equal near E_F, and the value of $N(E_F)$ changes little with Ru concentration. It should be noted that the Fermi level is within the range of abrupt changes in DOS (sharp increase in the density of Ru4*d* states), which may indicate the presence of anelectronic topological transition near 3at.% Ru.

To compare the solubility of these impurities, we calculated the mixing energies E_{mix} as a difference between total energy of alloy and its constituent elements. We obtained E_{mix} to be -0.016 eV and +0.005 eV for 3at.% concentration of Re and Ru additions, respectively. Thus, the solubility of rhenium in fcc Ni should be higher than that of ruthenium.

3.2. Stability of 15 phases in Ni-Re-Ru, Cr-Re-Ru, Mo-Re-Ru and W-Re-Ru systems

First, we optimized the lattice parameters (Table 2) and found the small differences in volumes of the A15 and ground state (fcc, bcc, hcp, hcp, bcc, bcc, respectively) phases of Ni, Cr, Re, Ru, Mo and W. For example, the calculated lattice constant of A15 Cr is equal to 4.545 Å (experiment provides 4.576 Å [26]) and the volume of A15 Cr is 11.736 Å^3/atom that is close to volume of 11.661 Å^3/atom for antiferromagnetic bcc Cr. Lattice parameter of A15 M_3X, where the metal atoms with coordinates (0, 0, 0) are replaced by X = Re or Ru, increases in accordance with the larger atomic size of the X atom. Ruthenium and rhenium increase the lattice parameter of the A15 phase based on 3d metals by 2% and almost do no influence on the lattice parameter is exerted by molybdenum-and tungsten-containing A15 phases. Comparison with fcc Ni shows that a lattice misfit between fcc Ni and A15 Cr is small (2.4%) and increases up to 14% for the A15 W and A15 Mo.

TABLE 2. Lattice parameter a, density of states at the Fermi level $N(E_F)$ and enthalpy formation ΔH for A15 phases in Ni–Re–Ru, Cr–Re–Ru, Mo–Re–Ru and W–Re–Ru systems

Phase	a, Å	$N(E_F)$, state/eV	ΔH (eV/atom)	Phase	a, Å	$N(E_F)$ state/eV	ΔH (eV/atom)
Ni	4.461	3.81	+0.084	Cr_3Re	4.648	1.27	+0.048
Cr	4.545	0.61	+0.071	Cr_3Ru	4.613	2.15	+0.080
Re	4.945	1.41	+0.160	$Cr_3Re_{0.5}Ru_{0.5}$	4.633	1.32	+0.060
Ru	4.923	0.94	+0.422	Mo_3Re	4.993	1.02	+0.005
Mo	5.023	0.54	+0.090	Mo_3Ru	4.964	1.21	+0.027
W	5.057	0.51	+0.122	$Mo_3Re_{0.5}Ru_{0.5}$	4.979	1.19	+0.018
Ni_3Re	4.574	1.62	+0.106	W_3Re	5.017	3.24	+0.034
Ni_3Ru	4.572	3.24	+0.204	W_3Ru	4.988	1.03	+0.091
$Ni_3Re_{0.5}Ru_{0.5}$	4.633	1.32	+0.127	$W_3Re_{0.5}Ru_{0.5}$	5.004	1.87	+0.064

The enthalpy of formation, ΔH, calculated relative to the total energies of elemental metals is positive for all A15 phases (Table 2). As one can see (Table 2), group VI metals (Cr,Mo) and Ni form A15 phases with enthalpies of formation less than 0.1 eV/atom. For elemental A15 phases, stability increases in the series: Cr > Ni > Mo > W > Re > Ru and the most stable A15 phases correspond to Cr, Ni and Mo, while A15 Ru is the most unstable. For binary A15 phases, stability increases as $Mo_3Re > W_3Re > Cr_3Re > Ni_3Re$ and $Mo_3Ru > Cr_3Ru > W_3Ru > Ni_3Ru$ (Table 2). Among the A15 M_3Re phases, very small positive values of ΔH were obtained for Cr_3Re (+0.048 eV/atom), Mo_3Re (+0.005 eV/atom) and W_3Re (+0.034 eV/atom), which are lower than those for the unalloyed A15 phases without Re. Thus, we conclude that formation of the metastable A15 phases should be more favorable in binary alloys with Re addition. However, ΔH is higher for Ni_3Re than for A15 Ni and the addition of Re in Ni matrix should not lead to the appearance of Ni-Re particles. The simultaneous presence of Re and the group VI metals in a Ni matrix favors the formation of close-packed A15 particles, which explains the experimental finding on the effect of Cr, Mo and W additions on the appearance of TCP phases.

The formation enthalpy of A15 phases with ruthenium is higher by 2-3 times than with rhenium and A15 M_3Ru is less stable for all considered metals M. There is a correlation between stability and density of states at the Fermi level, where the value $N(E_F)$ is less for the more stable phase. As shown in Fig. 3, the Fermi level E_F lies within the antibonding states for both Cr_3Re and Cr_3Ru. The larger number of valence Ru *d*-electrons in Cr_3Ru results in a shift of the Fermi level at a peak of antibonding states that weaken the bonding compared to Cr_3Re (Fig. 3). The ternary $Mo_3Re_{0.5}Ru_{0.5}$ and $W_3Re_{0.5}Ru_{0.5}$ are even more stable than the corresponding A15 metal phases, however, ruthenium destabilizes the all A15 M_3Re phases and ΔH increases as $Mo_3Re_{0.5}Ru_{0.5} > Cr_3Re_{0.5}Ru_{0.5} > W_3Re_{0.5}Ru_{0.5} > Ni_3Re_{0.5}Ru_{0.5}$.

To predict the elastic properties and mechanical stability of A15 phase, we calculated the elastic parameters for Mo_3Re, $Mo_3Re_{0.5}Ru_{0.5}$ and Mo_3Ru which are the most stable

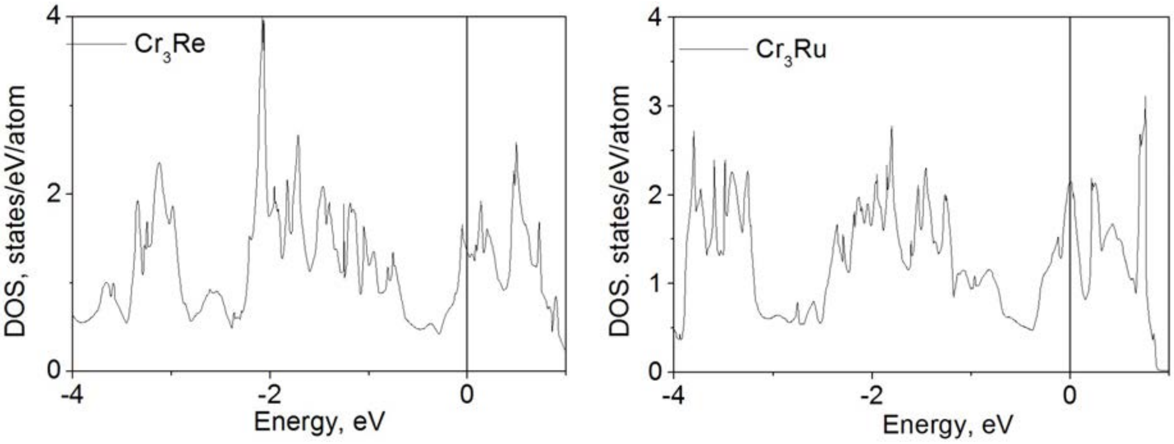

(a) (b)

Fig. 3. Density of *d*-states for 15 Cr_3Re (a) and Cr_3Ru (b). The Fermi level is at zero

among the considered A15 phases (Table 3). We found that ruthenium reduces the elastic constants C_{11}, C_{12} and C_{44} in accord with the weaker bonding in the Ru systems. The mechanical stability of cubic crystal requires $C_{11} - C_{12} > 0$, $C_{11} > 0$, $C_{44} > 0$, $C_{11} - 2C_{12} > 0$. As shown in Table 3, the elastic constants obey these stability criteria for all A15 Mo–Re and Mo–Ru phases.

Table 3. Elastic constants and moduli, anisotropy A and G/B for Mo_3Re, $Mo_3Re_{0.5}Ru_{0.5}$, Mo_3Ru

	C_{11}	C_{12}	C_{44}	B	G	A	G/B
Mo_3Re	499	190	98	293	154	0.64	0.52
$Mo_3Re_{0.5}Ru_{0.5}$	486	176	94	279	155	0.61	0.55
Mo_3Ru	465	175	87	272	145	0.60	0.53

Bulk and tetragonal shear moduli were calculated as $B = (C_{11} + 2C_{12})/3$ and $G = (C_{11} - C_{12})/2$. It is seen (Table 3) that both bulk modulus B and shear modulus G decrease with ruthenium. The anisotropy factor, calculated as $A = 2C_{44}/(C_{11} - C_{12})$, shows that all phases are anisotropic ($A \neq 1$), and the presence of ruthenium does not affect the anisotropy of elastic deformations. The ratio of G/B represents the Pugh's criterion [27]: a material behaves in a ductile manner if $G/B < 0.57$ and demonstrates brittleness when $G/B > 0.57$. For all the considered A15 phases, G/B is close to 0.57 and these phases should not have a plastic behavior, but rather demonstrate a tendency to be brittle and fracture.

4. Conclusions

Ab-initio calculations were performed to elucidate the effect of rhenium and ruthenium on the electronic structure and elastic properties of fcc Ni as well as on the stability of TCP phases. Both rhenium and ruthenium additions increase the lattice parameter and reduce the bulk modulus of fcc Ni, whereas the tetragonal shear only varies slightly. We found that the solubility of rhenium in fcc Ni should be higher than that of ruthenium. We established that the presence of chromium, molybdenum and tungsten favors to the formation of closely packed particles in rhenium containing nickel matrix and the concentration of these additions should be restricted in an alloy. The TCP particles are mechanically stable and their formation enthalpy is close to zero. Molybdenum has the greatest tendency to form TCP phases with A15 structure. The mechanism by which ruthenium exerts a positive effect on TCP particle formation is related to its decrease of their stability.

Acknowledgments

This work was supported by Research Program of Ural Branch of the RAS, Grant No. 12-U-3-1007.

References

[1] Darolia R., Lahrman D.F., Field R.D., *Superalloys* 1988 Edited by S. Reichman, D.N. Duhl, G. Maurer, S. Antolovich and C. Lund. The Metallurgical Society, p. 255 (1988).

[2] Bhadeshia H. K. D. H. *Nickel Based Superalloys.* University of Cambridge. http://www.msm.cam.ac.uk/phase-trans/2003/Superalloys/superalloys.html

[3] Reed R.C. *The Superalloys: Fundamentals and Applications.* Cambridge University Press, Cambridge (2006).

[4] Argence D., Vernault C, Desvallees Y, Fournier D. II Superalloys 2000. Eds. T.M. Pollock, R.D. Kissinger, R.R. Bowman et al. Champion (Pennsylvania). P. 829 (2000).

[5] Kablov E.N., Petrushin N.V. Physicochemical and technological features of creating metal-based high-superalloys. *Pure Appl. Chem.*, **076**(9), P. 1679–1689 (2004).

[6] Sims S. T. In Superalloys II, S. T. Sims, N. S. Stoloff, W. C. *Hagel* (Eds.), P. 217–240, Wiley-Interscience, New York (1987).

[7] Caron P. High γ' Solvus New Generation Nickel-based Superalloys for Single Crystal Turbine Blade Applications. Superalloys 2000, ed. T.M. Pollock, et al, (Warrendale, PA: TMS, 1996), P. 737–746.

[8] Murakami H., Honma T., Koizumi Y., Harada H., in:T.M. Pollock, R.D. Kissinger, R.R. Bowman, K.A. Green, M. McLean, S.L. Olson, J.J. Schirra (Eds.), Superalloys 2000, TMS, Champion, PA, 2000, p. 747.

[9] Koizumi Y, Kobayashi T., and Yokokawa T. at al. Development of next-generation of Ni-base single crystal superalloys. II Superalloys 2004 / Eds. by K.A. Green et al. Champion (Pennsylvania), 2004. P. 35–43.

[10] O'Hara K.S., Walston W.S., Ross , Darolia R. US Patent No 5482789.09.01.1996.

[11] Sato A., Harada H., Yokokawa T., Murakumo T., Koizumi Y., Kobayashi T., Imai H. The effects of ruthenium on the phase stability of fourth generation Ni-base single crystal superalloys. *Scripta Mater*, **54**(9), P. 1679–1684 (2006).

[12] L.J. Carroll, Q. Feng, J.F. Mansfield, T.M. Pollock, High Refractory, Low Misfit Ru-Containing Single-Crystal Superalloys. *Met. Mat. Trans.*, **37A**, P. 2927–2938 (2006).

[13] Tournier S, Vinet B, Pasturel A, Ansara I, Desre' PJ. Undercooling-induced metastable A15 phase in the Re-W system from drop-tube processing. *Phys Rev B*, **57**(6), P. 3340–3344 (1998).

[14] Federer JI, Steele RM. Identification of a Beta-Tungsten Phase in Tungsten-Rhenium Alloys. *Nature*, London, **205**, P. 587–588 (1965).

[15] Chu JP, Chang JW, Lee PY. Phase Transformation of A15 crystal structure chromium thin films grown by the sputter-deposition. *Mater Chem Phys.*, **50**(1), P. 31–36 (1997).

[16] Chu JP, Chang JW, Lee PY, Wu JK, Wang JY. On the formation of nonequlibrium A15 crystal structure chromium thin films grown by the sputter-deposition. *Thin Solid Films.* **312**(1-2), P. 78–85 (1998).

[17] Turchi PEA, Finel A. Ordering phenomena in *A*15-based alloys. *Phys Rev B*, **46**, P. 702–725 (1992).

[18] Medvedeva N.I., Gornostyrev Y.N., Freeman A.J., Carbon stabilized A15 Cr_3Re precipitates and ductility enhancement of Cr-based alloys. *Acta Mater.*, **50**(10), P. 2471–2476 (2002).

[19] Medvedeva N.I., Gornostyrev Y.N., Freeman A.J., Structural properties, electronic structure, Fermi surface, and mechanical behavior of bcc Cr-Re alloys. *Phys. Rev. B*, **67**(13), P. 134204-6 (2003).

[20] Hummershschmidt T., Seiser B., Pettifor, Superalloys-2012, Edited by E.S.Huron, et al, Willey TMS, p. 138

[21] Kresse G., Joubert D. From ultrasoft pseudopotentials to the projector augmented-wave method. *Phys. Rev. B*, **59**(3), P. 1758–756 (1999).

[22] Kresse G., Furthmüller J. Efficient iterative schemes for ab initio total-energy calculations using a plane-wave basis set. *Phys. Rev. B.*, **54**(16), P. 11169–11186 (1996).

[23] Perdew, K. Burke, M. Ernzerhof, Generalized gradient approximation made simple. *Phys. Rev. Lett.*, **77**(18), P. 3865–3868 (1996).

[24] Gorbunov J.P., Levin A.A., Mensch A., Meyer D.C., Tselev A., Paufler P., Pompe W., Eckert D. Formation of unusual intermetallic phases by vacuum PLD. *Applied Surface Sci.*, **B197**(3), P. 475–480 (2002).

[25] Guo G.Y., Wang H.H. Gradient-Corrected Density Functional Calculation of Elastic Constants of Fe, Co and Ni in bcc, fcc and hcp Structures. *Chinese J. Phys.*, **38**(5), P. 949–961 (2000).

[26] Kimoto K., Nishida I. An electron diffraction study on the crystal structure of a new modification of chromium. *J. Phys. Soc. Japan*, **22**(3), P. 744–756 (1967).

[27] Pugh S. F. Relations between the elastic moduli and the plastic properties of polycrystalline pure metals. *Phil. Mag.*, **45**(367), P. 823–843 (1953).

NANOSYSTEMS: PHYSICS, CHEMISTRY, MATHEMATICS, 2014, 5 (4), P. 494–508

ELECTRONIC STRUCTURE AND STABILIZATION OF C60 FULLERENES ENCAPSULATING ACTINIDE ATOM

M. V. Ryzhkov[1,*], A. L. Ivanovskii[1], B. Delley[2]

[1]Institute of Solid State Chemistry, Ural Branch of the Russian Academy of Sciences,
620990, Ekaterinburg, Russia

[2]Paul Scherrer Institut WHGA 123, CH-5232, Villigen PSI, Switzerland

*ryz@ihim.uran.ru

PACS 31.15A, 31.15ae, 31.15aj, 31.15E

The geometry optimization of the neutral molecules An@C_{60} (An = Th – Md) was carried out using the DFT based Dmol^3 method. In order to perform calculations for these complexes' electronic structures, the fully relativistic discrete variational method (RDV) was used. Two types of stable position of metal atom inside the C_{60} cage were obtained. The most stable non-central positions are favored over the position of actinide in the fullerene center for all An@C_{60} complexes. Systems containing light actinides have considerable energetic stability, which is noticeably greater than that of corresponding exohedral and "networked" complexes. The 5f-orbitals' contribution to chemical bonding was found to be noticeably less than that of the 6d-states, even for the complexes at the beginning of An@C_{60} row. The effective charges on the actinide atoms were calculated using integral scheme incorporated in RDV and Hirshfeld procedure of DMol^3 code.

Keywords: fullerenes, actinides, ab initio methods, relativistic calculations, molecular structure, stability.

1. Introduction

The earlier investigations of charged and neutral endohedral fullerenes An@C_{28} (An = Th – Md) [1,2] as well as An@C_{40} (An = Th – Md) [3] showed that some of these clusters can be very stable and therefore, may be useful for nuclear applications such as medicine or nuclear waste disposal. Since the discovery of C_{60} [4], these fullerenes have been widely studied both experimentally and theoretically. To date, we know only one actinide endohedral system U@C_{60}, which has been obtained experimentally, Diener et al. [5] reported that U@C_{60} was produced by subliming fullerenes from arc-produced soot onto a mass spectrometry target. Chang et al. [6] theoretically predicted its properties, according to these Restricted Hartree-Fock calculations the U@C_{60} and U^+@C_{60} complexes should be less stable than separated C_{60} and U. However, in Ref. [6] only one central position of various atoms inside the icosahedral carbon cage was considered. On the other hand, the radius of this fullerene (nearly 3.6 Å) is evidently too large for one actinide atom or ion, so the An@C_{60} structure with metal site just in the center of the cage could be less favorable than those where actinide atom is shifted to the cage wall and interacts with only few carbon neighbors.

Interest in C_{60} fullerene-encapsulated actinide atoms is also due to the possibility of 5f – states participation in bonding. It is evident that theoretical study of the electronic structure and chemical bonding of any systems containing actinides requires the inclusion of all relativistic effects in the computational method. The fully relativistic calculations of An@C_{28} clusters (An = Th – Md) [2] showed that 5f orbitals participate in chemical bonding of the first half of this series from Th@C_{28} to Cm@C_{28}. Conversely, in the fully relativistic calculations of An@C_{40} complexes (An = Th – Md) [3], we determined that An5f contributions to bonding are nearly three times less than that of the main An6d–C2p interaction even in the clusters at the beginning of this row (Th@C_{40} and Pa@C_{40}). These results are in agreement with the known sensitivity of 5f bonding features to the variation of bond-lengths, because an average radius of fullerene cage increases from 2.5 Å (C_{28}) to 3 Å (C_{40}). Since the radius of C_{60} molecule is close to 3.6 Å, one can expect that in a case of central position of metal atom the role of 5f states in bonding will be noticeably less than in An@C_{40}. On the other hand, some shift of actinide atom from the center to the cage wall can reduce the An–C bond lengths to the values, which are more typical for the An–C interactions in the molecules and solids.

The aim of the present paper was the search for most stable positions of actinide atom inside a C_{60} cage, the evaluation of geometrical parameters of the neutral An@C_{60} complexes for almost all actinides from Th to Md, the investigations of the chemical bonding and the role played by 5f states in the interaction between metal atom and the carbon shell. Another aim of the work presented here was the comparison of binding energies of the three competitive types of structures: (1) endohedral An@C_{60}; (2) exohedral AnC_{60}, where the actinide atom is bound to C_{60} from the outside of the cage; (3) "networked" C_{59}An, where the actinide atom is incorporated into the C_{60} cage, at least in the cases of most stable complexes. The results of present calculations also allow us to evaluate the electron density redistribution for various positions of metal atom and across this series.

2. Objects and methods of calculations

Geometry optimization of "empty" C_{60} molecule with I_h symmetry and C_{60} interacting with actinide atoms was performed using the DMol^3 method [7] in the scalar relativistic approach [8] and with the largest double numerical atomic basis set ("dnp"). The Coulombic potential was computed with the use of model density obtained as decomposition of charge density into multipolar components including those with $l = 3$. The generalized gradient approximation (GGA) in "BLYP" [10,11] and "PBE" [9] forms was used in all calculations. In a previous paper [2], we used "PBE" as well as "BLYP" [10,11] functionals, as was shown, the energetic and geometrical parameters obtained using both approaches were similar. Optimization of the molecular structures was done until the change in the maximum energy gradient values was less than 0.001 atomic unit, the global orbital cutoff was 8.0 Å. To confirm that the stationary points correspond to minima, the vibrational frequencies were computed for all clusters. To test the reliability of parameters used in the calculations, we performed geometry optimization for Th@C_{60}, Am@C_{60} and Md@C_{60} systems using the multipolar components with $l = 4$ and 10 Å for orbital cutoff. Though the computer time increased considerably, the changes in energy were less than 0.05 eV and the shifts in atomic coordinates were less than 10^{-3} Å.

For the investigation of the nature of chemical bonding and the role played by 5f electrons in An@C_{60} complexes, we also used the fully relativistic discrete variational method (RDV) [12,13]. For the most stable geometrical structures obtained by DMol^3, RDV calculations were performed. The RDV method is based on the solution of the Dirac-Slater equation for four-component wave functions, transforming according to irreducible representations of the double point group (C_S^* and C_{2V}^* in the present calculations). For calculation of the symmetry coefficients, we used the original code which realizes the projection-operators technique [12] and includes the matrices of irreducible representations of double point groups obtained in Ref. [14] and the transformation matrices presented in Ref. [15]. The extended bases of four-component numerical atomic orbitals (AO) obtained as the solution of the Dirac-Slater equation for isolated neutral atoms also included An$7p_{1/2}$ and $7p_{3/2}$ functions in addition to occupied AOs. Numerical Diophantine integration in matrix elements calculations was done for 126000 sample points, which provided the convergence of valence MO energies within 0.1 eV. The effective charges on atoms (Q_{eff}) were computed as integrals of electron density inside the domains bounded by the points of its minimum [16].

3. Results and Discussion

3.1. Results of geometry optimization

It is well known that optimized structure of $C_{60}(I_h)$ consists of 12 regular pentagons and 20 hexagons (Fig. 1). In our DMol calculations, we obtained that the radius for the empty fullerene is close to 3.55 Å. This value for the cage radius corresponds to the C–C bond lengths in pentagons and hexagons in the range 1.46 – 1.40 Å. In the calculations of Chang et al. [6] the interval of C–C bond lengths in $C_{60}(I_h)$ was slightly wider: 1.45 – 1.37 Å. For the evaluation of the relative stability of various An@C_{60} complexes, it is reasonable to consider the binding energy E_b (which is sometimes called the "total bond energy" or the "atomization energy"). The binding energy of a cluster is usually defined as $E_b = E_{tot} - E_{sum}$, where E_{tot} is the total energy of a cluster and E_{sum} is the sum of total energies of all isolated atoms in the cluster. The binding energies for all investigated fullerenes are summarized in Table 1.

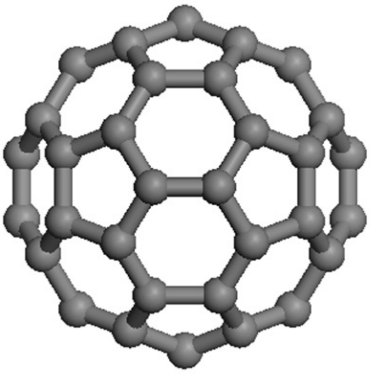

FIG. 1. The geometrical structure of fullerene C_{60}

We started by modeling the most symmetrical central position of actinide atom inside the C_{60} cage, the values of $E_b(I_h)$ obtained in these calculations are shown in the second column of Table 1. Comparison of the E_b values for C_{60} and An@C_{60} allows one to evaluate the stability of An@C_{60} clusters with respect to the dissociation limit An + C_{60} for all actinides. According to our results, the symmetrical complexes of Pa, U and Np are stable systems and the most stable one is Np@C_{60} with Np + C_{60} dissociation energy near 3.1 eV. In the cases of smaller endohedral fullerenes An@C_{28} [2] and An@C_{40} [3], the Pa@C_n were the most stable complexes with corresponding dissociation energies near 8.1 and 6.4 eV respectively. Although the stability of An@C_{60} (I_h) obtained in the present calculations is considerably less than that of the corresponding An@C_{28} and An@C_{40}, the uranium encapsulation reaction $U + C_{60} \to$ U@C_{60} (Table 1) is still exothermic (2.6 eV), whereas according to the results of Chang et al. [6] the U@C_{60} complex should be noticeably less stable than separated C_{60} and U (by ~ 3.5 eV). The analysis of geometrical parameters obtained for An@C_{60} (I_h) shows

Table 1. Binding and dissociation energies (eV), distances (Å) between the actinide atom and the nearest C atoms and effective charges (e) on actinide atoms in the investigated complexes

Complex	$E_b\,(I_h)$	E_b (C_s, C_{2v})	E_d (C_s, C_{2v})	R_{An-C} (C_s, C_{2v})	Q_{An} (C_s, C_{2v})	
					Hirshfeld	Integral
C_{60}	-452.7	-	-	-	-	
Th@C_{60}	-454.3	-458.5(C_s)	5.8	2.50 / 2.50 / 2.50	0.68	2.17
Pa@C_{60}	-455.0	-459.3(C_s)	6.6	2.44 / 2.44 / 2.44	0.71	1.93
U@C_{60}	-455.3	-458.9(C_s)	6.2	2.41 / 2.43 / 2.44	0.63	1.83
Np@C_{60}	-455.8	-458.4(C_s)	5.7	2.42 / 2.43 / 2.44	0.57	1.74
Pu@C_{60}	-453.5	-455.2(C_{2v})	2.5	2.36 / 2.51 / 2.51	0.66	1.41
Am@C_{60}	-453.3	-454.3(C_{2v})	1.6	2.36 / 2.52 / 2.52	0.62	1.34
Cm@C_{60}	-453.4	-454.5(C_{2v})	1.8	2.46 / 2.61 / 2.61	0.60	1.35
Bk@C_{60}	-453.4	-454.4(C_s)	1.7	2.60 / 2.61 / 2.63	0.75	1.22
Cf@C_{60}	-453.4	-454.4(C_s)	1.7	2.64 / 2.65 / 2.66	0.73	1.23
Es@C_{60}	-453.4	-454.2(C_s)	1.5	2.65 / 2.67 / 2.69	0.72	1.15
Fm@C_{60}	-453.4	-453.6(C_s)	0.9	2.65 / 2.67 / 2.70	0.62	1.14
Md@C_{60}	-453.4	-453.5(C_s)	0.8	2.78 / 2.79 / 2.79	0.64	1.06
PaC_{60}	-	-455.7	3.0	2.34	0.58	1.73
C_{59}Pa	-	-448.8	-3.9	2.17 / 2.25 / 2.25	0.78	2.44

that the deformation of the cage due to addition of any actinide atom is small: the radial expansion of the cage is less than 0.01 Å in all clusters.

The search for less symmetrical An@C_{60} structures was undertaken in a few ways: the various shifts of metal atom from the center in different directions were considered. These initial configurations were subjected to geometry optimization, leading to new stable, but less symmetrical An@C_{60} structures. The values of initial shift of actinide atom varied from 0.1 to 0.6 Å. However, small shifts (0.1 – 0.3 Å) led to a relaxation of the system into structures with An atom located near the center of C_{60} shell. Conversely, a shift of metal atom by 0.4 Å or greater led to rearrangement of the complex into a structure with an actinide atom located near the cage wall. This result means that the potential barrier for transformation of the geometry with central actinide position is quite small. The optimized structures with various symmetries were obtained (C_{2v}, C_s, C_1). According to results of DMol calculations, we can predict that there are two types of most stable geometry for "distorted" endohedral fullerenes, corresponding to C_s and C_{2v} symmetries. The structures of these complexes are illustrated in Figure 2. Though the difference in binding energy for these two isomers for each An@C_{60} cluster is within 0.1 eV, we can conclude that for complexes of Th, Pa, U and Np, the former type (C_s) is slightly more stable and should be considered as the ground structure. For the three clusters in the middle of the row (Pu, Am, Cm) the C_{2v} – isomer appeared to be slightly more stable. For the "end part" of the row from Bk to Md the E_b for C_s structures is slightly lower than that for C_{2v} isomers. The binding and dissociation energy values obtained for these structures are shown in the third and the fourth columns of Table 1 respectively. As can be seen from Fig. 2, in both "distorted" isomers, the actinide atom has six nearest carbon neighbors, which belong to one hexagon in C_s – structure and to the two adjacent hexagons ("X" – shape of carbon vicinity) in the C_{2v} structure.

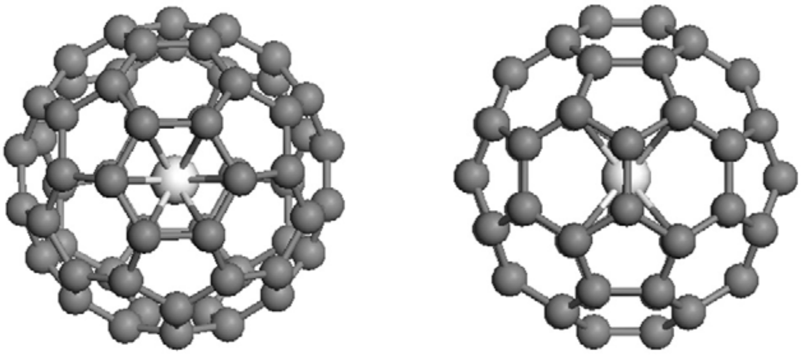

FIG. 2. The geometrical structures of endohedral complexes $An@C_{60}$ corresponding to C_s (left) and C_{2v} (right) symmetry

According to our results, complexes of Th, Pa, U and Np are more stable systems with An + C_{60} dissociation energy near 6 eV. The most stable cluster is $Pa@C_{60}$ with a dissociation energy close to 6.6 eV. As mentioned above, in the cases of smaller endohedral fullerenes the most stable complexes were also formed by encapsulation of protactinium atom [2,3]. It is interesting that stable systems were also obtained in the second half of the $An@C_{60}$ row: the complexes of Cm, Bk Cf and Es are noticeably more stable than separated C_{60} and An. Note that stable clusters for heavier actinides were also predicted for $An@C_{40}$ systems [3], moreover, for $An@C_{60}$ clusters the similar non-monotonic trend is obtained, particularly, in the case of $Am@C_{60}$ the absolute value of E_b is less than that for $Cm@C_{60}$. As can be seen, the values of E_b for all isomers of $Fm@C_{60}$ and $Md@C_{60}$ (near –453.5 eV) are lower than that of empty C_{60} (–452.7 eV).

The values of An–C bond lengths for the nearest carbon neighbors in the C_s and C_{2v} structures are shown in the fifth column of Table 1. Though the shapes of hexagons and pentagons in C_s and C_{2v} structures are very close to regular geometry of an empty C_{60}, the six nearest neighbors of actinide atom belong to the three and two nonequivalent types in C_s and C_{2v} isomers respectively. These atoms are labeled later as C1, C2 and C3 (C_s), while in C_{2v} clusters the two pairs of carbon atoms of C2 and C3 types are equivalent. In each complex of the C_s – type containing Th, Pa, U, Np and from Bk to Md, the distances between metal atom and C1, C2 and C3 are close to each other (Table 1). These results mean that the actinide atom is located just under the center of one hexagon. For the molecules of C_{2v} type ($Pu@C_{60}$, $Am@C_{60}$, $Cm@C_{60}$) we obtained noticeable variation of these bond lengths (by 0.15 – 0.16 Å). As can be seen, there is no complete correlation between the variation of average values of An–C bond lengths in $An@C_{60}$ row and the main trend of E_b variation, however, the increase of stability from $Th@C_{60}$ to $Pa@C_{60}$ and its decrease from $Pa@C_{60}$ to $Am@C_{60}$ and from $Cm@C_{60}$ to $Md@C_{60}$ are accompanied by the decrease and increase of corresponding An–C distances, as could be expected from general consideration. There is one noticeable exception to this rule: the An–C bond lengths in the less stable $Am@C_{60}$ are less than those in the more stable $Cm@C_{60}$, $Bk@C_{60}$ and $Cf@C_{60}$ complexes.

In Table 1 we also show the results obtained for the most stable example of exohedral fullerene (PaC_{60}) and "networked" complex ($C_{59}Pa$). The exohedral structures were generated from empty C_{60} particle by the addition of Pa atom from several spatial directions. These initial configurations were subjected to geometry optimization, leading to a few stable structures. The lowest-energy C_{2v} isomer is a distorted C_{60} fullerene, with the metal atom bonded to a pair of carbon atoms, another isomer, in which the actinide atom interacts with carbon hexagon appeared to be slightly less stable. The structure of this complex is illustrated in Figure 3. We obtained that in these complexes Pa–C distances are near 2.34 Å. The absolute value of binding energy of this most stable exohedral complex was found to be 455.7 eV, this value is noticeably less than that for the non-central endohedral position of Pa inside C_{60} cage (459.3 eV). However, the value of $|E_b|$ for exohedral cluster was greater than that for endohedral position in the center of fullerene (455.0 eV). Thus, the dissociation energy of PaC_{60} complex with respect to the $PaC_{60} \rightarrow Pa + C_{60}$ reaction is more than two times less than that obtained for the non-central endohedral position of protactinium atom. The distortion of fullerene cage in the PaC_{60} (C_{2v}) molecule due to interaction with metal atom led to increase of the number of non-equivalent carbon sites. However, the average value of r(C) in PaC_{60} system is close to the corresponding parameter of endohedral complex.

The "networked" $C_{59}Pa$ structure was generated from an empty C_{60} particle by the substitution of an actinide atom for a carbon site. Then, this initial structure was subjected to geometry optimization, leading to the new equilibrium positions for the metal and carbon atoms (Fig. 3). The parameters of this cluster were shown in Table 1. In contrast to endohedral and exohedral systems, the "networked" complex is less stable than an empty C_{60} cage (Table 1). This result is quite expected because the C–C bonds are certainly stronger than C–An bonds in such systems. We also obtained that during geometry optimization of $C_{59}An$ structure the initial distances between metal atom and the cage center increased from 3.55 Å to 4.96 Å. This considerable increase in the distances between metal atom and the center of the cage is accompanied by a corresponding increase in the bond lengths between actinide atom and its three nearest neighbors: these distances were found to be 2.17 Å, 2.25 Å and 2.25 Å. Nevertheless, the interatomic Pa–C distances in $C_{59}Pa$ as well as in PaC_{60} are noticeably less than those in more stable endohedral complex (2.44 Å).

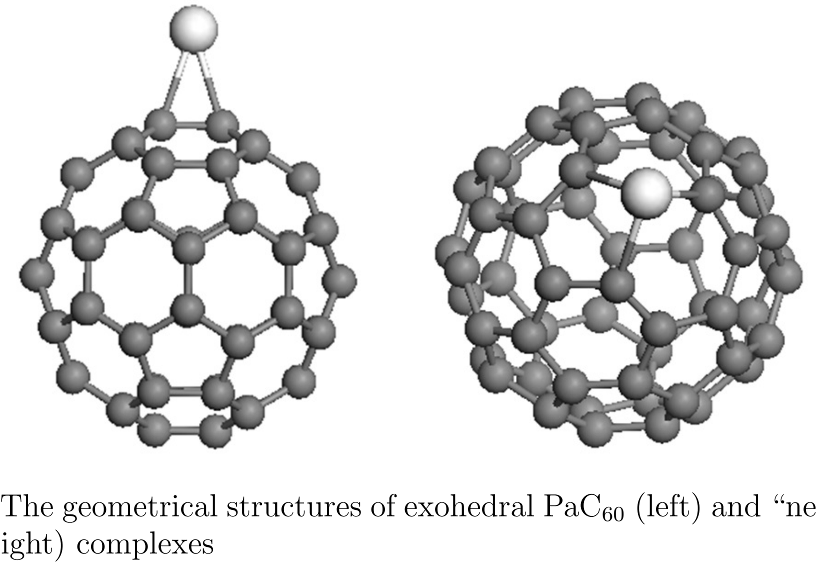

FIG. 3. The geometrical structures of exohedral PaC_{60} (left) and "networked" $C_{59}Pa$ (right) complexes

As mentioned above, the present DMol results were obtained in the scalar relativistic approach, however, the authors [1] evaluated the role of spin-orbit coupling in the $Pu^{4+}@C_{28}$ cluster and showed that the addition of these effects caused a maximum expansion of the Pu–C distance of 0.027 Å with respect to the scalar relativistic results. They also reported that the scalar relativistic bonding energy of the $Pu^{4+}@C_{28}$ increased by less than 8% when the spin-orbit coupling effects were included in the calculations.

3.2. RDV calculations

In Figure 4 we show the partial densities of states (DOS) obtained in the fully relativistic RDV calculations for the ground state isomers of $Th@C_{60}$ and $Pa@C_{60}$ clusters. In the cases of C2s and C2p DOS we show only the contributions from C1, C2 and C3 atoms, which are the nearest neighbors of metal ion. As can be seen from Fig. 4, the spin-orbital interaction is small for the "outer" bands, particularly the 0.9 eV splitting was obtained for $An5f_{5/2}$ and $An5f_{7/2}$ main peaks. The relativistic effects become considerable for deeper orbitals, that is, the main peak of $An6p_{1/2}$ band is shifted to the lower energies by ∼ 9 eV (Th) and ∼ 10 eV (Pa) from the highest intensity peak of $An6p_{3/2}$ DOS. In both complexes the most intensive part of occupied valence C2p band in the energy region from 0 to –10 eV (Fermi level is used as a zero of energy scale) contains some contributions from An6d AOs (near -6 – -4 eV) and An5f AOs (near -5 – 0 eV). The vacant MOs are formed by C2p, An5f, 6d, 7s and 7p orbitals in the energy region from 0 to 19 eV.

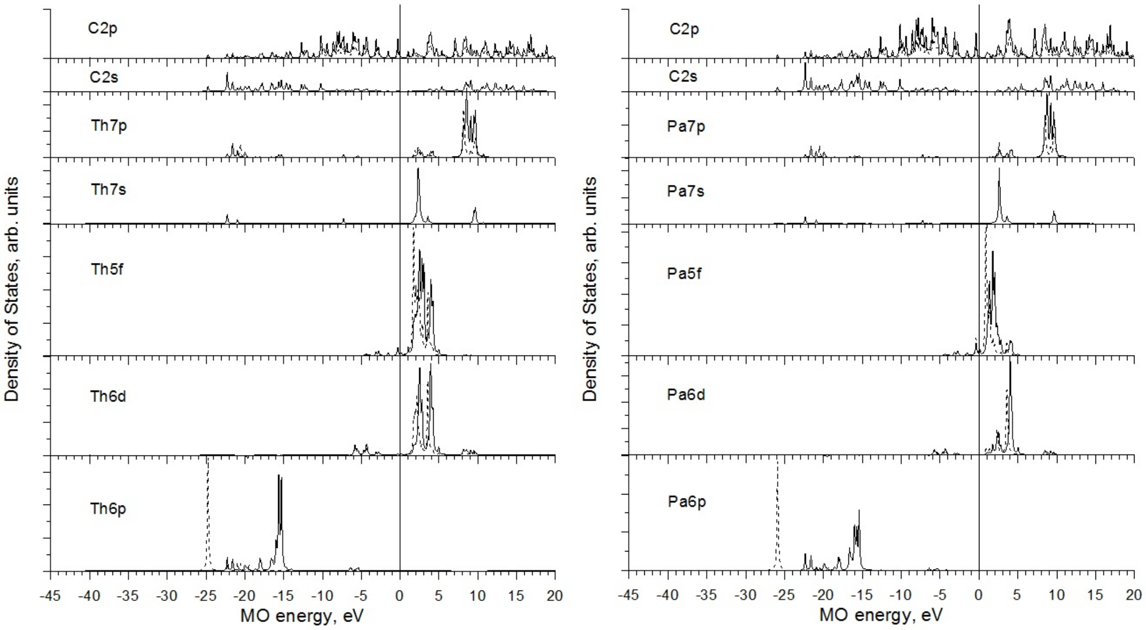

FIG. 4. Partial densities of states for the ground isomers of $Th@C_{60}$ (left) and $Pa@C_{60}$ (right) clusters. The broken lines correspond to $p_{1/2}$, $d_{3/2}$, and $f_{5/2}$ DOS, the solid lines correspond to $p_{3/2}$, $d_{5/2}$ and $f_{7/2}$ DOS (vertical line is the border between occupied and vacant states)

The energy gap between occupied and vacant molecular states, defined as the difference of energy of the highest occupied (HOMO) and the lowest unoccupied (LUMO) molecular orbitals, obtained in our relativistic calculations for $Th@C_{60}$, is near 0.4 eV. In similar calculations for $Th@C_{28}$ [2] and $Th@C_{40}$ [3], we obtained considerably greater HOMO – LUMO gaps (2.3 and 1.4 eV respectively). The latter gap values were noticeably greater than those for the empty C_{40} and C_{28} cages (near 0.05 and 0.6 eV respectively), on the other hand, the energy gap in empty C_{60} cage (1.6 eV) is considerably greater than that in any $An@C_{60}$ cluster studied in the present work. In $Th@C_{60}$ and $Pa@C_{60}$ complexes both the HOMO and LUMO are of predominantly C2p character with small contributions from

An5f states. According to our results, the Fermi level in Pa@C_{60} is located at the small C2p subband consisting of two MOs corresponding to Γ_3 and Γ_4 irreducible representations of C_s double point group, in this cluster one orbital is occupied and one is vacant. The energy splitting between this C2p band (the admixtures of Pa5f AOs are near 10%) and the next unoccupied levels, corresponding to the states with main contribution from $5f_{5/2}$ AOs ($\sim$ 80%), is nearly 0.8 eV (Fig. 4). Although the Th5f, 6d and Pa5f, 6d molecular levels are vacant, the covalent mixing between $5f_{5/2}$, $5f_{7/2}$, $6d_{3/2}$, $6d_{5/2}$ and C2p orbitals in the occupied valence band leads to noticeable Mulliken population of 5f and 6d AOs, which were obtained as $5f^{0.43}_{5/2}$, $5f^{0.43}_{7/2}$, $6d^{0.54}_{3/2}$, $6d^{0.64}_{5/2}$ (Th@C_{60}) and $5f^{1.24}_{5/2}$, $5f^{0.92}_{7/2}$, $6d^{0.52}_{3/2}$, $6d^{0.59}_{5/2}$ (Pa@C_{60}).

In the next molecule of this row, U@C_{60}, the HOMO is still of C2p character, but the admixtures of U5f AOs increase up to 20%, while the LUMO in this cluster is of $5f_{5/2}$ character (82%). The energy gap between occupied and vacant levels is near 0.4 eV. Though the molecular orbitals containing main contributions from 5f AOs are still vacant in U@C_{60} cluster, the hybridization of $5f_{5/2}$, $5f_{7/2}$ and C2p AOs in the occupied molecular orbitals are responsible for the essential Mulliken populations of U5f AOs ($5f^{1.98}_{5/2}$ and $5f^{1.25}_{7/2}$), which are greater than those in Pa@C_{60}. In contrast, the populations of U6d orbitals ($6d^{0.51}_{3/2}6d^{0.57}_{5/2}$) are nearly the same as in protactinium complex. In the neptunium cluster, both HOMO and LUMO contain main contributions from Np$5f_{5/2}$ AOs (80%), i.e. the Fermi level is located in the $5f_{5/2}$ band. In addition, the admixtures of Np5f states in the occupied MOs of C2p character considerably increase (up to 35–40%). The filling of $5f_{5/2}$ states and increasing hybridization of $5f_{5/2}$, $5f_{7/2}$ and C2p AOs in the valence band are responsible for the essential Mulliken population of Np5f AOs: $5f^{2.76}_{5/2}5f^{1.55}_{7/2}$, on the other hand, the populations of Np6d orbitals decrease ($6d^{0.48}_{3/2}6d^{0.54}_{5/2}$) as compared to the uranium cluster.

The ground structures of the next three molecules of this row Pu@C_{60}, Am@C_{60} and Cm@C_{60} correspond to C_{2v} –type. In Figure 5, we show the partial DOS obtained in RDV calculations of Pu@C_{60} and Cm@C_{60} clusters. In the cases of C2s and C2p DOS we show only the contributions from two C1 and four C2 atoms, which are the nearest neighbors of metal ion. As can be seen from Fig. 5, the peaks corresponding to An$6p_{1/2}$ bands are shifted to lower energies by $\sim$ 11 eV (Pu) and $\sim$ 12 eV (Cm) from the highest intensity peak of An$6p_{3/2}$ DOS. In both complexes, the An$5f_{5/2}$ bands are completely occupied, however, between $5f_{5/2}$ and $5f_{7/2}$ states the small band of C2p character is located. This C2p band contains six MOs, two of which are occupied in Pu@C_{60} and three and four orbitals are occupied in Am@C_{60} and Cm@C_{60} clusters respectively. As a result, the An$5f_{7/2}$ MOs are vacant in all these systems, however, the admixtures of An$5f_{7/2}$ AOs in the highest occupied molecular states increase from 17% in Pu@C_{60} to 35% in Am@C_{60} and to 39% in Cm@C_{60}. Thus, the HOMO and LUMO in these three complexes are the mixture of C2p and An$5f_{5/2}$, $5f_{7/2}$ AOs. The strong hybridization of both $5f_{5/2}$ and $5f_{7/2}$ AOs with C2p orbitals in occupied MOs is responsible for the non-integer Mulliken population of 5f AOs, which increases from $5f^{3.71}_{5/2}5f^{2.14}_{7/2}$ in Pu@C_{60} to $5f^{4.35}_{5/2}5f^{2.55}_{7/2}$ in Am@C_{60} and to $5f^{4.95}_{5/2}5f^{3.02}_{7/2}$ in Cm@C_{60}. As mentioned above, the populations of An6d orbitals decreases for heavier actinides, the same trend was obtained for Pu@C_{60} ($6d^{0.35}_{3/2}6d^{0.33}_{5/2}$), Am@$C_{60}$ ($6d^{0.32}_{3/2}6d^{0.29}_{5/2}$) and Cm@$C_{60}$ ($6d^{0.25}_{3/2}6d^{0.21}_{5/2}$) complexes.

The occupied molecular orbitals of $5f_{7/2}$ character (51%, 57% and 73%) are firstly achieved in Bk@C_{60} (Fig. 6), as a result, the Mulliken populations of Bk5f states are $5f^{5.43}_{5/2}5f^{3.62}_{7/2}$, i.e. the total number of 5f electrons in Bk@C_{60} ($\sim$9.05) is greater than that in Cm@C_{60} ($\sim$7.97) by 1.08. The LUMO in Bk@C_{60} is also a mixture of Bk$5f_{7/2}$ (75%)

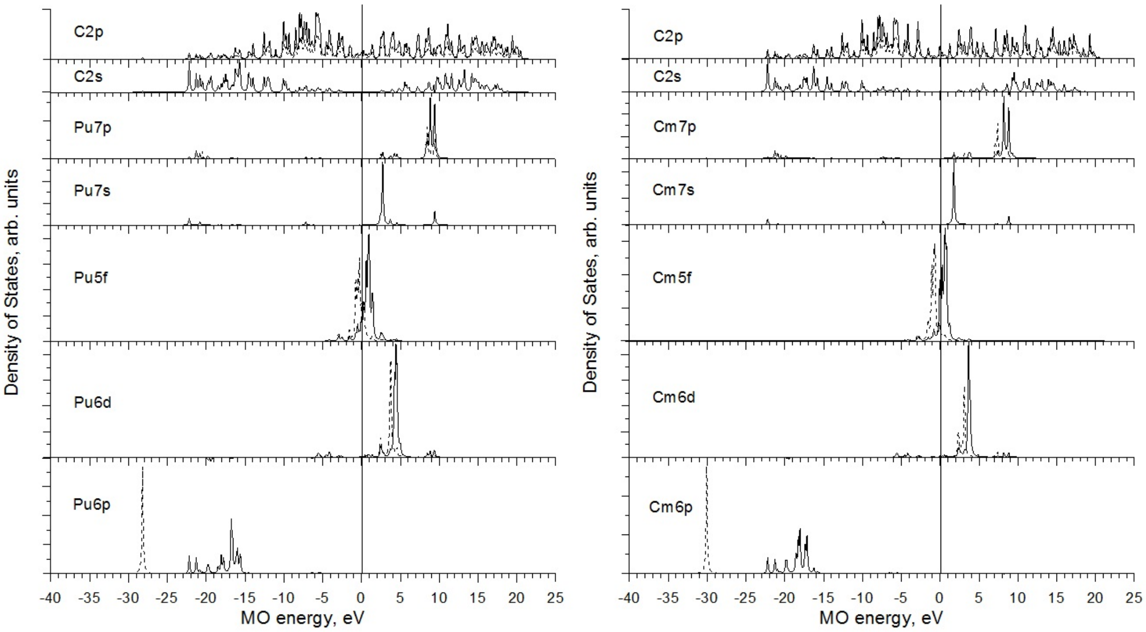

FIG. 5. Partial densities of states for the ground isomers of Pu@C_{60} (left) and Cm@C_{60} (right) clusters

and C2p AOs. On the other hand, the hybridization of Bk6d and C2p orbitals in the occupied C2p band is less than that in Cm@C_{60}, and a noticeable decrease of the Mulliken populations of Bk6d AOs was obtained ($6d^{0.18}_{3/2}6d^{0.12}_{5/2}$). Further filling of 5f shell and considerable depopulation of 6d shell were obtained for Cf@C_{60} ($5f^{5.71}_{5/2}5f^{4.40}_{7/2}6d^{0.11}_{3/2}6d^{0.04}_{5/2}$) and Es@$C_{60}$ ($5f^{5.86}_{5/2}5f^{5.28}_{7/2}6d^{0.10}_{3/2}6d^{0.02}_{5/2}$). The complete occupation of both $5f_{5/2}$ and $5f_{7/2}$ molecular orbital types was achieved in the Fm@C_{60} complex. The partial DOS obtained in RDV calculations of Fm@C_{60} are shown in Fig. 6. The LUMO in Fm@C_{60} are of almost purely C2p character (95%), the contributions from Fm5f AOs are nearly 3%. However, as a result of covalent mixing between the Fm atomic orbitals and the C_{60} cage orbitals the Mulliken populations of 5f AOs are $5f^{5.93}_{5/2}5f^{6.20}_{7/2}$, i.e. the total number of 5f electrons in the Fm@C_{60} cluster (12.1) is close to that of the isolated Fm atom. The energy gap between the occupied and vacant levels in Fm@C_{60} is near 0.9 eV, which is the greatest value obtained in our calculations for endohedral fullerenes An@C_{60}. In the “last” investigated Md@C_{60} complex, one more molecular orbital of C2p subband is occupied, thus both HOMO and LUMO are of almost purely C2p character and lie above the completely occupied Md$5f_{7/2}$ band by 0.4 eV. As expected, the admixtures of C2p AOs in the molecular orbitals of Md$5f_{7/2}$ type decrease and the Mulliken populations of Md5f shell are $5f^{5.98}_{5/2}5f^{7.16}_{7/2}$. As in the case of the fermium cluster, the total number of 5f electrons in the Md@C_{60} molecule (13.1) is close to that of isolated Md atom.

To compare the effects of spin-orbit coupling for the valence orbitals of the systems at the beginning and at the end of An@C_{60} series, one can use the splitting of the main peaks corresponding to $5f_{5/2}$ and $5f_{7/2}$ states. According to RDV calculations, the $5f_{5/2}$ – $5f_{7/2}$ peaks separation for Th@C_{60}, Pa@C_{60}, U@C_{60} and Np@C_{60} is close to 0.9 – 1.1 eV. For the Pu and Am complexes we obtained ∼1.2 eV, for Cm and Bk these values are close to 1.3 – 1.5 eV. In Cf@C_{60} and Es@C_{60} this spin-orbit splitting can be evaluated approximately as 1.6 – 1.7 eV. The noticeable increase of this value was obtained for the end of the row, i.e.

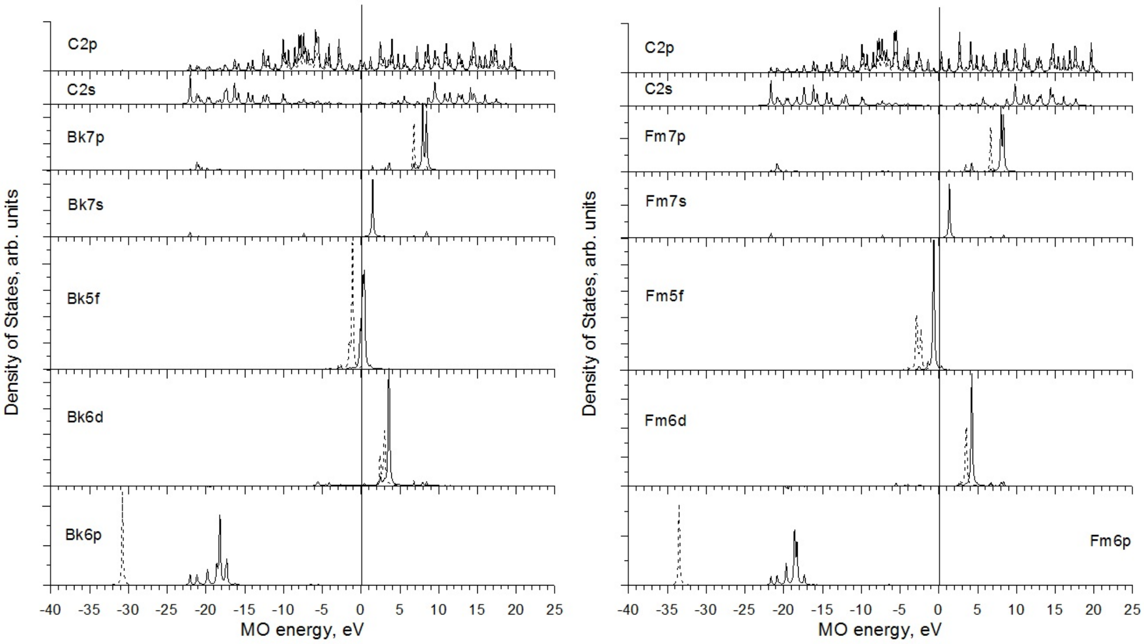

FIG. 6. Partial densities of states for the ground isomers of Bk@C_{60} (left) and Fm@C_{60} (right) clusters

for Fm@C_{60} and Md@C_{60} the splitting between $5f_{5/2}$ and $5f_{7/2}$ peaks is near 2.2 and 2.3 eV respectively (Fig. 6).

The molecular orbital structure of the most stable exohedral complex PaC_{60} noticeably differs from that of the corresponding endohedral system. In Figure 7, we show the partial DOS obtained in RDV calculation of PaC_{60} cluster. In the cases of C2s and C2p DOS we show only the contributions from two C1 atoms, which are the nearest neighbors of metal ion. As can be seen from Fig. 7, the hybridized C2s – Pa6$p_{3/2}$ subband in the energy region from -23 to -20 eV is absent in PaC_{60}, resulting in a more narrow distribution of $6p_{3/2}$ DOS. The positions of Pa6d, 5f and 7s levels become closer to the Fermi level (Fig. 7). These shifts of the 6d, 5f and 7s states lead to noticeable increases in their contributions to molecular orbitals in this energy region, particularly the admixtures of Pa5f and 6d AOs in HOMO and LUMO achieve 19% and 10% respectively. Although the Pa5f and 6d orbitals are also vacant in the PaC_{60} cluster, the hybridization of these states with occupied C2p orbitals leads to some Mulliken population of these AOs. According to our calculations, the occupations of these orbitals can be defined as $5f^{1.37}_{5/2}5f^{0.74}_{7/2}6d^{0.65}_{3/2}6d^{0.58}_{5/2}$. As seen, the populations of 5f AOs in PaC_{60} are slightly less than those in Pa@C_{60}, while the populations of 6d AOs in PaC_{60} are greater than those in Pa@C_{60} by 0.13. Surprisingly, in the case of a “networked” complex C_{59}Pa, we did not obtain the principal transformation of electronic structure (Fig. 7). The C2s – Pa6$p_{3/2}$ subband in the energy region from -23 to -20 eV is also absent in the C_{59}Pa cluster. The Pa6d, 5f and 7s DOS also shift to lower energies, however, their contributions in the valence band in the energy region from 0 to -4 eV become more important than those in endohedral and exohedral clusters. We can also note, that “networked” position of metal atom in the fullerene cage leads to some broadening of Pa6d, 7s and 7p bands in the energy region from 1 to 11 eV (Fig. 7).

The considerable hybridization between An5f and C2p AOs was obtained in all investigated fullerenes. However, the coefficients corresponding to An5f contribution in the molecular orbitals are not directly connected with the degree of 5f states delocalization. The

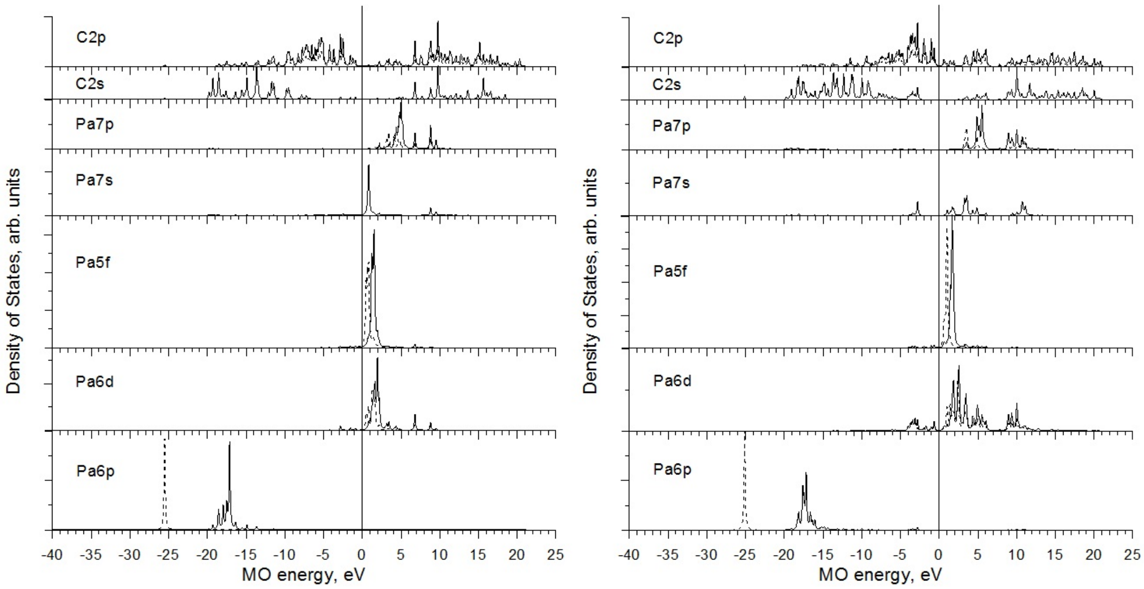

FIG. 7. Partial densities of states for the PaC_{60} (left) and $C_{59}Pa$ (right) clusters

latter effect could be evaluated qualitatively by an analysis of the shapes of corresponding molecular orbitals or more quantitatively by the values of overlap populations of various pairs of the metal and carbon AOs (n_{ij}). The values of n_{ij} can also give the bond orders of these states [17]. The values of overlap populations for C2p and 5f, 6d, 7s AOs of actinides obtained in our RDV calculations of endohedral clusters are listed in Table 2. As expected, the role of An7p-C2p interaction (not shown in Table 2) is anti-bonding in all investigated complexes.

TABLE 2. Overlap populations of An5f, 6d, 7s and C2p orbitals (10^{-3}e, per one pair of interacting atoms) in $An@C_{60}$ complexes

Orbitals		Th	Pa	U	Np	Pu	Am	Cm	Bk	Cf	Es	Fm	Md
An5f -	C_12p	36	41	37	32	22	18	12	8	3	2	1	0
	C_22p	35	42	39	34	18	15	11	8	4	2	1	0
	C_32p	35	39	36	31	-	-	-	7	3	1	1	0
An6d -	C_12p	98	84	83	84	64	62	60	50	40	38	35	29
	C_22p	97	83	85	84	50	49	49	46	41	37	35	27
	C_32p	96	83	84	84	-	-	-	47	40	37	34	28
An7s -	C_12p	15	16	16	16	9	9	10	12	9	9	10	3
	C_22p	15	16	16	16	18	19	18	13	7	9	8	2
	C_32p	14	16	16	16	-	-	-	13	8	7	9	2

Examination of Table 2 reveals that An6d orbitals play the main role in the chemical bonding of a metal atom and C_{60} cage in all of $An@C_{60}$ clusters. This result is quite expected, because in our earlier relativistic calculations of actinide oxides, fluorides [18,19] and $An@C_{40}$ clusters [3], the main contributions to bonding was also provided by An6d AOs and the next An5f contributions to bonding were considerably less. However, the earlier calculations of small endohedral fullerenes $An@C_{28}$ [2] showed that An6d and 5f orbitals play comparable roles in the chemical bonding of a metal atom and C_{28} cage in the first half of the An@C_{28} row. This difference in the bonding behavior of An5f states in An@C_{40}, An@C_{60} and An@C_{28} can be explained by the well known fact that An5f AOs participation in bonding is sensitive to the distances between actinide atom and its neighbors [19]. As mentioned above, the shortest An–C bond lengths in An@C_{40} and non-symmetrical An@C_{60} clusters are greater than the longest An–C bond lengths in An@C_{28} systems. As shown in Table 2, the overlap populations of An5f–C2p states increase when going from Th@C_{60} to Pa@C_{60} clusters and then monotonously decrease to zero at the end of this row. However, noteworthy is the considerable decrease of An5f contributions to bonding on going from Np@C_{60} to Pu@C_{60}. On the other hand, the slightly non-monotonous bonding behavior at the beginning of An@C_{60} row is detected for An6d orbitals. As can be seen from Table 2, a small increase of overlap populations for An6d–C2p states takes place for the U@C_{60} and Np@C_{60} molecules in comparison to the Pa@C_{60} cluster.

Comparison of the stability of endohedral complexes (Table 1) and corresponding bond orders (Table 2) shows that there is good correlation between DMol and RDV results. The increase of the dissociation energy (An@C_{60} $\rightarrow$ An + C_{60}) when going from Th@C_{60} to Pa@C_{60} is in agreement with the increase of contribution to bonding from Pa5f states, note that this contribution is the greatest in An@C_{60} row (Table 2). Further decrease of stability from Pa to Am correlates with a decrease of the overlap populations for An5f–C2p as well as for An6d–C2p AOs. The small increase of $|E_b|$ for Cm@C_{60} and Bk@C_{60} clusters (Table 1) can be explained by the role of spin-polarization, which is included in the scalar-relativistic DMol calculations, but is not treated in the standard Dirac theory. Note, that similar results were also obtained for An@C_{40} complexes [3].

The values of overlap populations for C2p and 5f, 6d, 7s AOs of protactinium obtained in our RDV calculations for the exohedral and “networked” complexes are listed in Table 3. The corresponding parameters for endohedral cluster are also shown in Table 3 for comparison. Note, that n_{ij} values presented in Tables 2 and 3 correspond to one pair of interacting atoms, hence, the sum of these values for the six nearest neighbors in endohedral cluster will be considerably greater than total overlap populations in exohedral system. However, as can be seen from Table 3, the interactions between actinide and a specific carbon atom in the C_{59}Pa and PaC_{60} are stronger than that in Pa@C_{60} complex. Examination of Table 3 reveals that Pa6d orbitals also play the main role in chemical bonding of metal atom and carbon cage in these clusters. The variation of n_{ij} for the Pa5f–C2p and Pa6d–C2p bonds also correlates with Pa–C bond lengths (Table 1). As shown in Table 3, the interaction between protactinium atom and each of three nearest neighbors in “networked” complex is considerably stronger than that in more stable endohedral cluster. However, as mentioned above, the actinide – carbon substitution in C_{60} cage is energetically disfavored process and the formation of C_{59}Pa complex does not provide a better way for the extraction of the actinides from some species.

The effective charges on actinide atoms (Q_{An}) obtained in our scalar relativistic (DMol) and fully relativistic calculations (RDV) are listed in Table 1. As shown, the effective charges obtained in DMol calculations using Hirshfeld scheme correlate with neither the variation of binding energy nor with the variation of An–C bond lengths. It is quite evident that the increase in charge transfer for the Pu@C_{60} and Am@C_{60} in comparison with Np@C_{60} as well as for the second half of the series (from Bk to Md) in comparison with Cm@C_{60} and the weaker interaction between cage and actinide atom are contradictory. On the other hand, the integral charges obtained in RDV calculations (Table 1) agree with the variation in the binding energy. Although the Q_{An} obtained in relativistic calculations are considerably greater than the DMol values, the effective charges on actinide atoms are less

TABLE 3. Overlap populations of An5f, 6d, 7s and C2p orbitals (10^{-3}e, per one pair of interacting atoms) in exohedral PaC_{60}, “networked” $C_{59}Pa$ and endohedral $Pa@C_{60}$ complexes

Orbitals		PaC_{60} (C_{2v})	$C_{59}Pa$ (C_s)	$Pa@C_{60}$ (C_s)
Pa5f -	$C_1$2p	46	67	41
	$C_2$2p	-	51	42
	$C_3$2p	-	-	39
Pa6d -	$C_1$2p	90	148	84
	$C_2$2p	-	112	83
	$C_3$2p	-	-	83
Pa7s -	$C_1$2p	24	36	16
	$C_2$2p	-	34	16
	$C_3$2p	-	-	16

than their formal valencies in solid compounds. The comparison of Tables 1 and 2 shows that the variation of the integral charges on going from $Th@C_{60}$ to $Md@C_{60}$ is mainly due to the decrease of An6d–C2p covalent mixing and overlap of these orbitals.

Although the chemical bonding between actinide atom and the carbon cage is weak for the clusters at the end of $An@C_{60}$ row, both the DMol and RDV calculations exhibit essential charge transfers of more than 0.6 electron from the actinide orbitals to the cage. Similar results were obtained in our calculations of $An@C_{40}$ row [3]. From our point of view, there is no contradiction between binding energy and charge transfer because a change in binding energy on going from superposition of isolated C_{60} (or C_{40}) cage and actinide atom to endohedral complex is due to contributions from: (1) interaction between actinide and the carbon atoms and (2) deformation of the initial fullerene structure. The latter contribution is certainly unfavorable and even in the case of $Md@C_{60}$ complex the interaction between metal and carbon atoms has the bonding character. On the other hand, the strong C–C bonds in the C_{60} (or C_{40} and C_{28}) cage are not accompanied by noticeable charge transfer, whereas in the $C_{59}Pa$ complex the considerable charge transfer (more than 2 electrons) was obtained for the weaker Pa–C bonds.

According to our calculations of endohedral complexes, the additional charge on the cage orbitals is distributed over all carbon atoms, i.e. the deformation of electron density takes place even for the carbon atoms, which are the most distant from actinide site. However, as expected, variation of the charge density on the nearest actinide neighbors is slightly greater than that for other atoms of the cage. Nevertheless, the effective charges on C1, C2 and C3 atoms are within -0.1 in endohedral fullerenes of the first half of the row and within -0.05 for the complexes of heavy actinides. In contrast, the main part of charge transfer from the metal atom in the exohedral and especially in the “networked” clusters is localized on the nearest carbon neighbors. For instance, in the $C_{59}Pa$ complex, the integral charges on one C1 and two C2 atoms are -0.76 and -0.67 respectively, i.e. the total electron density, which is accepted by these carbon atoms is close to 2.1.

4. Conclusions

Our investigations of the new class of organometallic nanoparticles An@C_{60} confirm earlier results [1-3] that endohedral fullerenes can be very stable. Moreover, the stable character of such species for the light actinides obtained for the An@C_{28} and for the major part of An@C_{40} clusters (from Th to Fm) is also predicted for the neutral endohedral fullerenes An@C_{60} from Th@C_{60} to Md@C_{60}. The dissociation energy for the most stable complex Pa@C_{60} (Pa@C_{60} → Pa + C_{60}) was found to be 6.6 eV, which is noticeably greater than that for the exohedral position of Pa atom on the outer surface of C_{60} cage. Comparison of the electronic structure of endohedral complexes based on C_s and I_h isomers showed that the former type is more favorable for the encapsulation of an actinide atom.

Analysis of the molecular orbital structure showed that strong hybridization takes place between C2p and An5f states for all An@C_{60} complexes. However, the calculated values of overlap populations of C2p–An5f AOs showed that the An5f contribution to bonding was more than two times less than that of the main An6d–C2p interaction, even in the neutral clusters at the beginning of An@C_{60} row. The analysis of chemical bonding of endohedral, exohedral and "networked" fullerenes showed that the strongest interaction between actinide atom and specific carbon atom in the C_{60} cage takes place for "networked" complex. However, the stability of the latter cluster is less than that of the corresponding endohedral systems, because: (1) in C_{59}Pa molecule the three Pa–C bonds substitute for the three stronger C–C bonds; (2) in An@C_{60} complexes the An–C interactions are additional to the C–C bonds in the cage. Two schemes for atomic effective charge calculations give quite different results for An@C_{60}, however, more realistic values were obtained using the spatial numerical integration procedure incorporated into the RDV method [16].

In this paper, we discussed the stability of endohedral fullerenes An@C_{60} with respect to the An + C_{60} fragmentation only. However, for the understanding of stability of these systems, it is important to consider the other competitive processes which can happen when An@C_{60} systems will ionize. It is interesting to calculate the ionization energy and the dissociation energy of An@C_{60}^{n+} systems, this work is in progress now and will be published in the separate paper.

Acknowledgments

This work was supported by the Russian Foundation for Basic Research, grant 10-03-00152.

References

[1] Dognon J.-P., Clavaguera C., Pyykko P. A predicted organometallic series following a 32-electron principle: An@C_{28} (An = Th, Pa^{+}, U^{2+}, Pu^{4+}). *J. Amer. Chem. Soc.*, **131**, P. 238–243 (2009).

[2] Ryzhkov M.V, Ivanovskii A.L., Delley B. Electronic structure of endohedral fullerenes An@C_{28} (An = Th – Md). *Comp. Theor. Chem.*, **985**, P. 46–52 (2012).

[3] Ryzhkov M.V., Delley B. Electronic structure of predicted endohedral fullerenes An@C_{40} (An = Th – Md). *Comp. Theor. Chem.*, **1013**, P. 70–77 (2013).

[4] Kroto H.W., Heath J.R., O'Brien S.C., Curl R.F., Smalley R.E. C-60 buckminsterfullerene. *Nature*, **318**, P. 162–163 (1985).

[5] Diener M., Smith C.A., Veirs D.K. Anaerobic preparation and solvent-free separation of uranium endohedral metallofullerenes. *Chem. Mat.*, **9**, P. 1773–1777 (1997).

[6] Chang A.H.H., Ermler W.C., Pitzer R.M. The ground and excited states of C60M and C60M+ (M = O, F, K, Ca, Mn, Cs, Ba, La, Eu, U). *J. Chem. Phys.*, **94**, P. 5004–5010 (1991).

[7] Delley B. An all-electron numerical method for solving the local density functional for polyatomic molecules. *J. Chem. Phys.*, **92**, P. 508–517 (1990).

[8] Koelling D.D., Harmon B.N. A technique for relativistic spin-polarized calculations. *J. Phys. C: Solid State Phys.*, **10**, P. 3107–3114 (1977).

[9] Perdew J.P., Burke K., Ernzerhof M. General gradient approximation made simple. *Phys. Rev. Lett.*, **77**, P. 3865–3868 (1996).

[10] Becke A.D. A multicenter numerical-integration scheme for polyatomic molecules. *J. Chem. Phys.*, **88**, P. 2547–2553 (1988).

[11] Lee C., Yang W., Parr R.G. Development of the Colle-Salvetti correlation-energy formula into a functional of the electron-density. *Phys. Rev.B.*, **37**, P. 785–789 (1988).

[12] Rosen A., Ellis D.E. Relativistic molecular calculations in the Dirac-Slater model. *J. Chem. Phys.*, **62**, P. 3039–3049 (1975).

[13] Adachi H. Relativistic molecular orbital theory in the Dirac-Slater model. *Technol. Reports Osaka Univ.*, **27**, P. 569–576 (1977).

[14] Pyykko P., Toivonen H. Tables of representation and rotation matrices for the relativistic irreducible representations of 38 points groups. *Acta Acad. Aboensis, Ser.B.*, **43**, P. 1-50 (1983).

[15] Varshalovich D.A., Moskalev A.N., Khersonskii V.K. *Quantum Theory of Angular Momentum.* World Scientific, Singapore, 439 p. (1988).

[16] Ryzhkov M.V. New method for calculating effective charges on atoms in molecules, clusters and solids. *J. Struct. Chem.*, **39**, P. 933–937 (1998).

[17] Mulliken R.S. Chemical bonding. *Annu. Rev. Phys. Chem.*, **29**, P. 1-30 (1978).

[18] Ryzhkov M.V., Kupryazhkin A.Ya. First-principles study of electronic structure and insulating properties of uranium and plutonium dioxides. *J. Nuclear Mater.*, **384**, P. 226–230 (2009).

[19] Ryzhkov M.V., Teterin A.Yu., Teterin Yu.A. Fully relativistic calculations of ThF_4. *Int. J. Quant. Chem.*, **110**, P. 2697–2704 (2010).

NANOSYSTEMS: PHYSICS, CHEMISTRY, MATHEMATICS, 2014, 5 (4), P. 509–516

BORON-DOPED ANATASE: ELECTRONIC BAND STRUCTURE, BORON ATOM LOCATIONS AND MAGNETIC STATE

V. P. Zhukov

Institute of Solid State Chemistry, Urals Branch of the Russian Academy of Sciences, Ekaterinburg, Russia

zhukov@ihim.uran.ru

PACS 71.20.Nr, 75.75.Lf, 78.20.-e

The first-principle spin-resolved GGA and GGA+U calculations for the electronic band structure of the boron-doped TiO_2 with anatase structure have been performed. The locations of boron atoms in the interstitial and oxygen position have been studied. We have found two interstitial positions: a stable one with three neighboring oxygen atoms, and a metastable one in the center of the flattened tetrahedron of oxygen atoms. The boron location in interstitial position is energetically more favorable than the location inside the oxygen position. In accordance with experiments, the GGA+U approach produces spin-polarized solutions for interstitial boron positions, whereas the GGA approach fails to produce a spin-polarized solution.

Keywords: anatase, boron doping, photocatalyses, optical absorption, band structure, first-principle calculations.

Received: 16 June 2014
Revised: 30 June 2014

1. Introduction

The subject of this work was initialized in course of discussions on the physicochemical properties of photocatalytic compounds where the contribution of Prof. A.L. Ivanovskii was invaluable.

The most promising compound for photocatalytic applications is probably anatase-structured titanium dioxide, a good reagent for the removal of pathogenic bacteria or chemical contaminants from the environment. This compound also has potential for employment in new photoelectric cells and hydrogen producing cells by means of water photolysis. Pure TiO_2 possesses a high photocatalytic activity (PCA) in the UV part of the electromagnetic spectrum, so in many works attempts have been carried out to extend its activity to the visible part of the solar spectrum, see [1]. The main aim of such studies was to obtain the TiO_2-based compounds that effectively absorb visible sunlight. Here, one of the most promising techniques is the doping of anatase with simple or transition elements, in particular, with boron, carbon or nitrogen [2,3].

However, such researches encounter a number of problems. Probably the most serious is that the obtained photocatalysts usually have a complex phase composition that is often difficult to elucidate. There are, for example, arguments in favor of the opinion that microscopic aggregates or fine-grained phases can be constituent parts of the obtained specimens. So, the data on the properties of the photocatalysts, in particular on the optical absorption, are often very contradictory and are associated with differences in the structure.

Consequently, the microscopic structure of the defects in the TiO_2-based photocatalysts and the effect of doping on the optical properties and PCA are difficult to understand. This is especially valid for the boron-doped anatase, which demonstrates high activity in many photoreactions [4–9]. It has been shown in previous studies [4–6] that the B-doping helps to shift the absorption threshold into the visible range compatibly with its high PCA. However, the authors of the papers [7, 8] observed shifts of the absorption threshold into the UV range, which contradicts the visible range PCA. Also, the data on the locations of the boron atoms inside the anatase structure are contradictory. Some of the data obtained, mainly by means of the X-ray emission spectroscopy, confirm the replacement of oxygen atoms with the boron atoms [5]; hereafter we mark this kind of defects as B_O. But there are also data in favor of the boron atoms located in interstitial positions [6, 10], we name this a B_I-defect, or these both kinds of defects can emerge [11].

A better understanding of the optical properties and photocatalytic activity can be achieved based on the first-principle calculations of the electronic band structure. In prior works [7, 8, 12, 13], such calculations have been done for the cases of boron atoms inserted into the oxygen, interstitial and titanium atom positions. Besides, in [7, 12], the calculations of the boron insertion energy have been performed. The authors of the work [12] affirmed that the energy of boron insertion into interstitial position is almost equal to that of insertion into oxygen position, so both kinds of defects can exist. On the other hand, they affirmed that the energy of titanium with boron atoms replacement is higher by about 5 eV, hence such kind of insertion is practically impossible. These calculations [7, 8, 12, 13] have demonstrated that the boron insertion into oxygen positions induces the emergence of boron impurity states above the band gap that correlates with the shift of the light absorption threshold into the visible range [4–6]. Conversely, the insertion into interstitial positions induces the boron impurity states inside the band gap, which correlates with the data of the work [7, 8].

However, the performed calculations are far from perfect. It is well known that the boron atoms inside anatase have a magnetic configuration, so the boron-doped samples demonstrate ESR spectra [11], but the calculations performed were spin-restricted. Additionally, the calculated band gap was much lower than its experimental value, 3.2 eV. Therefore the conclusions of the authors on the energy of the boron atoms states with respect to band gap are doubtful, which also makes their conclusions on the optical absorption of boron-doped anatase doubtful. The performed calculations do not help to recognize the location of boron atoms inside the anatase structure.

Therefore, we have performed new first-principle calculations for the electronic structure of the boron-doped anatase. Our calculations are free from the above mentioned drawbacks, which helps to obtain more reliable conclusions on the effect of the boron doping on the optical and photocatalytic properties of the doped anatase. Besides, we have performed first-principle calculations for the energy of the boron insertion into anatase. Comparing our data with experimental results, we draw conclusions about the most probable positions of the dopant boron atoms.

2. Method of research

Typically, high-activity photocatalysts have the forms of nano-structured aggregates because the nano-structurization brings about an increase in the surface area. The evaluated optimal size of the anatase nano-particles for photocatalytic applications is 5–6 nm [14, 15]. In principle, the optical absorption of the nano-particles and the locations of the doping atoms are influenced by quantum-size effects that become essential when the size of the

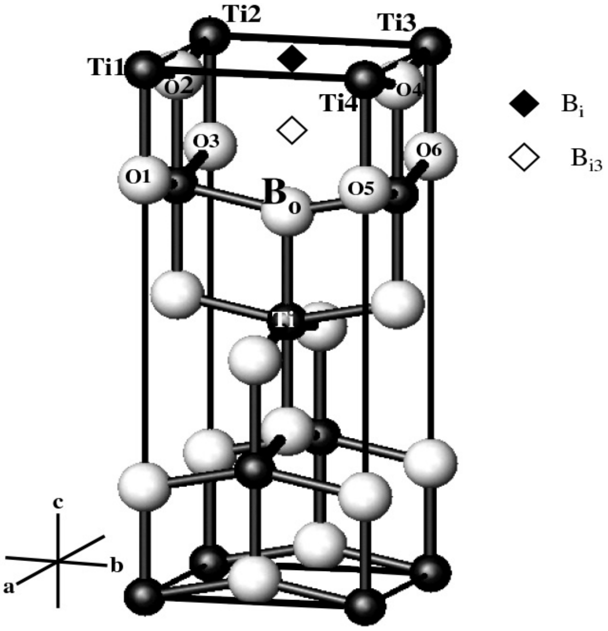

FIG. 1. The conventional unit cell of anatase. The presumed positions of boron atoms are shown. Here B_i and B_{i3} are the initial interstitial positions, B_O is the initial oxygen replacement position - see text.

nano-particles is less than or equal to the de Broglie's wavelength. Evaluations of this wavelength leads to ~ 0.7 nm for anatase and ~ 0.2 nm for rutile [16]. Since these are much smaller than the optimal nano-particle size, we can neglect the quantum-size effects and employ the first-principle calculation methods utilized for the bulk crystals.

Our approach is based on considering the cell of anatase that is obtained by duplicating the primitive unit cell Ti_2O_4 along all the three crystallographic axes. By doing so, we arrive at the 48-atomic unit cell. Replacing one of the oxygen atom by the boron atom we can then model the electronic structure of the $TiO_{1.9375}B_{0.0625}$ compound; inserting one boron atom we study the $TiO_2B_{0.0625}$ compound. The positions of the boron atoms are easier to discuss considering the conventional unit cell of bulk anatase shown in Fig. 1.

The location of the boron atom that replaces the oxygen atom (B_O defects)is quite evident; it is inside the triangle of Ti atoms. However, the interstitial positions of the boron atoms are not so easy to define. We start with two assumptions. The first one is that due to the repulsion of the atomic cores, the interstitial position should probably be the most distant from all neighboring atoms. This is the center of the prism that consists of the $O1, O2, O3-O4, O5, O6$ atoms (position B_{i3} in the figure). Our second supposition is that if the boron atom can form chemical bonds with oxygen atoms, it can be located in the center of the $Ti1-Ti2-Ti3-Ti4$ square. This position (B_i in the figure) is also the center of the O_4 tetrahedron essentially flattened along the c-axis. The actual interstitial positions we find by relaxing the crystal structure and looking for the minima of the total energy employing electronic band structure calculations.

We use in the calculation the pseudo-potential plane wave approach realized in the Quantum Espresso (QE) computer code based on the the density functional theory (DFT) [17, 18]. The ultra-soft pseudopotentials with gradient-corrected exchange-correlation (GGA) potential of Perdew, Burke and Ernzerhof [19] provided by the authors

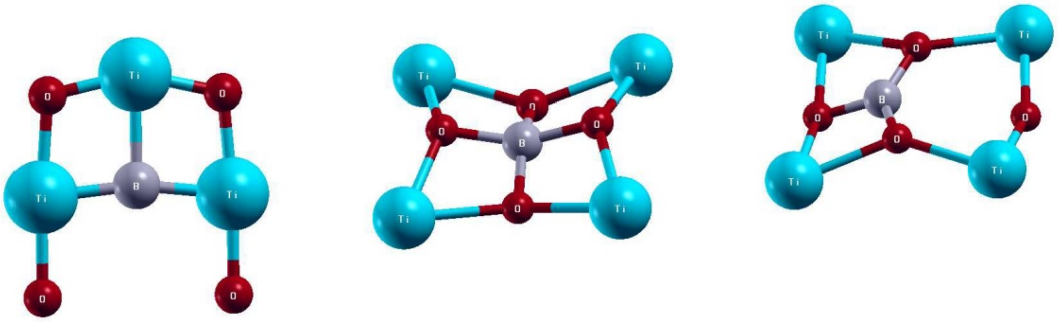

FIG. 2. The nearest vicinity of the boron atoms inserted into the anatase structure. Left image: boron atom in the relaxed B_O position; middle image: boron atom in the relaxed B_i position; right image: boron atom in the B_{i2} position.

of the QE code, was employed. Spin polarization for the energy band structure was allowed. A plane-wave basis set with an energy cutoff of 50 Ry was employed for the wave function and of 300 Ry for the electron density expansion. A grid of 72 wave-vectors per irreducible wedge of the Brillouine zone was used for the electron density calculations. The underestimation of the energy gap between the valence 2pO-like band and 3dTi-like conduction band, typical for the methods based on the DFT theory, has been eliminated by employing the single-site hubbard-like corrections to the exchange-correlation potential within the so-called GGA+U approach described in [20]. The only parameter of this approach is the $U - J$ value where U and J are the correction parameters for the Coulomb and exchange interactions, respectively. We apply these corrections to the Ti 3d states with $U - J = 6.5$ eV that provides the calculated band gap value equal to the experimental data, 3.2 eV.

It is essential that the application of the Hubbard-like corrections within the GGA+U approach is necessary for obtaining spin-polarized solutions: we will later show that the GGA approach leads only to spin-restricted solutions for the interstitial boron positions .

The DFT GGA approach possesses a high precision, sufficient for evaluating crystal lattice distortions near the B, C or N atoms inserted into the oxide semiconductors [21]. This evaluation is done by looking for the minima of the total energy of the unit cell. The shifts of the atoms are evaluated in correspondence to the calculated forces that act on the atoms. An iterative process of atomic shifting is realized until the forces become negligible. The results obtained by this approach, closest in vicinity to the boron atoms, is inserted into anatase as is shown in Fig. 2.

In the case of the B_O defect, the most interesting feature of the local crystal structure is the high value of the $Ti - B - Ti$ angle, 168°, which reflects the trend of the boron atoms to form linear bonds with neighboring titanium atoms [21]. Very interesting are the results of the crystal structure optimization for the B_i and B_{i3} cases. The B_{i3} position appears to be unstable. Boron atoms set initially in this position shift upwards and finally form three short boron-oxygen bonds, with one B – O length equal to 1.40 and two bonds equal to 1.38 Å. The total energy calculation (Table 1) demonstrates that this new position, which we denote B_{i2}, is stable. The relaxation of the structure with the boron atom set into the B_i position leads to the shift of the nearest oxygen atoms towards the boron atom. Owing to this shift, four short boron-oxygen bonds occur whose lengths, 1.44 Å, are much less than the $Ti - O$ bond length, 2.06 Å. This position is metastable, however. This means

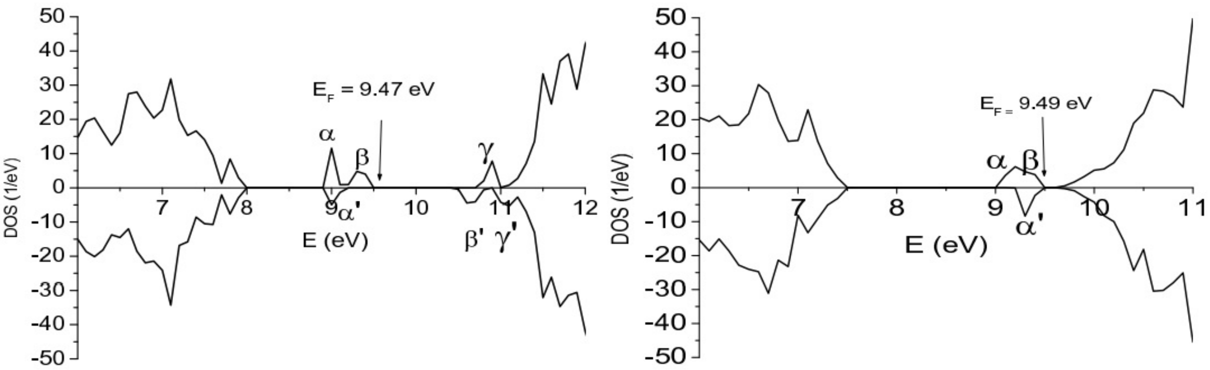

FIG. 3. The spin-resolved densities of states for anatase containing the B_O defect with the U-J exchange-correlation corrections considered (left panel) and neglected (right panel). The densities of spin-down states are shown with negative sign. The boron-like states are those marked as α, β and γ for spin-up states and α' for spin-down states.

that the total energy of the structure with this kind of defect is higher than the energy of the structure with the B_{i2} defect. However, the final forces acting on the boron atom set in the relaxed B_i position are very small, less than 0.002 Ry/at.unit. Infinitely continuing the process of lattice relaxation, we do not find that the boron atom shifts from the B_i into the B_{i2} position.

The results, discussed below, for the density of states and total energy were obtained for optimized B_O, B_i and B_{i2} structures.

3. Discussion of results

In Fig. 3, the spin-resolved densities of states are shown for anatase containing the B_O defect, which were calculated by means of the GGA+U and GGA approaches.

With the GGA+U approach, the states below 8 eV are 2pO valence band states, whereas the states above 11 eV are the 3dTi conduction band states. The boron-like spin-up band states α, β, γ and spin-down states α' are located inside the band gap. Since there are two spin-up and one spin-down occupied states, the boron atom has a magnetic moment of 1 μ_B. The energy gap between the Fermi level and the bottom of the conduction band is equal to 1.53 eV, so the calculations predict that anatase with such a defect should have absorption in the visible range. The calculated band structure is in principle similar to that calculated before by means of the LMTO-TB method [21], but our new boron-like bands have the energy, with respect to the bottom of the conduction band, lower by 0.8 eV. The most probable explanation for this difference is that the LMTO-TB method uses a simplified spherically-symmetric potential inside atomic spheres whereas the more exact QE method is free of this simplification. The only-GGA approach also leads to the spin-polarized solution with boron magnetic moment equal to 1 μ_B, but with the 2pO-3dTi band gap which is approximately 2.2 eV. Although the experimental data on this gap are contradictory, one can hardly expect that the doping with typically small concentration of boron atoms can markedly reduce the value of the gap. So, the results for the band gap calculated with the GGA approach band is unreliable. The densities of states for anatase with the B_i defect are shown in Fig. 4. The main features of the DOS are similar to that in Fig. 3. The GGA+U solution is also spin-polarized with a magnetic moment of 1 μ_B per boron atom, with the boron-like states having a higher energy. The essential circumstance

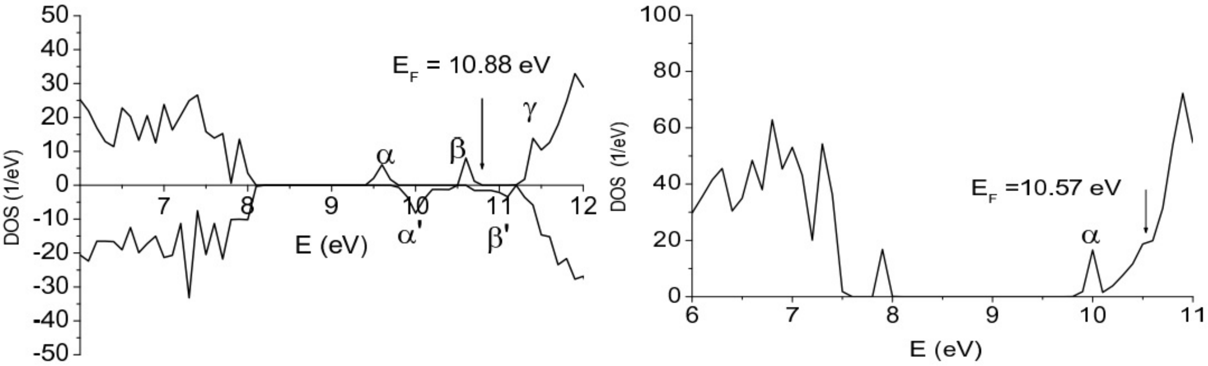

FIG. 4. The spin-resolved densities of states for anatase containing the B_i defect. The destinations of the lines and the marks are the same as in Fig. 3

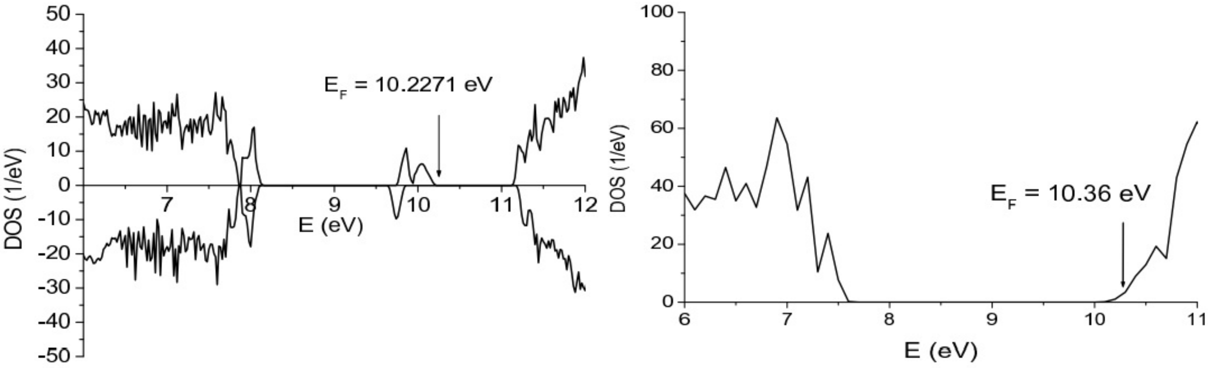

FIG. 5. The spin-resolved densities of states for anatase containing the B_{i2} defect. The destinations of the lines and the marks are the same as in Fig. 4

is that the only-GGA solution started with the trial boron magnetic moment more than 1 μ_B converges to the spin-restricted solution. The densities of states for the case of the B_{i2} defect are shown in Fig. 5. The GGA+U solution is also spin-polarized, however, the only-GGA solution is spin-restricted.

When one considers that the experimental ESR data demonstrate the presence of a magnetic moment on the boron atom, we are forced to conclude that the spin-restricted GGA-approach, is in this case inaccurate. We can come to a definite conclusion on the admissible approximation and to reveal also the preferable location of the boron atom using the first-principle calculations for the energy of defect formation.

The standard definition for the energy of the B_O kind of defect formation can be written as

$$E_f(B_O) = [E_{tot}(Ti_{16}O_{31}B) + \mu(O)] - [E_{tot}(Ti_{16}O_{32}) + \mu(B)]\,, \tag{1}$$

where $E_{tot}(\ldots)$ are the total energies of the unit cells, $\mu(O)$ and $\mu(B)$ are the chemical potentials of the oxygen and boron atoms inside the reaction medium. Similarly, the energy of formation for an interstitial defect $I = i$ or i_2 is written as:

$$E_f(B_I) = E_{tot}(Ti_{16}O_{32}B_I) - [E_{tot}(Ti_{16}O_{32}) + \mu(B)]\,. \tag{2}$$

A problem of such an approach is the evaluation of chemical potentials. Since the doping reactions are usually realized in an oxygen atmosphere, we can admit that $\mu(O)$ is equal to one half the energy of an oxygen molecule. This value, calculated in the GGA approach with spin polarization included, and pseudo-potential identical to that in the band structure calculation, is equal to -31.94 Ry. However, the chemical potential of the boron atom is difficult to evaluate because of very complicated and rather indefinite structures of the compounds that serve as boron sources. We therefore define the value that we name the interstitial site preference energy as follows:

$$E_{pr}(B_I) = E_f(B_I) - E_f(B_O) = E_{tot}(Ti_{16}O_{32}B_I) - E_{tot}(Ti_{16}O_{31}B_O) - \mu(O). \quad (3)$$

TABLE 1. The values of unit cell total energy E_{tot} and interstitial site preference energy E_{pr} calculated with different approaches

Energy characteristics	GGA approach	GGA + sp approach	GGA+sp+U approach
$E_{tot}(i)(Ry)$	-2905.35	-2905.35	-2897.92
$E_{tot}(i2)(Ry)$	-2905.43	-2905.43	-2898.02
$E_{tot}(B_O)(Ry)$	-2872.86	-2872.87	-2865.47
$E_{pr}(i)(eV)$	-7.50	-7.37	-6.91
$E_{pr}(i2)(eV)$	-8.63	-8.50	-8.23

The boron chemical potential is absent here, so this value is easy to calculate. All the values necessary for this evaluation are given in Table 1. We see that E_{pr} has a large negative value with all the approaches used, so a robust conclusion follows that the formation of interstitial defects B_i and B_{i2} is much more favorable in comparison to the replacement defect B_O. Moreover, the absolute value of the preference energy is essentially higher for the B_{i2} defect than for B_i defect. The conclusion then follows that the B_{i2} defect, with three short boron-oxygen bonds, is the most probable kind of defect.

4. Conclusion

We have performed the electronic band structure calculations for anatase with two kinds of boron atom incorporation: insertion into interstitial positions and replacement of oxygen atoms with boron atoms. The spin-polarization of the band structure was allowed; the Hubbard-like corrections for the Coulomb and exchange correlations in atoms have been included in order to cancel the under-evaluation of the band gap. The total energy of the compounds has been optimized, which helped to find three possible positions of the boron atoms, one of oxygen replacement position and two interstitials. The most stable interstitial position is that inside a trio of oxygen atoms with very short boron-oxygen bonds, whereas the second position, in the center of flattened tetrahedron of oxygen atoms, is metastable. First-principle calculations for the interstitial site preference energy have shown that the insertion of boron atoms into the interstitial positions is energetically more favorable than the replacement of an oxygen atom. The calculations predict that this kind of doping leads to absorption in the visible part of the solar spectrum, which improves its photocatalytic activity.

Our calculations help to elucidate the applicability of two approaches, GGA and GGA+U. The calculations within the both approaches, including and disregarding the spin polarization, lead to equal conclusions on the localization of boron atoms. However, the GGA+U approach that includes the Hubbard-like corrections is preferable since it produces a spin-polarized band structure, whereas the only-GGA calculations for the most stable boron position converge to non-magnetic solutions that contradicts experimental observations.

Acknowledgements

This research has been supported by the grants of RFBR numbers 12-03-00453-a, 13-03-00265-a and partially supported by the projects of the Urals Branch of the Russian Academy of Sciences numbers 12-Y-3-1009 and 12-Y-3-1001. The calculations have been performed using the URAN cluster of the Institute of mathematics and mechanics of the Urals Branch of RAS.

References

[1] Carp O. , Huisman C., Reller A. Photoinduces reactivity of titanium dioxide. *Progress in Solid State Chemistry*, **32**, P. 33–177 (2004).

[2] Diebold O. The surface science of titanium dioxide. *Surface Science Reports*, **48**,P. 53–229 (2003).

[3] Zaleska A. Doped-TiO_2: A review. *Recent Patents on Engineering*, **2** (3), P. 157–164 (2008).

[4] Zhao W., Ma W., Chen C., Zhao J., Shuai Z. Efficient Degradation of Toxic Organic Pollutants with Ni_2O_3 /$TiO_{2-x}B_x$ under Visible Irradiation. *JACS communications*, **126**, P. 4782–4783 (2004).

[5] In S., Orlov A., et al. Effective Visible Light-Activated B-Doped and B,N-Codoped TiO_2 Photocatalysts. *J. Am. Chem. Soc.*, **129** (45), P. 13790–13791 (2007).

[6] Yuan J., Wang E., et al. Doping mode, band structure and photocatalytic mechanism of BN-codoped TiO_2. *Applied Surface Science*, **257** (16), P. 7335–7342 (2011).

[7] Gombac V., Rogatis L.D., et al. TiO_2 nanopowders doped with boron and nitrogen for photocatalytic applications. *Chemical Physics*, **339**, P. 111–123 (2007).

[8] Feng N., Zheng A., et al. Boron Environments in B-Doped and (B, N)-Codoped TiO_2 Photocatalysts: A Combined Solid-State NMR and Theoretical Calculation Study. *J. Phys. Chem. C.*, **115** (6), P. 2709–2719 (2011).

[9] Bettinelli M., Dallacasa V., et al. Photocatalytic activity of TiO_2 doped with boron and vanadium. *J. Hazard. Mater.*, **146**, P. 529–534 (2007).

[10] Chen D., Yang D., Wang Q., Jiang Z. Effects of Boron Doping on Photocatalytic Activity and Microstructure of Titanium Dioxide Nanoparticles. *Ind. Eng. Chem. Res.*, **45** (12), P. 4110–4116 (2006).

[11] Fittipaldi M., Gombac V., et al. A high-frequency (95 GHz) electron paramagnetic resonance study of B-doped TiO_2 photocatalysts. *Inorg. Chim. Acta*, **361**, P. 3980–3987 (2008).

[12] Geng H., Yin S., et al. Geometric and electronic structures of the boron-doped photocatalyst TiO_2. *J. Phys. C: Condens. Matter*, **18**, P. 87–96 (2006).

[13] Yang K., Dai Y., Huang B. Origin of the photoactivity in boron-doped anatase and rutile TiO_2 calculated from first principles. *Phys. Rev. B*, **76** (19), P. 195201 (2007).

[14] Cao L, Huang A., Spiess F.-J., Suib S.L. Gas-Phase Oxidation of 1-Butene Using Nanoscale TiO_2 Photocatalysts. *Journ. of Catalysis*, **188** (1), P. 48–57 (1999).

[15] Soria J., Sanz J., et al. Water-Hydroxyl Interactions on Small Anatase Nanoparticles Prepared by the Hydrothermal Route. *Journ. Phys. Chem. C*, **114** (39), P. 16534–16540 (2010) .

[16] Zhukov V., Zainullina V. *Electronic structure, optical properties and photocatalityc activity of the oxide semiconductors*. - Saarbrüken: Lambert Academic Publishing, 2013, 86 p.

[17] Quantum espresso, `http://www.quantum-espresso.org` and `http://www.pwscf.org` (2010).

[18] Baroni S., de Gironcoli S., Corso A.D. Phonons and related crystal properties from density-functional perturbation theory. *Rev. of Modern Physics*, **73** (2), P. 515–562 (2001).

[19] Perdew J, Burke K., Ernzerhof M. Generalized Gradient Approximation Made Simple. *Phys. Rev. Lett.*, **77** (18), P. 3865–3868 (1996).

[20] Cococcioni M., de Gironcoli S. Linear response approach to the calculation of the effective interaction parameters in the LDA+U method. *Phys. Rev. B*, **71** (3), P. 035105 (2005).

[21] Zhukov V., Zainullina V., Chulkov E. Ab initio approach to structural, electronic and optical properties of B-, C- and N-doped anatase. *Int. J. of Modern Physics*, **24** (31), P. 6049–6067 (2010).

NANOSYSTEMS: PHYSICS, CHEMISTRY, MATHEMATICS, 2014, 5 (4), P. 517–539

ELECTRONIC PROPERTIES OF MoS_2 MONOLAYER AND RELATED STRUCTURES

A. N. Enyashin[1], G. Seifert[2]

[1]Institute of Solid State Chemistry UB RAS, Ekaterinburg, Russia
[2]Physical Chemistry, Dresden University of Technology, Dresden, Germany
enyashin@ihim.uran.ru, gotthard.seifert@chemie.tu-dresden.d

PACS 61.46.-w, 61.50.Ah, 61.72.-y, 61.82.Fk

The present review provides an overview of the transition metal dichalcogenides discovered newly at the level of two dimensions. A special emphasis is given to the electronic structure of semiconducting representatives of this family, which can depend on many factors like thickness, environment, mechanical strain and structural imperfections of the layers. Both calculations and experimental data available to date on example of MoS_2 compound evidence that, semiconducting dichalcogenide layers could become successful counterparts of graphene and nanosilicon as the materials of flexible nanoelectronics. However, current technologies for the fabrication of single mono- and multilayers of transition metal dichalcogenides still do not offer a large-scale and cost-effective product with the tuned quality to reveal all abilities predicted for these nanostructures.

Keywords: Inorganic graphene, molybdenum sulfide, layered chalcogenides, monolayer.

Received: 16 June 2014
Revised: 30 June 2014

1. Introduction

Layered compounds were intensively studied in the 1970's and early 1980's (see e.g. Levy [1]). Among them, a large variety of the pure and mixed compounds from the group of layered d-metal chalcogenides (TMCN) attracted the largest attention in view of their possible applications. The stratiform structure of these compounds, their sufficient chemical endurance and impossibility of the formation of monolithic structures under a high load predetermine their excellent antifriction properties, which found a wide technological application in the automotive and aerospace industries [2]. The latter stimulated an extensive research of structural, electronic and optical, chemical and galvanomagnetic phenomena within the bulks of these compounds, which were already reviewed at that time [3–5].

Recent fabrication and preliminary characterization of single layers of some metallic and semiconducting d-metal chalcogenides have demonstrated their high potential as the materials for two-dimensional electronics [6]. The first nanoelectronic devices — field-effect transistors, logical circuits, and amplifiers — have already been manufactured in labs [7–9]. Transparent TMCN monolayers with a distinct band gap can possess a high enough mobility for charge carriers at room temperature, high thermal stability and ultra-low standby power dissipation, which make them also attractive materials for the optoelectronics and energy harvesting industry.

All this has already renewed interest in their research by means of new experimental and computational techniques, which were essentially evaluated over the last 30 – 40 years. This review collects the present data about modulation of electronic properties of single and a few layer d-metal chalcogenides and their related systems upon such factors as mechanical deformation, intrinsic defects and impurities, interface formation. Taking into account the huge variety of compounds, special emphasis was given to their most famous representative —

molybdenum disulfide MoS2 as a prominent and prospective semiconducting compound with well established low-cost production.

2. Electronic structure of ideal monolayers and their slabs

As for many other types of layered materials, the electronic properties of layered chalcogenides are at a first glance determined by the bonding behavior within the layer and only modified secondarily by the interactions between the layers. Pioneering studies of the electronic properties of semiconducting MX_2 chalcogenides (M = Mo, W; X = S, Se) with hexagonal 2H crystal structure (see Fig. 1) date back to the 1950's and 1960's (Lagrenaudie [10], Fivaz and Mooser [11]). Also, heterojunctions of such compons were previously described in the 1980's [12].

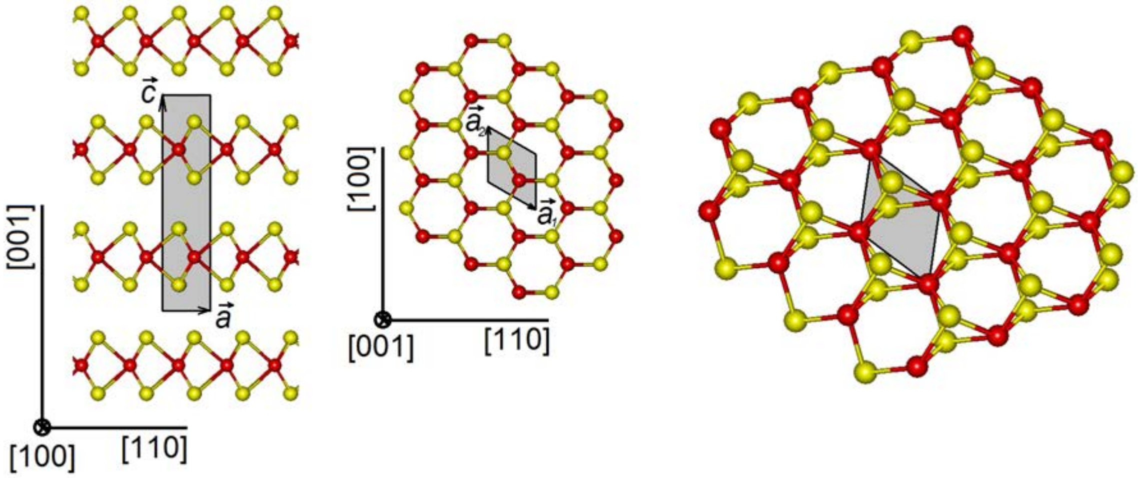

FIG. 1. Crystal structure of the bulk 2H-MoS_2 (space group $P6_3/mmc$) from the side and top views (along [100] and [001] directions) and a fragment of a single monolayer. Unit cells are shaded in gray

The structural units of TMCN layers and accordingly also of the corresponding bulk stacks can be deduced using group theory for d^4sp and d^5s electronic configurations of metal atom as having coordination number 6 and octahedral O_h or trigonal prismatic D_{3h} symmetry [13, 14]. While these coordination types have not been predicted for other electronic configurations (d^4s, d^3s^2, etc.), all layered dichalcogenides are composed either of MX_6 octahedra or prisms.

A first rough qualitative picture of the electronic structure of a single TMCN triple layer (X–M–X) structure can be deduced from a simple ligand field model. Formation of MX_2 compound is possible due to $XsXp$–$MdMs$ hybridization and full occupation of the s- and p-shells of chalcogen atoms by 16 electrons. Towards that end, metals of IVb, Vb and VIb group keep 0, 1 or 2 d-electrons, respectively. In the case of the trigonal prismatic coordination of the metal, the d-states split into a1, e′ and e″ states, and from this picture, a simple band structure of a single layer TMCN can be understood (Fig. 2).

E.g., in the case of MoS_2, the lower part of the valence band is determined by the Mo-d–S–p 'bonding' states, followed by the almost 'non-bonding' d_z^2, d_{xy} and $d_{x^2-y^2}$ states at Mo. The band of the 'antibonding' Mo–d–S–p states are located above. Consideration of the 6 Mo valence electrons and a formal charge of -2 for the sulfur gives a formal charge of +4 for Mo in MoS_2. The 'd_z^2-band' is fully occupied, easily explaining the semiconducting behavior of MoS_2. The same qualitative picture holds for $MoSe_2$ and the sulfides and selenides

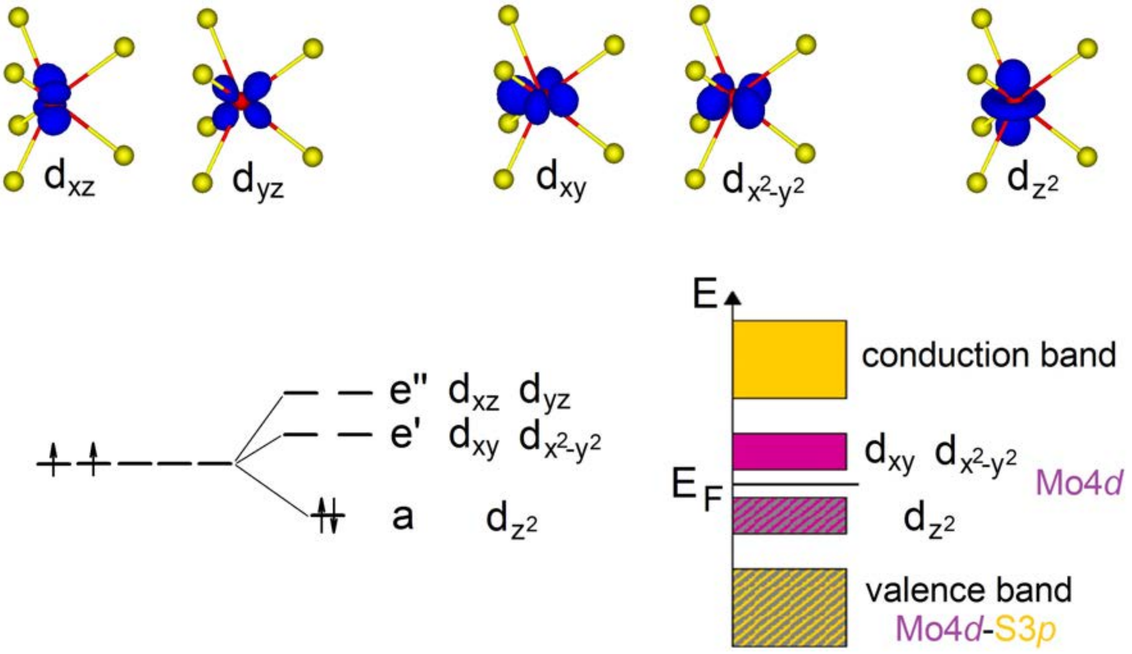

FIG. 2. Ligand field picture and corresponding d-orbitals for a trigonal prismatic coordination (D3h symmetry) in a d-metal dichalcogenide with a d2 configuration of metal atom and schematic band structure for a single MoS_2 layer

of Tungsten. I.e., the upper edge of the valence band and the lower edge of the conduction band are determined by metal d states. This model also explains why the chalcogenides of the group Vb metals (Nb, Ta) are metallic. Five valence electrons at the metal lead to a half occupation of the 'd_z^2-band'. The Sulfur states are predominantly involved in the M–S bonding, and therefore, in the stability of the structure, but play only a minor role in the electronic transport and optical properties. Since the sulfur atoms are 'saturated' and the metal d-states do not range out of the S–M–S triple layer, this simple model does not make a difference between the electronic structure of a single triple layer (1H structure) and the 2H-bulk structure. It also qualitatively explains the inertness and robustness of the TMCN surface. However, this model oversimplifies the real situation to some extent, as was already discussed by Mattheiss [15]. Mattheiss showed that a realistic size of the ligand field is not sufficient to produce a semiconducting gap, but consideration of the hybridization between the d_z^2, d_{xy} and $d_{x^2-y^2}$ states for Mo qualitatively gives the proper band splitting with a fully occupied narrow d-subband in the case of MoS_2 and half-filled for the group Vb TMCNs.

The first semi-empirical tight-binding calculations of the band structure for the bulk layered chalcogenide have already been performed, only in two-dimensional limit and assuming the similarity in the electronic properties of the bulk and single layer crystals [16]. Indeed, the comparison of the results [16] with APW calculations [15] confirmed this similarity of the 1H and the 2H band structure of MoS_2. Yet, late calculations by Galli et al. within a single DFT GGA scheme [17] have established a fine difference in the band structure of MoS_2 of different dimensionality: close to the Γ-point, due to the interlayer interaction, the splitting becomes larger, leading to transition from a direct gap (1H single layer) to an indirect gap (2H bulk allotrope) (Fig. 3).

The uppermost states at the Γ-point of the valence band originate mainly from d_z^2 orbitals on Mo atoms and contributions of p_z orbitals on S atoms. Due to the antibonding nature of these states, their energy diminishes with increasing interlayer distance and decreasing of the

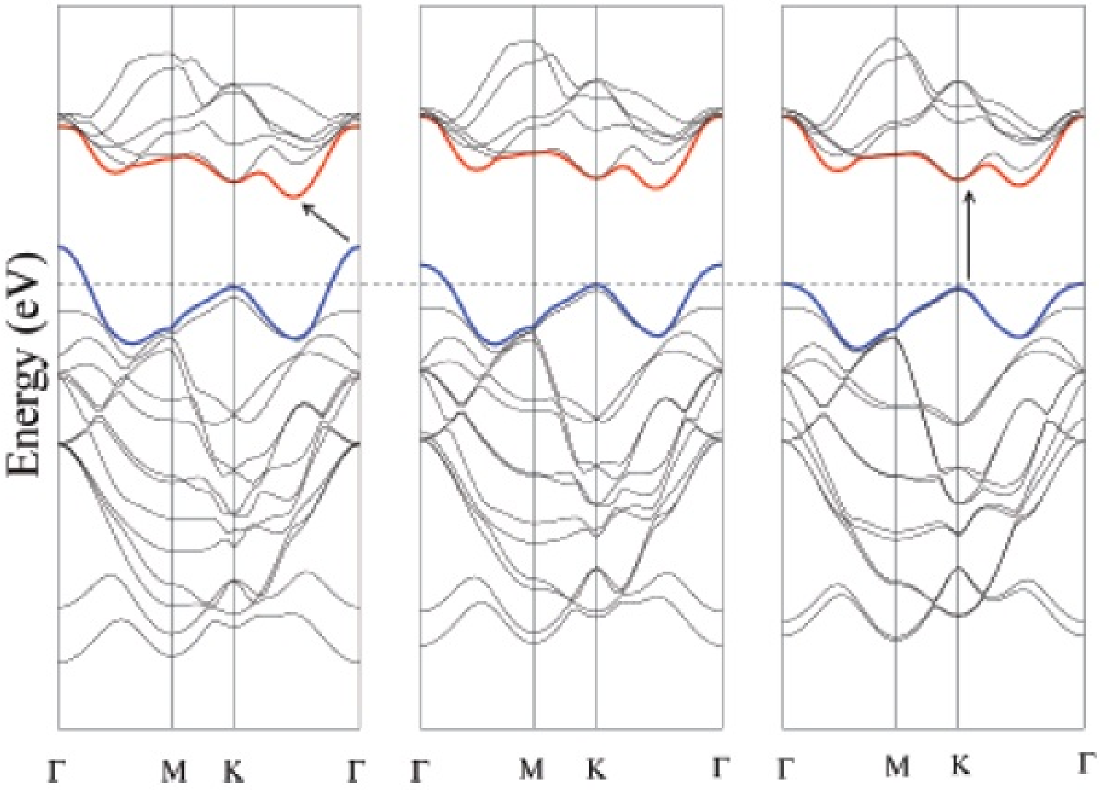

FIG. 3. Band structure of 2H-MoS_2 with increasing interlayer separation w (2.58 Å, 2.98 Å, and 3.58 Å – from left to right). For comparison, the energies are aligned with respect to the valence band top at the K-point. (Adapted from [17])

layer-layer interaction [17]. Conversely, the states at the top of the valence band and the bottom of the conduction band near the K-point, which are nearly exclusively d_{xy} and $d_{x^2-y^2}$ states for Mo, are accordingly unaffected by a change in the interlayer separation. Therefore, the gap between the valence band and the conduction band remains nearly constant at K ($\sim$ 1.8 eV GGA) with increasing interlayer separation, whereas the energy of the states at the top of the valence band at Γ decreases – see Fig. 3. For the limiting case of infinite layer separation (1H – single layer) the gap is determined by the states at the K-point and a transition from an indirect gap (Γ →K) to a direct gap (K→K) semiconductor. This behavior was confirmed by Lebegue et al [18].

The results were also confirmed experimentally [19,20]. Of course, the discussion of the variation of the band-structure on the basis of KS-LDA or KS-GGA orbital energies, especially with respect to size and character of the gap, has to be viewed with caution. However, quasi-particle calculations within the GW approximation qualitatively confirm this picture [21].

Kuc et al. [22] studied in more detail also other semiconducting and metallic TMCN with respect to the number of layers within multilayered slabs. The results of their DFT GGA calculations showed similar behavior to MoS_2. When going from the bulk 2H-structure to a single 1H-WS_2 layer, the system becomes a direct gap semiconductor with an increase of the gap from about 1.3 to 2.1 eV, respectively [16]. This phenomenon has already been observed by the authors when switching from a double-layered slab to a single layer. It is worth noting that the shape of the d-bands in the band structure of NbS_2 slabs also demonstrates the drift of maximum and minimum at Γ and 1/2(Γ–K) points by the variation of the number of layers, yet, these systems always remain metallic, due to the half-occupied d_z^2 band.

3. Electronic structure of the monolayers under mechanical deformation

Measurements of the stiffness and failure strength of MoS_2 monolayers and bilayers using atomic force microscopy [23] demonstrate the elastic mechanism of their deformation with an effective Young's modulus of 270±100 GPa. Breaking occurs at an effective strain between 6 and 11 % with the average breaking strength of 23 GPa. These results show that single layers of chalcogenides possess exellent mechanical properties and could be suitable for a variety of applications such as reinforcing elements in organic composites and for fabrication of flexible electronic devices. Yet, all aforementioned theoretical studies of electronic structure of TMCN layers implied their ideal planar and strain-free structure. However, the semiconducting properties may be essentially changed under strain after embedment into real electronic devices, e.g. due to bending or stretching induced by the surface of a substrate or by a polymeric matrix. This problem has been considered in a few recent theoretical works.

The electronic properties of MoS_2 single and double layers under tensile or compressive biaxial strain have been investigated within the DFT GGA scheme [24]. The value of the band gap of mono- and bilayer systems reduces upon the application of any kind of deformation, which is in agreement with similar studies on the variation of the energy band gap as a function of pressure in the bulk MoS_2 [25]. For the monolayer, a transition from direct-to-indirect gap can be observed upon the application of relatively small strain (∼ 2 %), when the energy of the top band of occupied states increases at Γ-point and energy of the bottom of unoccupied band decreases at K-point. A large tensile strain of about 8 % or a compressive strain of about 15 % should already lead to the semiconductor–metal transition. Application of uniaxial strain to single layered MoS_2 as well leads to a reduction of its band gap and transforms it to an indirect band gap semiconductor [26]. According to the more sophisticated quasiparticle GW calculations, for a strain of 1 %, the single MoS_2 should still have a direct gap, but for larger strains the transition to an indirect gap was confirmed [27].

The theoretical gap of MoS_2 monolayer reduces linearly with the stretching, until the material eventually becomes metallic at a certain strain level [24, 26]. This phenomenon can be interesting for possible application in nanoelectromechanics and optoelectronics engineering. Stretched semiconductors are likely to expose states near the Fermi level due to elongated bonds with a weaker orbital overlapping, which hence would not contribute essentially to electrical conductance. Thus, simple analysis of the band structure of strained semiconductor may not be sufficient and the transport properties should be elucidated.

First quantum conductance calculations on the mechanically deformed monolayers of MoS_2 and WS_2 were performed using the nonequlibrium Green's functions method combined with the Landauer-Büttiker approach for ballistic transport together with the density-functional-based tight binding method DFTB [28]. While DFTB calculations of the band gap response on the applied biaxial isotropic strain were found to be in agreement with *ab initio* data [24, 26], they also revealed a significant increase in the electrical conductivity at the Fermi level (Fig. 4). At the critical strain level (∼ 11 %), when the band gaps of semiconducting layers vanish to zero, the transport channels are completely open and current flow is enabled. The electronic transport in the case of isotropic deformation (tensile or compression) does not depend on the direction of the current and remains almost the same for both *zigzag* and *armchair* directions of the layer.

The electron conductivity of MoS_2 monolayer under uniaxial strain demonstrates a different behavior [28] being applied in the parallel or in the perpendicular directions to the

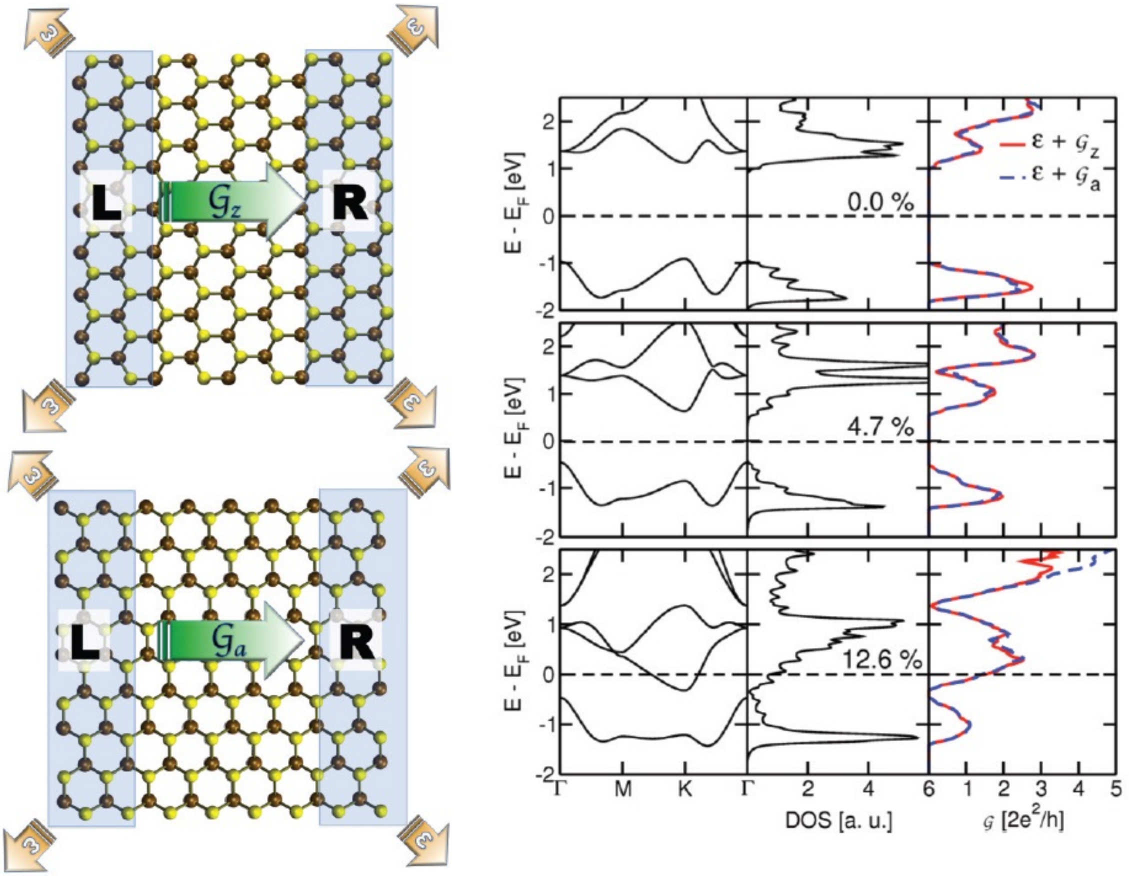

FIG. 4. Band structure, density of states and electron conductivity of MoS_2 monolayer under isotropic tensile strain as revealed by nonequlibrium Green's functions method in DFTB approach. Ga and Gz denote electron conductivity along armchair and zigzag directions of the layer, respectively. Adapted from [28]

transport axis. Even under high strain, the monolayer still shows semiconducting behavior with the known tendency of the band gap reduction. Yet, the electron conductivity of such strained monolayer would be predetermined by the direction of strain relative to the direction of current. Strain perpendicular to the current reduces the band gap without a significant change in the conductivity. In contrast, strain in the same direction as the current results in a reduced band gap, and also in reduced conductance for electron energies lower than the Fermi energy level. At energies higher than the Fermi level, such strain enhances the conductance drastically. Similar calculations performed on example of metallic NbS_2 monolayer have shown that the magnitude of conductivity may be also varied upon both isotropic and uniaxial deformations. These results highlight the importance of the strain direction for nanoelectromechanical applications of semiconducting as well as metallic layers. Noticeably, the critical strain for semiconductor-metal transition is too close to the limit of mechanical stability of this material under stretching, which is experimentally characterized by failure strain 6 – 11 % [20].

Besides 'in-layer' deformations, a certain interest should be devoted to the influence of the bending of TMCN layers on their electronic properties. The first clues on the band gap behavior and type of transition by this deformation mode have been obtained by numerous experimental and theoretical studies of chalcogenide nanotubes — in fact, the layers bent into nonsuture cylinders [29–33]. The band gaps of all semiconducting sulfide nanotubes are defined by the degree of curvature, and are smaller than the band gap of their planar counterparts.

Moreover, the type of the transition within nanotubes can be different and is defined by the folding of band structure of two-dimensional system along certain direction. E.g., the gap size of *zigzag* MoS_2 nanotubes is intimately related to that at the K-point in MoS_2 monolayer [29]. It gives evidence that bending of an infinite monolayer should lead to the reduction of the band gap and possibly to a change in the transition type, depending on the direction of the bending.

The locally bent parts can occur within a monolayer even without any external action, but due to thermal excitation. HRTEM, AFM and optical measurements reveal spontaneous rippling of MoS_2 layers [34]. The intrinsic dynamics of MoS_2 monolayer with the formation of oscillating ripples and its influence on the electronic structure and the conductance was studied by means of DFTB method in conjuction with Born-Oppenheimer molecular dynamics [35]. Both experimental and theoretical studies estimated the average characteristic length of ripples as 6 – 10 Å at a typical layer length of 60 – 100 Å. MD simulations unambiguously point on the thermal origin of this rippling. The average size of the ripples increases with temperature and the estimated ripple oscillation frequencies also increase. Expectedly, the phenomenon of ripple formation leads to a reduction in the band gap of MoS_2 monolayer due to the lowering of the lowest conduction band energies. Although, the transport calculations using DFTB method reveal a drastic reduction of the conductance in the direction across a ripple: in the most distorted structures, the transmission decreases 75 % compared to that of the flat layer.

It is noteworthy that experimental [34] and theoretical [35] studies of rippling formation have been performed on an example of the membranes — free parts of MoS_2 monolayer, which were not in contact with the substrate. The effect of the substrate on the mechanical deformation of a deposited TMCN layer has not been systematically studied yet. Though, it can be speculated that it may be depend on the strength of interfacial bonding. In the case of weak van der Waals interaction, the rippling can be suppressed, and the layer flattening would lead to the conductivity of ideal flat layer. The influence of a strong interface interaction is less predictable. It may lead not only to the flattening, but also to the stretching or tensile deformation of layer, which can reduce its conductivity, as was discussed above.

On the other hand, simulation of nanoindentation experiments, using an atomic force microscope, of single MoS_2 layers suspended over circular holes [20], shows the exceptional electronic robustness of the MoS_2 sheets towards local mechanical deformation [35].

4. Intrinsic conductivity of defect-free monolayers

The structure of layered chalcogenide semiconductors results in a highly inert surface with a relatively low defect concentration, which enables the fabrication of field effect transisors (FETs) with an intrinsically low field-effect threshold. The semiconductor gap makes the realization of FETs based on these materials even more attractive than those of graphene, where the missing gap creates serious problems for its application in corresponding devices. Field effect transistors of WSe_2 with a high mobility of charge carriers were fabricated [36]. However, these WSe_2 based transistors were characterized by high doping levels and showed reasonable *trans*-conductance characteristics only at low temperatures. Consequently, the fabrication of FETs based on single and a few layered MoS_2 has been demonstrated, but the observed electron mobility in the single layer MoS_2 is unexpectedly low (from 0.1 – 10 to tens of cm^2 /(Vs)) [6, 8,37]. These materials were also characterized as doped semiconductors, and their low mobility of charge carriers was explained by high density of charge trap states within the MoS_2 layer. Concurrently, the use of hafnium oxide as gate dielectric allows one to reach mobility in single-layer MoS_2, at least to 200 cm^2/(Vs) at a room-temperature, similar to that of graphene nanoribbons [7].

Indeed, already the first electrical measurements have clarified that the conductivity of bulk chalcogenides can be widely varied, depending on the purity of samples (see reviews [1,4]). A typical dependence for logarithm of resistance on inverse temperature for bulk layered chalcogendies consists of two regions with activation energies < 0.1 eV at low temperature and 0.4 – 0.9 eV at high temperatures ($\sim$ 400 K and above), which can be attributed to extrinsic and intrinsic conductivity, respectively. The problem of purification of these compounds and uncontrollable distribution of an impurity may explain the poor reproducibility of the measurements, even for samples with formally equal doping levels. The electrical conductivity measured for the crystals of dichalcogenides grown in various conditions may vary more than 106 times for MoS_2, 105 for $MoSe_2$ and 103 for WSe_2 [38]. The reason for these deviations was explained not only by the doping content, but also by the temperature controlled size of the chalcogenide grains. An annealing of the samples can lead to the increase of average size of the grains, i.e. to decrease the number of intergrain contacts with a high electrical resistance.

The understanding and revelation of intrinsic conductivity is important to determine the maximal possible performance and the feasibility of a chalcogenide layer as a material for nanoelectronics. Already, Fivaz and Mooser [11] have shown that the mobility in bulk metal chalcogenides, such as MoS_2, is limited by the phonon scattering – interaction with optical phonon modes (A2$''$ – mode 481 $\mathrm{cm}^{-1} = 0.06$ eV, the IR-active antisymm vibration perpendicular to the MoS_2 plane). This has been confirmed and discussed in detail for the single MoS_2 layer by Kaasbjerg et al. [39]. They have calculated effective electron mass, the scattering rate and phonon-limited mobility in the layer as a function of carrier energy, temperature and carrier density. The intrinsic electron mobility was characterized as dominated by optical phonon scattering and estimated as $\sim$ 410 cm^2/(Vs). These findings suggest that low experimental mobilities, on the order of $\sim$ 1 cm^2/(Vs) reported in Ref. [6, 8], are indeed dominated by other scattering mechanisms, e.g., by scattering on some charged impurities or defects. Obviously, the latter is screened using deposition of a high-k dielectric material on MoS_2 surface. A comparison of the temperature dependence of the mobility in samples with and without the top-gate structure performed in [39] clarifies in this manner the observed enhancement in the mobility to $\sim$ 200 cm^2/(Vs) [7].

5. Possible routes for fabrication of monolayers and the origin of defects

There are several possible origins for scattering centers in the layers of TMCN, which are able to affect electronic properties: vacanices within metal or chalcogen sublattices, point-like reconstructions and extended line defects, grain boundaries, doping or adsorbed atoms. To a large extent, the types and amounts of these centers and their combinations are defined by the history of the sample. At present, a few top-down and bottom-up fabrication techniques have been evaluated.

The first of them implies an exfoliation of a bulk layered crystal. For example, the most inspiring measurements of the mobility and FET design have been performed on samples of MoS_2 layers extracted from a naturally occurring form of MoS_2 – molybdenite mineral – using a micromechanical cleavage technique [6, 7]. The strength of strongest MoS_2 monolayer membranes created from molybdenite is about 11 % of its Young's modulus, which is quite close to the upper theoretical limit calculated in the approximation of ideal lattice and indicates that such material can be highly crystalline and almost defect-free [23]. However, the gate-controlled character of the conductivity suggests the presence of at least charged defects. These can be likely presented in molybdenite by substitutionally doping Re atoms in amount from a few ppm to 1 % [40]. Currently, there is no route known for the purification of molybdenite, and the minor admixtures cannot be removed from such prepared layers. Definitely, cleavage could be processed from the synthetic chalcogenide bulk crystals, grown using gas transport techniques [38]. Yet, this option is not explored profoundly and this technique is not sufficiently evaluated for this purpose. Layers of synthetic chalcogenide crystals are known to contain dislocations, grain boundaries, intercalated metal atoms, which would require an additional annealing. Another noteworthy disadvantage of micromechanical cleavage is low mass production. The desired single layer particles are barely present in the wide distribution of the cleaved multilayered flakes.

An early known mass production method employs chemical exfoliation and includes preliminary intercalation of the bulk chalcogenide by lithium or other alkali metal and subsequent sinkage of intercalate in aqueous solvent [41]. Apparently, it is limited by the chemical stability of chalcogenide lattice against such reducing agents and the final products will contain numerous defects such as vacancies or even amorphous nonstoichiometric phases. To overcome the problem of an intercalant, the utilization of direct liquid exfoliation of the bulk compound can be suggested, which would depend on the solubility of the compound in an appropriate solvent. Recently, it was demonstrated that many layered chalcogenides can be efficiently and in large quantities dispersed in a range of common solvents [42]. Due to the physisorptive nature of exfoliation, the quality of the final product in this case would be as well predetermined mainly by the state of the bulk crystal itself. Despite of the advantages of the latter technique over mechanical cleavage and chemical exfoliation, it also gives a mixture of mono- and few-layer flakes containing trace amounts of solvent .

The extrusion of the single layers from the ‘mess’ of multilayers is a common feature of top-down methods, which hampers the subsequent transfer of the layer onto a substrate and further operations. The bottom-up approach may be a more successful alternative, providing controllable deposition of the material with required number of the layers on desired substrate. By this means, much progress has been achieved in the fabrication of single-layered MoS_2 islands with the sizes varying from dozens atoms [43] to dozens nanometers [44] by subsequent S and Mo atomic depositions and annealing on a metal surface. The large-area growth of MoS_2 thin films with scalable thickness and size up to several millimeters was achieved using chemical vapor deposition (CVD) method on SiO_2/Si substrates with different pretreatments [45, 46] or using thermolysis of thiomolybdates on SiO_2/Si or sapphire [47]. It is noteworthy that the bottom-gated transistors, constructed from such deposited MoS_2 monolayers, have frequently demonstrated lower carrier mobility, than those built from mechanically cleaved monolayers. This is clear evidence that the MoS_2 layers prepared under such extreme conditions can have randomly grained structure and contain numerous defects, including vacancies and dislocations [46].

Thus, the challenging application of single-layered chalcogenides in electronics also keenly urges on the search for appropriate synthetic routes, which could provide the high purity and crystallinity of the layers together with the ease, accuracy and low cost of manipulation on a layer after its production. While these methods are still being evaluated, essential progress has been achieved in the defect characterization of TMCN monolayers at an atomistic level.

6. Intrinsic defects within the monolayers and their influence on electronic structure

One of the most simple and prevalent intrinsic defects, which can occur within the lattice of chalcogenide layers, are single atom vacancies. The most profound study on the formation of these defect types by irradiation treatment was performed by Komsa et al. [48]. DFT-GGA calculations for a large family of TMCNs layers have been employed for the estimation of vacancy formation energies, threshold energies for atomic displacements and displacement cross sections under electron irradiation. Sulfur vacancy within a semiconducting layer leads to the occurence of an occupied bonding type vacancy state close to valence band gap maximum and an empty antibonding state in the mid gap, which stabilizes structure. The formation energy for the vacancy in a non-metal sublattice was found to be smaller than the displacement threshold energy in the same compound. The calculated data allowed to estimate the electron threshold energies. The formation energies for selenides and tellurides are smaller than for sulfides, but due to the higher atomic weights, the creation of vacancies through ballistic electron impacts requires significantly higher electron energies. In the case of MoS_2, $MoSe_2$ and $MoTe_2$ electron threshold energies were estimated at about 90, 190 and 270 keV, respectively. Thus, particularly, the production of S vacancies is within the energies commonly used in TEM studies. The displacement thresholds for chalcogen atoms in the top plane facing the beam proved to be considerably higher than for the bottom chalcogen layer as the displaced atom is ‘stopped’ by the other layers. The threshold energies for the metal vacancies are also higher, due to higher coordination number; e.g., the electron energy to displace Mo atom in MoS_2 was estimated as 560 keV, which is far beyond the stability of the monolayer. Yet, the formation of such defects with a slight chalcogen surplus in the samples cannot be excluded during the synthesis of chalcogenide layers. These theoretical results were supported by an experimental TEM study of natural molybdenite MoS_2 layer evolution under 80 keV electron beam. During continuous imaging, an increasing number of vacancy sites (exclusively on the S sublattice) were found (Fig. 5). The contrast TEM images even allowed us to distinguish single and double vacancies.

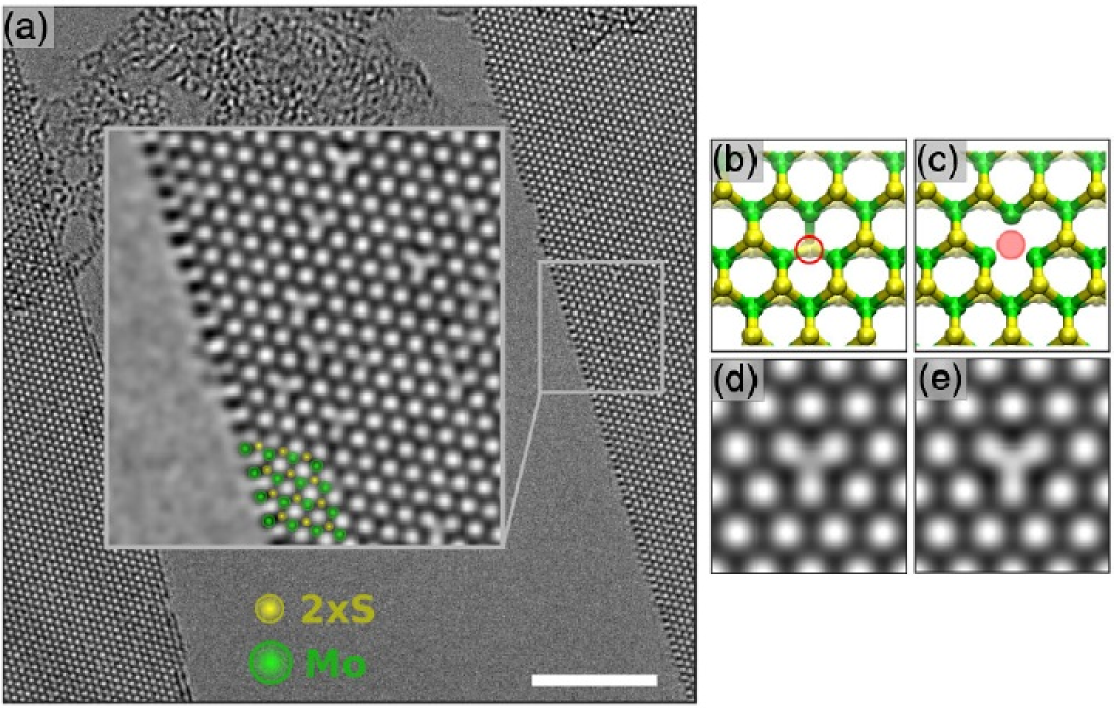

FIG. 5. AC-HRTEM image of a single MoS_2 layer under electron irradiation shows an increasing number of point defects: S single and double vacancies (scale bar is 5 nm) (a). Structure models and corresponding simulated HRTEM images for both vacancy types are shown in (b),(d) for the single (b,d) and for the double vacancy (c,e). Adapted from [48]

The possibility of vacancy formation in the layers under electron irradiation may not only be an objectionable effect, but could also be used for the modification of the electronic structure using single atom doping. The authors [48] have suggested that the created vacancies can be subsequently filled with different species (other than chalcogen), deliberately injected into the TEM chamber. The formation energy of substitutional defects in MoS_2 by isoelectronic O, S, Se, Te, electron donating F, Cl, Br, I and accepting N, P, As, C, Si atoms have been found as energetically favored. The filling of S vacancies by the atoms was detected experimentally in TEM images, yet, their nature was not identified. Furthermore, HRTEM experiments have been established for the production, diffusion and agglomeration of sulfur vacancies within MoS_2 layer under electron irradiation [49]. Single vacancies can be mobile under an electron beam and tend to agglomerate into lines of a few different kinds, which orientation should be sensitive to mechanical strain.

Atomic-resolution annular dark field (ADF) imaging on abberation-corrected scanning transmission electron microscope (STEM) was performed on MoS_2 samples, which were CVD grown on SiO_2 substrate and posses n-type conductivity [50]. As was mentioned above, synthetic chalcogenide crystals can possess a large number of dislocations. Indeed, a rich variety of intrinsic structural defects such as point defects and dislocation cores, grain boundaries were directly observed within single MoS_2 monolayers. Grain boundary structures in TMCN binary compounds were identified to be more complex than those in graphene and consisting of 4|4, 5|7, 6|8 and 4|6 dislocation core structures containing homonuclear Mo-Mo bonds or hypercoordinated S atoms (Fig. 6). A rich variety of the defects and their complex structures give rise to a wealth of possible honeycomb orientations of neighboring grains. The electronic structures of the experimentally observed grain boundaries were explored using DFT calculations. In all cases, the presence of a grain boundary causes the occurrence of new states in the band gap of MoS_2. Fig. 6c shows the band structure and local density of states for so-called 4|4E grain boundary as an example. It can be imagined as a perfect 1D metallic quantum wire embedded into the semiconducting MoS_2 matrix with dispersive bands crossing the Fermi level, which was proven by visualization of partial charge density.

The crystal structure of CVD-grown MoS_2 microcrystals on Si/SiO_2 substrate was also analyzed using TEM, ADF-STEM and electron diffraction techniques by van der Zande et al. [51]. A few types of microcrystals were identified: single-crystal triangles with Mo or S edge terminations and polycrystalline crystals. The first type of nanoparticles has been characterized by a negligible amount of point defects, which however were readily formed under extended imaging. The polycrystalline nanoparticles were described as merged by means of line defects represented as with tilt or mirror twin boundaries formed by 8- and 4-memebered rings in such manner, that hexagons of honey-comb structures of two neighbor grains are oriented under 180 ° angle. DFT calculations performed on a set of a few defective structures have also given evidence for the appearance of mid-gap states, which are mainly localized at the boundary atoms.

Other types of grain boundaries were identified in double layers of MoS_2 using HRTEM imaging combined with DFTB calculations [52]. The grain boundaries can be represented as a line defect consisting of either homonuclear Mo–Mo bonds or of two S bridge atoms (Fig. 7), which would link always two grains with *zigzag* either S or Mo termination. The high stability of these types of covalent linking was demonstrated by MD simulations, even at 600 K. Calculated DOS for all defects includes localized trap states near the Fermi level and in the band gap region. The electronic properties of layers containing such defects should stem mainly from the edge states of the two opposite domains, in a similar way as described in the literature for triangular MoS_2 nanoplatelets and nanostripes with metallic-like edges [53, 54].

The results of DFT calculations [50–52] unambiguously claim the presence of mid-gap states in semiconducting TMCN layers with grain boundaries independent of their origin. These states could affect the electrical transport and optical properties of a semiconductor. Van der

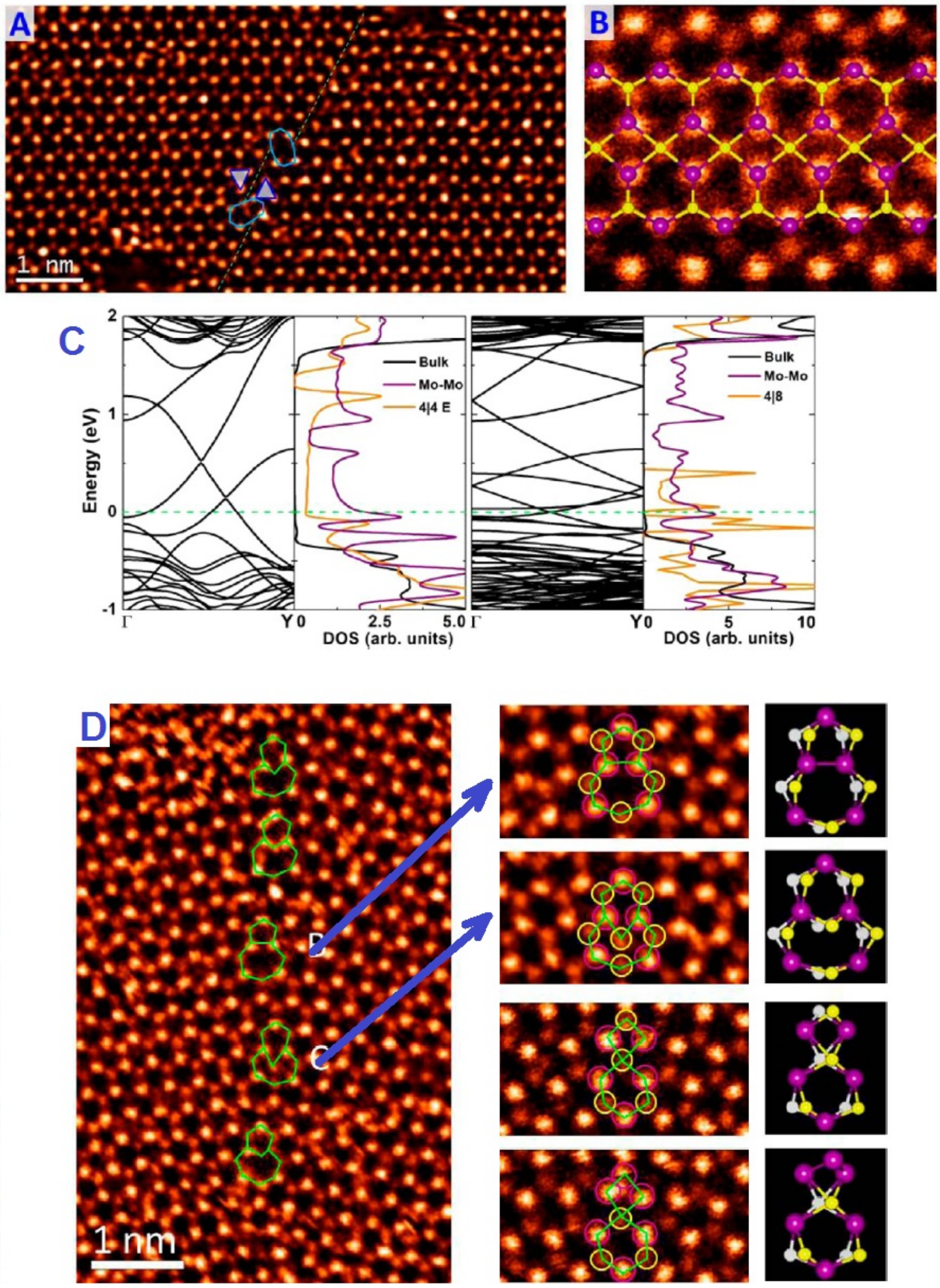

FIG. 6. STEM-ADF images and structural models of some grain boundaries in single layer MoS_2: (A) a 4—4P 60 ° grain boundary; (B) magnified part of (A) with the structural model overlaid; (C) Band structures, total and partial densities of states of the 4—4E and 4—8 grain boundaries; (D) Small-angle grain boundaries consisting of 5—7, 6—8 and 4—6 fragments in single layer MoS_2 and their 3D structural models. Adapted from [50]

Zande et al. have engineered a set of FET devices from MoS_2 islands containing a single grain boundary and studied the conductance across and along both twin and tilt type grain boundaries [51]. The pristine devices constructed on a single MoS_2 grain show n-type behavior with mobilities of 3 – 4 $cm^2/(Vs)$, which is comparable to those reported for gated FETs

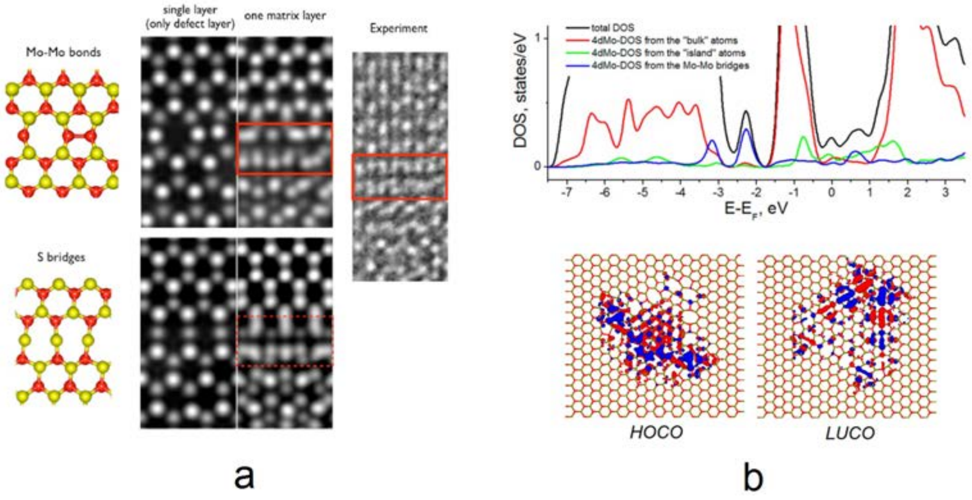

FIG. 7. (a) Structural models, calculated and experimental HRTEM images of homonuclear line defects in single and double layer MoS_2. The central part shows the images simulated for the Mo–Mo bond defect and the –S– bridges defect. The experimental data show a consistent match with the simulated images for the defect with Mo–Mo bond. (b) Total and partial DOS calculated for the single MoS_2 layer with the embedded island interlinked either via three Mo–Mo line defects bonds. Γ-point isosurfaces of highest occupied and lowest unoccupied crystal orbitals (HOCO and LUCO) are also depicted. Adapted from [52]

fabricated from mechanically exfoliated MoS_2 in the absence of high-k dielectrics [6, 8]. The transport across a twin grain boundary shows nearly identical performance to pristine devices, indicating a minor effect on channel conductivity. The electrical characteristics of the devices measured along the boundaries are different and demonstrate a 25 % larger on-state conductivity and 60 % larger off-state conductivity compared to the pristine material. Furthermore, the measurements indicate that these few-atom wide twin boundaries have similar conductivity of up to 1 μm wide strip of pristine material. In contrast to the mirror twin, FET devices of tilt boundaries show a decrease in conductance in both parallel and perpendicular directions with decreases of 5 – 80 % compared to pristine devices. Such variability points to a tight influence of the boundary structure on electric properties.

Electron transport measurements have been performed also by Najmaei et al. [55] on the samples of defective single and a few layered MoS_2 sheets with a larger variation of grain boundary types described in Ref. [50]. The results for generic electrical performance of these devices are quite similar to the aforementioned results: n-type semiconductivity with an average mobility of 4 $cm^2/(Vs)$ was observed, independent of the sheet thickness.

Thus, the structure of the grain boundaries and mutual orientations of grain honeycombs visualized in Ref. [50–52] reveal that this type of intrinsic defect often would not be removed even after annealing or additional healing by chalcogen or metal atoms. Of course, this fact could be used for the engineering of electronic properties of a semiconducting layer. Yet, control of defect formation or grain boundary growth cannot be achieved. At present, the occurrence of intrinsic defects in an uncontrolled manner should be considered mainly as an interfering factor for the application of semiconducting TMCNs in FET devices. The charge carrier mobility can be poor reproducible from the device to device, depending on the uncontrollable content and orientation of boundaries, i.e. on the fabrication route. Low mobility, due to a scattering on the structural defects, obviously, cannot be easily increased using the appropriate electrostatic environment. Thus, a careful growth technique should be always evaluated for TMCN semiconductors to provide a monocrystalline structure without grain boundaries and other intrinsic defects, which affect electrical performance.

Apart from intrinsic defects, the electron transport measurements of defective MoS_2 structures can be interfered with many other factors, like doping, substrate induced potential or resistance at the contacts of experimental setup. The theoretical calculations allow one to distinguish the role of these factors. In general, they confirm the peculiarities of intrinsic defects in transport properties. As well, they point to new phenomena, which still have to be proven in experiments. E.g., it has been theoretically predicted that a finite atomic line of S vacancies created on a planar MoS_2 substrate, like those designed in Ref. [49], can function as a pseudoballistic wire for electron transport [56]. Removal of surface S atoms introduces electronic states within the band gap. Each S vacancy introduces a symmetric molecular orbital of mainly Mod_z^2 character near the top of the valence band and a degenerate pair of molecular orbitals of mainly Mod_{xz} and d_{yz} character near the center of the band gap. Mixing of the degenerate orbitals on neighboring vacancies causes the gradual formation of two overlapping energy bands near the Fermi level, which create pseudoballistic electron transport channels.

The electronic properties and the quantum transport in MoS_2 monolayer containing one of several structural defects were studied by means of DFTB method in conjunction with the Green's function approach [57]. A rich set of point and line defects was taken into account: vacancies in Mo and S sublattices, holes, add-atoms, 4|8 and 5|7 Stone-Wales-like rearrangements as the fragments of grain boundaries observed in Ref. [50], the line defects and their loops as obtained in Ref. [52]. All types of defects studied in this work show significant changes in the electronic structure close to the Fermi level and introduce mid-gap states within the band gap of MoS_2 (1.5 eV in this approach). This has already been reported in previous studies on defective MoS_2 [48, 50–52]. The mid-gap states are strongly localized in the vicinity of the defects and are mostly of Mo4d type (Fig. 7b). Due to this localization, these defect states should be considered as scattering centers. Although the defect states reduce the band gap significantly, their scattering character prevents opening any new conduction channels close to the Fermi level. The occurrence of defects reduces the conductivity in comparison with the pristine layer at 1.2 eV above and below the Fermi level. Expectedly, the conductivity depends strongly on the type and concentration of the point defects. Surprisingly, the electron conductivity of the systems with point defects also becomes strongly dependent on the direction of current, namely, the conductivity is suppressed much stronger for the armchair transport direction. The only exception is the single S-vacancy, where the transport seems to be independent of the considered direction; e.g., in the case of transport in *armchair* and *zigzag* directions, the electron conductance of MoS_2 with a single Mo-vacancy (in amount 1 %), is suppressed by 75 % and 90 % compared with the pristine layer. Conversely, the single S vacancy (in amount 0.55 %) shows higher electron conductivity due to the electron injection directly to the conduction band. Furthermore, for Stone-Wales defects, the conductance is reduced by less than 50 % with respect to the pristine structure. The conductance perpendicular to the line defects also reduces with increasing channel length, keeping the band gap unchanged.

7. Impurities within the monolayers and their influence on electronic structure

As was shown for the example of a MoS_2 semiconductor, CVD grown layers often are not free of intrinsic structural defects and, obviously, the layers exfoliated from natural samples demonstrate a better structural quality. Despite this, natural samples can be heavily contaminated by other d-metals, usually by Re [40]. The latter may affect the semiconducting properties due to formation of donor or acceptor levels as well as the electron mobility [6, 8] due to scattering or trapping on the charged point defects — the atoms of such a dopant.

The electronic structure of semiconducting MoS_2 layers, doped by substitution with Re atoms, was considered theoretically using DFTB method depending on the amount and distribution of atoms of dopant [58–60]. The single rhenium atoms in low concentration at Mo sites only slightly changed the DOS profile. This change manifested itself through the occurrence of an impurity level at $\sim$ 0.2 eV below the conduction band of MoS_2 and with a significant $5d$Re character (Fig. 8). These findings are reminiscent of an n-type doping of a semiconductor. A doping of MoS_2 monolayer by many separated rhenium atoms up to 1.6 % Re with random distribution does not change cardinally the DOS profile and leads to the increased intensity and the position of the band of the donor levels. The absence of large broadening at such high doping levels gives evidence that the electrons in the donor band should be strongly localized, which can be demonstrated using a visualization of the crystal orbitals for corresponding donor levels (Fig. 8). Clear localization of impurity states is also preserved for the case of island-like Re atom distribution. Though, with this type of distribution, the DOS profile of the impurity band is split into two bands, occupied and unoccupied. These bands are located at $\sim$ 0.5 eV and $\sim$ 0.1 eV below the conduction band of MoS_2, respectively. Gradual increase of the rhenium content leads to the occurrence of new impurity bands in the band gap of MoS_2 and to the increase of DOS of Re$5d$ states. The impurity states are also located exclusively in the band gap of MoS_2.

Apparently, a more drastic change of the electronic structure of a layered TMCN compound can be obtained due to the phase transition induced by doping. In addition to the allotrope formed from prismatic MX_6 units (1H structure), TMCN layers can be formed by the units with octahedral coordination (1T structure) [1]. In terms of crystal field theory, the splitting of d-orbitals in an O_h-MX_6 unit can be described as splitting into two groups: three degenerate $d_{xy,yz,xz}$ orbitals with low energy and two degenerate d_z^2 and $d_{x^2-y^2}$ with high energies (Fig. 9). For MoS_2 compound, in this case, the lowest d-orbitals are populated only with two electrons. The incomplete occupation of Mo$4d_{xy,yz,xz}$ orbitals in 1T-MoS_2 leads to the metallic ground state and also decreases the stability of this allotrope. Therefore, by doping the 1T-MoS_2 layers with an electron donating atom, the additional electrons occupy the Mo$4d_{xy,yz,xz}$ orbitals and increase the stability of the T-phase. On the contrary, when such doping occurs in the semiconducting 1H-MoS_2 allotrope, the electrons which are donated to the Mo$4d_{xy,yz,xz}$ orbitals and to the Mo$4d_{x^2-y^2}$ orbitals result in the metallic-like character of the electronic structure, and this causes destabilization of the lattice. Thus, the transition from the semiconducting 1H- to the metallic 1T-phase in MoS_2 may occur after adsorption of the electron-donating atoms of alkali metals or as a result of substitutional doping by atoms of d-elements, which can serve as electron donors (as Re, Tc, and Mn). DFTB calculations for both allotropes of MoS_2 monolayers and bilayers doped with different amounts of Re atoms support this tendency [60]. The higher the Re content is within $Mo_{1-x}Re_xS_2$ phase, the more stable 1T-$Mo_{1-x}Re_xS_2$ becomes. Recently, this phenomenon was proven by TEM study of related systems — multiwalled WS_2 nanotubes doped by Re, where both allotropes coexist. Yet, the same can be expected for the monolayers or thin flakes of MoS_2 and WS_2. Exceptional doping can induce new phase state and change the type of conductivity or at least facilitate a partial structural reorganization, which would lead to the change of mobility.

Substitutional doping of MoS_2 monolayer at the Mo site with single atoms of $4d$ elements and Re was considered in details by means of DFT LSDA calculations [61]. These results also demonstrated the n-type character of Re doping. To that end, the magnetic state of Re impurity with magnetic moment 1 μB was found lower in energy. In general, for all the substitutional

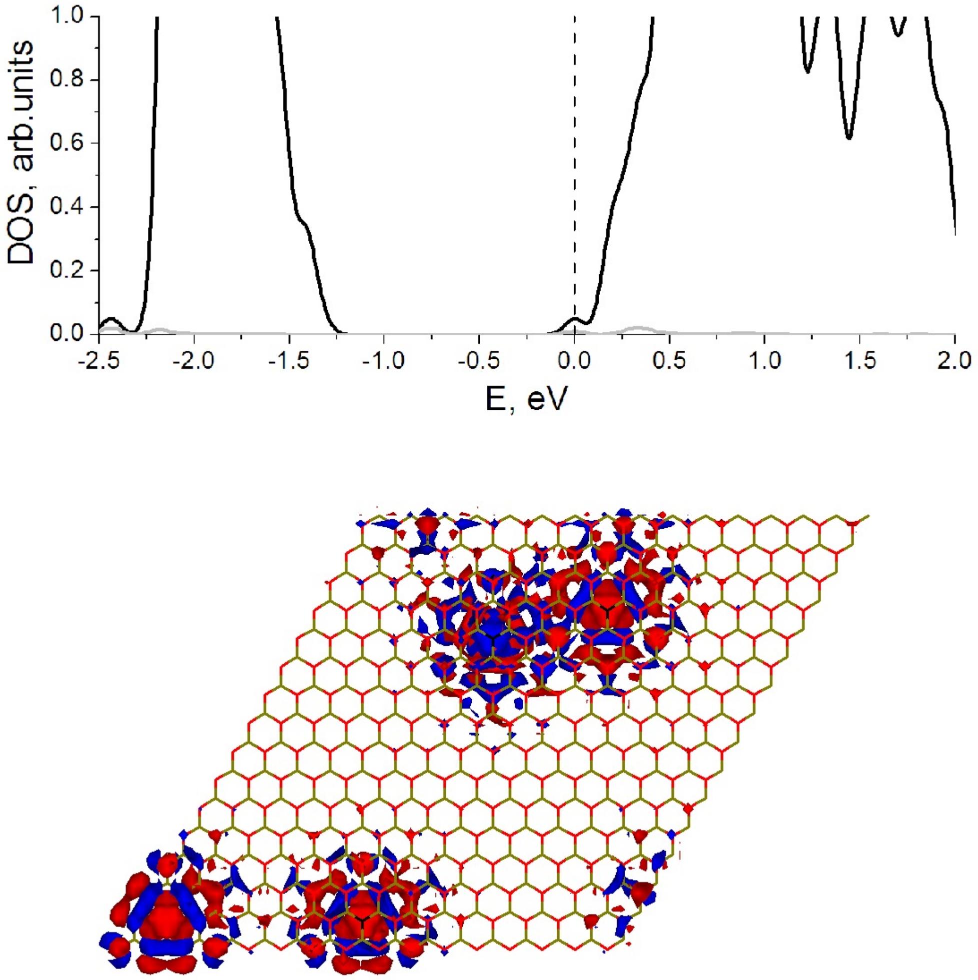

FIG. 8. DOS calculated for the single MoS_2 layer doped by a single Re atom and Γ-point isosurface of the highest occupied crystal orbitals for the single MoS_2 layer with random distribution of Re atoms. Adapted from [59]

atoms having a d occupancy larger than Mo, the ground state is found to be spin polarized, while Y, Zr, and Nb have a diamagnetic ground state. For dopants having occupancy of d-orbitals larger than Re atom, an increasing number of gap states is formed within the band gap, so that the excess electrons do not fill the MoS_2 conduction band. The excess electrons first fill up the majority spin states of the host d-orbitals, until the magnetic moment of the impurity reaches the largest value of 4 μB for Pd. Then, the magnetic moment decreases for Ag and Cd as the additional electrons start to populate the minority spins states. Nb, Zr and Y dopants cause p-type semiconductivity and shift the Fermi level to the top of valence band. The highest states in this band are still delocalized like in pristine MoS_2, therefore, the mobility in MoS_2 upon such p-doping can be expected rather large.

The influence of the doping of non-metal sublattice was also theoretically considered for a semiconducting MoS_2 monolayer. In general, DFT GGA [48] and LSDA calculations [61] give similar results for the change of electronic structure. The doping by atoms of elements with higher number of valence electrons than sulfur (F, Cl, Br, I), leads to n-type character for conductivity with localization of the donor electron near the dopant atom. This situation is quite similar to that for Re doping of Mo-sublattice. The atoms of elements with smaller number of valence electrons (N, P, As and Sb) behave as acceptors. Accordingly, the position of impurity

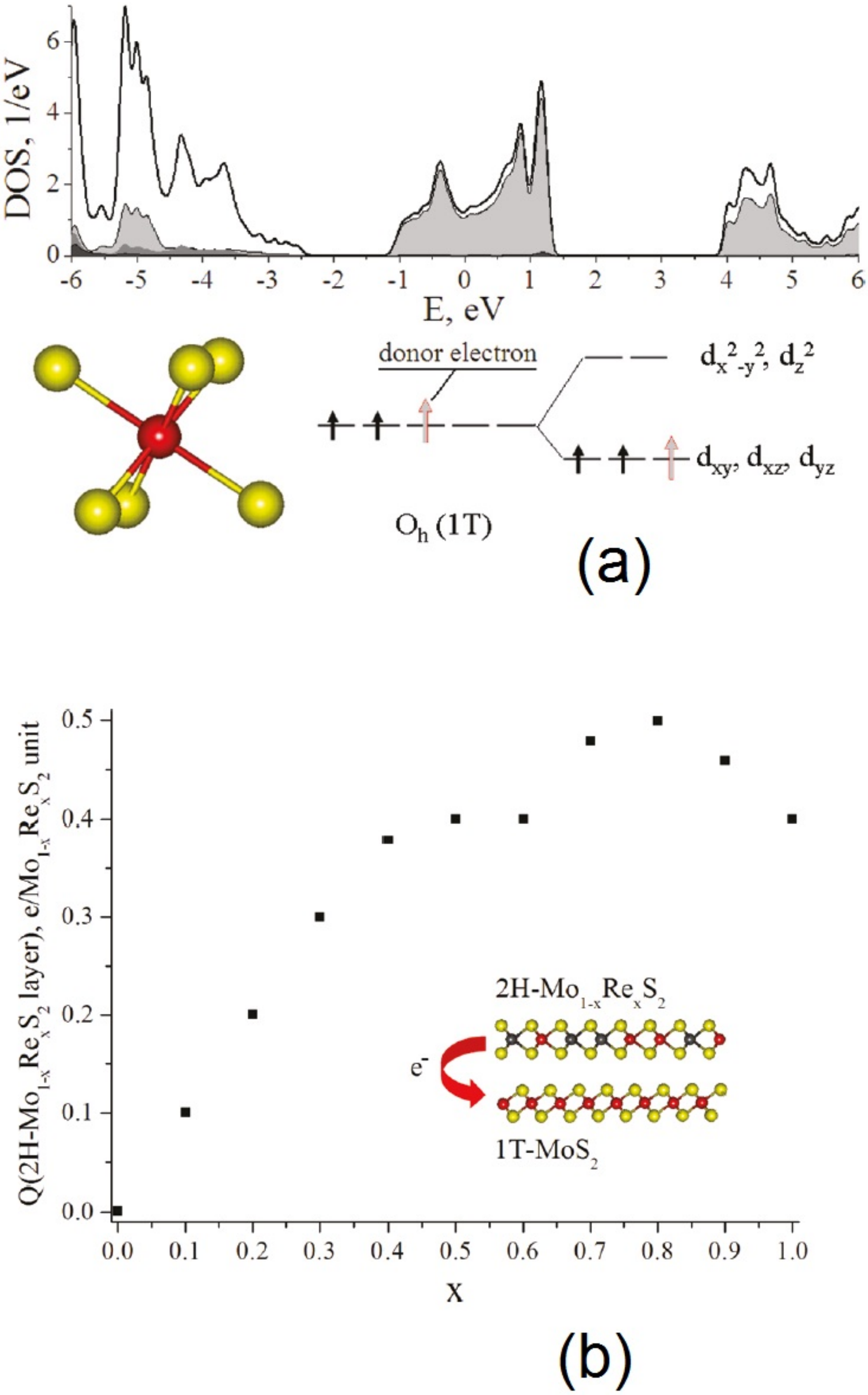

FIG. 9. (a) DOS calculated for the single layer of 1T-MoS$_2$ phase and ligand field picture for octahedral coordination (Oh symmetry) of Mo atom demonstrating a preferability of electron doping for stabilization of 1T-phase (Mo4d-states are in grey); (b) Charge transfer within double T-MoS$_2$—H-Mo$_{1-x}$Re$_x$S$_2$ layer as a function of the Re content. Adapted from [60]

levels depends on the row number of doping element. Namely, N and P atoms have magnetic moments of about 1 μB and their p-states, hybridized with Mo4d-states, can be found in the band gap of MoS_2 just above the edge of valence band [61]. When the row number is increased, these states shifts towards the valence band, and in the case of As doping, the spin splitting vanishes. The replacement of sulfur by C and Si atoms also leads to p-type conductivity, while the impurity states are well distributed within the valence band of MoS_2.

Isoelectronic doping of MoS_2 monolayer of metal (by M = W) and non-metal (by X = Se or Te) sublattices was investigated by means of DFT GGA calculations [62]. They do not reveal a crucial qualitative change in the band structure. As both pure constituents — MoS_2 and MX_2 — the monolayers of the d-metal chalcogenide solid alloys are semiconductors with direct band gap at the K-point and in the absence of localized states. Thus, the value of the band gap depends on the alloy composition and can be varied between the values of pure compounds, which has potential for the fabrication of a large family of single and a few layer semiconducting chalcogenide materials.

8. Interfaces with the TMCN monolayers

All aforementioned references have been devoted to the properties of the TMCN layers themselves. Though, many variations in the characteristics of a TMCN material can be explained by the measurement conditions and the complexity of a device. While interferences in the 'ideal' electric properties of semiconducting TMCN nanodevices were explained often by the quality of semiconductor itself, the alternative causes can be searched among the environment of semiconductor [62, 63].

Popov et al. suggested that the observed low electron mobility in single layer MoS_2 can be represented not only as an intrinsic material property, but is also biased by unfavorable contacts with the electrodes, i.e. as a $MoS_2|$metal interface problem [62]. Au is the most common contact metal in the fabrication of electrodes in electronic nanodevices due to the ease of cleaning and high chemical endurance. Yet, this noble inertness, together with the inertness of chemically saturated sulfur within MoS_2 cannot provide an essential bonding during contact and forms a tunnel barrier at the interface, which is not favorable for electron injection into MoS_2. Searching for better contacts than provided by Au, transition metals like Sc, Ti and Zr were suggested as the most suitable candidates with a low work function and good overlapping of their d-orbitals with Mo4d-states. Furthermore, a few basic factors have been taken into account and analyzed comparing with Au using the results of DFT GGA calculations: favorable interface geometry and bonding, the electronic density of states, and the potential barrier at the interface. Among these metals, Ti seems to be an ideal candidate for the modeling due to a small lattice mismatch of Ti(0001) surface with MoS_2 layer.

Comparing with $MoS_2|$Au(111) surface, the equilibrium separation of contact surfaces within $MoS_2|$Ti(0001) interface is smaller (2.0 vs 2.6 Å) and calculated binding energy is 2.5 times higher, which indicates good conditions for a larger wave function overlap at $MoS_2|$Ti interface. This is supported by the DOS analysis (Fig. 10). The most striking difference between $MoS_2|$Au and $MoS_2|$Ti interfaces associated with higher DOS at the Fermi level and significant contribution of broadened peaks of S3p and Mo4d_{xy} states in the case of $MoS_2|$Ti. Electron density maps show a much larger charge carrier density in the interface region between MoS_2 and Ti, than with Au. At the same time, the maps of electrostatic potential and estimated contact tunnel barriers give evidence that electrons in the $MoS_2|$Ti system have to bypass the much lower and narrower barrier from the metal surface to the delocalized states of MoS_2 layer, than in $MoS_2|$Au (0.45 eV and 0.9 versus 1.03 eV and 1.59 Å). Thus, Ti could be a more suitable alternative as an electrode material, since it forms a low-resistance Ohmic contact.

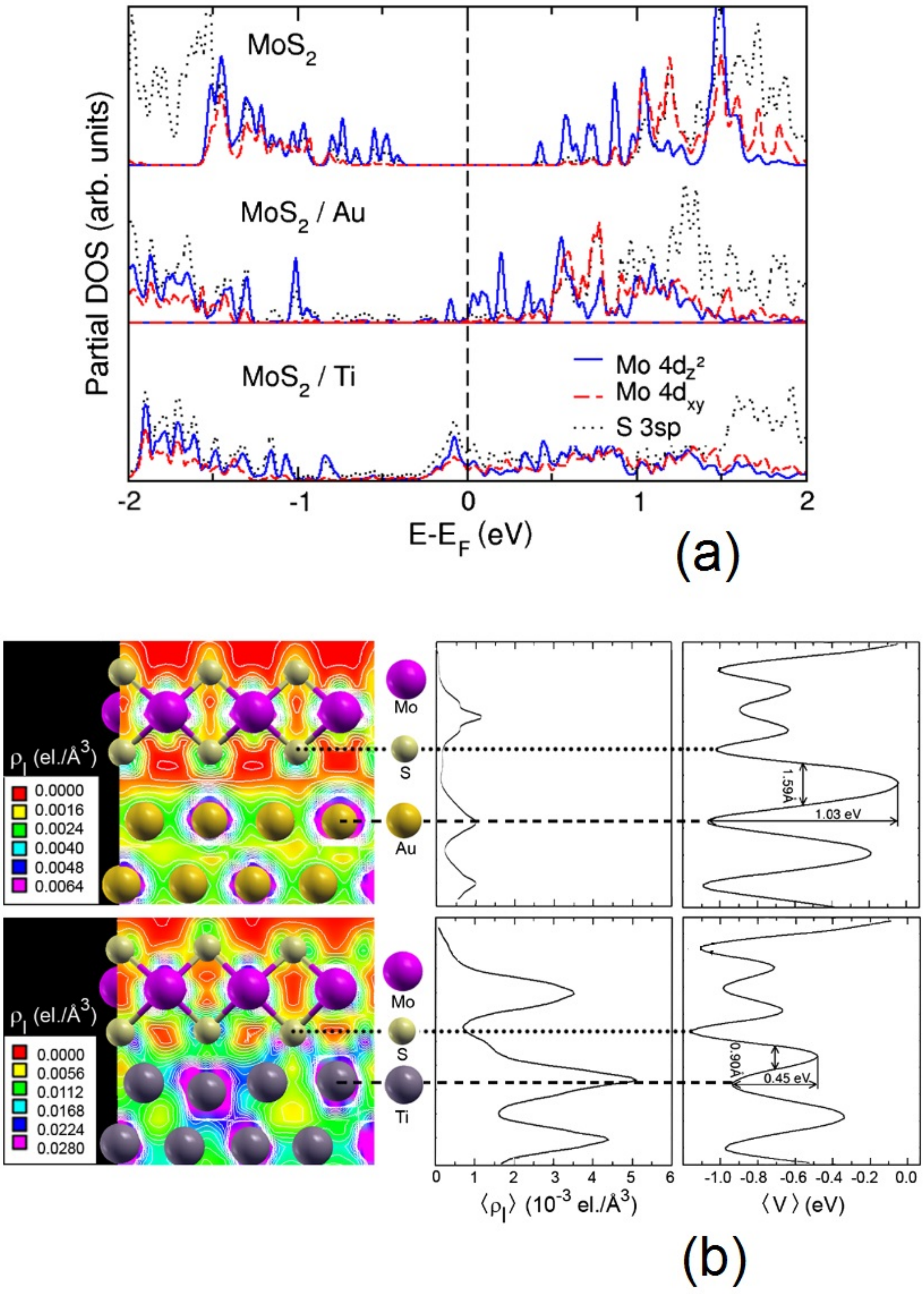

FIG. 10. (a) DOS calculated for the single MoS_2 layer and interfaces MoS_2—Ti(0001) and MoS_2—Au(111); (b) Electronic density $\langle \rho \rangle$ map and electrostatic potential $\langle V \rangle$ along the interfaces MoS_2—Ti(0001) and MoS_2—Au(111). Adapted from [62]

A detailed experimental study of metal contacts to MoS_2 surface was performed for the metals with low work function, such as Sc and Ti as well as with high work function as Ni and Pt [63]. From the temperature-dependent study that considers both thermoionic emissions over the Schottky barrier as well as thermally assisted tunneling, the barrier heights were found as ~ 230, ~ 150, ~ 50 and ~ 30 meV in the row Pt, Ni, Ti and Sc. The field effect mobilities of multilayer micromechanically exfoliated MoS_2 flakes were measured for the case of different metal electrodes and different flake thicknesses using a back-gated geometry. It was found, that the mobility values are strongly determined by the type of metal electrode, i.e. intrinsic mobility is masked by the presence of the aforementioned barrier at the source and drain contacts. Moreover, the mobility of the devices with the top joined source/drain contacts was found to depend on the flake thickness in a nonmonotonic fashion, which suggests an influence of substrate on the performance of FET. While the contacts are directly connected only to the top MoS_2 layer of a flake, the access to deeper layers leads to an additional interlayer resistance. Gating, on the other hand, impacts the deepest layers most, and charge screening results in a decreased number of charges for top MoS_2 layers. For small layer thicknesses, the absence of sufficient screening of the substrate can result in a lower mobility value than observed in the bulk MoS_2. Finally, the highest mobility values were obtained for the flake thickness ~ 10 nm. In this case, the extracted mobility values were found to be 21, 90, 125 and 184 $cm^2/(Vs)$ for Pt, Ni, Ti and Sc contacts, respectively. This is much higher than obtained in earlier studies employing single MoS_2 layer and Au contacts [6–8]. A further significant enhancement in the field effect mobility up to 700 $cm^2/(Vs)$ was achieved by covering the top of the back-gated transistor with high-k dielectric 15-nm-thick Al_2O_3 and in the case of Sc electrodes. This clearly indicated that improving the contact quality and a proper choice of substrate are also essential for obtaining intrinsic material properties.

Dolui et al. have speculated that defects in a high-k dielectric oxide substrate also can affect the conductivity properties of semiconducting TMCN sheets [64]. Charged defects at the surface of such substrate could lead to an inhomogeneous electrostatic potential and serve as charge traps located at the interface. This effect should be most pronounced for a single TMCN layer, where all sheet is in contact with the substrate, and the charged defects at the interface are not screened. In order to affirm a possible role of defects in the substrate on electronic properties of interface, *ab initio* calculations of the DOS were performed for the MoS_2 single layer deposited on a SiO_2 surface with silanol or siloxane termination. As the possible defects of SiO_2 surface the impurity Na or H atoms and O-dangling bonds have been considered. Indeed, a defect-free SiO_2 surface does not affect significantly the electronic properties of these $MoS_2|SiO_2$ interfaces: both the top of valence band and the bottom of conduction band of MoS_2 are located within the wide band gap of SiO_2. However, when a Na or H atom is placed at the interface, a trap state occurs below the conduction band. With Na ‘doping’, the $MoS_2|SiO_2$ interface becomes a n-type semiconductor with low activation energy, while substituting a H atom forms a trap state located 0.9 eV below the conduction band. In contrast, O-dangling bonds give rise to the states located below the edge of valence band, making $MoS_2|SiO_2$ interface similar to a p-type semiconductor.

9. Concluding remarks

Bulk TMCN layered materials have been explored for a long time due to their highly anisotropic structure. While in the past, the main attention was given to their lubricative and tribological phenomena related with interlayer intercalation, the recent progress in the controlled exfoliation of these compounds allowed the research of their constituents up to the level of single layers. The latter emerges a new perspective of TMCN as the low-dimensional materials for nanoelectronics applications, especially, for semiconducting TMCNs such as MoS_2 and WS_2. Numerous experimental and theoretical studies of electronic structure of the TMCN sheets have demonstrated a large facility for varying the semiconducting properties, depending on the number of the layers, controlled doping and mechanical action.

Yet, we should accept that the suggested applications still remain in their infancy and cannot yet compete with the Silicon technology, which has been thoroughly evaluated for more than half a century. Despite a long history of TMCN material science and the boosting growth of new results, much of the improvement work should be done already at the level of materials themselves. Former applications of TMCN as the components of antifrictional coatings and lubrication agents did not require high purity materials as is necessary for semiconductor-based electronics. Modern technologies for the fabrication of single and multilayers of TMCNs still do not offer a product, which would be free of native and non-controlled impurities or defects. While latter factors have been theoretically proposed as the drivers for further manipulation of the properties, currently, they should be considered rather as a nuisance. They may essentially restrict proper characterization of the material and limit the performance of devices made from TMCN layers.

Acknowledgments

The support of the ERC project INTIF 226639 is gratefully acknowledged. A. E. thanks grant RFBR 13-03-00272-a.

References

[1] *Physics and Chemistry of Materials with Layered Structures*, **1–8**, Series Eds.: F. Lévy, Springer Netherlands, (1976–1986).

[2] Yang J.F., Parakash B., Hardell J., Fang Q.F. Tribological properties of transition metal di-chalcogenide based lubricant coatings. *Frontiers of Materials Science*, **6** (2), P. 116–127 (2012).

[3] Wilson J.A., Yoffe A.D. The transition metal dichalcogenides discussion and interpretation of the observed optical, electrical and structural properties. *Advances in Physics*, **18** (73), P. 193–335 (1969).

[4] Yoffe A.D. Layer compounds. *Annual Review of Materials Science*, **3** (73), P. 147–170 (1973).

[5] Opalovskii A.A., Fedorov V.E. Molybdenum chalcogenides. *Russian Chemical Reviews*, **35** (3), P. 186–204 (1966).

[6] Novoselov K.S, Jiang D., et al. Two-dimensional atomic crystals. *Proceedings of the National Academy of Sciences of the United States of America*, **102**, P. 10451–10453 (2005).

[7] Radisavljevic B., Radenovic A., et al. Single-layer MoS_2 transistors. *Nature Nanotechnology*, **6**, P. 147–150 (2011).

[8] Ghatak S., Nath Pal A., Ghosh A. Nature of Electronic States in Atomically Thin MoS_2 Field-Effect Transistors. *ACS Nano*, **5** (10), P. 7707–7712 (2011).

[9] Radisavljevic B., Whitwick M.B., Kis A. Integrated Circuits and Logic Operations Based on Single-Layer MoS_2. *ACS Nano*, **5** (12), P. 9934–9938 (2011).

[10] Lagrenaudie J. Comparisondes composes de la famille de MoS_2 (structure et proprietes optiques et electriques). *Journal de Physique et le Radium*, **15**, P. 299 (1954).

[11] Fivaz R., Mooser E. Mobility of Charge Carriers in Semiconducting Layer Structures. *Physical Review*, **163** (3), P. 743–755 (1967).

[12] Späh R., Elrod U., et al. *pn* junctions in tungsten diselenide. *Applied Physics Letters*, **43** (1), P. 79–81 (1983).

[13] Hultgren R. Equivalent Chemical Bonds Formed by s, p, and d Eigenfunctions. *Physical Review*, **40**, P. 891–907 (1932).

[14] Kimball G.E. Directed Valence. *Journal of Chemical Physics*, **8**, P. 188–198 (1940).

[15] Mattheiss L.F. Band Structures of Transition-Metal-Dichalcogenide Layer Compounds. *Physical Review B*, **8** (8), P. 3719–3740 (1973).

[16] Bromley R.A. A semi-empirical tight-binding calculation of the band structure of MoS_2. *Physics Letters A*, **33**, P. 242–243 (1970).

[17] Li T., Galli G. Electronic Properties of MoS_2 Nanoparticles. *The Journal of Physical Chemistry C*, **44**, P. 16192–16196 (2007).

[18] Lebègue S., O. Eriksson O. Electronic structure of two-dimensional crystals from ab initio theory. *Physical Review B*, **79** (11), P. 115409 (2009).

[19] Mak K.F., Lee C., et al. Atomically Thin MoS_2: A New Direct-Gap Semiconductor. *Physical Review Letters*, **105** (13), P. 136805 (2010).

[20] Splendiani A., Sun L., et al. Emerging Photoluminescence in Monolayer MoS_2. *Nano Letters*, **10** (4), P. 1271–1275 (2010).

[21] Komsa H.-P., Krasheninnikov A.V. Effects of confinement and environment on the electronic structure and exciton binding energy of MoS_2 from first principles. *Physical Review B*, **86** (24), P. 241201 (2012).

[22] Kuc A., Zibouche N., Heine T. Influence of quantum confinement on the electronic structure of the transition metal sulfide TS2. *Physical Review B*, **83**, P. 245213 (2011).

[23] Bertolazzi S., Brivio J., Kis A. Stretching and breaking of ultrathin MoS_2. *ACS Nano*, **5**, P. 9703–9709 (2011).

[24] Scalise E., Houssa M., et al. Strain-induced semiconductor to metal transition in the two-dimensional honeycomb structure of MoS_2. *Nano Research*, **5** (1), P. 43–48 (2012).

[25] Li W., Chen J.F., He Q., Wang. T. Electronic and elastic properties of MoS_2. *Physica B*, **405**, P. 2498–2502 (2010).

[26] Li T. Ideal strength and phonon instability in single-layer MoS_2. *Physical Review B*, **85** (23), P. 235407 (2012).

[27] Shi H., Pan H., Zhang Y.-W., Yakobson B.I. Quasiparticle band structures and optical properties of strained monolayer MoS_2 and WS2. *Physical Review B*, **87** (15), P. 155304 (2013).

[28] Ghorbani-Asl M., Borini S., Kuc A., Heine T. Strain-dependent modulation of conductivity in single layer transition-metal dichalcogenides. *Physical Review B*, **87**, P. 235434 (2013).

[29] Seifert G., Terrones H., et al. Structure and electronic properties of MoS_2 nanotubes. *Physical Review Letters*, **85** (1), P. 146–149 (2000).

[30] Teich D., Lorenz D., et al. Structural and electronic Properties of helical TiS2 Nanotubes Studied with Objective Molecular Dynamics. *The Journal of Physical Chemistry C*, **115**, P. 6392–6396 (2011).

[31] Enyashin A.N., Popov I., Seifert G. Stability and electronic properties of rhenium sulfide nanotubes. *Physica status solidi (b)*, **246** (1), P. 114–118 (2009).

[32] Scheffer L., Rosentzveig R., et al. Scanning tunneling microscopy study of WS2 nanotubes. *Physical Chemistry Chemical Physics*, **4**, P. 2095–2098 (2002).

[33] Kaplan-Ashiri I., Cohen S.R., et al. Mechanical behavior of individual WS2 nanotubes. *Journal of Materials Research*, **19** (2), P. 454–459 (2004).

[34] Brivio J., Alexander D.T.L., Kis A. Ripples and Layers in Ultrathin MoS_2 Membranes. *Nano Letters*, **11** (12), P. 5148–5153 (2011).

[35] Lorenz T., Joswig J.-O., Seifert G. Layered Nanostructures — Electronic and Mechanical Properties. *MRS Proceedings*, **1549** (2013).

[36] Podzorov V., Gershenson M.E., et al. High-mobility field-effect transistors based on transition metal dichalcogenides. *Applied Physics Letters*, **84** (17), P. 3301–3303 (2004).

[37] Ayari A., Cobas E., Ogundadegbe O., Fuhrere M.S. Realization and electrical characterization of ultrathin crystals of layered transition-metal dichalcogenides. *Journal of Applied Physics*, **101**, P. 014507 (2007).

[38] Kalikhman V.L., Umanskii Ya.S. Transition-metal chalcogenides with layer structures. *Soviet Physics Uspekhi*, **15** (6), P. 728–741 (1973).

[39] Kaasbjerg K., Thygesen K.S., Jacobsen K.W. Phonon-limited mobility in n-type single-layer MoS_2 from first principles. *Physical Review B*, **85** (11), P. 115317 (2012).

[40] Rouschias G. Recent advances in the chemistry of rhenium. *Chemical Reviews*, **74** (5), P. 531–566 (1974).

[41] Ramakrishna Matte H.S.S., Gomathi A., et al. MoS_2 and WS2 Analogues of Graphene. *Angewandte Chemie International Edition*, **49** (24), P. 4059–4062 (2010).

[42] Coleman J.N., Lotya M., et al. Two-Dimensional Nanosheets Produced by Liquid Exfoliation of Layered Materials. *Science*, **331** (6017), P. 568–571 (2011).

[43] Lauritsen J.V., Kibsgaard J., et al. Size-dependent structure of MoS_2 nanocrystals. *Nature Nanotechnology*, **2** (1), P. 53–58 (2007).

[44] Kim D., Sun D., et al. Toward the Growth of an Aligned Single-Layer MoS_2 Film. *Langmuir*, **27** (18), P. 11650–11653 (2011).

[45] Zhan Y., Liu Z., et al. Large-Area Vapor-Phase Growth Characterization of MoS_2 Atomic Layers on a SiO_2 Substrate. *Small*, **8** (7), P. 966–971 (2012).

[46] Lee Y.H., Zhang X.Q., et al. Synthesis of Large-Area MoS_2 Atomic Layers with Chemical Vapor Deposition. *Advanced Materials*, **24** (17), P. 2320–2325 (2012).

[47] Liu K.K., Zhang W., et al. Growth of Large-Area and Highly Crystalline MoS_2 Thin Layers on Insulating Substrates. *Nano Letters*, **12** (3), P. 1538–1544 (2012).

[48] Komsa H.P., Kotakoski J., et al. Two-Dimensional Transition Metal Dichalcogenides under Electron Irradiation: Defect Production and Doping. *Physical Review Letters*, **109**, P. 035503 (2012).

[49] Komsa H.P., Kurash S., et al. From point to extended defects in two-dimensional MoS_2: Evolution of atomic structure under electron irradiation. *Physical Review B*, **88**, P. 035301 (2013).

[50] Zhou W., Zou X., et al. Intrinsic Structural Defects in Monolayer Molybdenum Disulfide. *Nano Letters*, **13**, P. 2615–2622 (2013).

[51] Van der Zande A., Huang P.Y., et al. Grains and grain boundaries in highly crystalline monolayer molybdenum disulphide. *Nature Materials*, **12**, P. 554–561 (2013).

[52] Enyashin A.N., Bar-Sadan M., Houben L., Seifert G. Line Defects in Molybdenum Disulfide Layers. *The Journal of Physical Chemistry C*, **117**, P. 10842–10848 (2013).

[53] Bollinger M.V., Lauritsen J.V., et al. One-Dimensional Metallic Edge States in MoS_2. *Physical Review Letters*, **87**, P. 196803 (2001).

[54] Erdogan E., Popov I., Enyashin A.N., Seifert G. Transport properties of MoS_2 nanoribbons: edge priority. *European Physical Journal B*, **85** (1), P. 33 (2001).

[55] Najmaei S., Liu Z., et al. Vapour phase growth and grain boundary structure of molybdenum disulphide atomic layers. *Nature Materials*, **12**, P. 754–759 (2013).

[56] Yong K.S., Otalvaro D.M., et al. Calculation of the conductance of a finite atomic line of sulfur vacancies created on a molybdenum disulfide surface. *Physical Review B*, **77**, P. 205429 (2008).

[57] Ghorbani-Asl M., Enyashin A.N., et al. Defect-induced conductivity anisotropy in MoS_2 monolayers. *Physical Review B*, **88**, P. 245440 (2013).

[58] Deepak F.L., Popovitz-Biro R., et al. Fullerene-like $Mo(W)_{1-x}Re_xS_2$ Nanoparticles. *Chemistry — An Asian Journal*, **3**, P. 1568–1574 (2008).

[59] Yadgarov L., Stroppa D.G., et al. Investigation of Rhenium-Doped MoS_2 Nanoparticles with Fullerene-Like Structure. *Zeitschrift für Anorganische und Allgemeine Chemie*, **638** (15), P. 2610–2616 (2012).

[60] Enyashin A.N., Yadgarov L., et al. New Route for Stabilization of 1T-WS2 and MoS_2 Phases. *The Journal of Physical Chemistry C*, **115**, P. 24586–24591 (2011).

[61] Dolui K., Rungger I., Pemmaraju C.D., Sanvito S. Possible doping strategies for MoS_2 monolayers: An ab initio study. *Physical Review B*, **88**, P. 075420 (2013).

[62] Popov I., Seifert G., Tomanek D. Designing Electrical Contacts to MoS_2 Monolayers: A Computational Study. *Physical Review Letters*, **108**, P. 156802 (2012).

[63] Das S., Chen H.-Y., Penumatcha A.V., Appenzeller J. High Performance Multilayer MoS_2 Transistors with Scandium Contacs. *Nano Letters*, **13**, P. 100–105 (2013).

[64] Dolui K., Rungger I., Sanvito S. Origin of the n-type and p-type conductivity of MoS_2 monolayers on a SiO_2 substrate. *Nano Letters*, **13**, P. 100–105 (2013).

NANOSYSTEMS: PHYSICS, CHEMISTRY, MATHEMATICS, 2014, 5 (4), P. 540–545

CUBIC ORDERED MODIFICATION OF TITANIUM MONOXIDE WITH STRUCTURAL VACANCIES ON METAL AND NONMETAL SUBLATTICES: ELECTRONIC STRUCTURE AND STABILITY

M. G. Kostenko[1], A. V. Lukoyanov[2,3], V. P. Zhukov[1], A. A. Rempel[1,3*]

[1]Institute of Solid State Chemistry, Ural Branch of the Russian Academy of Sciences,
620990 Pervomayskaya 91, Ekaterinburg, Russia
[2]Institute of Metal Physics, the Ural Branch of the Russian Academy of Sciences,
620990 S. Kovalevskoy 18, Ekaterinburg, Russia
[3]Ural Federal University named after the first President of Russia B. N. Yeltsin,
620002 Mira 19, Ekaterinburg, Russia

rempel@ihim.uran.ru, tel: +7 (343) 374 73 06, fax: +7 (343) 374 44 95

PACS 61.72.Bb, 61.72.Jd, 71.20.Ps

The electronic structure of the recently suggested cubic ordered phase $Ti_5O_{5(cub.)}$ of titanium monoxide has been studied by means of accurate first-principles calculations within the density functional theory with pseudo-potential approach based on the plane wave basis. It was found that $Ti_5O_{5(cub.)}$ is the only phase of titanium monoxide without *p-d* gap in the occupied states region. In this sense, calculated DOS's of the cubic modification is closer to the experimental electronic spectrum of the ordered titanium monoxide than that of the well studied ordered monoclinic modification $Ti_5O_{5(mon.)}$. The enthalpy of formation of $Ti_5O_{5(cub.)}$ is higher than the enthalpy of $Ti_5O_{5(mon.)}$ but is less than that of the disordered cubic phase $TiO_{1.0}$.

Keywords: vacancies,ordering, titanium monoxide, electronic structure.

Received: 16 June 2014
Revised: 30 June 2014

Nonstoichiometric titanium monoxide TiO_y is a unique compound owing to (a) wide homogeneity region from $TiO_{0.7}$ to $TiO_{1.25}$, (b) high vacancy content both in metallic and nonmetallic sublattices and (c) formation of new phases under ordering of the vacancies [1–4]. The compound has a $B1$ (NaCl) type of crystal structure. At stoichiometric composition $y = 1.0$, about 16 % of the sites are vacant in every sublattice. Another compound with similar high concentration of structural vacancies in both metallic and nonmetal sublattices is vanadium monoxide VO_y, but ordering for $VO_{1.0}$ was not found [1]. With allowance for the vacancies in the sublattices, the chemical formula for titanium monoxide can be written as Ti_xO_z or $Ti_x\blacksquare_{1-x}O_z\square_{1-z}$, where x and z are the fractions of vacancies in titanium and oxygen sublattices, respectively, $\blacksquare$, $\square$ are the symbols for titanium and oxygen vacancies, respectively. The composition y in the formula TiO_y equals z/x.

Disordered cubic titanium monoxide is an equilibrium phase at the temperatures higher than 1600 K [1]. At these temperatures, the vacancies are nearly randomly distributed. Heat treatment below 1600 K leads to redistribution of the vacancies on the $B1$ lattice sites and the ordered phases form. The type of the ordered structure depends on the composition of the titanium monoxide and treatment conditions. At present, only the structures of monoclinic $Ti_5O_{5(mon.)}$ ($Ti_5\blacksquare_1O_5\square_1 \equiv Ti_{10}\blacksquare 2O_{10}\square_2$) and tetragonal Ti_4O_5 ($Ti_4\blacksquare_1O_5 \equiv Ti_8\blacksquare_2O_{10}$) phases are described fairly [1–4]. The other $B1$ derived ordered structures: cubic $Ti_5O_{5(cub.)}$, orthorhombic $Ti_3O_{2(orth.)}$ and $Ti_2O_{3(orth.)}$ are poorly studied. From the last group, the cubic $Ti_5O_{5(cub.)}$ is the most interesting superstructure, as it corresponds to the equiatomic composition and is an alternative to the well-studied monoclinic $Ti_5O_{5(mon.)}$. The unit cell of $Ti_5O_{5(mon.)}$ is shown in fig. 1.

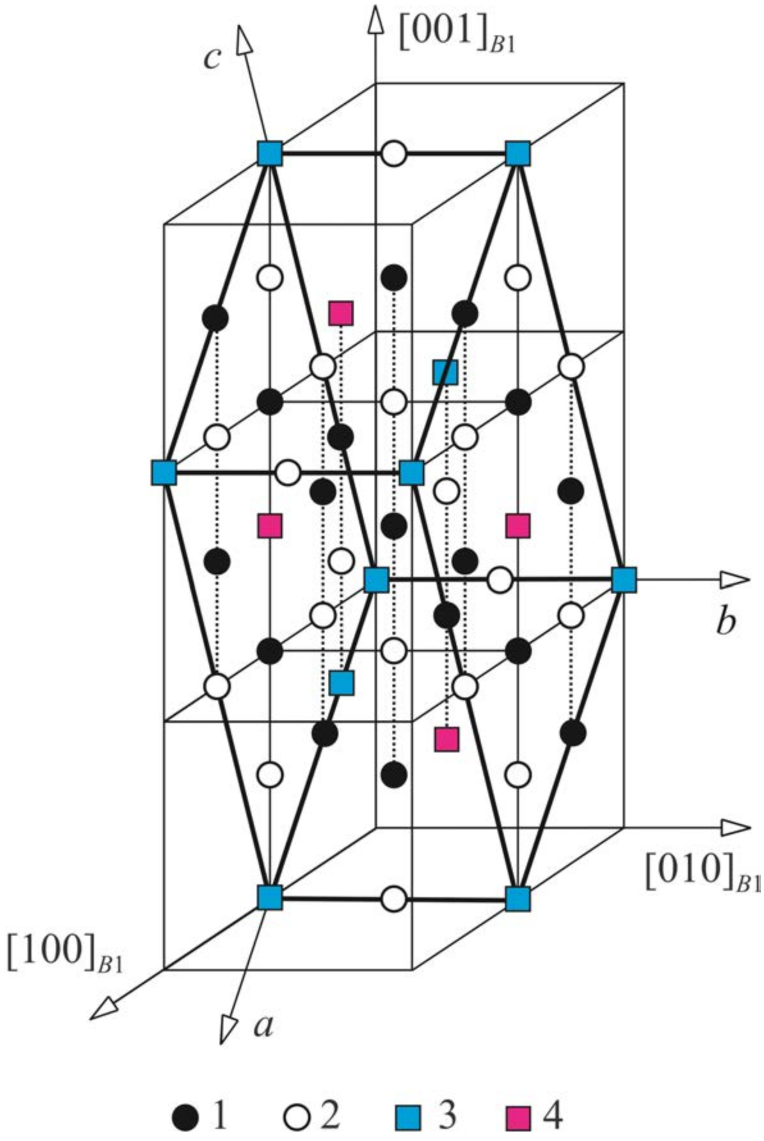

FIG. 1. Position of the monoclinic (space group C2/m (A12/m1)) unit cell in the basic B1 structure [4]: 1 — titanium, 2 — oxygen, 3 — titanium vacancy, 4 — oxygen vacancy. The axes a, b, c of the superstructure and the crystallographic directions of B1 structure are shown

The fact that the Ti–O system has an ordered phase with cubic symmetry having a composition of nearly 50 % O was noted in short report by Hilti in 1968 [5]. He pointed out that the phase has threefold lattice constant in comparison with that of $B1$ and belongs to one of the following possible space groups: $Fm3m$, $F\bar{4}3m$, $F432$, or $Fm3$. The atomic model of the cubic structure was not proposed and the distribution of vacancies in the unit cell was unknown. Since then, no attempt has been made to synthesize the cubic modification and identify its structure. The existence of the cubic modification was also ignored in numerous theoretical studies devoted to the role of vacancies in $B1$ structure and mechanism of ordering [6–9]. The experimental data [4, 10, 11] obtained for the samples of ordered phase were always interpreted using the notion of the monoclinic structure only.

The model of crystal structure for the cubic modification was proposed in 2012 [12, 13]. When analyzing the possible structure, the authors [12, 13] proceeded from two requirements: (a) the lattice constant is three times higher than that of $B1$ structure and (b) the concentration of the vacancies equals to $1/6$ in every sublattice. It was proved that these conditions cannot be satisfied for the space groups proposed earlier [5]. The only possible space group is $Pm\bar{3}m$. For this group, there are 8 variants of vacancy distributions in one of the sublattices, 5 of them implying statistical distribution. From the other 3, the even distribution has been chosen. The unit cell proposed in [12, 13] is shown in fig. 2. It contains 90 titanium atoms, 90 oxygen atoms, 18 titanium and 18 oxygen vacancies. The chemical formula can be written as $\mathrm{Ti}_{90}\blacksquare_{18}\mathrm{O}_{90}\square_{18}$.

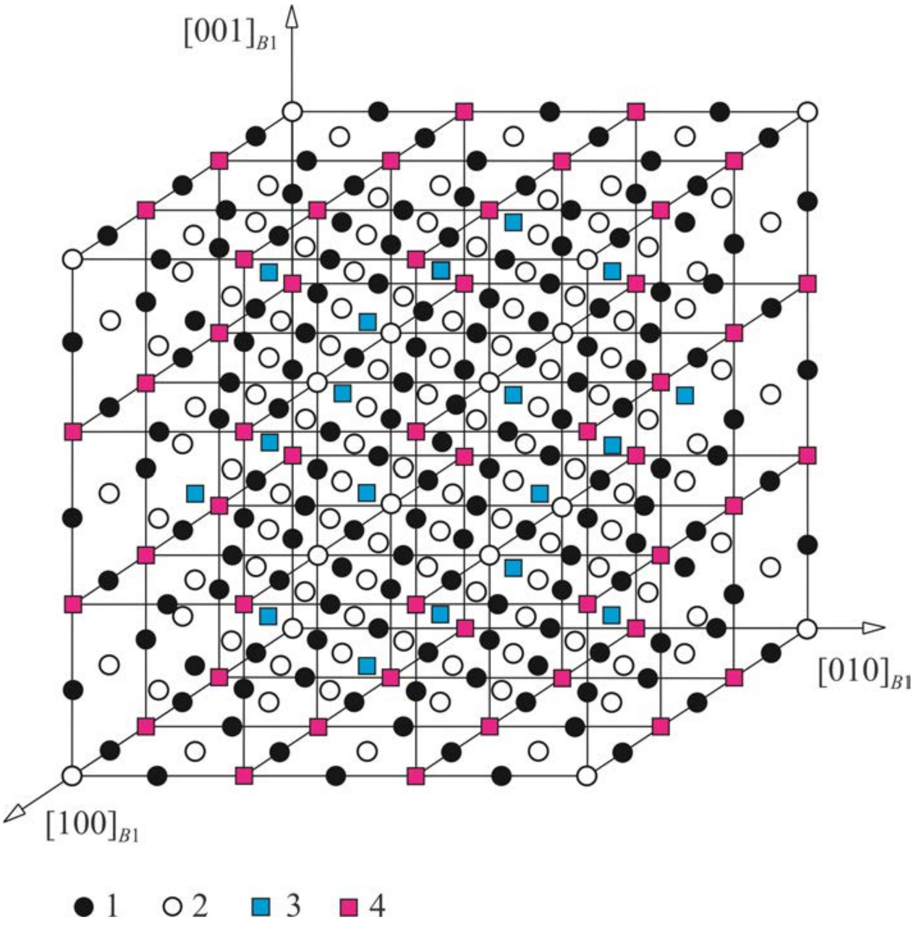

FIG. 2. Unit cell of the cubic superstructure $\mathrm{Ti}_{90}\blacksquare_{18}\mathrm{O}_{90}\square_{18}$ (space group $Pm\bar{3}m$) [12, 13]: 1 — titanium, 2 — oxygen, 3 — titanium vacancy, 4 — oxygen vacancy. The crystallographic directions of B1 structure are shown

The XRD spectrum of the cubic modification resembles one of the monoclinic phase [13]. Two phases can be reliably distinguished only with the reflections at small angles that are not seen in laboratory XRD experiments. The structure of the ordered phase obtained in [4] was identified as monoclinic from the XRD analysis. Later the samples [4] were studied with electron microdiffraction [10]. Only some of the observed superstructure reflections are referred to the monoclinic modification. In [12] it was demonstrated that all the reflections could belong to the cubic superstructure. So there could be two alternative experimentally confirmed types of vacancy ordering for the composition $y = 1.0$.

The present work is the next step in the investigation of the recently proposed cubic modification and has as its aim the theoretical study of its electronic structure and stability. Calculations were performed within the density functional theory using the generalized gradient approximation (GGA), as implemented in the PBE [14] form of exchange-correlation potential. The phase was treated with the PWSCF code of the QUANTUM-ESPRESSO package [15] based on plane waves (PW) and pseudo-potentials. Titanium $3s3p$ semi-core levels were included in the Ti pseudopotential. The lattice constant was assumed to be 417.4 pm [4]. Relaxation of the atomic positions within the cell was realized using quasi-Newton algorithm in PWSCF code. The stability of the phase was estimated by calculating the enthalpy of formation ΔH from the following equation:

$$\Delta H = k\left(E_{\mathrm{TiO}} - N_{\mathrm{Ti}}\cdot E_{\mathrm{Ti}} - \frac{1}{2}N_{\mathrm{O}}\cdot E_{\mathrm{O}_2}\right)/N, \tag{1}$$

where k is the coefficient for conversion from eV to kJ/mol, E_{TiO} is the full energy of titanium monoxide calculated for one unit cell, N_{Ti} and N_{O} are the numbers of titanium and oxygen in the cell, respectively, E_{Ti} is the energy of titanium in its ground state calculated per one atom, E_{O_2} is the energy of an oxygen molecule that includes the effect of spin polarization, N is the number of Ti-O atomic pairs in the cell.

The density of states for the ordered cubic phase is shown in fig. 3a. For comparison, the results for the ordered monoclinic phase, disordered cubic phase [16], and vacancy-free TiO are presented in figs. 3b, 3c, and 3d respectively. The low energy part of the occupied states region of all the phases generally consists of O $2p$. The Ti $3d$ states are mainly in the high energy part. Vacancy-free TiO and $\mathrm{Ti_5O}_{5(mon.)}$ have a distinct *p-d* gap between O $2p$ and Ti $3d$ peaks. Disordered cubic phase has the states with a very small density in the *p-d* gap position [16]. The gap is completely filled in $\mathrm{Ti_5O}_{5(cub.)}$. The existence of the *p-d* gap is the main discrepancy between the results of theoretical [6–9, 16, 17] and experimental [11, 17] studies. The calculations predicted the gap for $\mathrm{Ti_5O}_{5(mon.)}$, vacancy-free TiO, disordered cubic TiO_y (with a very small density of states in the gap), and also for modeled structures $\mathrm{Ti}_{10}\blacksquare_2\mathrm{O}_{12}$ and $\mathrm{Ti}_{12}\mathrm{O}_{10}\square_2$ with vacancies in one of the sublattices. Only the cubic phase is appeared to be out of this regularity. In experiments for $\mathrm{Ti_5O}_{5(mon.)}$ [11], vacancy-free TiO [11], and disordered cubic TiO_y [17] the *p-d* gap was not detected.

The present results for $\mathrm{Ti_5O}_{5(cub.)}$ demonstrate that the reason for the disagreement between theoretical and experimental findings is possibly in misconstruction of the real structures of the ordered and disordered phases. The specimens of the ordered titanium monoxide used in [11] were referred to monoclinic phase after XRD analysis. As mentioned above, electron diffraction permits cubic symmetry of ordered structure. Another possible interpretation is that the monoclinic phase [11] had imperfect long-range order. In this case, some number of vacancies out of its native positions in the superstructure could occupy the atomic positions not randomly but with some short-range order. This would lead to the situation when the occupation of the vacancies in the nearest coordination spheres of some atoms is identical to that for some atomic positions of the cubic superstructure. The influence of the gradual disordering on the electronic structure was studied in [18] but the short range order was not accounted for.

The vacancy-free TiO used in [11] is considered in [7] to contain substantial fraction of residual vacancies. The correlation between these vacancies could lead to the formation of short-range order and the filling of the *p-d* gap in the occupied states region. Hereby the allowance for the features of the real crystal and atomic structure is the crucial point for

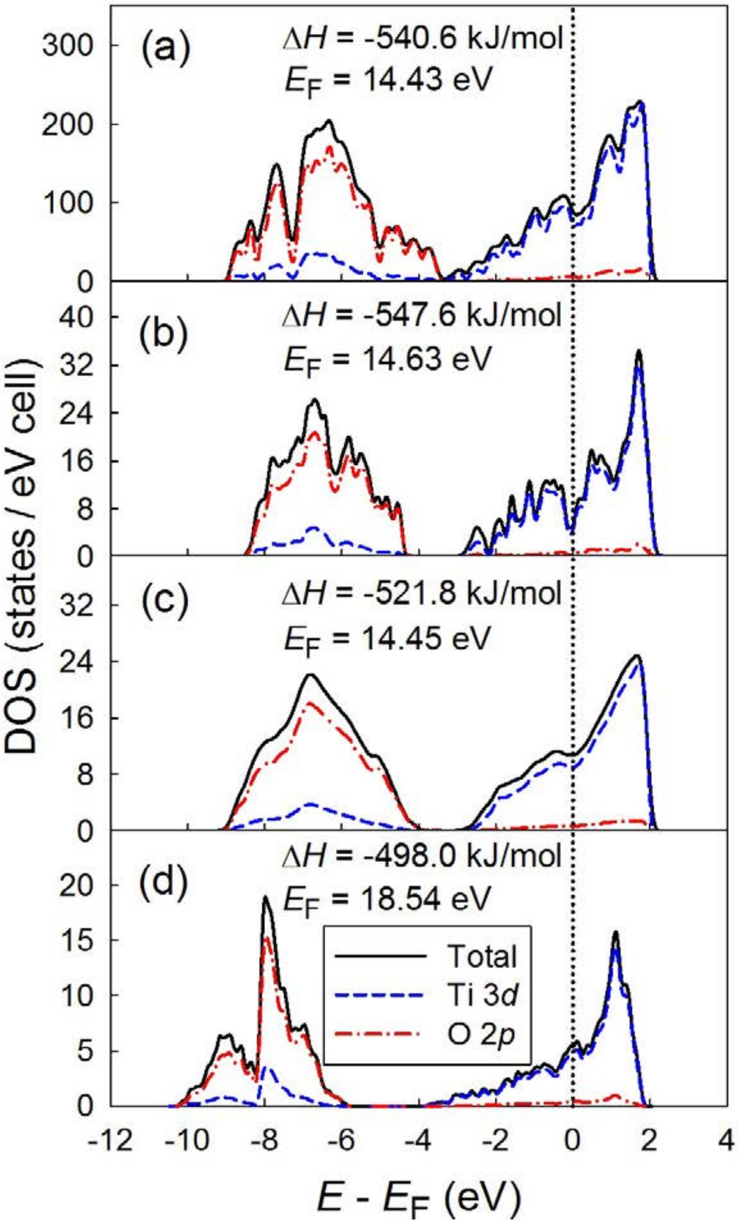

FIG. 3. Density of states calculated for (a) ordered cubic phase, (b) ordered monoclinic phase, (c) disordered cubic phase [16], and (d) vacancy-free TiO. The values of enthalpy of formation and Fermi energy are shown

correct interpretation of the experimental data. The correlations between defects in strongly nonstoichiometric compounds [1] need detailed investigation. First of all this implies modeling of the structures of the disordered and partially ordered modifications with allowance for the short-range order.

As to stability of the cubic ordered phase, the calculation of the enthalpy of formation has demonstrated (fig. 3) that $Ti_{90}\blacksquare_{18}O_{90}\square_{18}$ type of ordering is less advantageous as compared to monoclinic $Ti_{10}\blacksquare_{2}O_{10}\square_{2}$ type but preferable as compared to the disordered state. This agrees with the assertions [5, 13] that $Ti_{90}\blacksquare_{18}O_{90}\square_{18}$ is intermediate ordered modification of titanium monoxide. The existence of one more energetically favorable type of ordering in addition to monoclinic one allows us to expect that some new ordered phases of titanium monoxide can be found. In fact, the sequence of phase transition in titanium-oxygen system is poorly studied. This issue requires additional theoretical and experimental investigations. This is also true for other strongly nonstoichiometric compounds [1], especially for vanadium monoxide VO_y, for which no ordered phase for $VO_{1.0}$ has yet been found.

Acknowledgements

The authors thank A. A. Valeeva for advice provided and interest in this work. The study was financially supported by Ural Brunch of the Russian Academy of Sciences (Project No. 12-M-23-2001 and 14-31-NP-100) and by RFBR (research project No. 14-02-00636). Calculations were performed using 'Uran' supercomputer in the Institute of Mathematics and Mechanics UB RAS.

References

[1] A. I. Gusev, A. A. Rempel, A. Magerl, Disorder and Order in Strongly Non-Stoichiometric Compounds. Transition Metal Carbides, Nitrides and Oxides, Springer, Berlin (2001).
[2] D. Watanabe et al. The ordered structure of TiO. *Acta Cryst.*, **23**, P. 307 (1967).
[3] D. Watanabe, et al. Electron microscopic study on the structure of low temperature modification of titanium monoxide phase. In: L. Eyring, M. O'Keefe (Eds.). *The Chemistry of Extended Defects in Non-Metallic Solids*, North-Holland, Amsterdam, P. 238 (1970).
[4] A.A. Valeeva, A.A. Rempel, A.I. Gusev. Ordering of cubic titanium Monoxide into Monoclinic Ti_5O_5. *Inorg. Mater.*, **37** P. 603 (2001).
[5] E. Hilti. Neue phasen im System Titan-Sauerstoff. *Naturwissenschaften*, **55**, P. 130 (1968).
[6] C. Leung et al. First-principles study of titanium oxides. *Phys. Rev. B*, **54** (11), P. 7857 (1996).
[7] D.A. Andersson, P.A. Korzhavyi, B. Johansson. Thermodynamics of structural vacancies in titanium monoxide from first-principles calculations. *Phys. Rev. B*, **71**, P. 144101-1 (2005).
[8] J. Graciani, A. Márquez, Javier Fdez. Sanz. Role of vacancies in the structural stability of a–TiO: A first-principles study based on density-functional calculations. *Phys. Rev. B*, **72**, P. 054117 (2005).
[9] M.G. Kostenko et al. Vacancies in ordered and disordered titanium monoxide: Mechanism of B1 structure stabilization. *J. Sol. State Chem.*, **204**, P. 146 (2013).
[10] A.A. Valeeva et al. Identification of atomic Vacancies in titanium monoxide by electron microdiffraction and positron annihilation. *Phys. Stat. Sol.*, **224** (b), R1 (2001).
[11] S. Bartkowski et al. Electron structure of titanium monoxide. *Phys. Rev. B*, **56**, P. 10656 (1997).
[12] A.I. Gusev, A.A. Valeeva. Diffraction of electrons in the cubic Ti_5O_5 superstructure of titanium monoxide. *JETP Letters*, **96** (6), P. 364 (2012).
[13] A.I. Gusev. New cubic superstructure of titanuim monoxide with double structure imperfection. *J. Sol. State Chem.*, **199**, P. 181 (2013).
[14] J.P. Perdew, et al., Generalized gradient approximation made simple. *Phys. Rev. Lett.*, **77**, P. 3865 (1996).
[15] P. Giannozzi, et al. Quantum espresso: a modular and open-sourse software project for quantum simulation of materials. *J. Phys. Condens. Matter*, **21**, P. 395502 (2009).
[16] M.G. Kostenko, et al. Electronic structure of disordered titanium monoxide TiO_y dependind on stoichiometry. *JETP Letters*, **95** (12), P. 647 (2012).
[17] M.A. Korotin, et al. *JETP Letters*, **95** (12), P. 641 (2012).
[18] M.G. Kostenko et al. Effect of the long-range order in the vacancy distribution on the electronic structure of titanium monoxide $TiO_{0.1}$. *JETP Letters*, **96** (8), P. 507 (2012).

NANOSYSTEMS: PHYSICS, CHEMISTRY, MATHEMATICS, 2014, 5 (4), P. 546–552

RELATIONS BETWEEN ACTIVATION ENERGIES FOR NUCLEATION AND OF GROWTH OF CRYSTALS

O. D. Linnikov

Institute of Solid State Chemistry, Ural Branch of the Russian Academy of Sciences,
Ekaterinburg, Russia

linnikov@mail.ru

PACS 81.10 Dn

The attempt to consider the influence of particle solvation of dissolved substances on the nucleation and growth of crystals during crystallization from solutions in classical thermodynamic theory of nucleation has been undertaken. A number of interesting relations between the activation energies of nucleation and of crystal growth are obtained. Comparison to the published literature data is carried out.

Keywords: activation energy, solvation, nucleation, growth of crystals, solution, dissolved substance, hydration.

Received: 16 June 2014

Revised: 30 June 2014

According to classical thermodynamic theory, the rate of nucleation of new phase in the volume of metastable (mother) phase is a fluctuating process and is directly proportional to concentration of critical nuclei of the appearing new phase [1–8]:

$$J = Z \cdot \omega \cdot n_c^*, \tag{1}$$

$$n_c^* = n^* \exp\left(-\frac{A_c}{k_B T}\right), \tag{2}$$

$$A_c = \frac{4}{3}\pi R_c^2 \sigma, \tag{3}$$

where J is the rate of nucleation in the volume of vapor, of gas, of melt or of solution, $\mathrm{s}^{-1}\cdot\mathrm{m}^{-3}$; Z is the nonequilibrium factor of Zeldovich; ω is the frequency of addition of particles of crystallizing substance to critical nuclei (after that, the nuclei transform into stable crystallization growth centers), s^{-1}; n_c^* is the concentration of critical nuclei of new phase, m^{-3}; n^* is the concentration of particles of crystallizing substance in supersaturated mother phase, m^{-3}; k_B – is Boltzmann constant, J/K; T is the temperature, K; A_c is the work of formation of critical nucleus of new phase, J; R_c is the radius of critical nucleus of new phase, m; σ is the specific surface energy (the surface tension), $\mathrm{J/m}^2$.

Equations (1)–(3) are correct for crystallization from vapor and gas phases. There is great interest present on the question of changing these equations of classical thermodynamic theory and applying them to crystallization from solution, if in the first approximation one takes into account hydration (for nonaqueous solution – solvation) of particles of crystallizing substance in solution. From first principles, for more clear detection of differences in crystallization processes for various condensed media, we will consider process of nucleation in molecular melts. It should be noted that usually the equations of classical nucleation theory describing nucleation from vapor and gas phases automatically, almost without changing, with little limitation, translate to crystallization in condensed media. It is clear, this is not completely right. Moreover, in the explicit form, the direct registration of nucleation differences in condensed media from nucleation in vapor and gas phases has not still been done. Below, we make an attempt to bridge this gap (in the first very rough approximation).

So, in the formation of a new phase in molecular melts (i.e. solidification of such melt), as opposed to crystallization from the vapor and gas phase, it is necessary to take into account the additional energy barrier that is specified with overcoming by particles of crystallizing substance of intermolecular forces connecting them with a melt. In other words, it is necessary to take into account the diffusion of particles of crystallizing substance in a melt. Therefore, Eq. (2) must be transformed into the form:

$$n_c^* = n^* \exp\left(-\frac{A_c}{k_B T}\right) \exp\left(-\frac{E_D}{RT}\right), \tag{4}$$

where E_D is the activation energy of diffusion of crystallizing substance in the volume of condensed medium, J/mol; R is the universal gas constant, J/(K·mol).

If the nucleus of new phase has form of a sphere with radius R_c, then for crystallization in a molecular melt, factor ω in Eq. (1) is defined by the equation [2,5]:

$$\omega = 4\pi R_c^2 K_n n^* a f_0 \exp\left(-\frac{E_D}{RT}\right), \tag{5}$$

where K_n is the coefficient of proportionality involving steric factor (the probability of suitable particle orientation) and others unaccounted factors; a is the length of diffusion jump of the particle of crystallizing substance, m; f_0 is the frequency of thermal vibrations of the particle of crystallizing substance, s^{-1}.

The radius of critical nucleus can be found using Gibbs-Thomson relationship [3–8]:

$$R_c = \frac{2\sigma \cdot \Omega}{k_B N_A T \ln\left(\frac{n^*}{n_0^*}\right)}, \tag{6}$$

where Ω is the volume of one mole of the nucleus substance, m^3/mol; n_0^* is the equilibrium concentration of particles of crystallizing substance in mother phase at given temperature, m^{-3}; N_A is the Avogadro's number, mol^{-1}.

Taking into account Eqs. (1)–(6), one can find the equation for nucleation rate in molecular melts:

$$J = \frac{16 Z \pi a f_0 K_n \sigma^2 \Omega^2 \cdot (n^*)^2}{(RT)^2 \ln^2\left(\frac{n^*}{n_0^*}\right)} \exp\left(-\frac{E_1}{RT}\right) \exp\left(-\frac{16\pi N_A \sigma^3 \Omega^2}{3(RT)^3 \ln^2\left(\frac{n^*}{n_0^*}\right)}\right), \tag{7}$$

where $R = k_B N_A$; E_1 is the activation energy of nucleation process in the volume of condensed phases, J/mol, as is seen, for molecular melts $E_1 = 2E_D$.

For the transition from molecular melts to the aqueous (and non-aqueous) solutions of inorganic salts it is necessary to take into account that in such solutions the crystallizing (dissolved) substance is in the form of hydrated (solvated) molecules and ions. Hence, an attachment of molecule or ion to the critical nucleus (and also formation of the critical nucleus) will be apparently connected with overcoming an additional potential barrier that is specified by hydration (solvation) of molecules and ions of dissolved substance in solution.

It is known that dissolution of solid substances in liquids and, particularly, of inorganic salts, is caused by interaction of molecules of solvent with molecules and ions of soluble substance. This brings a reduction of intermolecular interactions and links between ions in solid substance. As a result, molecules and ions of solid substance begin to pass into solution, and the solid substance dissolves. Under such conditions, the molecules and ions of dissolved substance in solution are hydrated and solvated, i.e. are surrounded by shell of solvent molecules. Therefore, for reverse transfer from the liquid phase into the solid one they must drop this shell. Last is connected with overcoming corresponding potential barrier. Hence, the attachment of molecules and of ions of dissolved substance to a critical nucleus (and also formation of the critical nucleus) will be possible only after their partial (or full) dehydration (desolvation). Thus, new additional factors it is necessary to introduce into Eqs. (4) and (5):

$$n_c^* = n^* \exp\left(-\frac{A_c}{k_B T}\right) \exp\left(-\frac{E_D}{RT}\right) \exp\left(-\frac{E_{ds}}{RT}\right), \tag{8}$$

$$\omega = 4\pi R_c^2 K_n n^* a f_0 \exp\left(-\frac{E_D}{RT}\right) \exp\left(-\frac{E_{ds}}{RT}\right), \tag{9}$$

where E_{ds} is the energy of dehydration (desolvation) of particles of dissolved substance at their transition from the volume of liquid phase into solid one, J/mol.

If one considers that $n^* = [C] \cdot 10^3 \cdot N_A$, where $[C]$ is the molar concentration (mol/l) of a supersaturated solution of crystallizing substance then one can find the equation for the rate of nucleation in a salt solution:

$$J = \frac{16 \cdot 10^6 Z \pi a f_0 K_n \sigma^2 \Omega^2 N_A^2 [C]^2}{(RT)^2 \ln^2\left(\frac{[C]}{[C_0]}\right)} \exp\left(-\frac{E_1}{RT}\right) \exp\left(-\frac{16\pi N_A \sigma^3 \Omega^2}{3(RT)^3 \ln^2\left(\frac{[C]}{[C_0]}\right)}\right), \tag{10}$$

where $E_1 = 2(E_D + E_{ds})$.

Now let's examine a process of heterogeneous nucleation on foreign and the crystallizing substrates. So, the rate of surface nucleation on a foreign substrate and the concentration of critical nuclei on the surface of the substrate, according to approved assumptions, are defined by expressions:

$$J_S = Z \cdot \omega_S \cdot n_{cs}^*, \tag{11}$$

$$n_{cs}^* = n_s^* \exp\left(-\frac{A_c}{k_B T}\right) \exp\left(-\frac{E_{DS}}{RT}\right) \exp\left(-\frac{E_{dsad}}{RT}\right), \tag{12}$$

where J_S is the rate of surface nucleation on a foreign substrate, $\text{s}^{-1} \cdot \text{m}^{-2}$; ω_S is the frequency of attachment of particles of crystallizing substance to critical nuclei on the surface of the substrate (after this the critical nuclei transform into stable growing centers of crystallization), s^{-1}; n_{cs}^* is the concentration of critical nuclei on the surface of the substrate, m^{-2}; n_s^* is the concentration of particles of dissolved substance adsorbed on the surface of the substrate, m^{-2}; E_{DS} is the activation energy of surface diffusion of particles of crystallizing substance along the surface of the substrate, J/mol; E_{dsad} is the energy of dehydration (desolvation) of particles of crystallizing substance at their attachment from adsorbed layer on the surface of the substance to critical nucleus, J/mol.

Note, that according to the classical theory of nucleation, [3, 5] Eq. (11) supposes that critical nuclei arise from particles of crystallizing substance adsorbed onto the surface of a substrate.

With heterogeneous nucleation, as with nucleation in a volume, the formed nuclei of critical size will transform into centers of crystallization and maintain their strong growth only after attachment to at least of one particle (molecule or ion) of crystallizing substance. However, as opposed to homogeneous nucleation, in present case, this attachment can proceed in two ways [5]: (1) due to the connection of particles (molecules or ions) of the dissolved (crystallizing) substance from the volume of solution and (2) by means of addition of particles (molecules or ions) of the dissolved (crystallizing) substance adsorbed on the surface of the substrate and their subsequent surface diffusion to the formed nucleus of new phase.

If with nucleation on a foreign substrate, the critical nucleus has a ball segment form and its subsequent growth proceeds due to the attachment of particles (molecules or ions) of the dissolved (crystallizing) substance from the volume of solution, then, according to [5] and accepted assumptions, Eq. (9) becomes:

$$\omega_S = 2\pi R_c^2(1-\cos\theta)K_n n^* a f_0 \exp\left(-\frac{E_D}{RT}\right)\exp\left(-\frac{E_{ds}}{RT}\right). \tag{13}$$

If subsequent growth of the critical nucleus proceeds by means of attachment of particles (molecules or ions) of the dissolved (crystallizing) substance adsorbed on the surface of the substrate, then one can obtain by analogy the following:

$$\omega_S = 2\pi R_c \sin\theta \cdot K_n n_s^* a f_0 \exp\left(-\frac{E_{DS}}{RT}\right)\exp\left(-\frac{E_{dsad}}{RT}\right). \tag{14}$$

In the first approximation, one can also take that:

$$n_s^* = K_{na}\cdot n^* \cdot \exp\left(-\frac{E_D}{RT}\right)\exp\left(-\frac{E_{dsa}}{RT}\right), \tag{15}$$

where K_{na} is the coefficient of proportionality; E_{dsa} is the energy of dehydration (desolvation) of particles of crystallizing substance at their adsorption on the surface of the substrate (at transition from the volume of liquid phase on the surface of the substrate), J/mol. Obviously, $E_{ds} = E_{dsa} + E_{dsad}$.

Then, after corresponding substitutions, the equation describing the rate of heterogeneous nucleation on a foreign substrate in solution may be obtained:

$$J_S = \frac{8\cdot 10^6 Z\pi a f_0(1-\cos\theta)K_n K_{na}\sigma^2\Omega^2 N_A^2[C]^2}{(RT)^2\ln^2\left(\frac{[C]}{[C_0]}\right)}\exp\left(-\frac{E_2}{RT}\right)\exp\left(-\frac{16\pi N_A\sigma_{ef}^3\Omega^2}{3(RT)^3\ln^2\left(\frac{[C]}{[C_0]}\right)}\right), \tag{16}$$

$$J_S = \frac{4\cdot 10^6 Z\pi a f_0 \sin\theta\cdot K_n K_{na}^2\sigma\Omega N_A^2[C]^2}{RT\ln\left(\frac{[C]}{[C_0]}\right)}\exp\left(-\frac{E_3}{RT}\right)\exp\left(-\frac{16\pi N_A\sigma_{ef}^3\Omega^2}{3(RT)^3\ln^2\left(\frac{[C]}{[C_0]}\right)}\right), \tag{17}$$

where $E_2 = 2(E_D + E_{ds}) + E_{DS}$ is the activation energy of the surface nucleation at growth of critical nucleus due to the attachment of particles (molecules or ions) of the dissolved (crystallizing) substance from the volume of solution, J/mol; $E_3 = 2(E_D + E_{DS} + E_{ds})$ is the activation energy of surface nucleation at growth of critical nucleus by means of connection of particles (molecules or ions) of the dissolved (crystallizing) substance adsorbed on the surface of the substrate, J/mol; σ_{ef} is the efficient specific surface energy, J/m^2 [3–6].

As is seen, if our assumptions are true, then $E_3 = E_2 + E_{DS}$. From this, it follows that due to lower activation energy, heterogeneous nucleation in solutions must proceed predominantly by means particles (molecules or ions) attachment of the dissolved (crystallizing) substance from the volume of solution.

Heterogeneous nucleation on the crystallizing substrate, in contrast to heterogeneous nucleation on foreign substrate, proceeds due to the formation not three-dimensional but two-dimensional nuclei, not the analogous three-dimensional particles [3–8]. In the case, if the critical nucleus has the form of a disk, its radius (R_{cs}) and the work of formation (A_{cs}) are [3–8]:

$$R_{cs} = \frac{\sigma \cdot \Omega}{RT \ln\left(\frac{n^*}{n_0^*}\right)}, \tag{18}$$

$$A_{cs} = \frac{\pi \cdot \Omega \sigma^2 a_0}{RT \ln\left(\frac{n^*}{n_0^*}\right)}, \tag{19}$$

where a_0 is the parameter of crystal lattice of crystallizing substance, m.

Similarly, as before, one can propose that the surface nucleation on the crystallizing substrate may occur in two ways: (1) due to the attachment of particles of the crystallizing substance from the volume of solution and (2) by means of addition of adsorbed on the surface of the substrate particles of the crystallizing substance. Corresponding substitutions give equations for the rate of nucleation on the crystallizing substrate:

$$J_S^* = \frac{2 \cdot 10^6 Z\pi a f_0 (1-\cos\theta) K_n K_{na} \sigma^2 \Omega^2 N_A^2 [C]^2}{(RT)^2 \ln^2\left(\frac{[C]}{[C_0]}\right)} \exp\left(-\frac{E_2}{RT}\right) \exp\left(-\frac{a_0 \pi N_A \sigma^2 \Omega}{(RT)^2 \ln\left(\frac{[C]}{[C_0]}\right)}\right), \tag{20}$$

$$J_S^* = \frac{2 \cdot 10^6 Z\pi a f_0 \sin\theta \cdot K_n K_{na}^2 \sigma \Omega N_A^2 [C]^2}{RT \ln\left(\frac{[C]}{[C_0]}\right)} \exp\left(-\frac{E_3}{RT}\right) \exp\left(-\frac{a_0 \pi N_A \sigma^2 \Omega}{(RT)^2 \ln\left(\frac{[C]}{[C_0]}\right)}\right). \tag{21}$$

Now, we consider the growth of crystals (the kinetic mode, when diffusion is negligible). In the case of atomically roughened crystal faces and normal growth mechanism, the particles of the crystallizing substance can attach to the growing crystal at any point on its surface, and the crystal growth rate is described by the first order equation related to the supersaturation of a solution [5]:

$$V = k_1 \exp\left(-\frac{E_4}{RT}\right)([C] - [C_0]), \tag{22}$$

where V is the linear growth rate of a face of a crystal, m/s; k_1 is the coefficient of proportionality; E_4 is the activation energy of the normal mechanism of crystal growth process, J/mol.

It is obvious, that if crystals have atomically roughened faces, then the particles of the crystallizing substance, before being incorporated into the crystal lattice of growing crystal, as for nucleus formation, in the beginning, must carry out a diffusion jump from the volume of a liquid phase to a kink in the surface of the crystal, and after that, to drop the surrounding shell of solvent molecules. Then, it should be expected that:

$$E_4 = E_D + E_{ds}. \tag{23}$$

With the dislocation growth mechanism of crystal faces and low supersaturation of solution [5]:

$$V = k_2 \exp\left(-\frac{E_5}{RT}\right)([C]-[C_0])^2, \tag{24}$$

where k_2 is the coefficient of proportionality; E_5 is the activation energy of the dislocation mechanism of crystal growth process, J/mol.

In the dislocation mechanism of crystal growth, similarly to the heterogeneous nucleation process, the incorporation of crystallizing substance particles into the lattice of the growing crystal can occur in two ways: (1) due to the direct attachment of the particles of crystallizing substance from the volume of solution and (2) by means of incorporation of particles of the crystallizing substance adsorbed on the crystal surface and their subsequent surface diffusion to the steps of growth. In the first way the activation energy of the crystal growth process must be also described by Eq. (23) (i.e. $E_5 = E_4$), in the second way, taking into account the process of the surface diffusion, one may obtain:

$$E_5 = E_D + E_{DS} + E_{dsad} + E_{dsa} = E_D + E_{DS} + E_{ds} = E_4 + E_{DS}. \tag{25}$$

If the assumptions we make are true, then it may be found the next relations among the activation energies of growth and nucleation processes of crystals:

$$E_1 = 2E_D + 2E_{ds} = 2E_4, \tag{26}$$

$$E_2 = 2(E_D + E_{ds}) + E_{DS} = 2E_4 + E_{DS} \approx 2E_4. \tag{27}$$

From the above expressions, it follows that the activation energy of homogeneous nucleation in molecular melts [please see Eq. (7)] must be equal to the doubled activation energy of diffusion of particles of crystallizing substance in the volume of the melt, and heterogeneous nucleation and growth of crystals in solution occur mainly by attachment of crystallizing substance particles directly from the volume of solution, since the activation energy of these processes are below the activation energy for the attachment of crystallizing substance particles from an adsorbed layer onto the surface of a crystal or substrate. Besides, processes of heterogeneous nucleation on foreign and similar substrates must have almost equal activation energies.

It is interesting to compare the obtained relations with published experimental data. Unfortunately, there are few published results allowing us to test this [9–13].

In two of our previous papers [9, 10], it was shown that the rates of heterogeneous nucleation of calcium sulphate on a foreign substrate (stainless steel) and on the same substrate are really best described by Eqs. (16) and (20), and their activation energies are almost identical. So, according to [9, 10], the activation energy of nucleation of calcium sulphate on the surface of stainless steel (a foreign substrate) is 100.9±15.6 kJ/mol, and on itself – 139.4±40.8 kJ/mol (the significance level is 0.05). As is seen, within the limits of experimental error, they coincide. Next, the activation energy for the process of dislocation growth (the quadratic dependence of the growth rate on supersaturation of solution) of the crystal face (120) of gypsum crystals was 59.1±7.8 kJ/mol (the significance level was 0.05) [10]. This also confirms the above-obtained relation (27): $E_2 = 139.4 \pm 40.8$ kJ/mol $\approx 2E_4 = 2 \times (59.1 \pm 7.8)$ kJ/mol $= 118.2 \pm 15.6$ kJ/mol.

In [11], the energies of hydration for KCl and NaCl were calculated by the method of thermodynamic cycle and are 60.8 – 61.5 kJ/mol and 47.4 – 47.8 kJ/mol, respectively. Experimental data on the activation energies for normal growth processes of KCl and NaCl crystals in spontaneous crystallization of these salts from aqueous solutions were found in works [12, 13]. They are 61.8 – 65.2 kJ/mol [12] and 49.1±5.9 kJ/mol respectively [13]. Meanwhile, according to Eq. (23) the activation energy of process of growth of crystals at normal mechanism must be approximately equal to the dehydration energy for the salt [the activation energy of diffusion in water solution has value about several kJ/mol, therefore, it may be omitted in Eq. (23)]. It is seen, from published data of works [11–13], the surprisingly precise realization of this relationship is observed.

References

[1] Volmer M. *Kinetic der Phasenbildung*. Steinkopff, Leipzig. 1939.

[2] Frenkel Ya.I. *Kinetic Theory of Liquids*. Nauka, Leningrad. 1975 (in Russian).

[3] Hirth J.P., Pound G.M. Condensation and evaporation: Nucleation and Growth Kinetics. *Progress in materials science*, **11**. Pergamon Press, Oxford, London, Paris, Frankfurt, 1963.

[4] Anisimov M.P. Nucleation: Theory and Experiment. *Russ. Chem.Rev.*, **72**, P. 591 (2003).

[5] Chernov A.A., Givargizov E.I., et al. *Modern Crystallography*. Nauka, Moscow, Vol. 2, 1980 (in Russian). (

[6] Sangwal K. *Etching of crystals: Theory, Experiment, and Application*. North-Holland, Amsterdam, Oxford, New York, Tokio, 1987.

[7] Mullin J.W. *Crystallization* (4th ed.). Butterworth-Heinemann, Oxford, 2001, 594 p.

[8] Strickland-Constable R.F. *Kinetics and mechanism of crystallization*. Academic Press, London and New York, 1968.

[9] Linnikov O.D. Investigation of the initial period of sulphate scale formation. Part 1. Kinetics and mechanism of calcium sulphate surface nucleation at its crystallization on a heat-exchange surface. *Desalination*, **122**,P. 1–13 (1999).

[10] Linnikov O.D. Investigation of the initial period of sulphate scale formation. Part 2. Kinetics of calcium sulphate surface crystal growth at its crystallization on a heat-exchange surface. *Desalination*, **128**, P. 35–46 (2000).

[11] Goroshchenko Ya.G., Kuprina R.V. Calculation of energies of hydration and of dissociation of chlorides of lithium, sodium and potassium in aqueous solutions. *J. Phys. Chem.*, **57** (1), P. 54–57 (1983)(in Russian).

[12] Linnikov O.D. Spontaneous crystallization of potassium chloride from aqueous and aqueous-ethanol solutions. Part 1: Kinetics and mechanism of the crystallization process. *Crystal Research and Technology*, **39** (6), P. 516–528 (2004).

[13] Linnikov O.D. Spontaneous crystallization of sodium chloride from aqueous-ethanol solutions. Part 1. Kinetics and mechanism of the crystallization process. *Crystal Research and Technology*, **41** (1), P. 10–17 (2006).

NANOSYSTEMS: PHYSICS, CHEMISTRY, MATHEMATICS, 2014, 5 (4), P. 553–563

SYNTHESIS AND PHOTOCATALYTIC ACTIVITY OF QUASI-ONE-DIMENSIONAL (1-D) SOLID SOLUTIONS $\mathbf{Ti_{1-x}M_xO_{2-2x/2}}$ (M(III)= Fe(III), Ce(III), Er(III), Tb(III), Eu(III), Nd(III) and Sm(III), $0 \leq x \leq 0.1$)

E. V. Polyakov, V. N. Krasilnikov, O. I. Gyrdasova, L. Yu. Buldakova, M. Yu. Yanchenko

Institute of Solid State Chemistry UB RAS, str. Pervomajskaya, 91,
620990,Ekaterinburg, Russia

Polyakov@ihim.uran.ru, tel.: +7 343 3744814, fax.: +7 343 3744495

PACS 82.33.Pt, 82.50.-m

Quasi-one-dimensional (1–D) solid solutions $\mathrm{Ti_{1-x}M_xO_{2-x/2}}$ (M(III)=Fe(III), Ce(III), Er(III), Tb(III), Eu(III), Nd(III), Sm(III), $0 < x \leq 0.1$) with the anatase structure have been synthesized by heating glycolate $\mathrm{Ti_{1-x}M_x(OCH_2CH_2O)_{2-x/2}}$ in air at a temperature above 450 °C. A method was proposed for the production of iron-and carbon-doped titanium dioxide with the anatase structure $\mathrm{Ti_{1-x}Fe_xO_{(2-x/2)-y}C_y}$ and of composites based thereon containing an excessive carbon content. It was shown that the oxide solid solutions exhibit photocatalytic activity in the hydroquinone photooxidation reaction during irradiation in the ultraviolet spectrum. A correlation was established between the hydroquinone oxidation rate and the concentration of the substituting ions 'M' in the catalyst. In the framework of the theory of ion-covalent binary solid solutions, a correlation was found between the energy of the photocatalytic reaction and the estimated mixing enthalpy of binary solid solutions formation.

Keywords: glycolates, three-charged cations, anatase, synthesis, photocatalytic properties.

Received: 16 June 2014
Revised: 30 June 2014

1. Introduction

Titanium oxides are the basis of advanced ceramics, pigments, membranes, sorbents, phosphors, and catalysts, including materials for direct decomposition of water under exposure to light and for photocatalytic oxidation of organic substances [1]. The drawback of powdered titanium oxide as a photocatalyst is its relatively high recombination rate of electron-hole pairs and consequently a low quantum yield for photooxidation. Improvement of photocatalytic properties of $\mathrm{TiO_2}$ and its derivative composites is an important problem of materials science since these are environmentally-friendly and easily-produced materials. The activity of $\mathrm{TiO_2}$-based photocatalysts depends on the acid-base properties of materials, the morphology of constituent particles, and on the nature of the photocatalytic reactions [2, 3]. Attempts to enhance the photocatalytic characteristics of $\mathrm{TiO_2}$ were directed at controlling its phase composition by temperature treatment, doping with transition metal or non-metal ions, or by modification of the bulk and surface properties of titania by semiconducting phases of other oxide compounds or coloring agents to improve the spectral properties of the photocatalyst [1–18]. Recently, numerous studies of nano-sized extended (quasi-one-dimensional) morphological analogues of powdered titanium oxide (wires, whiskers, tubes) were performed. Theoretical analysis of the electronic structure of quasi-one-dimensional titanium oxides predicts that unusual catalytic properties can appear for these materials as a result of varying their morphology and chemical composition [1–11]. These approaches for shifting the oxides' photoactivity from the typical ultraviolet spectrum to the visible region holds a special place in the investigations of quasi-one-dimensional titanium oxides. An efficient method for the synthesis of nanodispersed quasi-one-dimensional TiO_2 is the so-called precursor technique, based on pseudomorphic transformation of the precursor into oxide during heating [12–15]. A bathochromic shift of photocatalytic activity of titanium dioxide from the ultraviolet to visible spectrum is the main objective of titania doping with d-, f-elements, halogens, boron, carbon, nitrogen, bismuth, and sulfur [2, 16–21]. For example, these problems were comprehensively solved by employing the glycolate $\mathrm{Ti_{1-x}V_x(OCH_2CH_2O)_2}$ as a precursor of doped titania. Namely, a quasi-one-dimensional anatase of the compositions $\mathrm{Ti_{1-x}V_xO_2}$ and $\mathrm{Ti_{1-x}V_xO_{2-y}C_y}$ was synthesized, which has a high photocatalytic activity in the oxidation of hydroquinone in an aqueous solution during irradiation both in the ultraviolet and visible (blue) regions [22, 23]. Solid solutions of the compositions $\mathrm{Ti_{1-x}Ce_xO_2}$ and $\mathrm{Ti_{1-x}Ln_xO_{2-x/2}}$, where Ln is Nd, Sm, Eu, Tb, Er or Yb, having aggregates of different morphology [24, 25], have been also synthesized by thermolysis of $\mathrm{Ti_{1-x}Ln_x(OCH_2CH_2O)_{2-x/2}}$, but the anticipated high activity of $\mathrm{Ti_{1-x}Ln_xO_{2-x/2}}$ in the photocatalytic oxidation of hydroquinone was not reached. In contrast, it was reported [3, 19, 25, 26] that the introduction of Fe(III) cations into the structure of TiO_2 grains can increase its catalytic activity in the photooxidation of toxic organic compounds and even shift it into the visible region. At the same time, no data on the synthesis and photocatalytic activity of quasi-one-dimensional (1-D) iron-doped titanium dioxide are available in the literature. Therefore, the main aims of our work were the preparation of elongated fibers of Fe(III)-doped titanium dioxide $\mathrm{Ti_{1-x}Fe_xO_{2-x/2}}$ and comparison of its photocatalytic activity with that of morphologically similar lanthanide-substituted solid solutions in the titanium oxide phase using the hydroquinone oxidation reaction in water as an example, as well as elucidation of the reasons for the change of the catalytic activity of titanium oxides in the series of tricharged doped cations.

2. Experimental

2.1. Materials and Synthesis

All the reagents were analytically pure and were used in the experiment without further purification.

$\mathrm{Ti_{1-x}Fe_xO_{2-x/2}}$ was synthesized by the precursor method [14, 15] using the glycolate $\mathrm{Ti_{1-x}Fe_x(OCH_2CH_2O)_{2-x/2}}$ as a precursor, which was produced in the reaction:

$$\mathrm{(1-x)Ti(OH)_4 + xFe(OH)_3 + (2-x/2)HOCH_2CH_2O =} \\ \mathrm{Ti_{1-x}Fe_x(OCH_2CH_2O)_{2-x/2} + (4-x/2)H_2O.} \quad (1)$$

Ti(IV) and Fe(III) hydroxides required for reaction (1) were obtained by co-precipitation from aqueous solutions $\mathrm{TiOSO_4 \cdot 2H_2O}$ and $\mathrm{Fe_2(SO_4)_3 \cdot 9H_2O}$ (p.a.) with addition of an aqeous solution of ammonia to pH 7.5 to 8. The precipitates were washed with distilled water until a negative reaction to $\mathrm{SO_4^{2-}}$ ions was reached both in rinsing water and in the precipitates, then they were partially dehydrated on a vacuum filter and were mixed with ethylene glycol (p.a.) in a molar ratio $\mathrm{Ti(OH)_4}$, $\mathrm{Fe(OH)_3/HOCH_2CH_2OH} = 1/50$. The resulting mixtures were heated in 250 ml heat-resistant cone flasks at temperatures below the ethylene glycol boiling point (197.6 °C) for 2 to 5 h. Since ethylene glycol was used simultaneously as a reactant and a reaction medium, it was taken in excess with respect to reaction (1) of the titanium and iron hydroxides transformation. $\mathrm{Ti_{1-x}Fe_x(OCH_2CH_2O)_{2-x/2}}$ precipitate was crystallized in a supersaturated solution by evaporation of excess ethylene glycol. The resulting precipitates

$\mathrm{Ti_{1-x}Fe_x(OCH_2CH_2O)_{2-x/2}}$ were separated from excessive unreacted ethylene glycol by vacuum filtration, then were washed with acetone and dried at a temperature of about 50 °C to remove residual acetone. Finally, they were placed into airtight weighing bottles for storage. In order to compare the effect of tricharged cations on the photocatalytic properties of doped titania, we have synthesized the samples of glycolates of some rare-earth elements with a fixed concentration of the dopant, $\mathrm{Ti_{1-x}Ln_x(OCH_2CH_2O)_{2-x/2}}$, where Ln is Nd, Sm, Eu, Tb, or Er and $\mathrm{x} = 0.025$. In addition, the cerium-substituted glycolate $\mathrm{Ti_{1-x}Ce_x(OCH_2CH_2O)_{2-x/2}}$ ($\mathrm{x} = 0.05, 0.1, 0.2$ and 0.3) was synthesized.

2.2. Characterization

Phase analysis of the synthesized samples was performed with a POLARAM S-112 polarized microscope in transmitted light and a STADI-P (STOE, Germany) X-ray diffractometer in CuKα radiation; thermogravimetric analysis was carried out using a Setaram SetsysEvolution thermal analyzer during heating in air at a rate of 10 °C/min. The form and shape of the precursor particles and the products of their thermolysis were determined by the scanning electron microscopy method on a JSM JEOL 6390LA device. Elemental analysis of the examined samples for titanium and iron content was performed by the atomic adsorption spectroscopy method in an air-acetylene flame on a Perkin-Elmer device and by atomic emission technique on a inductive-plasma spectrum analyzer. The content of carbon was determined according to the technique described in detail in work [22]. IR spectra of the powders were registered on a Spectrum–One spectrometer (Perkin-Elmer from 4000 to 400 cm^{-1}. The solutions were irradiated in 50 ml quartz cells with a UV-BUF-15 lamp ($\lambda_{\mathrm{max}} = 253$ nm); for irradiation in the visible spectrum, we used a blue luminescent lamp with maximum irradiation from 440–460 nm.

2.3. Photocatalytic experiments

The photocatalytic activities of the $\mathrm{Ti_{1-x}Fe_xO_{2-x/2}}$ and $\mathrm{Ti_{1-x}Ln_xO_{2-x/2}}$ catalyst samples were examined in terms of hydroquinone (substrate, HQ) solution decomposition. In a typical experiment, 100 mg of the catalyst were magnetically stirred in a 50 ml 0.10 mmol/l HQ solution in darkness for 1 hr in order to achieve the adsorption–desorption equilibrium between HQ and the catalyst. The suspension of the catalyst in the solution was then irradiated with an ultraviolet light using a BUF 15 lamp ($\lambda_{\mathrm{max}} = 253$ nm) during assigned exposure time from zero to one hour. The level of photocatalytic decomposition of the substrate was evaluated using current–voltage characteristics [22]. Preliminary sorption experiments in the system 'catalyst – HQ' at different HQ concentrations and different masses of the catalyst have showed that the distribution of HQ between the solution and the catalysts obeys the Langmuir's law. Thus, the selected initial concentration of HQ in the photocatalytic experiments allowed us to carry out HQ sorption and photocatalysis within the Henry's law region < 0.4 mM.

Quantitative variation of the HQ concentration in the solution during photocatalytic oxidation in the presence of $\mathrm{Ti_{1-x}Fe_xO_{2-x/2}}$ and $\mathrm{Ti_{1-x}Ln_xO_{2-x/2}}$ catalysts was estimated by the voltammetry method on a PU-1 polarograph with the rate of potential scanning of 0.03 V/s [22, 23]. The PU-1 polarograph was coupled with a cylindrical carbon indicator electrode with working surface area of 0.44 cm^2 and with an additional AgCl-electrode EVL-1M3. The substrate concentration was determined at the cathode potential of -0.5 V. Anode polarization of the electrodes in the region 0.0–1.0 V was used every time after cathode polarization to purify the electrode surface.

3. Results and discussions

3.1. Characterization of catalysts

According to X-ray phase, microscopic analyses and IR spectroscopy data, the products of reaction (1) are found to be solid solutions of the composition $\mathrm{Ti_{1-x}Fe_x(OCH_2CH_2O)_{2-x/2}}$ $(0 < x \leq 0.1)$ formed by substitution of Fe(III) for Ti(IV) in the structure of titanium glycolate $\mathrm{Ti(OCH_2CH_2O)_2}$. Depending on the reaction conditions and quantitative ratios of reagents, they can be produced as extended $0.5 - 2 \times 5 - 20$ μm crystalline fibers of approximately the same length with cross-sections of about 50–100 nm. Most thin fibrous crystals $\mathrm{Ti_{1-x}Fe_x(OCH_2CH_2O)_{2-x/2}}$ are formed during slow evaporation of the solvent — ethylene glycol from its saturated solutions. However, the glycolate crystals formed at the initial stage of evaporation tend to display longitudinal intergrowth, which leads to the formation of aggregates with the cross-section greater than 0.5 μm. Depending on the content of iron, the color of $\mathrm{Ti_{1-x}Fe_x(OCH_2CH_2O)_{2-x/2}}$ powders varies from pale yellow ($x \leq 0.05$) to orange ($0.05 < x \leq 0.1$). Close similarity of IR spectra for $\mathrm{Ti(OCH_2CH_2O)_2}$ and $\mathrm{Ti_{1-x}Fe_x(OCH_2CH_2O)_{2-x/2}}$ at $x \leq 0.1$ is indicative of a small distortion of the initial crystal structure of the titanium glycolate as a result of the substitution of Fe(III) for Ti(IV) cations. The same similarity is typical of the IR spectra of $\mathrm{Ti_{1-x}V_x(OCH_2CH_2O)_2}$ [14,22] and $\mathrm{Ti_{1-x}Ln_x(OCH_2CH_2O)_{2-x/2}}$ [24], which implies a similar nature of the solid solutions based on titanium glycolate $\mathrm{Ti(OCH_2CH_2O)_2}$. A very intense band at 1058 cm^{-1} corresponds to vibrations of bonds C–O– in the metal-coordinated bis-alkoxide ion $\mathrm{OCH_2CH_2O^{2-}}$ in the IR spectra of $\mathrm{Ti_{0.9}Fe_{0.1}(OCH_2CH_2O)_{1.95}}$ and $\mathrm{Ti(OCH_2CH_2O)_2}$, while in the spectrum of liquid ethylene glycol two bands of the same intensity are present in this region at 1087 and 1043 cm^{-1} [27]. Intense absorption bands with maxima at 918 and 880 cm^{-1} displaced to the high-frequency region relative to those in the IR spectrum of liquid ethylene glycol (883 and 862 cm^{-1}) are attributed to torsional vibrations of the C–C bonds.

Aggregates of $\mathrm{Ti}_{1-x}\mathrm{Fe}_x\mathrm{O}_{2-x/2}$ solid solutions, formed by heating the $\mathrm{Ti_{1-x}Fe_x(OCH_2CH_2O)_{2-x/2}}$ precursor at 500 °C in air, have a morphology of elongated fiber-like aggregated particles. At low iron concentrations ($0.005 \leq x \leq 0.025$), the cross-section of these $\mathrm{Ti_{1-x}Fe_xO_{2-x/2}}$ fibers is 50 to 100 nm, but as the concentration of Fe(III) increases, the thickness of the fibers increases (Fig. 1), obeying the tendency of primary precursor crystals to display intergrowth. Consequently, the thermal decomposition of $\mathrm{Ti_{1-x}Fe_x(OCH_2CH_2O)_{2-x/2}}$ during heating in air to 500 °C gives rise to solid solutions which are pseudo-isomorphous to the precursor. The synthesized oxide $\mathrm{Ti_{1-x}Fe_xO_{2-x/2}}$ fibers inherit the shape and morphology of the precursor fibrous crystals. We see that the shape of the $\mathrm{Ti_{1-x}Fe_xO_{2-x/2}}$ oxide does not depend on the precursor thermal treatment conditions and remains unchanged upon heating in air or in an inert gaseous atmosphere up to 1300 °C. Moreover, it does not change as a result of the phase transformation of anatase to rutile, whose initial temperature exhibits a complicated dependence on the content of iron in $\mathrm{Ti}_{1-x}\mathrm{Fe}_x\mathrm{O}_{2-x/2}$. Here we observe the following regularity: in the series of $\mathrm{Ti_{1-x}Fe_xO_{2-x/2}}$ samples, the anatase to rutile phase transition onset temperature increases for $x < 0.05$ and decreases for $0.05 \leq x \leq 0.1$. Heating of $\mathrm{Ti_{0.95}Fe_{0.05}(OCH_2CH_2O)_{1.975}}$ samples in air at 500 to 600 °C for 2 hr shows that the anatase to rutile phase transition in the resulting oxide $\mathrm{Ti_{0.95}Fe_{0.05}O_{1.97}}$ begins at 550 °C. At the same time, for the product of thermolysis of $\mathrm{Ti_{0.9}Fe_{0.1}(OCH_2CH_2O)_{1.95}}$, a phase with the rutile structure is observed already at 450 °C (Fig. 2). The products of thermolysis of $\mathrm{Ti_{1-x}Fe_x(OCH_2CH_2O)_{2-x/2}}$ in helium atmosphere are black fibers, whose X-ray diffraction patterns contain very broad lines belonging to iron-doped titania with the anatase structure. The black color of the powders is due to the presence of

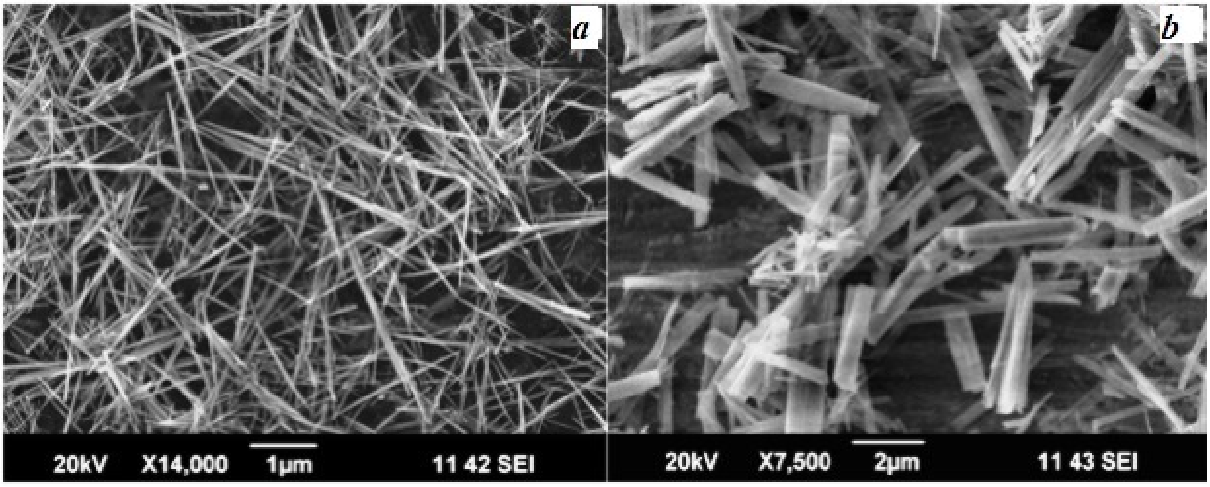

FIG. 1. SEM images of $Ti_{1-x}Fe_xO_{2-x/2}$ aggregates (a — $x = 0.01$, b — $x = 0.075$) obtained by heating of $Ti_{1-x}Fe_x(OCH_2CH_2O)_{2-x/2}$ in air at 500 °C

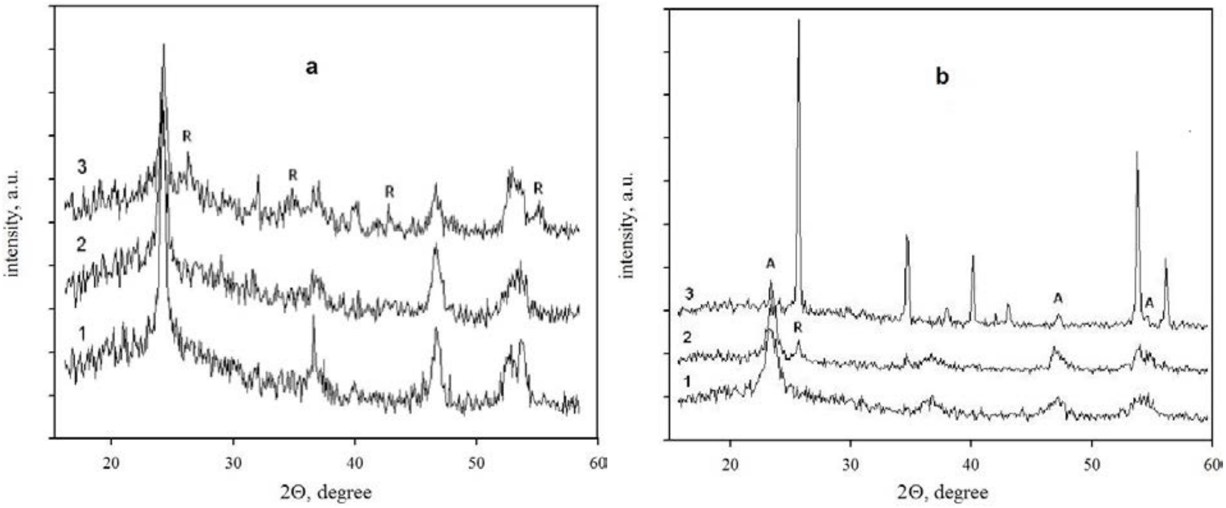

FIG. 2. a — X-ray diffraction patterns of thermolysis products of in air at 450 °C. 1 — $x = 0.025$, 2 — 0.05, 3 — 0.1. The tag 'R' denotes the lines of the rutile phase. b — X-ray diffraction patterns of thermolysis products of in helium atmosphere. 1 — 600, 2 — 800, and 3 — 900 °C. The tags 'R' and 'A' denote the lines of rutile and anatase phases

X-ray amorphous carbon: according to elemental and thermogravimetric (TG) analyses data, its content in all of the examined samples is about 18 mass %. Optical microscopy of the powders shows stretched black aggregates, which include both the anatase and black amorphous carbon particles. X-ray diffraction patterns of the $Ti_{0.95}Fe_{0.05}(OCH_2CH_2O)_{1.975}$ glycolate thermolysis products, which were heated for 2 hr in helium atmosphere to 600, 800,and 1000 °C, demonstrate high thermal stability of the anatase phase under an inert atmosphere. Even after 2 h exposure of the precursor at 1000 °C, the product contains an admixture of the phase with the anatase structure.

The TG and DTA curves of the glycolate $Ti_{0.95}Fe_{0.05}(OCH_2CH_2O)_{1.975}$ displayed in Fig. 3a show that the process of thermal decomposition of this material in air with a heating

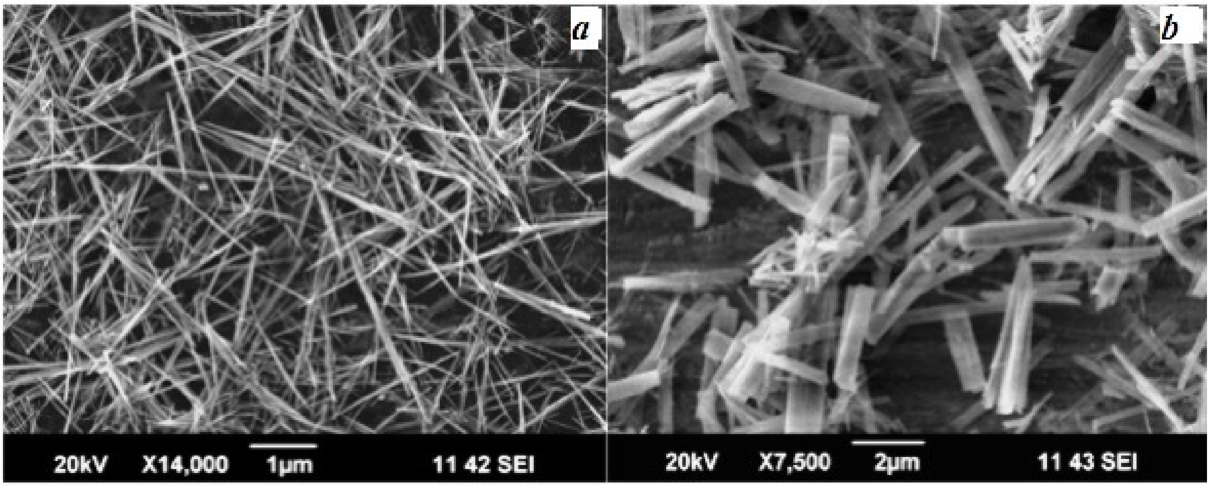

FIG. 3. a — TG and DTA curves of thermolysis product of $Ti_{0.95}Fe_{0.05}(OCH_2CH_2O)_{1.975}$ heated in air. b – TG and DTA curves of thermolysis product of $Ti_{0.95}Fe_{0.05}(OCH_2CH_2O)_{1.975}$ heated in helium atmosphere at 500 °C for 2 h.

rate of 10 °C/min has a complicated character and is exothermic from $\sim$ 250–500 °C with a maximum on the DTA curve at 315 °C. The mass loss value for the sample ($\Delta m = 52.33$ mass %) determined from the TG curve differs insignificantly from that ($\Delta m = 52.26$ mass %) calculated in the assumption that the oxide $Ti_{0.975}Fe_{0.025}O_{1.9875}$ is formed. The plateau on the TG curve in the temperature interval from $\sim$ 330 to 475 °C is due to the oxidation of X-ray amorphous carbon, formed as a result of redox decomposition of the glycolate ion $OCH_2CH_2O^{2-}$ at temperatures below 350 °C. The formation of carbon during the heating of $Ti_{1-x}Fe_x(OCH_2CH_2O)_{2-x/2}$ in air is confirmed by elemental analysis data, according to which, the samples exposed in air at 400 and 450 °C for 2 hr contain 1.2 and 0.58 mass % of structurally bound carbon, respectively. Fig. 3b demonstrates TG and DTA curves of the glycolate $Ti_{0.95}Fe_{0.05}(OCH_2CH_2O)_{1.975}$ exposed for 2 hr in a helium atmosphere at 500 °C. The DTA curve exhibits an exothermal effect with a maximum at 363 °C, to which the mass loss of 17.95 % (w) corresponds. According to elemental analysis, the total amount of carbon in this sample is 18.06 % (w). Thus, by annealing in air the thermolysis products of $Ti_{1-x}Fe_x(OCH_2CH_2O)_{2-x/2}$, obtained by heating in a helium atmosphere, it is possible to register a certain amount of carbon in them. The quantity of chemically bonded carbon in these products depends on the temperature and the time of oxidizing annealing. This technique enables one to synthesize the iron- and carbon-doped titanium dioxide $Ti_{1-x}Fe_xO_{(2-x/2)-y}C_y$ with the anatase structure and to produce composites based thereon having an excess elemental carbon content.

It is known that doping of titanium dioxide with cations may lead not only to an increase in its liquid-medium photocatalytic activity in oxidation reactions of toxic and colored organic substances, but also to its bathochromic shift to the visible spectral region [3, 19, 22, 23, 25]. In the case of vanadium and carbon co-doping of the titania powder, the bathochromic shift in its catalytic activity may be extended to the blue light region for the samples of the composition $Ti_{0.50}Fe_{0.50}O_{2-y}C_y$ [22].

To evaluate the chemical stability of the doped catalysts during photocatalytic oxidation of hydroquinone, three consistent irradiation cycles of the same catalyst with the newly prepared solution were performed. Before each new cycle, the catalyst was washed with distilled water. These experiments indicated that the catalysts $Ti_{1-x}Fe_xO_{2-x/2}$ are chemically stable and do not

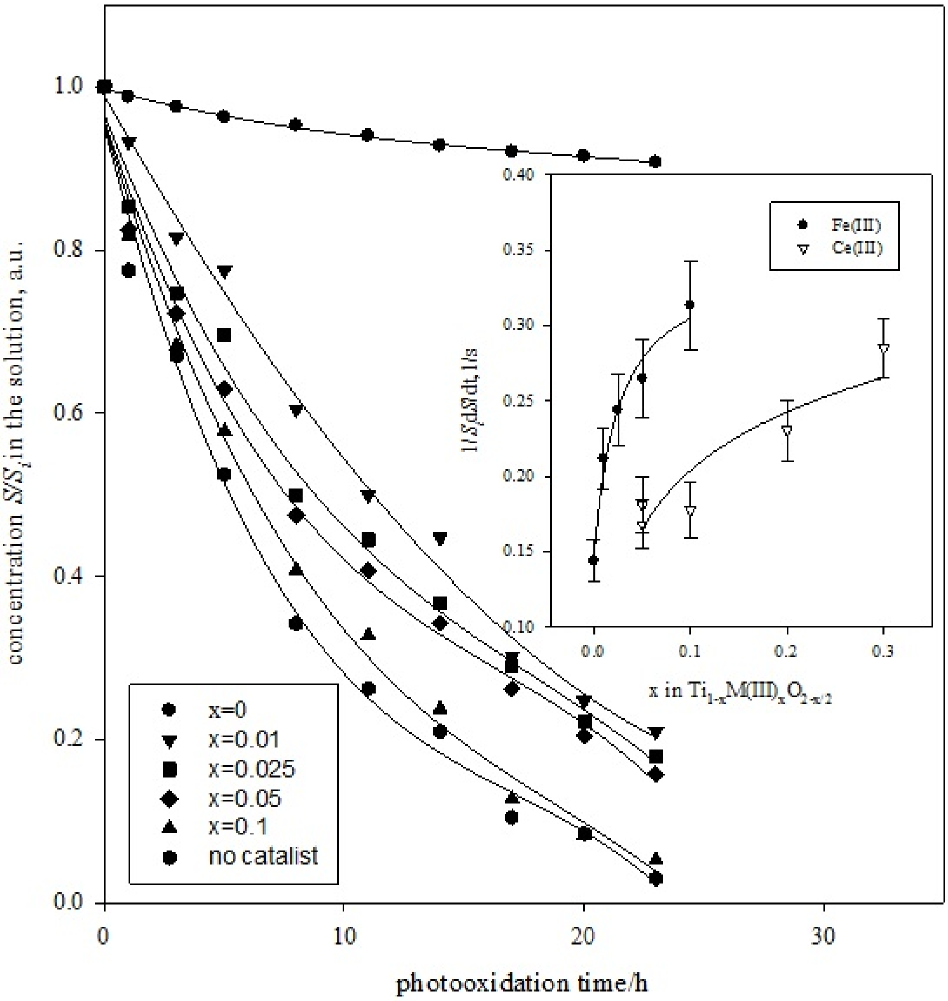

FIG. 4. The relative concentration of hydroquinone (S/S_i) versus the time of irradiation with ultraviolet light in the presence of $Ti_{1-x}Fe_xO_{2-x/2}$. In the inset the initial rate of hydroquinone photooxidation $1/S_i \cdot (dS/dt)_{t=0}$ versus the concentration (x) of M(III) atoms in the Ti(IV) oxide solid solution is depicted and lines on the graph show qualitative tendency of variation. Here S and S_i are current and initial concentration of HQ in solution, mM/l

change their chemical composition at least during three photo-oxidation cycles. Fig. 4 is a typical example of the experimental dependence of the related concentration of HQ (S/S_i) on their radiation time for a series of solid solutions $Ti_{1-x}Fe_xO_{2-x/2}$ ($x = 0.01$; 0.025; 0.05; 0.1).

The inset in Fig. 4 depicts the observed correlation of the initial S/S_i (relative) rate of hydroquinone photooxidation on the concentration 'x' of dissolved in the titania catalyst metal M (M=Fe(III), Ce(III)). One can see that the initial rate of the photocatalytic reaction increases with the concentration of the dopant (Fig. 4).This implies that the rate of photooxidation at the initial stage of the process is a function of structural and energetic changes in the solid solution, which are due to doping of titania with M(III) cations.

3.2. Discussion and modeling

Doping is a key factor for fabricating light-sensitive photocatalysts with advanced properties. Though solid solution formation is one of the convenient ways for empirical photocatalysts 'tuning', no methodology is available to prove enhanced catalysis through titania doping [28]. One of the parameters, which allows estimating the above energetic effect of solid solution formation on the photocatalytic activity, is mixing enthalpy of the solid solution formation (ΔH_{mix}) [29]. If so, we can expect a certain functional correlation between the terms $-1/S_i \cdot (dS/dt)$ (or the energy of photooxidation of HQ by M-doped titania, $\Delta E_r \sim \ln[-1/S_i \cdot (dS/dt)]$) on one hand and ΔH_{mix} on the other hand.

In terms of the concept of regular solid solutions, which is a first approximation in the case of low levels of M ions solubility in titania, the mixing enthalpy ΔH_{mix} for the binary ionic crystal $\mathrm{Ti_{1-x}Fe_xO_{2-x/2}}$ [29,30] is:

$$\Delta H_{mix} \sim c(1-x)x(\Delta R/R)^2, \tag{2}$$

where R is the average M–O–M($\mathrm{Ti^{4+}}$–$\mathrm{O^{2-}}$–$\mathrm{Fe^{3+}}$) distance in the solid solution estimated by using Vegard's rule in the form $R = R_{Ti^{4+}}(1-x) + R_{Fe^{3+}}x$, nm, and the term $\Delta R = R_{Fe^{3+}} - R_{Ti^{4+}}$ [30]. Here, $R_{Ti^{4+}} = (r_{Ti^{4+}} + r_{O^{2-}})$, $R_{Fe^{3+}} = (r_{Fe^{3+}} + r_{O^{2-}})$, and $r_{Ti^{4+}}, r_{Fe^{3+}}, r_{O^{2-}}$ are the ionic radii of the ions with the coordination number 6 [31], nm. 'c' in (2) is the empiric coefficient, which depends on the iconicity of M–O bonds, on the coordination number of cations in the crystal, and on the Madelung constant [30]. The term $(1-x)x(\Delta R/R)^2$ in (2) is a semiempirical approximation of ΔH_{mix} values variation in our experiments since the substituting cations M in the solid solution $\mathrm{Ti}_{1-x}\mathrm{M}_x\mathrm{O}_{2-x/2}$ have the same charge end coordination. Comparison of the variation of the terms $\ln[-1/S_i \cdot (dS/dt)]$ and $(1-x)x(\Delta R/R)^2$ in a series of photocatalytic experiments with the catalysts $\mathrm{Ti_{1-x}M_xO_{2-x/2}}$, M=Fe(III), Ce(III), revealed a linear correlation between these variables in any of the considered series. This allows us to conclude that the mixing enthalpy ΔH_{mix} is one of the driving forces for the photooxidation of HQ in the solid solutions $\mathrm{Ti_{1-x}M_xO_{2-x/2}}$, in which M is not only Fe(III), Ce(III) (Fig. 5, curves 1,2), but also tricharged ions of Er, Tb, Eu, Nd, Sm (Fig. 5, curve 3). In accordance with the accepted semi-empiric approach, the general difference in the catalytic activity of different series of catalysts can be ascribed to the curvature of the correlation lines plotted in the coordinates $\ln[-1/S_i \cdot (dS/dt)]$ and $(1-x)x(\Delta R/R)^2$, Fig. 5. According to Fig. 5, the slope of the correlation line is a constant for a given solid solution of ion 'M' in the series $\mathrm{Ti_{1-x}M_xO_{2-x/2}}$ and it differs for different 'M' ions. For tricharged ions of REE, such as Er, Tb, Eu, Nd and Sm, the difference in the slopes is negligible, due to a small difference in their ionic radii and in the M–O distances of these ions in the corresponding solid solutions. This is why only one line describes the whole series with REE ions except for $\mathrm{Ti_{1-x}Ce_xO_{2-x/2}}$. For Ce(III), the value of the slope may be a relative measure of photocatalytic activity of the $\mathrm{Ti_{1-x}M_xO_{2-x/2}}$ solid solutions. As to the effect of mixing enthalpy on the initial rate of HQ photooxidation, Eq. (2), the difference in the activity in the series $\mathrm{Ti_{1-x}M_xO_{2-x/2}}$ with different M is due to the difference of the empiric coefficient c, which depends on the iconicity of M–O bonds, coordination number of cations in the crystal, and on the Madelung constant [30]. Observed linear correlation between variables $\ln[-1/S_i \cdot (dS/dt)]$ and $(1-x)x(\Delta R/R)^2$ in the series of the solid solutions is a direct energetic consequence of the formation of the solid solution by the catalyst. This is why the energy of the photocatalytic reaction is proportional to the mixing energy of the solid solution $\mathrm{Ti_{1-x}Fe_xO_{2-x/2}}$, $\Delta E_r \sim \Delta H_{mix}$. The difference in the activity of Fe(III)- and Ln(III)-doped catalysts may be attributed to the marked ability of Fe(III) to drastically increase the charge-carriers lifetime in titania [3]. Thus, the lifetime of the

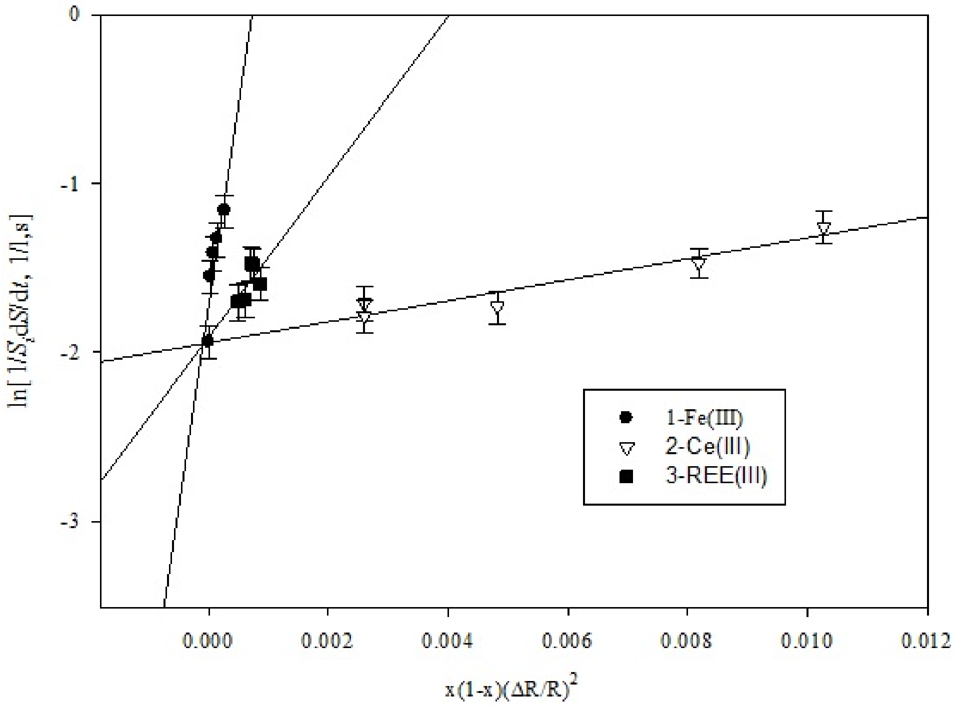

FIG. 5. The change in the initial rate of hydroquinone photo-oxidation ($\ln [1/S_i \cdot (dS/dt)_{t=0}]$) in the series of photocatalysts $Ti_{1-x}M_xO_{2-x/2}$, versus estimate of their solid solution mixing enthalpy $\Delta H_{mix} \sim (1-x)x(\Delta R/R)^2$; the dopants are Fe(III) for the $x = 0 - 0.0003$ (1), Ce(III) for $x = 0.05 - 1.00$ (2) and tricharged REE — Ce, Er, Tb, Eu, Nd, Sm for the $= 0.025$ (3)

carriers is connected with the mixing enthalpies of the solid solution formation for Fe(III) and for Ce(III), Er(III), Tb(III), Eu(III), Nd(III), Sm(III) in titania with fiber-like morphology.

The ability to create extended non-equilibrium solid solution by doping of titania with cations provides conditions for increasing the photocatalytic activity of the solid solution in the assigned spectral region. Conversely, in contrast to $\mathrm{Ti_{1-x}V_xO_{2-y}C_y}$ and $\mathrm{Ti_{1-x}V_xO_2}$ [22,23], the iron-doped quasi-one-dimensional titanium dioxide, like $\mathrm{Ti_{1-x}Ln_xO_{2-x/2}}$ [24], does not activate the hydroquinone photooxidation process under blue light irradiation.

4. Conclusions

In summary, the studies performed show that with the use of $\mathrm{Ti_{1-x}Fe_x(OCH_2CH_2O)_{2-x/2}}$ as a precursor, it is possible to obtain quasi-one-dimensional (1-D) solid solutions $\mathrm{Ti_{1-x}M_xO_{2-x/2}}$ ($0 \le x \le 0.3$, M(III) = Fe, Ce, Er, Tb, Eu, Nd and Sm), which exhibit different photocatalytic activity in the HQ photooxidation under ultraviolet irradiation. The transformation of the precursor into oxide takes place in an isomorphous manner during heating both in air and in an inert atmosphere. In an inert gaseous atmosphere, the aggregates of $\mathrm{Ti_{1-x}Fe_x(OCH_2CH_2O)_{2-x/2}}$ thermolysis products contain about 18 mass % carbon, which can be removed during subsequent aerobic annealing during the formation of anatase phases $\mathrm{Ti_{1-x}Fe_xO_{(2-x/2)-y}C_y}$ and $\mathrm{Ti_{1-x}Fe_xO_{2-x/2}}$. In the framework of ion-covalent binary solid solutions theory, a correlation is found between the energy of the photocatalytic reaction and the estimated mixing enthalpy of binary solid solutions formation. This approach may be useful for the semiempirical search for new ways of tuning the photocatalytic activity of binary solid solutions.

Acknowledgments

The work was supported by the RFBR (projects 12-03-00453-, 13-03-00265-a), RFBR-Urals (project 13-03-96061), the Presidium of RAS (projects 12-P-3-1915, 12-U-3-1009 and 12-T-3-1009), the Presidium of RAS (Urals Branch), the Science school (project SS-5669.2012.3).

References

[1] Carp O., Huisman C.L., Reller A. Photoinduced reactivity of titanium dioxide. *Progress in Solid State Chemistry*, **32** (1–2), P. 33–177 (2004).

[2] Kubo W., Tatsuma T. Photocatalytic remote oxidation with various photocatalysts and enhancement of its activity. *J. Mater. Chem.*, **15** (30), P. 3104–3108 (2005).

[3] Banerjee S., Gopal J., et al. Physics and chemistry of photocatalytic titanium dioxide: Visualization of bactericidal activity using atomic force microscopy. *Current Sci.*, **90**, P. 1378 (2006).

[4] Egerton T., Kessel L., Tooley I.R., Wang L. Photogreying of TiO_2 nanoparticles. *J. Nanoparticle Res.*, **9** (2), P. 251–260 (2007).

[5] Pavasupree S., Jaturong J., Yoshikawa S. Hydrothermal synthesis, characterization, photocatalytic activity and dye-sensitized solar cell performance of mesoporous anatase TiO_2 nanopowders. *Mater. Res. Bull.*, **43**, P. 149–157 (2008).

[6] Balcerski W., Ryu S.Y., Hoffmann M.R. Gas-Phase Photodegradation of Decane and Methanol on TiO_2: Dynamic Surface Chemistry Characterized by Diffuse Reflectance FTIR. *Intern. J. Photoenergy*, Art. ID 964721 (2008).

[7] Kitano M., Tsujimaru K., Anpo M. Hydrogen Production Using Highly Active Titanium Oxide-based Photocatalysts. *Top. Catal.*, **49** (1–2), P. 4–17 (2008).

[8] Xia M., Zhang Q., et al. The large-scale synthesis of one-dimensional TiO_2 nanostructures using palladium as catalyst at low temperature. *Nanotechnology*, **20** (5), P. 055605 (2009).

[9] Kumar S.G., Devi L.G. Review on modified TiO_2 photocatalyst under UV/visible light: Selected Results and Related Mechanisms on interfacial charge carrier transfer dynamics. *J. Phys. Chem. A*, **115**, P. 13211–13241 (2011).

[10] Xiao Yutang, Xu ShuangShuang, Li ZhiHua, et al. Progress of applied research on TiO_2 photocatalysis-membrane separation coupling technology in water and wastewater treatments. *Chinese Sci. Bull.*, **55** (14), P. 1345–1353 (2010).

[11] Tueng S., Kanaev A., Chhor K. New homogeneously doped Fe(III)-TiO_2 photocatalyst for gaseous pollutant degradation. *Appl. Catal. A: General*, **399**, P. 191–197 (2011).

[12] Wang D., Yu R., Chen Y., et al. Photocatalysis property of needle-like TiO_2 prepared from a novel titanium glycolate precursor. *Solid State Ionics*, **172**, P. 101–104 (2004).

[13] Jiang X., Wang Y., Herricks T., Xia Y. Ethylene glycol-mediated synthesis of metal oxide nanowires. *J. Mater. Chem.*, **14** (4), P. 695–703 (2004).

[14] Krasilnikov V.N., Shtin .P., et al. Vanadyl and titanium glycolates as precursors for the preparation of oxide materials in the form of elongated microparticles and nanoparticles. *Nanotechnologies in Russia*, **3** (3), P. 106–111 (2008).

[15] Krasilnikov V.N., Shtin .P., et al. Synthesis and properties of titanium glycolate $Ti(OCH_2CH_2O)_2$. *Russian Journal of Inorganic Chemistry*, **53** (7), P. 1065–1069 (2008).

[16] Zaleska A. Doped-TiO_2: A Review. *Recent Patents Eng.*, **2** (3), P. 157–164 (2008).

[17] Nishijima K., Kamai T., et al. Photocatalytic Hydrogen or Oxygen Evolution from Water over S- or N-Doped TiO_2 under Visible Light. *Intern. J. Photoenergy*, Art. ID 173943 (2008).

[18] Su Y., Han S., et al. Preparation and visible-light-driven photoelectrocatalytic properties of boron-doped TiO_2 nanotubes. *Mater. Chem. Phys.*, **110** (2–3), P. 239–246 (2008).

[19] Carriazo J.G., Moreno M., Molina R.A., Moreno S. Incorporation of titanium and titanium-iron species inside a smectite-type mineral for photocatalysis. *Appl. Clay Sci.*, **50** (3), P. 401–408 (2010).

[20] Sun H., Wang S., et al. Halogen element modified titanium dioxide for visible light photocatalysis. *Chem. Eng. J.*, **162**, P. 437–447 (2010).

[21] Yang J., Chen D.-X., et al. Visible-light-driven photocatalytic degradation of microcystin-LR by Bi-doped TiO_2. *Res. Chem. Intermed.*, **37** (1), P. 47–60 (2011).

[22] Krasilnikov V.N., Shtin .P., et al. Synthesis and photocatalytic activity of $Ti_{1-x}V_xO_{2-y}C_y$ whiskers in hydroquinone oxidation in aqueous solutions. *Russian Journal of Inorganic Chemistry*, **58** (8), P. 1184–1194 (2010).

[23] Zainullina V.., Zhukov V.P., et al. Electronic structure and the optical and photocatalytic properties of anatase doped with vanadium and carbon. *Physics of Solid State*, **52**, P. 271–280 (2010).

[24] Krasilnikov V.N., Shtin .P., et al. Glycolate $Ti_{1-x}Ln_x(OCH_2CH_2O)_{2-x/2}$ as an efficient precursor for synthesis of titanium dioxide doped with lanthanides $Ti_{1-x}Ln_xO_{2-x/2}$. *Doklady Chemistry*, **437** (2), P. 112–115 (2011).

[25] Baklanova I. V., Krasil'nikov V. N., Perelyaeva L. A., Gyrdasova O. I. Stability of the anatase phase in nanodimensional titanium dioxide doped with europium(III), samarium(III), and iron(III). *Theoretical and Experimental Chemistry*, **47** (4), P. 215–218 (2011).

[26] Sathishkumar P., Anandan S., et al. Synthesis of Fe3+ doped TiO_2 photocatalysts for the visible assisted degradation of an azo dye. *Colloids and Surfaces. A: Physicochem. Eng. Aspects*, **375**, P. 231–236.

[27] Matsuura H., Miyazawa T. Infrared Spectra and Molecular Vibrations of Ethylene Glycol and Deuterated Derivatives. *Bull. Chem. Soc. Japan*, **40** (1), P. 85–94 (1967).

[28] Ohtani B. Photocatalysis A to Z-What we know and what we do not know in a scientific sense. *Journal of Photochemistry and Photobiology C: Photochemistry Reviews*, **11**, P. 157–178 (2010).

[29] Urusov V. S. Crystal Chemical and Energetic Characterization of Solid Solution. *Thermodynamic Data Advances in Physical Geochemistry*, **10**, P. 162–193 (1992).

[30] Urusov V.S. Comparison of Semi-Empirical and Ab Initio Calculations of the Mixing Properties of MO–M'O Solid Solutions. *Journal of Solid State Chemistry*, **153** (2), P. 357–364 (2000).

[31] Shannon R.D. Revised effective ionic radii and systematic studies of interatomic distances in halides and chalcogenides. *Acta Crystallogr. A*, **32**, P. 751–767 (1976).

NANOSYSTEMS: PHYSICS, CHEMISTRY, MATHEMATICS, 2014, 5 (4), P. 564–573

EFFECT OF HIGH PRESSURES AND HIGH TEMPERATURES ON STRUCTURAL AND MAGNETIC CHARACTERISTICS OF NANOSTRUCTURED SOLID SOLUTIONS $Zn_{1-x}Fe_xO$

T. V. Dyachkova[1], V. N. Krasil'nikov[1], O. I. Gyrdasova[1], E. V. Shalaeva[1],
A. P. Tyutyunnik[1], V. V. Marchenkov[2], Yu. G. Zaynulin[1], H. W. Weber[3]

[1]Federal State government-financed research institution Institute of Solid State Chemistry of the Ural Branch of the Russian Academy of Sciences, Ekaterinburg , Russia

[2]Federal State government-financed research institution Institute of Metal Physics of the Ural Branch of the Russian Academy of Sciences, Ekaterinburg, Russia

[3]Atominstitut, Vienna University of Technology, Vienna, Austria

dyachkova@ihim.uran.ru, kras@ihim.uran.ru, gyrdasova@ihim.uran.ru,
shalaeva@ihim.uran.ru, tyutyunnik@ihim.uran.ru, march@imp.uran.ru,
zaynulin@ihim.uran.ru, weber@ati143.ac.at

PACS 71.20.Nr, 73.63.Bd, 75.50.Pp

Nanostructured solid solutions of the composition $Zn_{1-x}Fe_xO$ ($0 \leqslant x \leqslant 0.075$) with tubular aggregate morphology, synthesized by the precursor method, were subjected to thermobaric treatment at P = 5 GPa and T = 600–700°C. Using the samples with $x = 0.05$ as an example, it was shown that the application of pressure leads to morphology variation, reduction of structural parameters and to an increase in ferromagnetism.

Keywords: High pressure - high temperature, nanomaterials, glycolate, semiconductors.

Received: 16 June 2014
Revised: 30 June 2014

1. Introduction

Increased interest in zinc oxide, doped with cations of ferromagnetic metals, such as manganese, iron, cobalt and nickel, is due to the need to find new magnetic materials for spintronics that open up possibilities of developing magnetoresistive memory cells, spin light-emitting diodes and field-effect transistor, as well as magnetic field sensors and quantum computer components [1–3]. Although such materials as solid solutions $Zn_{1-x}M_xO$ contain only several atomic percents of magnetic impurities with negligibly small exchange interaction between them, ferromagnetism can occur in them even at room temperature. The magnetically ordered state observed for low-dimensional forms of zinc oxide, for example, nanopowders and thin films, consists not only in a greater degree of imperfection of such structures as compared with bulk objects, but also in the appearance of quantum-dimensional effects that manifest themselves during the transition into the nanodimensional state [2, 4–11]. The unique combination of semiconducting and ferromagnetic properties of the solid solutions $Zn_{1-x}Fe_xO$ makes them promising materials for practical application in the development of devices based on the spin-dependent transport effect and attracts the attention of a wide range of specialists including those concerned in synthesis of nanomaterials, whose efforts are directed at the elaboration of new methods for synthesis of samples with preassigned composition that provide the possibility to control the degree of dispersity and structure imperfection and to affect their magnetic properties [7–11].

Among the methods of synthesis of room-temperature ferromagnetics based on iron-doped zinc oxide described in the literature, the most widespread techniques are solid-phase synthesis [12, 13], self-propagating high-temperature synthesis [14, 15], solvothermal synthesis [11, 16], sol-gel synthesis [17, 18] and synthesis by deposition from aqueous solution in the form of hydroxides [19, 20]. A method for the production of polycrystalline ferromagnetic samples of the composition $Zn_{0.99}Fe_{0.01}O$ from mixtures of ZnO and Fe_3O_4 oxides by the solid-phase reaction technique combined with high-temperature treatment (2 and 5 GPa) has been reported previously [21].

The problem of synthesizing nanostructured iron-doped zinc oxide with a high degree of dispersity and intrinsic imperfection can be solved via the precursor method, the most important advantage of which is the possibility of dosed replacement of zinc by a magnetic metal in the precursor matrix. Thermal treatment of precursor under selected conditions allows the synthesis of oxides with a preset composition and expected morphological and dimensional aggregate parameters. So, as a result of heating in air at temperatures above 400°C, the octahedral crystals of $Zn_{1-x}Fe_x(OCH_2CH_2O)$ glycolate undergo a pseudomorphous transformation into octahedral aggregates of the oxide $Zn_{1-x}Fe_xO$, while extended crystals of formate glycolate $Zn_{1-x}Fe_x(HCOO)(OCH_2CH_2O)_{1/2}$ – into oxide nanotubes with diameters of 150–300 nm consisting of 10–15 nm crystallites [22].

The aim of this work was to examine the effect of annealing temperature and pressure on the structural and magnetic properties of nanodispersed solid solutions $Zn_{1-x}Fe_xO$ with tubular aggregates. In the synthesis of the samples, the advantages of the precursor method were combined with the advantages of thermobaric treatment. Nanotubular samples of the composition $Zn_{0.95}Fe_{0.05}O$, preliminarily synthesized by the precursor technique [22], were treated at quasi-hydrostatic pressure (5 GPa) at a temperature of 600–700°C; after that, their phase composition, microstructure and magnetic characteristics were studied.

2. Experiment technique

For the production of nanostructured iron-doped zinc oxide with tubular aggregate morphology, we employed the precursor method; the precursor was the formate glycolate of the composition $Zn_{1-x}Fe_x(HCOO)(OCH_2CH_2O)_{1/2}$, which was synthesized by the following reaction [22–23]:

$$\begin{gathered} Zn_{1-x}Fe_x(HCOO)_2 \cdot 2H_2O + 1/2HOCH_2CH_2OH = \\ Zn_{1-x}Fe_x(HCOO)(OCH_2CH_2O)_{1/2} + HCOOH \uparrow + 2H_2O \end{gathered} \tag{1}$$

The formate $Zn_{1-x}Fe_x(HCOO)_2{\cdot}2H_2O$ necessary for reaction (1) was synthesized by reaction between dilute formic acid and mixtures of zinc oxide and iron with heating:

$$(1-x)ZnO + xFe + 2HCOOH + H_2O = Zn_{1-x}Fe_x(HCOO)_2 \cdot 2H_2O + xH_2 \uparrow \tag{2}$$

Using microscopic analysis, it was found that formate glycolate $Zn_{1-x}Fe_x(HCOO)(OCH_2CH_2O)_{1/2}$ is isolated from the solution in ethylene glycol in the form of fibrous or needle-shaped crystals (reaction 1) upon exposure at 120°C for 2 h. The degree of substitution of iron for zinc in $Zn_{1-x}Fe_x(HCOO)(OCH_2CH_2O)_{1/2}$ does not exceed 10 at. %. In order to produce solid solution samples of the composition $Zn_{1-x}Fe_xO$ with tubular aggregate morphology, the precursor was heated in air with a rate of 10°C/min up to 500°C, exposed at this temperature for 2 h and cooled to room temperature with the furnace. The synthesized samples in the form of finely-dispersed orange powders that served as precursors were examined using X-ray diffraction analysis and then were subjected to thermobaric treatment. The experiments were carried out on a hydraulic press in a standard toroid-type high-pressure chamber. The powder of the composition $Zn_{0.95}Fe_{0.05}O$ was tamped tightly into a graphite cup that served simultaneously as a heater and then it was placed into a container made of lithographic stone – a natural mineral consisting mainly of calcium carbonate $CaCO_3$. To prevent contamination of the sample with carbon, the inside walls of the heater were isolated with boron nitride. The sample was compressed between the press anvils until the necessary pressure was reached, and after that, the temperature was raised. Upon exposure at a preset temperature, the sample under pressure was quenched by abrupt decrease of temperature. Then the pressure was released and the container with the samples was removed from the press. The experimental conditions and the structural characteristics of the produced preparations are given in Table 1.

TABLE 1. The crystallographic characteristics of the $Zn_{0.95}Fe_{0.05}O$ sample before treatment (1) and after treatment at P = 5 GPa, T = 600°C (2) and P = 5GPa, T = 700°C (3)

Sample No.	*a* (Å)	*c* (Å)	P (GPa)	T (°C)	Sp. gr.	Content, weight %	CSR (nm)
1	3.2502	5.2074	–	–	$P6_3mc$	100 m%	46.04
2	3.2509	5.2059	5	600	$P6_3mc$	100 m%	123.61
3	3.2489	5.2034	5	700	$P6_3mc$	84.0 m %	93.83
	3.2690	5.2247			$P6_3mc$	9.4 m %	33.65

The phase analysis of the precursors and the products of their thermolysis was performed be means of a POLAM S–112 polarizing microscope in transmitted light (the refractive indices were determined by the immersion method) and a STADI–P X-ray powder automated diffractometer (STOE, Germany) in $CuK_{\alpha 1}$ radiation using the X-ray diffraction database PDF-2 (Release 2009). Thermogravimetric analysis was carried out on a SETSYS EVOLUTION thermal analyzer (SETARAM, France) at a heating rate of 10°C/min in air. The size and shape of the particles of the thermolysis products were determined by scanning electron microscopy on a JSM JEOL 6390LA device. The structure of the thermolysis products was studied by transmission electron microscopy on a JEM–200 CX microscope. To determine the content of zinc and iron, elemental analysis was performed by the atomic absorption spectroscopy method in acetylene-air flame on a Perkin-Elmer device and by atomic emission method on a JY–48 spectrum analyzer with inductively coupled plasma. The magnetic properties of the synthesized $Zn_{1-x}Fe_xO$ samples were measured in the Atom Institute of the Vienna University of Technology on a MPMS XL7 SQUID magnetometer produced by Quantum Design in magnetic fields to 10 kOe in the temperature range from 4.2 to 330 K, as well as in the Multiple Access Center at the IMP UB RAS on a 7407 VSM vibration magnetometer produced by Lake Shore Cryotronics in magnetic fields to 17 kOe at room temperature.

3. Results and discussion

According to the X-ray phase analysis data, the thermolysis products of the precursor in air are solid solutions of the composition $Zn_{1-x}Fe_xO$ ($0\leqslant x \leqslant 0.075$) with wurtzite structure

(Fig. 1). Thermal decomposition of formate glycolate $Zn_{1-x}Fe_x(HCOO)(OCH_2CH_2O)_{1/2}$ is an exothermic process, occurring in two stages from ~280–500°C, which agrees with the presence of two anion types, $HCOO^-$ and $OCH_2CH_2O^{2-}$, in the crystal structure of this compound. The mass loss of the $Zn_{0.95}Fe_{0.05}(HCOO)(OCH_2CH_2O)_{1/2}$ sample determined by thermogravimetric analysis differed insignificantly from that calculated with allowance for its transformation into $Zn_{0.95}Fe_{0.05}O$. The common feature of thermal decomposition of $Zn_{1-x}M_x(HCOO)(OCH_2CH_2O)_{1/2}$ (M = V, Cr, Mn, Fe, Co, Ni, Cu) – the solid solutions, in which d metals substitute for zinc in the $Zn(HCOO)(OCH_2CH_2O)_{1/2}$ structure – is that the fibrous crystals of this substance transform during heating in air into aggregates of $Zn_{1-x}M_xO$ oxide having a tubular structure [22–29]. The size and microstructure of $Zn_{0.95}Fe_{0.05}(HCO)$ tubes depend on the formation conditions of precursor crystals and their heat treatment, as well as on the type and concentration of the dopant. The length of the tubular aggregates $Zn_{1-x}Fe_xO$ can exceed 30 μm and their diameter is 100–300 nm depending on the iron concentration (Fig. 2 a,b). As the concentration of iron increases, the tube walls become thinner and during rapid heating this can lead to their rupture in the direction parallel to their lengthening.

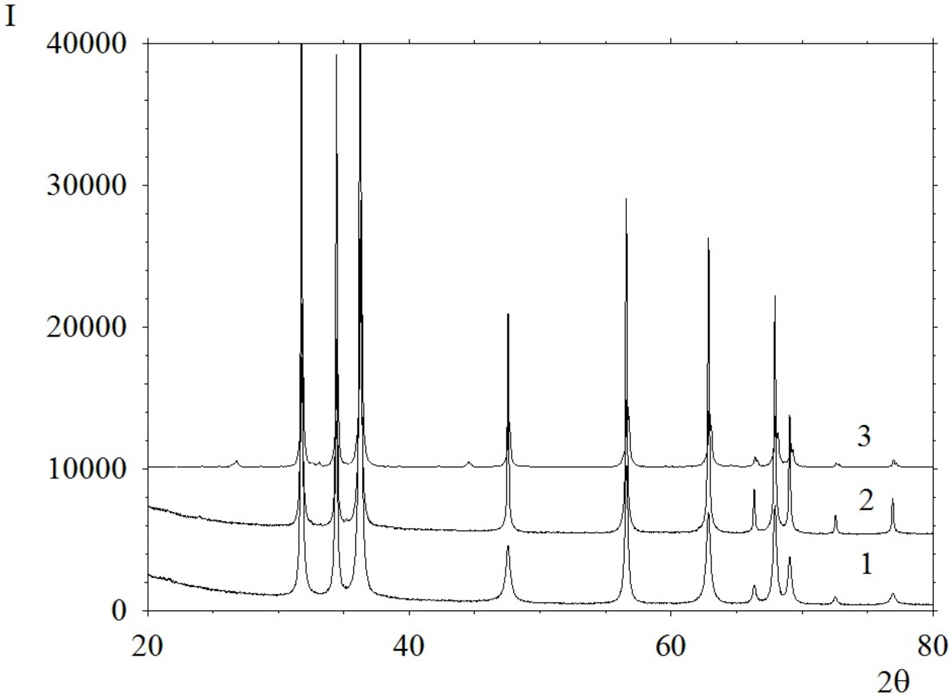

FIG. 1. The X-ray diffraction patterns of $Zn_{0.95}Fe_{0.05}O$ sample with tubular morphology: before treatment (1) and after treatment at P = 5 GPa at T = 600°C (2) and T = 700°C (3)

The bright-field electron-microscope images of $Zn_{0.95}Fe_{0.05}O$ oxide aggregates formed in the thermal decomposition of $Zn_{0.95}Fe_{0.05}(HCOO)(OCH_2CH_2O)_{1/2}$ during heating in air show that they are tubular quasi-one-dimensional structures built of crystallites with an average dimension of ~10 nm (Fig. 3 a,b). The Debye selected-area diffraction pattern (Fig. 3c) and the dark-field image (Fig. 3d) in $(100)_{ZnO}$, $(002)_{ZnO}$ and $(101)_{ZnO}$ reflections correspond to the polycrystalline nanodispersed structure of quasi-one-dimensional compounds $Zn_{0.95}Fe_{0.05}O$.

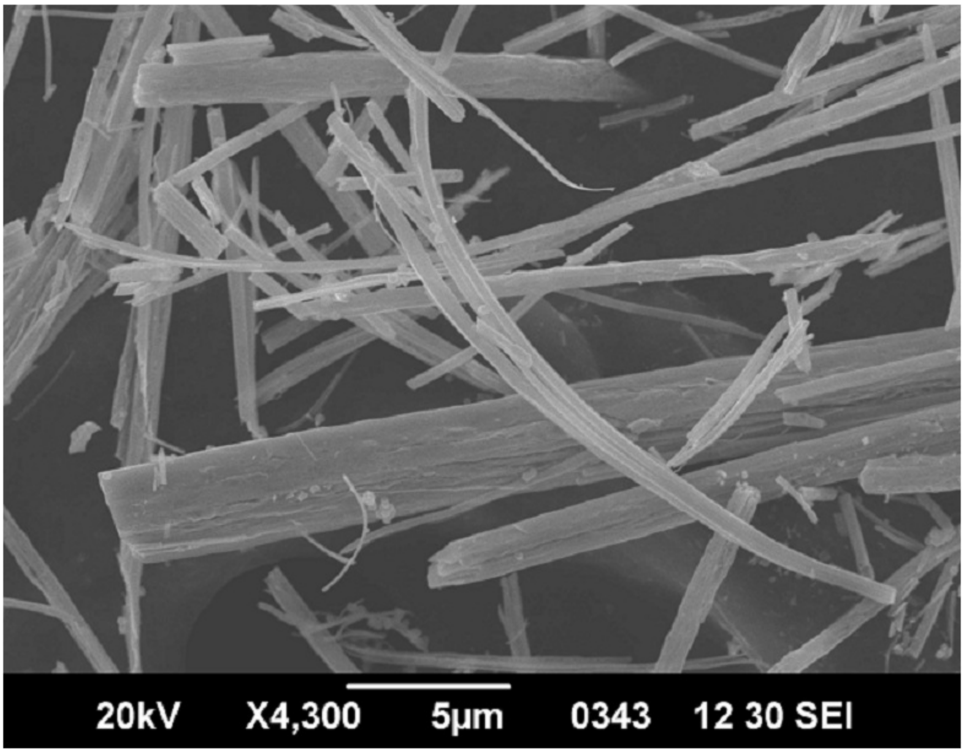

FIG. 2. The XEM image of the sample of the composition $Zn_{0.95}Fe_{0.05}O$ produced by thermolysis of $Zn_{0.95}Fe_{0.05}(HCOO)(OCH_2CH_2O)_{1/2}$ at 500°C in air

The powders of the composition $Zn_{0.95}Fe_{0.05}O$, produced by the precursor method were treated at different pressures (P = 5 – 9 GPa) and temperatures (T = 500, 600, 700, 900°C). The experiments showed that the initial wurtzite ZnO structure (sp. gr. – *P6₃mc*) remains only in a very narrow interval of pressures P = 5 GPa and temperatures T = 600–700°C. Under softer treatment conditions, an impurity phase of the composition $Zn_5(OH)_6(CO_3)_2$ is found, whereas under more rigorous conditions, the high-temperature cubic phase ZnO (sp. gr. – *Fm3m*) and $ZnFe_2O_4$ emerge. As is seen from Fig. 1 and Table 1, the crystal structure typical of the initial sample $Zn_{0.95}Fe_{0.05}O$ with tubular-shaped aggregates (1) remains after thermobaric treatment at 600°C (2). However, the morphology of the samples changes dramatically – the tubular form of the particles transforms into a round shape with lamellar inclusions (Fig. 4a). When the temperature is increased to 700°C (3), two phases with different lattice parameters are formed, one of which is iron-rich (84.0 mass %) and the other, on the contrary, is iron-depleted (9.4 mass %). The shape of the particles becomes more rounded (Fig. 4b). Besides the principal lines belonging to different forms of $Zn_{1-x}Fe_xO$, the X-ray diffraction pattern (Fig. 1) contains lines of boron nitride and graphite (heater material). According to our estimates, the coherent scattering region (CSR) increases with temperature.

Figure 5 presents the magnetization curves at T = 4.2 K (-268.95°C) for $Zn_{0.95}Fe_{0.05}O$ samples 2 and 3 (see Table 1) treated at P = 5 GPa, T = 600°C and T = 700°C. It is seen that a hysteresis loop with coersive force of 165 and 400 Oe is observed for the both samples, respectively. The values of magnetization M estimated in 10 kOe field are $M = 9.71 \cdot 10^{-2}$ emu/g (or $4.1 \cdot 10^{-2}$ μ_B/Fe) and $M = 2.02 \cdot 10^{-1}$ emu/g (or $8.5 \cdot 10^{-2} \mu_B$/Fe), respectively. The temperature dependences M(T) in 1000 Oe field displayed in Fig. 6 allow us to suppose that the ferromagnetic state can be observed up to room temperatures at least in sample 3.

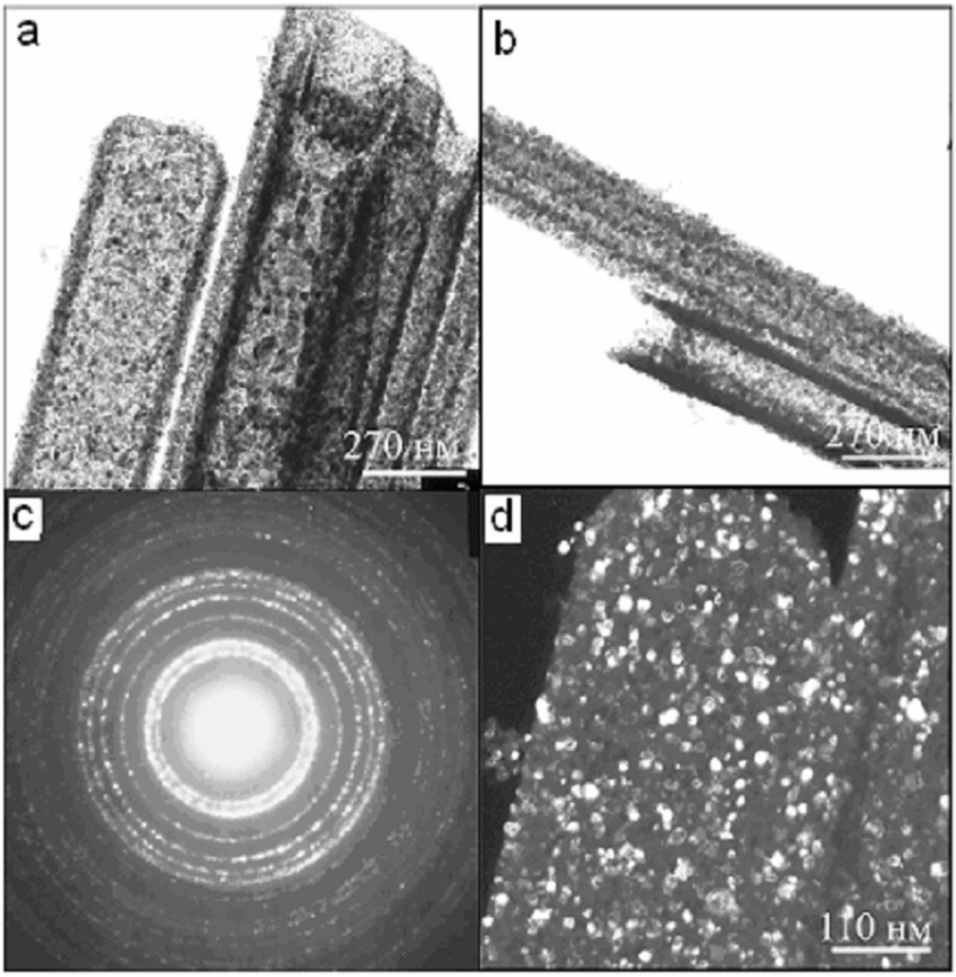

FIG. 3. The bright-field electron-microscope images of quasi-one-dimensional $Zn_{0.95}Fe_{0.05}O$ with tubular morphology (a, b). The Debye selected-area diffraction pattern (c) and the dark-field image (d) in $(100)_{ZnO}$, $(002)_{ZnO}$ and $(101)_{ZnO}$ reflections correspond to the polycrystalline nanodispersed structure of quasi-one-dimensional compounds. The average size of the crystallites is ~10 nm

Therefore the magnetization curves have been measured at T = 290 K (17°C) (Fig. 7). It was found that at room temperature, sample 2 is paramagnetic, i. e. magnetization increases linearly with a stronger magnetic field, while hysteresis is absent. By contrast, for sample 3, a hysteresis loop with coercive force of 100 Oe is observed, and magnetization estimated in 10 kOe field is $M = 8.25 \cdot 10^{-2}$ emu/g (or $3.5 \cdot 10^{-2} \mu_B$/Fe). Thus, it is shown that the increase in the treatment temperature from T = 600°C to T = 700°C results in more than twofold enhancement of magnetization in the region of liquid helium temperatures (transition from sample 2 to sample 3). At room temperature, sample 2 transforms into a paramagnetic state, whereas sample 3 still exhibits ferromagnetic properties. In work [21], investigations have been performed into magnetization of $Zn_{0.99}Fe_{0.01}O$ samples synthesized by annealing of a mixture of ZnO and Fe_3O_4 at P = 0; 2 and 5 GPa and T = 600°C for 30 min, which exhibited ferromagnetism in the temperature range from 5 K (-268°C) to 300 K (27°C). Moreover, the authors [21] also observed that magnetization grows when the pressure is increased during synthesis up to P = 5 GPa at constant temperature T = 600°C. Like in

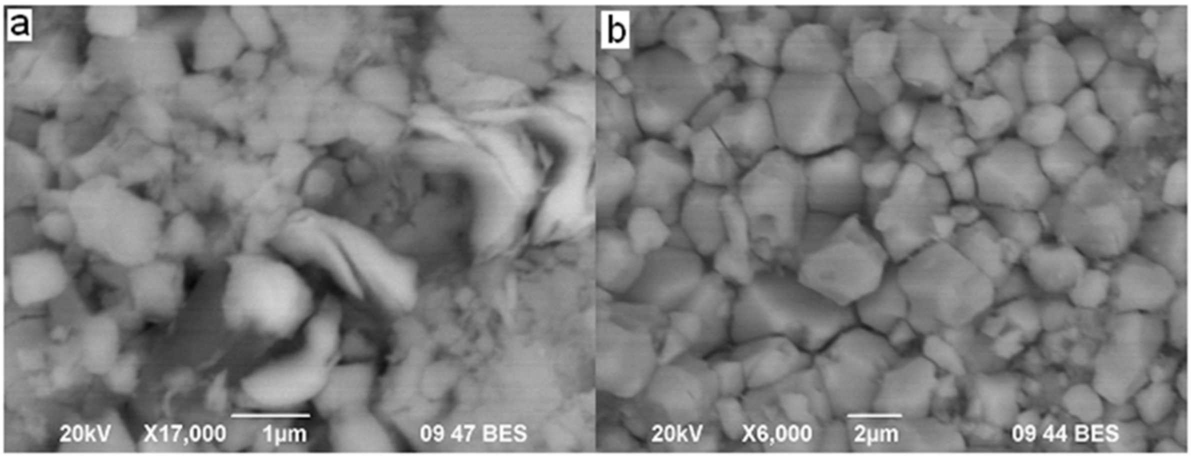

FIG. 4. The XEM images of the particles of the sample with the initial composition $Zn_{0.95}Fe_{0.05}O$ after heating under a pressure of 5 GPa at 600 (a) and 700°C (b)

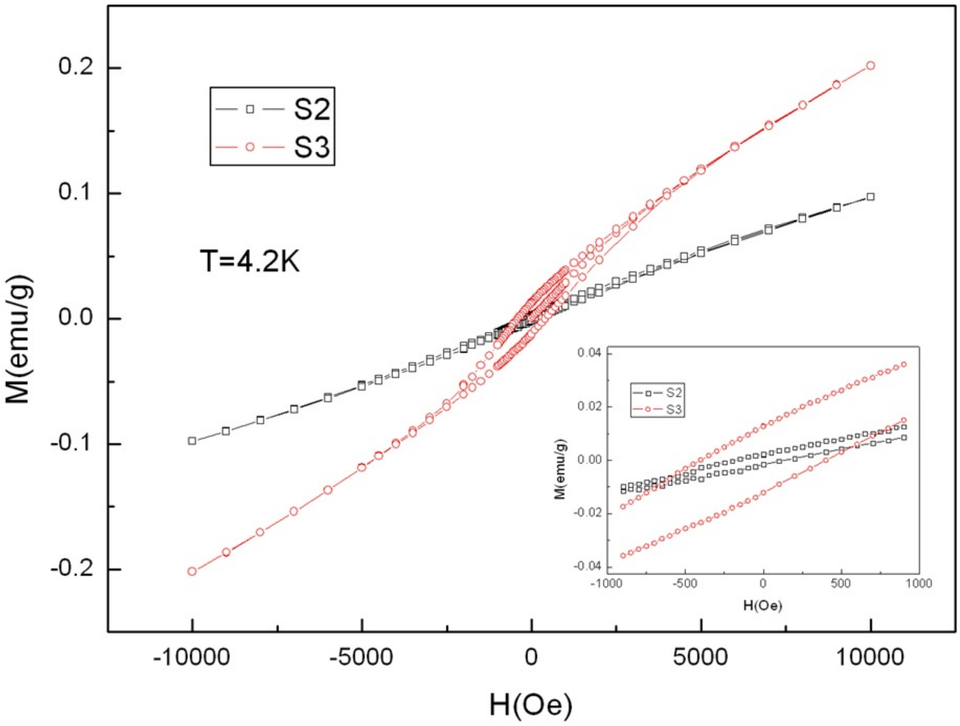

FIG. 5. The magnetizations curves of samples 2 (S2) and 3 (S3) at T = 4.2 K. The hysteresis loops for the both samples are shown in the inset

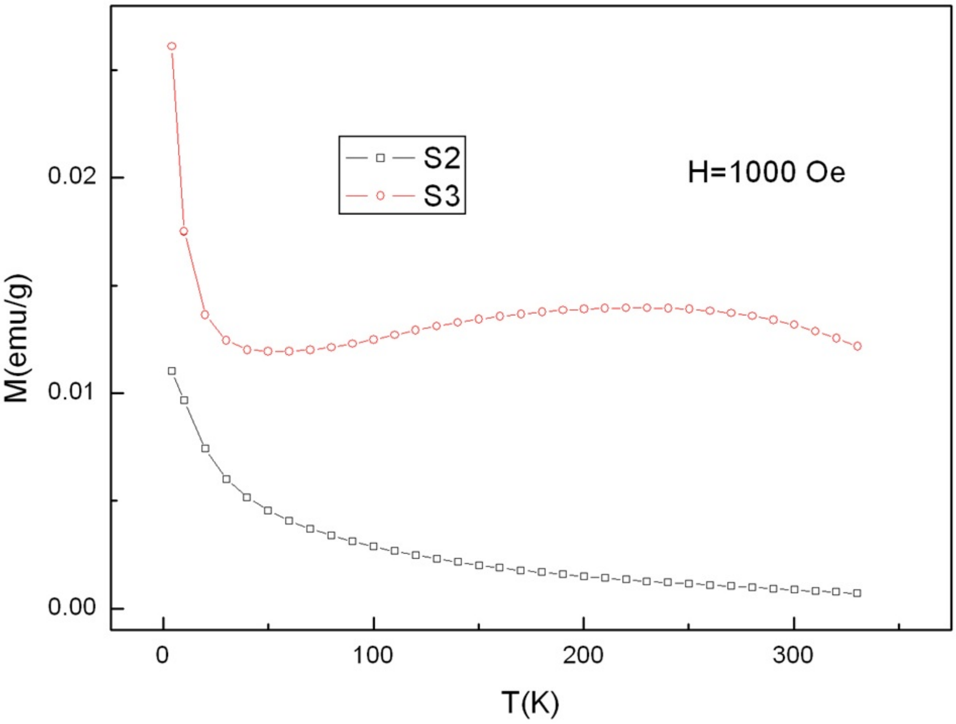

FIG. 6. The temperature dependences of magnetization for samples 2 (S2) and 3 (S3) in 1000 Oe field

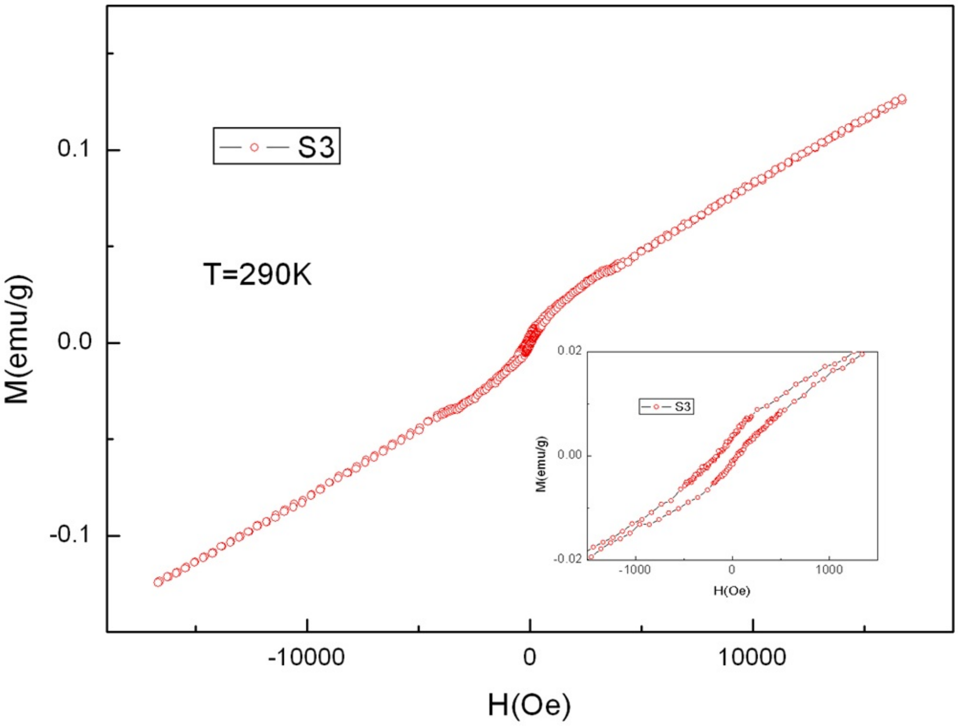

FIG. 7. The magnetizations curves of samples 2 (S2) and 3 (S3) at T = 290 K. The hysteresis loop is shown in the inset

work [21], we obtained comparable magnetization values for iron-doped zinc oxide samples, though their saturation fields are higher.

Thus, in the studies performed, it was established that thermobaric treatment of the oxide of the composition $Zn_{0.95}Fe_{0.05}O$ with tubular-shaped aggregates at T = 600°C and P = 5 GPa leads to the appearance of ferromagnetism and to the transformation of nanotubes into agglomerates having a rounded shape, which is similar to the shape of the particles of room-temperature ferromagnetics produced by solid-phase annealing of ZnO and Fe_3O_4 oxide mixtures under identical conditions [21].

Acknowledgments

The work was supported by the RFBR (grant No. 12-03-00453-) and the Presidium of RAS (project No. 12--3-1009).

References

[1] Cheng H., Cheng J., Zhang Y., Wang Q.-M. Large-scale fabrication of ZnO micro-and nano- structures by microwave thermal evaporation deposition. *Journal of Crystal Growth*, **299**(1), P. 34–40 (2007).

[2] Singh R. Unexpected magnetism in nanomaterials. *Journal of Magnetism and MagneticMaterials*, **346**, P. 58–73 (2013).

[3] Yilmaz C., Unal U. Synthesis and Characterization of Hierarchical ZnO Structures by a Single-Step Electrodeposition under Hydrothermal Conditions. *Electrochimica Acta*, **123**, P. 405–411 (2014).

[4] Murugadoss G. Synthesis and Characterization of Transition Metals Doped ZnO Nanorods. *J. Mater. Sci. Technol.*, **28**(7), P. 587–593 (2012).

[5] Ahmed F., Kumar S., Arshi N., et al. Direct relationship between lattice volume, band gap, morphology and magnetization of transition metals (Cr, Mn and Fe)-doped ZnO nanostructures. *Acta Materialia*, **60**, P. 5190–5196 (2012).

[6] Wibowo J.A., Djaja N.F., Saleh R. Cu- and Ni-Doping Effect on Structure and Magnetic Properties of Fe-Doped ZnO Nanoparticles. *Advances Mater. Phys. Chem.*, **3**, P. 48–57 (2013).

[7] Karmakar D., Dasgupta I., Das G.P., Kawazoe Y. High Temperature Ferromagnetism in Fe-Doped ZnO: a Density Functional Investigation. *Materials Transactions*, **48**(8), P. 2119–2122 (2007).

[8] Samariya A., Sighal R.K., Kumar S., et al. Defect-induced reversible ferromagnetism in Fe-doped ZnO semiconductor: An electronic structure and magnetization study. *Mater. Chem. Phys.*, **123**(2-3), P. 678–684 (2010).

[9] Limaye M.V., Sngh S.B., Das R., et al. Room temperature ferromagnetism in undoped and Fe doped ZnO nanorods: Microwave-assisted synthesis. *J. Solid State Chem.*, **184**, P. 391–400 (2011).

[10] Panigrahy B., ASlam M., Bahadur D. Effect of Fe doping concentration on optical and magnetic properties of ZnO nanorods. *Nanotechnology*, **23**, P. 11601 (2012).

[11] Lokesh R.N., Balakrishnan L., Jeganathan K., et al. Role of surface functionalization in ZnO:Fe nanostructures. *Mater. Sci. Eng. B*, **183**, P. 39–46 (2014).

[12] Colak H., Turkoglu O. Synthesis, Crystal Structural and Electrical Conductivity Properties of Fe-Doped Zinc Oxide Powders at High Temperatures. *J. Mater. Sci Technol*, **28**, P. 268–274 (2012).

[13] Wang F., Huang W.-W., Li S.-Y., et al. The magnetic properties of $Fe_xZn_{1-x}O$ synthesized via the solid-state reaction route: Experiment and theory. *Journal of Magnetism and Magnetic Materials*, **340**, P. 5–9 (2013).

[14] Denisha M.L., Jayanna H.S., Ashoka S., Chndrappa G.T. Temperature dependent electrical conductivity of Fe doped ZnO nanoparticles prepared by solution combustion method. *J. Alloys Compd*, **485**, P. 538–541 (2009).

[15] Dhiman P., Sharma S.K., Knobel M., Ritu R., Singh M. Magnetic Properties of Fe doped ZnO Nanosystems Synthesized by Solution Combustion Method Res. *J. Resent Sci*, **1**(8), P. 48–52 (2012).

[16] Behera A.K, Mohapatra N., Chatterjee S. Effect of Fe Doping on Optical and Magnetic Properties of ZnO Nanorods. *J. Nanosci. Nanotechnol*, **14**(5), P. 3667–3672 (2014).

[17] Wu G.S., Xie T., Yuan X.Y., et al. Controlled synthesis of ZnO nanowires or nanotubes via sol–gel template process. *Solid State Communications*, **134**, P. 485–489 (2005).

[18] Liu H., Yang J., Zhang Y., Yang L., Wei M., Ding X. Structure and magnetic properties of Fe-doped ZnO prepared by the sol–gel method. *J. Phys.: Condens. Mater.*, **21**, P. 145803 (2009).

[19] Zhang H.-W., Wei Z.-R., Li Z.-Q., Dong G.-Y. Room-temperature ferromagnetism in Fe-doped, Fe- and Cu-codoped ZnO diluted magnetic semiconductor. *Materials Letters*, **61**(17), P. 3605–3607 (2007).

[20] Wang Y.Q., Yuan S.L., Liu L., et al. Ferromagnetism in Fe-doped ZnO bulk samples. *J. Magnet. Magnetic Mater.*, **320**(8), P. 1423–1426 (2008).

[21] Wang Y.Q., Cheng X.R., Su L., et al. The structure and magnetic properties of $Zn_{0.99}Fe_{0.01}O$ synthesized under high pressure. *Solid State Commun.*, **152**(7), P. 581–584 (2012).

[22] Krasil'nikov V.N., Gyrdasova O.I., Buldakova L.Y., et al. Synthesis and Photocatalytic Properties of Highly Dispersed Zinc Oxide Doped with Iron. *Doklady Chemistry*, **437**(2), P. 496–498 (2011).

[23] Zhukov V.P., Krasil'nikov V.N., Perelyaeva L.A., et al. Electronic Band Structure and Optical Absorption of Nanotubular Zinc Oxide Doped with Iron, Cobalt, or Copper. *Phys. Solid State*, **55**(12), P. 2331–2339 (2013).

[24] Krasil'nikov V.N., Gyrdasova O.I., Buldakova L.Y., Yanchenko M.Y. Synthesis and Photocatalytic Properties of Low-Dimensional Cobalt-Doped Zinc Oxide with Different Crystal Shapes. *Russ. J. Inorg. Chem.*, **56**(2), P. 145–151 (2011).

[25] Gyrdasova O.I., Krasil'nikov V.N.., Shalaeva E.V., et al. Synthesis and Structure of Quasi-One-Dimensional Zinc Oxide Doped with Manganese. *Russ. J. Inorg. Chem.*, **57**(1), P. 72–78 (2012).

[26] Gyrdasova O.I., Krasil'nikov V.N., Melkozerova M.A., et al. Synthesis, Microstructure, and Native Defects of Photoactive $Zn_{1-x}Cu_xO$ Solid Solutions ($0 \leqslant x \leqslant 0.1$) with Tubular Aggregates. *Doklady Chemistry*, **447**(1), P. 258–261 (2011).

[27] Gyrdasova O.I., Melkozerova M.A., Krasil'nikov V.N., et al. Synthesis and Native Defectivity of $Zn_{1-x}V_xO$ ($0 \leqslant x \leqslant 0.03$) Photocatalysts. *Bull. Russ. Acad. Sci. Phys.*, **77**(3), P. 305–308 (2013).

[28] Melkozerova M.A., Krasil'nikov V.N., Gyrdasova O.I., et al. Effect of Doping with $3d$ Elements (Co, Ni, Cu) on the Intrinsic Defect Structure and Photocatalytic Properties of Nanostructured ZnO with Tubular Morphology of Aggregates. *Phys. Solid State*, **55**(12), P. 2340–2345 (2013).

[29] Gyrdasova O.I., Krasil'nikov V.N., Shalaeva E.V., et al. Optical and Photocatalytic Properties of Quasi-One-Dimensional ZnO Activated by Carbon. *Mendeleev Commun.*, **24**, P. 143–144 (2014).

NANOSYSTEMS: PHYSICS, CHEMISTRY, MATHEMATICS, 2014, 5 (4), P. 574–578

RHENIUM CARBIDES PREPARED BY THERMOBARIC TREATMENT OF NANOSIZED PRECURSORS

T. V. Dyachkova[1], A. P. Tyutyunnik[1], Yu. G. Zainulin[1], S. A. Gromilov[2,3]
[1]The Institute of Solid State Chemistry of the Ural Branch of the Russian Academy of Sciences, Ekaterinburg, Russia
[2]Nikolaev Institute of Inorganic Chemistry Siberian Branch of Russian Academy of Sciences, Novosibirsk, Russia
[3]Novosibirsk State University, Novosibirsk, Russia
dyachkova@ihim.uran.ru, tyutyunnik@ihim.uran.ru, zaynulin@ihim.uran.ru, grom@niic.nsc.ru

PACS 61.05.cp; 61.50.Ks

The products of thermobaric treatment ($P = 6$ GPa; $T = 1800$ °C) of mechanical mixtures of nanosized rhenium powder and sibunit have been studied. The formation of high-temperature phases with composition Re_2C has been revealed.

Keywords: rhenium, carbide, high-pressure cell, X-ray phase analysis.

Received: 16 June 2014
Revised: 30 June 2014

1. Introduction

Until the middle of the 20th century it was believed that rhenium did not form carbides [1–3], and there were no phases in the system, except for the interstitial solid solution based on the hexagonal close-packed (hcp) structure of rhenium. First, the partial Re–C diagram was drawn in reference [2], and solubility of carbon in rhenium at 2480 °C (eutectic temperature) was shown to be about 11.7 at.%. This solubility drops to 4.2 at.% at 1800 °C. The diagram and extent of the solubility of carbon in rhenium were confirmed in [4], and in addition, some considerations were expressed about the possibility of the existence of rhenium di- and monocarbides. In [5], the formation of rhenium-carbon compounds has been shown by thermal decomposition of rhenium carbonyl on the surface of molybdenum and graphite substrates heated up to 450–1180 °C. The authors, however, note that in such circumstances, one cannot exclude the formation of oxycarbide phases, as observed, for example, in the decomposition of tungsten carbonyl [6]. Indeed, the unit cell constants of the phase obtained in [5] (see Table 1) considerably exceed those of the hcp-lattice of rhenium [7] and the interstitial solid carbon-based solutions [2, 8]. In reference [9], a series of coatings were obtained by chemical vapor deposition of $Re_2(CO)_{10}$ and $Re(CO)_3(Cp)$ in conditions similar to [5]. It was shown that one can distinguish two groups. The first corresponds to the samples obtained at deposition temperatures ≥ 450 °C, the second – below this value. Unit cell constants of the first group coincide with the reference values of pure crystalline rhenium [7]. The second group is characterized by markedly increased unit cell constants, indicating the formation of interstitial solid solutions of carbon in rhenium (hereinafter $Re(C_x)$).

Significant progress in the synthesis of rhenium carbides is associated with the use of high temperature and pressure. For example, in [10] a phase, which the authors attributed to the γ'-C type of structure, was prepared at 6 GPa and 800 °C. Later, in [11], a phase with cubic NaCl type structure was obtained at 16–18 GPa and 1000 °C. Crystal data for the cubic and hexagonal

TABLE 1. Crystallographic data for rhenium carbides

Phases	a, Å c, Å	V/Z, Å^3 Sp. gr. (No.)	Cite
Re	2.7609 4.4576	14.71 $P6_3/mmc$ (194)	[7]
Re($C_{0,2}$)	2.792 4.471	15.09 — ·· —	[2]
Re($C_{0,11}$)	2.803 4.461	15.18 — ·· —	[8]
Re($C_{0,28}$)	2.794 4.460	15.08 — ·· —	[8]
Re_2C	3.02 4.76	18.80 — ·· —	[5]
ReC	4.005	$Fm-3m$	[11]
Re_2C	2.840(1) 9.85(1)	17.21 $P6_3/mmc$ (190)	[10]
Re_2C	2.8425(1) 9.8599(2)	17.25 — ·· —	[13]
Re_2C	2.8407(1) 9.8580(6)	17.31 — ·· —	[14]
Re_2C	2.845(1) 9.877(3)	17.31 — ·· —	[15]

rhenium carbides are shown in the Table 1. A phase with cubic symmetry has been also found in the products of electro spark processing of rhenium [12], but the question of its composition is still open. Thus, its formation has not been confirmed [13, 14]. In the study of rhenium-carbon diagram at pressures up to 70 GPa and temperatures up to 3730 °C, the authors argue that the formation of rhenium carbides below 10 GPa is impossible. However, in [15] hexagonal Re_2C was prepared at pressures of 2–6 GPa and temperatures of 600–1600 °C. In [16] we found such an impurity phase, which is formed in the experiment for obtaining Re_7B_3, through reaction of rhenium with the walls of the graphite heater. However, the thermobaric treatment of a mixture of nanocrystalline powder of rhenium and soot (high-pressure cell, 4 GPa, 2000 °C) did not result in the formation of Re_2C [17].

A model of the Re_2C crystal structure was first proposed in reference [10]. The authors showed that the phase belongs to the γ'-C structure type (space group $P6_3/mmc$, $Z = 4$). In the framework of this model, the most probable positions of carbon atoms were found by full-profile refinement of x-ray diffraction pattern [13]. The authors of [15] proposed to consider the Re_2C in the frame of ReB_2 type of structure, where the rhenium atoms occupy the $4f$ site (1/3; 2/3; 0.6085), and carbon atoms occupy the 2 site (1/3; 2/3; 0.25). In addition, they showed that the Vickers hardness of Re_2C reaches 17.5 GPa. Taking into account that hardness of ReB_2 is compatible with those of cubic BN and diamond [18], it seems to be interesting to study the possibility of formation of the rhenium carboborides. Several rhenium borides (ReB_2, Re_7B_3, Re_3B) have been prepared by us under high pressure and temperature (high-pressure cell, 10 GPa, 1800 °C) from mixtures of nanocrystalline rhenium and amorphous boron [16]. Preparation of phases in a high-pressure cell depends on a number of parameters. Besides the selection of the optimal program, describing the increase in pressure and temperature, holding time and decrease in pressure and temperature, the characteristics of the reaction mixture are

TABLE 2. Condition of the thermobaric treatment and results of X-ray phase analysis

No.	Ratio Re/C, weight	P, GPa T, °C t, min.	Phases	Content, weight %	a; c, Å	No. space group V, Å^3
1	2 : 1	6; 1800; 10	Re(C)	38	2.799; 4.466	194; 30.30
			Re_2C	62	2.843; 9.858	190; 69.00
2	1 : 0.8	6; 1800; 10	Re(C)	4	2.804; 4.466	194; 30.41
			Re_2C	96	2.843; 9.850	190; 68.95
3	1 : 0.85	6; 1800; 20	Re_2C	100	2.842; 9.855	190; 68.93
4	1 : 1	10; 1800; 20	Re_2C	100	2.842; 9.856	190; 68.94
5	1 : 0.5C : 0.5B	10; 1800; 15	Re_7B_3*	69*	7.516; 4.877	186; 238.6
			ReB_2	31**	2.900; 7.480	194; 5448
6	1 : 0.5C : 1.5B	10; 1800; 15	Re_7B_3	60***	7.514; 4.879	186; 238.6
			ReB_2	33	2.901; 7.481	194; 54.48

* The sample contained 2 wt.% of CCO_3 (material of high-pressure cell).

** For Re_7B_3: $a = 7.509$, $c = 4.880$ Å [19]; for ReB_2: $a = 2.8985$, $c = 7.4798$ Å.

*** The sample contained 7 wt.% of graphite.

extremely important. These characteristics are associated with a history of preparation of reagents: homogenization, compacting, pressing, preliminary annealing, etc. These operations in turn depend on the fineness of the starting materials. Using nanocrystalline reagents can fundamentally change the course of synthesis. Preparation of rhenium-containing phases forces us to consider such a factor as the fast oxidation of polycrystalline rhenium. The form of carbon can play a decisive role for synthesis of rhenium carbides. As already mentioned, processing of the mixture of nanocrystalline rhenium powder and soot (high-pressure cell, 4 GPa, 2000 °C) did not result in formation of rhenium carbides. It seems interesting to replace the soot for the alternative reagent — sibunit, characterized by chemical stability, high electrical conductivity, high specific surface, etc. [19].

2. Experimental

Nanocrystalline powder of rhenium (coherent scattering region ~ 30 Å) was prepared analogously to [16] by decomposition of $NH_4(ReO_4)$ in hydrogen. Mixtures of rhenium and sibunit powders taken in desired ratios were thoroughly mixed. Thermobaric treatment of mechanical mixtures was performed in a 'toroid' type high-pressure cell in standard scheme [20]. The sample was compressed between the press anvils to the required pressure, and then temperature was slowly increased (~ 100 °/min). After holding under pressure at a given temperature the sample was quenched by a sharp decrease in temperature. Then the pressure was released and container with the sample was removed. Samples with boron (black amorphous boron was used) were prepared in similar way. Experimental conditions are given in Table 2.

Samples obtained in the experiments were mechanically strong pellets. For x-ray powder diffraction study, a part of the sample was cut and ground in heptane. Then, the suspension was applied on the polished side of a standard cell. After drying the samples consisted of layer of thickness ~ 100 microns. Polycrystalline silicon, prepared analogously, was used as an external standard. X-ray powder diffraction data were collected on the diffractometers STADI-P (STOE) (CuKα1 radiation, transmission geometry, linear PSD) and ARL X'TRA (CuKα radiation, Bragg-Brentano geometry, semiconductor detector) at room temperature. Unit

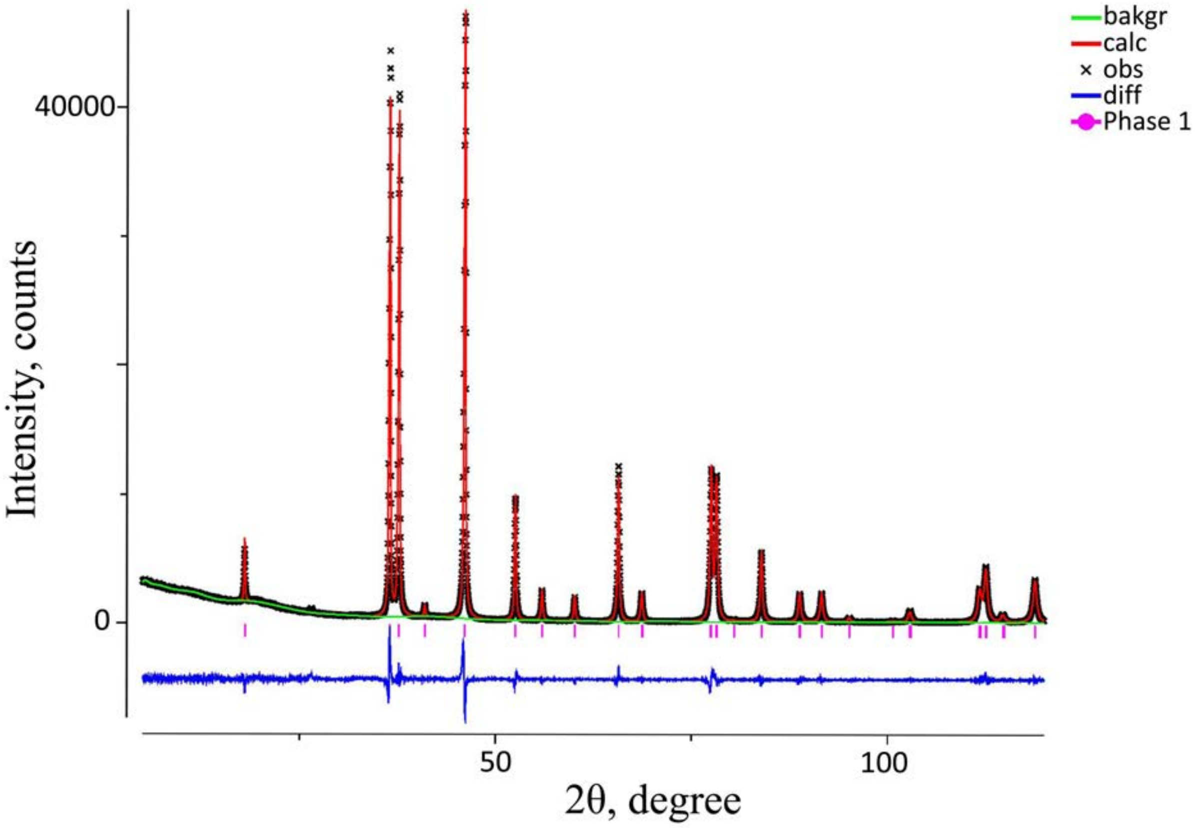

FIG. 1. Result of full-profile refinement of X-ray powder diffraction data for the sample obtained in experiment No. 4. $wRp = 6.42$, $Rp = 4.66$, $\mathrm{CHI}^2 = 5.107$, $R(F^2) = 1.41$ %

cell constants were determined using Rietveld refinement with Powder Cell 2/4 program [21], the crystallographic data are given in Table 2.

3. Discussion and conclusion

An analysis of data in Table 1 and 2 leads to the following conclusions. In contrast to the experiments carried out in reference [17], where treatment (high-pressure cell, 4 GPa, 2000 °C, 3 min) of a mixture of rhenium and soot resulted in Re(C_x) only, use of sibunit [19] under approximately the same conditions allowed us to obtain samples containing Re_2C (experiments 1–4). Sibunit is a synthetic porous composite material which is obtained from soot. Using sibunit and nanocrystalline rhenium in our experiment allowed the reduction of synthesis time by a factor three compared to reference [17].

The single phase samples of Re_2C were shown to be formed only with an excess of carbon. The same conclusion was reached by the authors of [17], where single phase products were obtained by treatment of mixtures with Re/C ratios from 1:2 to 2 : 0.5 at 6 GPa and 1600 °C. In our experiments, single phase products were obtained by treatment of mixtures Re/C = 1 : 0.85 (exp. No. 3) and Re/C = 1 : 1 (exp. No. 4). The good agreement of the unit cell constants for Re_2C obtained in our experiments, as well as in [13–15], indicates good reproducibility of the composition for this phase. The results of full-profile refinement of x-ray powder diffraction data of sample No. 4 using GSAS [22] in the frame of ReB_2 type of structure (Re — 1/3; 2/3; 0.6085; C — 1/3; 2/3; 0.25) are shown in Fig. 1.

There were no rhenium carboborides found as a product of treatment of mixtures of nanocrystalline rhenium, sibunit and amorphous boron (exp. No. 5–6).

References

[1] Trzebiatovski W. Über die Beziehungen des Rheniums zum Kohlenstoff. *Z. Anorg. Chem.*, **223**, P. 376–377 (1937).

[2] Hughs J.E. A survey of the rhenium-carbon system. *J. Less-Common Metals*, **1** (5), P. 377–381 (1959).

[3] Savitskii E.M., Tylkina M.A., Povarova K.B. *Rhenium alloys*. Science, Moscow, 1965, 335 p.

[4] Evstyuhin A.I., Godin Yu. G., Kohtev S.A., Suchkov I.I. Metallurgy and Metal science pure metals. Gosatomizdat, Moscow, **5**, P. 149–159 (1963).

[5] Babad-Zahryapin A.A., Lysenko L.T., Gert L.M., Valyavko L.R. *Inorganic Materials*, **5**, P. 1133–1135 (1969).

[6] Babad-Zahryapin A.A., Valyavko L.R., Gert L.M. *Inorganic Materials*, **4**, P. 1366–1367 (1968).

[7] Wasilevski R.J. Physical and mechanical properties of rhenium. *Transaction of the Metallurical Society of Aime*, **221**, P. 1081–1082 (1961).

[8] Har'kova A.M., Velikanova T.Yu. The structure of alloys of rhenium-carbon in an area rich in rhenium. *Powder metallurgy*, **12**, P. 52–56 (1987).

[9] Gelfond N.V., Morozova N.B., et al. Structure of rhenium coatings produced by MOCVD. *Journal of Structural Chemistry*, **50** (6), P. 1179–1186 (2009).

[10] Popova S.V., Boiko L.G. A new rhenium carbide formed by high-pressure treatment. *High Temperature - High Pressures*, **3**, P. 237–238 (1971).

[11] Popova S.V., Fomicheva K.N., Khvostantsev L.G. Synthesis and superconducting properties of cubic rhenium monocarbide. *JETP Letters*, **16** (11), P. 609–610 (1972).

[12] Asanov U.A. The synthesis of compounds of metals in terms of their electron destruction in liquid dielectrics: Author. Diss., Alma-Ata, 1972, 50 p.

[13] Juarez-Arellano E.A., Winkler B., et al. Reaction of rhenium and carbon at high pressures and temperature. *Z. Kristallogr.*, **223**, P. 492–501 (2008).

[14] Juarez-Arellano E.A., Winkler B., et al. Stability field of the high-(P, T) Re_2C phase and properties of an analogous osmium carbide phase. *J. Alloys and Compounds*, **481**, P. 577–581 (2009).

[15] Zhao Z., Cui L., et al. Re_2C: crystal structure, hardness, and ultra-imcompressibility. *Crytal Growth & Design*, **10** (12), P. 5024–5026 (2010).

[16] Tyutyunnik A.P., Dyachkova T.V., Zainulin Yu.G., Gromilov S.A. The structure of the monoclinic modification Re_3B. *Journal of Structural Chemistry*, **55** (1), P. 88–93 (2014).

[17] Gromilov S.A., Shubin Yu.V., et al. X-ray diffraction study of the products of thermobaric treatment of solid solution $Re_{0,67}Rh_{0,33}$. *Journal of Structural Chemistry*, **48** (1), P. 52–57 (2008).

[18] Chung H-Y, Weinberger M.B., et al. Synthesis of Ultra — Incompressible Superhard Rhenium Diboride at Ambient Pressure superhard rhenium diboride at ambient pressure. *Science*, **316**, P. 436–439 (2007).

[19] Plaksin G.V. Porous carbon materials such Sibunit. *Chemistry for Sustainable Development*, **9**, P. 609–620 (2001).

[20] Bradley C.C. *High pressure methods in solid state research*. London, Butterworth, 1969.

[21] Kraus W., Nolze G. POWDER CELL — a program for the representation and manipulation of crystal structures and calculation of the resulting X-ray powder patterns. *J. Appl. Cryst.*, **29**, P. 301 (1996).

[22] Larson A.C., Von Dreele R.B. General Structure Analysis System (GSAS). Los Alamos National Laboratory, Report LAUR 86-748 (2004).

NANOSYSTEMS: PHYSICS, CHEMISTRY, MATHEMATICS, 2014, 5 (4), P. 579–589

A FACILE ROUTE OF COUPLING OF ZnO NANORODS BY CdS NANOPARTICLES USING CHEMICAL BATH DEPOSITION

N. S. Kozhevnikova, O. I. Gyrdasova, A. S. Vorokh, I. V. Baklanova, L. Yu. Buldakova

Institute of Solid State of the Ural Branch of Russian Academy of Sciences,
Ekaterinburg, Russia

kozhevnikova@ihim.uran.ru

PACS 71.20.Nr, 71.55.Gs, 78.30.Fs

Cadmium sulfide nanoparticles (NPs) coupled to zinc oxide nanorods (NRs) were synthesized in a two step deposition process at relatively low temperatures. The ZnO NRs were grown using solvothermal method, followed by the deposition of CdS NPs at 50 °C using *in-situ* and *ex-situ* synthesis from aqueous solutions. The samples were characterized by X-ray diffraction, scanning electron microscopy, and optical absorption. When the ZnO NRs are coated by the CdS NPs, the optical absorption is enhanced and band edge is shifted towards visible region as compared with ZnO NRs. Photocatalytic activity of the synthesized ZnO NRs / CdS NPs composites in the photooxidation of hydroquinone $C_6H_4(OH)_2$ in aqueous solution is closely connected with the coupling route.

Keywords: Cadmium sulfide nanoparticles, zinc oxide nanorods, coupled inorganic semiconductors, chemical bath deposition.

Received: 16 June 2014
Revised: 30 June 2014

1. Introduction

Inorganic nanostructures have become ideal systems for revealing novel phenomena at nanoscale, leading to a wide range of applications [1–3]. Depending upon the dimensionality and the capability of tailoring the morphology, they are becoming essential for smart and functional materials. Foremost, numerous research efforts have been concentrated on the environmental use of semiconductor inorganic materials as photocatalysts in processes such as the decomposition of toxic organic compounds and hydrogen production via water photolysis [4]. A variety of geometrical morphologies [5–8] are being investigated for the different semiconductor nanostructures to explore novel properties out of those materials. Among the various photocatalytic semiconductor materials, metal-oxide semiconductors such as ZnO (3.2 eV), TiO_2 (3.2 eV), α-Fe_2O_3 (3.1 eV) and WO_3 (2.8 eV) have been researched intensively as practically applicable photocatalysts, because of their high photocatalytic activities and economical synthetic routes [9, 10]. However, these single metal-oxide photocatalysts have wide band-gap energies, which are disadvantageous for the absorption and use of the visible light region of solar energy. To improve photocatalytic activities, composite semiconductor photocatalyst systems with different geometry [11–16] have received a great deal of attention because of two important reasons. First, in the composite semiconductor systems with different energy levels, wide band-gap semiconductors can utilize visible light by coupling narrow/mid band-gap semiconductors (CdS, In_2S_3, Bi_2O_3) which are visible light active materials [17, 18]. Second, charge injection from one semiconductor into another can lead to efficient and longer charge separation by reducing the electron – hole pair recombinations [19, 20]. The coupled semiconductors, in particular, are attracting attention not only for their successful implementation in the photocatalytic degradation of organic pollutants, but also in renewable energy conversion [21, 22] as a new generation of solar cells.

Among the different photoactive semiconductor nanostructures, the ZnO based nanocomposites [12–14] gained extreme importance for its different advantages, such as direct band gap, ease of crystallization, anisotropic growth, nontoxicity, higher excitation binding energy of 60 meV, higher electron mobility (200 $cm^2V^{-1}s^{-1}$) and simplicity in tailoring the morphology. CdS (bulk band gap 2.42 eV) is one of the most appropriate sensitizer for ZnO. Recently, many groups have attempted to develop different synthetic routes for the efficient creation of CdS–ZnO heterojunctions with different morphology. The study of CdS/ZnO system for photocatalytic effect not only varies in synthesis technique but also has wide variety of efficiency, according to the structure of the composite. Different CdS–ZnO systems, e.g. flower-like CdS-ZnO nanocomposite [11], urchin like CdS@ZnO [16], nanotubes arrays of CdS/ZnO [23], partially or fully covered CdS nanoparticles on ZnO nanorods [24], ZnO/CdS core shell nanorods [14], CdS nanoparticles/ZnO nanowires heterostructure [25, 26] have been reported. Nevertheless, such key factors like the development of facile methods for the synthesis, surface modification, linking and sensitizing CdS NPs to ZnO still remain unsolved. This problem is very urgent, because despite the advantages known for using coupled semiconductors, the conversion efficiency of such structures is still not very high and requires further development. Two possible reasons for the low photovoltaic performance are the difficulty of assembling NPs into mesoporous oxide film and the presence of a large number of unpassivated or partially passivated surface states. These surface states can act as trap centers for holes and electrons, leading to lower photovoltage and photocurrent [27].

Today for the sensitization of semiconductor NPs to TiO_2, generally two routes are followed:

(i) *In-situ* synthesis and deposition of NPs by chemical bath deposition (CBD) [28] or successive ionic layer adsorption and reaction (SILAR) [29] method. In this route the NPs are directly grown onto the oxide material surface by the chemical reaction of respective ionic species.

(ii) *Ex-situ* route linking the synthesized colloidal NPs to the oxide material surface via a bifunctional linker [30].

Both routes have their own advantages and disadvantages. The former route shows better performance due to less spatial distance between the NPs and the substrate surface. While the latter route has an advantage of controlling the NPs properties like size and shape. In both routes, the growth rate is controllable by solution, pH, temperature and relative concentrations of the reactants in the bath solution.

In this work, we report our observations following the use of both routes for the coupling of CdS NPs to the ZnO nanorods (NRs) which were grown using the solvothermal method. We have analyzed the effect of chemical route on the coverage quality of ZnO NRs by CdS NPs. The structural and optical properties of the coupled semiconductor ZnO NRs – CdS NPs have been investigated. This composite semiconductor showed the visible light absorption and photocatalytic activity.

2. Experimental

2.1. Materials used

To synthesize ZnO NRs, the following precursors were used: zinc oxide ZnO, formic acid HCOOH and ethylene glycol $HO(CH_2)_2OH$. The precursors employed to synthesize CdS

NPs by CBD include cadmium chloride hydrate $CdCl_2{\cdot}2H_2O$, thiourea $SC(NH_2)_2$, aqueous ammonia (NH_4OH) (19 %) and ethylenediaminetetraacetic acid disodium salt dihydrate $C_{10}H_{14}N_2Na_2O_8$ (Na_2EDTA). Sodium hydroxide NaOH was used for adjusting the pH. Sodium sulfide nonahydrate $Na_2S{\cdot}9H_2O$ was used for synthesis of colloid CdS NPs. All the chemicals were purchased and used as procured for all stock solution preparations.

2.2. Preparation of ZnO NRs

Firstly, ZnO NRs were synthesized by solvothermal method based on the thermolysis of the organometallic complexes and reported elsewhere [31–33]. For the present investigation, the formate glycolate zinc complexes $Zn(HCOO)(OCH_2CH_2O)_{1/2}$ with fiber shaped crystals were pre-synthesized via two steps

$$\mathrm{ZnO + 2HCOOH + H_2O \Rightarrow Zn(HCOO)_2 \cdot 2H_2O}, \tag{1}$$

$$\begin{gathered}\mathrm{Zn(HCOO)_2 \cdot 2H_2O + 1/2HOCH_2CH_2OH \Rightarrow} \\ \mathrm{Zn(HCOO)(OCH_2CH_2O)_{1/2} + HCOOH \uparrow + 2H_2O}.\end{gathered} \tag{2}$$

The latter interaction of zinc formate $Zn(HCOO)_2{\cdot}2H_2O$ with ethylene glycol was carried out at temperature not higher than 120 °C. The solid reaction products were separated from the liquid phase by vacuum filtration, washed with anhydrous acetone, and dried at 40 °C to remove acetone. Thermal decomposition of fibrous $Zn(HCOO)(OCH_2CH_2O)_{1/2}$ to ZnO in air is an exothermic process that occurred at 450 °C over 4 h. The post-annealed particles of the formed ZnO NRs acquired the fibrous shape of the $Zn(HCOO)(OCH_2CH_2O)_{1/2}$ precursor crystals.

2.3. Preparation of CdS aqueous colloid solution

To prepare stable aqueous colloidal solutions of CdS nanoparticles, solutions of 12.5 mM $CdCl_2$, 12.5 mM Na_2S, 12.5 mM Na_2EDTA were mixed at room temperature under continuous stirring. The starting concentration ratio of the precursor ions in a solution was equal to $Cd^{2+} : S^{2-} : EDTA^{4-} = 1 : 1 : 1$ [34, 35]. While mixing the precursor solutions, two reactions occur:

$$\mathrm{CdCl_2 + Na_2EDTA \Rightarrow Cd(EDTA) + 2NaCl}, \tag{3}$$

$$\mathrm{Cd(EDTA) + Na_2S \Rightarrow CdSv + Na_2EDTA}. \tag{4}$$

Both aggregate and sedimentation stability of the colloidal solution is achieved through the formation of double ion and the adsorption-solvate layers at the adsorption of ions $EDTA^{4-}$ on the surface of the CdS disperse phase [34, 35].

2.4. Coupling of ZnO NRs by CdS NPs

In-situ synthesis (CBD): The CdS NPs were deposited on ZnO NRs from a chemical bath containing: (i) 5 mM $CdCl_2$, 25 mM thiourea and 2 % NH_4OH at pH = 12.5 (sample 1); (ii) 5 mM $CdCl_2$, 25 mM thiourea and 10 mM Na_2EDTA at pH = 13.5 (adjusted with NaOH) (sample 2). In both cases, the ZnO NRs powder was immersed in the chemical bath solution for 180 min at 50 °C. Aqueous ammonia and Na_2EDTA solution act as a complexing agents forming intermediate cadmium complexes $[Cd(NH_3)_4^{2+}]Cl_2$ or [Cd(EDTA)] releasing cadmium ions. The alkaline medium provides sulfide ions via the conversion of thiourea to cyanamide.

During CBD the CdS NPs are directly grown onto the ZnO NRs surface by the overall chemical reactions of respective ionic species:

$$\mathrm{Cd(NH_3)_4Cl^{2+} + SC(NH_2)_2 + 2NH_4OH \Rightarrow CdS + H_2NCN + 4NH_3 + 2NH_4Cl + 2H_2O}, \quad (5)$$

$$\mathrm{Cd(EDTA) + SC(NH_2)_2 + 2NaOH \Rightarrow CdS + H_2NCN + Na_2EDTA + 2H_2O}. \quad (6)$$

Using ammonia complexes, $Cd(NH_3)_4Cl_2$ leads to supersaturation with respect to $Cd(OH)_2$ and as a result, to $Cd(OH)_2$ crystal formation at the first stage of the CBD process [36,37]. The second stage leads to the CdS solid phase formation. The overall reaction (5) should be written as

$$\mathrm{Cd(NH_3)_4Cl_2 + 2NH_4OH \Rightarrow Cd(OH)_2 + 4NH_3 + 2NH_4Cl}, \quad (7)$$

$$\mathrm{Cd(OH)_2 + SC(NH_2)_2 \Rightarrow CdS + H_2NCN + 2H_2O}. \quad (8)$$

The presence of the Cd(EDTA) complex prevents formation of the oxygen containing compound while CdS synthesis and is described by (6).

Formation of $Cd(OH)_2$ phase is important synthetic factor for two reasons. Firstly, it is well known that interdiffusion occurs between the CdS sensitized layers during the annealing in oxide and chalcogenide solar cells [38]. Sulfur diffusion is responsible for the thinning of the CdS film and this may result in poor device performance. Oxygen has been shown to reduce the diffusion of S. The reason is likely the Cd–O bonds at the grain boundaries, which reduce the S diffusion [39]. Secondly, it is an experimental fact that high quality adherent CdS layers and films can be obtained from alkaline baths, which are in a formal sense supersaturated with respect to the precipitation of the oxygen containing compound, namely $Cd(OH)_2$, and this holds irrespective of the substrate employed and substance sensitized [40]. It is well known that the carboxylic group in the dyes plays vital role for the adsorption of the dyes upon oxide surface in quantum dot sensitized solar cells [41].

For these reasons we decide to synthesize ZnO–CdS composites both with and without $Cd(OH)_2$ and trace the influence of $Cd(OH)_2$ on microstructure and properties of composites.

Ex-situ synthesis (colloid synthesis): The powder of ZnO NRs was immersed into the aqueous colloid solution of CdS NPs and maintained for 180 min at 50 °C. The CdS NPs are then linked onto the ZnO NRs surface via the absorption processes (sample 3).

After the CBD and colloid synthesis, the powder samples were filtered, washed with deionized water and air dried.

2.5. Crystal structure, microstructure, optics and photocatalytic activity measurements

X-ray diffraction (XRD) patterns of ZnO NRs / CdS NPs composites were obtained using a Shimadzu MAXima-X XRD-7000 automatic diffractometer with CuKα ($\lambda = 1.5406$ Å) with 2θ angle step 0.03 ° and exposition time of 10 sec. The scanning electron microscopy (SEM) was carried out in order to analyze the microstructure and morphology of all synthesized samples using JEOL-JSM LA 6390. To confirm the change in bandgap, the UV and Vis spectra in the wavelength range of 300–700 nm ($BaSO_4$ was used as the standard) of bare ZnO NRs and ZnO NRs / CdS NPs composites were recorded using Shimadzu UV-2401 PC spectrophotometer.

To examine the photocatalytic activity, hydroquinone $C_6H_4(OH)_2$ (HQ) dye was chosen for the photodecomposition study. The ZnO NRs coupled by CdS NPs composite samples were immersed in 0.4 mM of HQ aqueous solution and irradiated by a blue light fluorescent lamp with the emission maximum in the wavelength range of 440–460 nm. The remaining amounts of HQ in the solution were determined by voltammetry on a PU-1 polarograph at a potential sweep rate of 0.030 V/s.

3. Results and discussion

X-ray diffraction patterns of CdS–ZnO composites (Fig. 1) show narrow peaks of highly crystalline ZnO (space group No. 186, $P6_{3mc}$) and broad peaks of nanostructured CdS. The crystal structure of CdS can be identified as random close-packed structure (RCP) with an average lattice having unit cell parameters $a = 0.236$ nm and $c = 0.334$ nm [42]. The Cd and S atoms in the unit cell of the average lattice occupy single positions as $P6$ and 1(a) with the coordinates (0 0 z), where $z = 0$ and $1/\sqrt{24}$, respectively; the filling factor of these positions is 1/3. In sample 2, some broad peaks pointed to the high probability of ordering CdS nanoparticles to hexagonal closepacked structure (HCP, space group No. 186, $P6_{3mc}$). In sample 3, the crystal structure of CdS NPs is amorphous. Sample 1 contains crystalline $Cd(OH)_2$ (space group No. 164, $P-3m1$) and phase ratio are equal ZnO : CdS : $Cd(OH)_2$ = 17 : 52 : 31. Samples 2 and 3 do not contained hydroxide, and CdS portion is 19 % (vol.) in sample 2, and less the 1 % in sample 3.

The photo gallery of Fig. 2 shows the typical SEM images of the synthesized ZnO and ZnO–CdS nanocomposite structure. Particles of bare ZnO are extended micrometer-sized aggregates with a fine fibrous structure (Fig. 2a) which may be called NRs. Fig. 2 (b–d) shows the morphology of ZnO NRs while coupling by CdS. To corroborate the chemical and phase analysis, EDX was carried out and the results show the existence of Cd, S, Zn and O elements in CdS–ZnO nanocomposites, but the atom space distribution in the samples 1–3 is quite different. On the scale of SEM, sample 1 is a mixture of ZnO NRs and well-shaped hexagonal prisms of nearly the same size in the micrometer range (Fig. 2b). With a focused beam, EDX exclusively confirmed Cd, O and S species were found inside these hexagonal prisms, therefore they are identified as $Cd(OH)_2$ polycrystals containing about 10 at.% of CdS. The highest concentration of CdS in sample 1 is located on the ZnO NRs surface. Sample 2 is also predominantly a mixture of ZnO NRs and nanocrystalline CdS particles (Fig. 2c). It is evident from Fig. 2d that the sample 3 is ZnO NRs – CdS NPs composite material formed by polycrystals of a nearly uniform fiber like morphology.

Image 2(a–d) clearly exhibits the porous nature of the ZnO NRs. This porous structure of ZnO helps in the coupling of CdS NPs, because when NPs are embedded on ZnO, NPs actually occupy these pores where they get adsorbed.

The fulfilled XRD phase analysis of sample 1 confirmed by SEM proves the reaction mechanism of CdS formation to be considered the same as proposed by Kitaev et al. [36] (see eq. 7, 8).

Figure 3 shows the optical absorption spectra of the of bare ZnO NRs and ZnO NRs / CdS NPs composite samples 1–3, which were synthesized according to the procedure described above. The increase in the absorption spectra of samples 1–3 at 420–480 nm suggests the presence of at least two phases, confirming XRD and SEM data. As can be seen from this figure, the fundamental absorption band edge of the ZnO NRs / CdS NPs composite is shifted toward lower energies with respect to the absorption band of the initial bare ZnO. In order to determine the effective band gaps, the absorption spectra were converted to the form $(\alpha h\nu)^2 = f(h\nu)$. The dependence of the absorption coefficient for ZnO as a direct band gap semiconductor on the frequency near the absorption edge is described by equation (9)

$$\alpha(\nu) = \left[A(h\nu - E_g)^{1/2}\right]/h\nu, \tag{9}$$

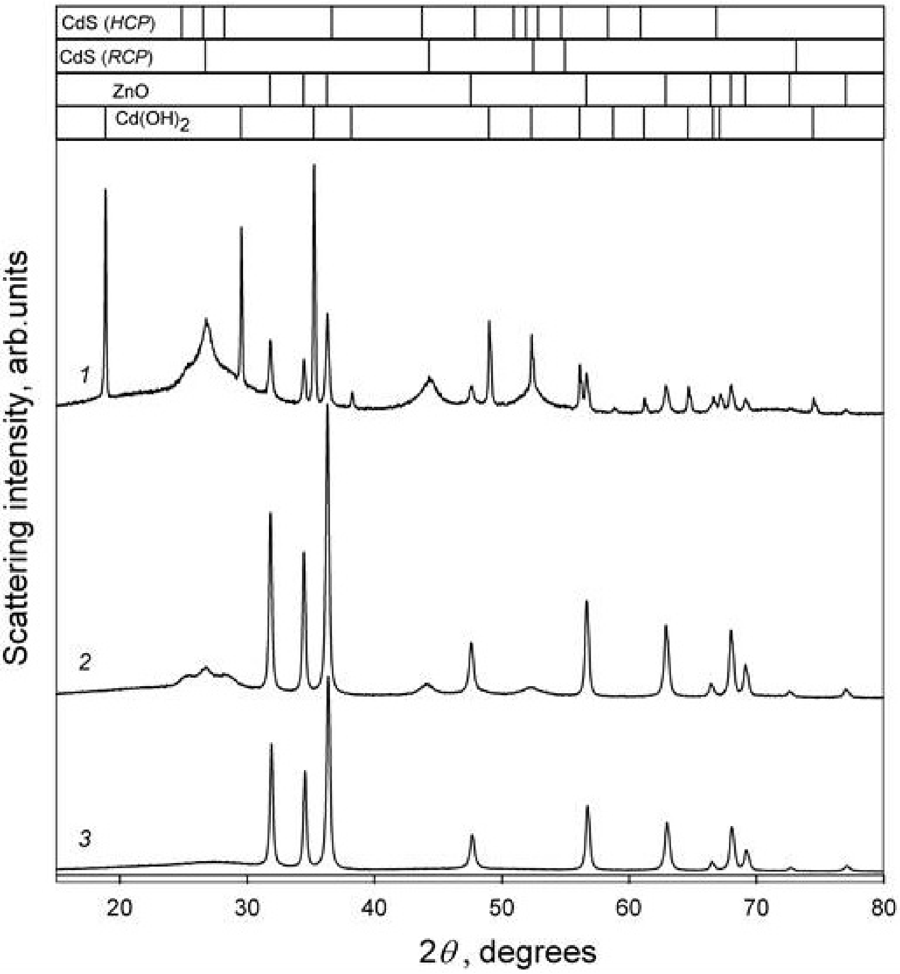

FIG. 1. X-ray diffraction patterns of ZnO-CdS nanocomposites. ZnO NRs are coupled by CdS NPs in aqueous solutions via following routes: 1 — *in-situ* CBD synthesis using ammonia complexes $Cd(NH_3)_4^{2+}$; 2 — *in-situ* CBD synthesis using EDTA complexes $Cd(EDTA)^{2-}$; 3 — *ex-situ* synthesis using pre-synthesized CdS colloid solution

where α is the absorption coefficient, $h\nu$ is the photon energy, E_g is the optical band gap, and A is a constant that does not depend on the frequency ν [43]. According to this equation, the optical band gap can be obtained by the extrapolation of the linear part of the $(\alpha h\nu)^2 = f(h\nu)$ to the intersection with the abscissa axis. The determined Eg values are presented in Table 1.

Optical absorption data suggest the following conclusions. The intensity of absorption from 440–480 nm after coupling ZnO NRs to CdS NPs increases with increased CdS content and reaches its maximum for sample 1. Furthermore, the blue shift of the absorption edge is due to exciton confinement in CdS NPs. For this reason, CdS NPs with size of 2 nm (sample 3) reduce the absorption intensity greatly from 440–480 nm.

To demonstrate the effects of visible light absorption ability of the ZnO NRs / CdS NPs composites on photocatalytic activity, we tested the samples under conditions similar to that of natural solar-light irradiation. The photocatalytic properties of the synthesized ZnO NRs / CdS NPs composites are examined using model reaction of HQ oxidation in aqueous medium. The kinetic curves of HQ oxidation, demonstrating a change in the HQ concentration with time under visible light irradiation (440-460 nm), are shown in Fig. 4. The inset of Fig. 4 shows

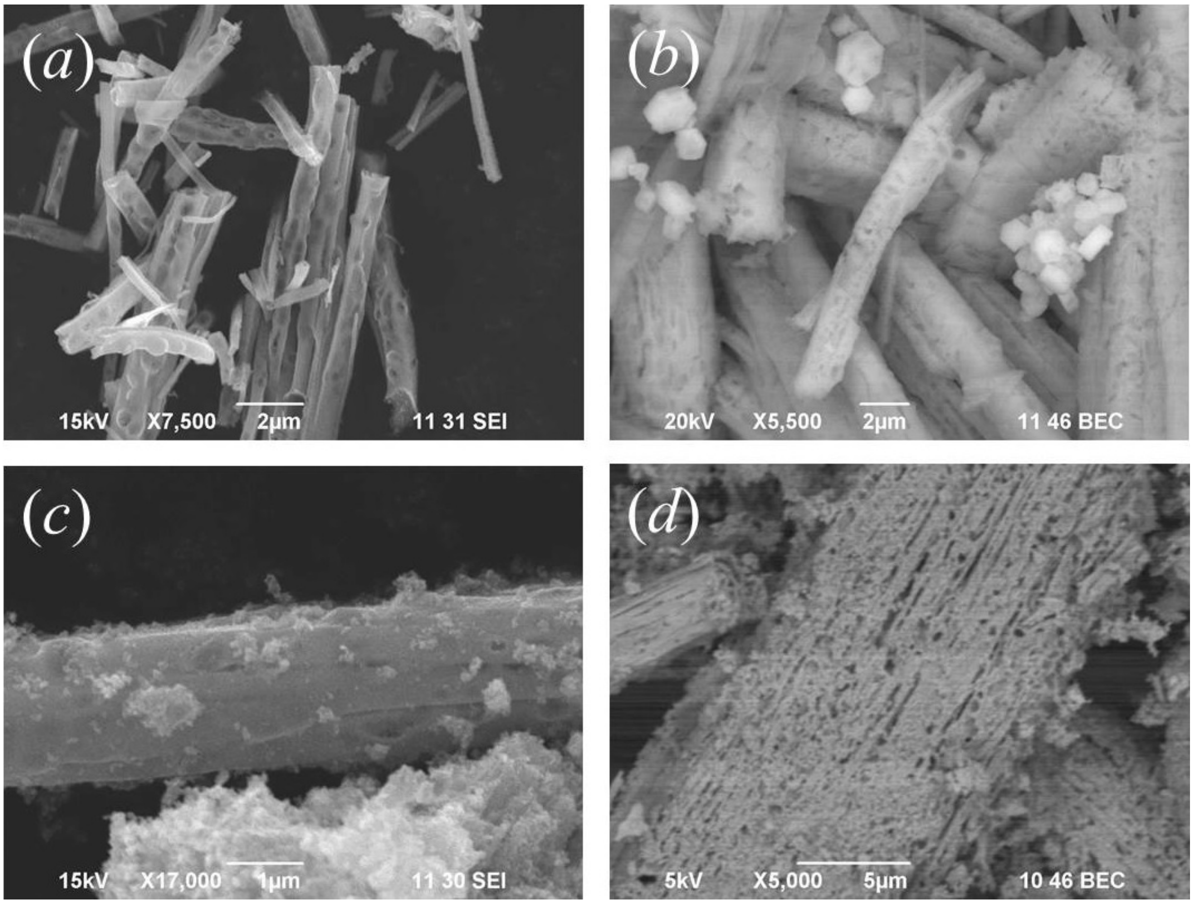

FIG. 2. Typical SEM images of bare ZnO NRs (a) and ZnO NRs / CdS NPs composite material (b–d). ZnO NRs are coupled by CdS NPs in aqueous solutions via *in-situ* CBD synthesis (b — sample 1, c — sample 2) and *ex-situ* synthesis in the pre-synthesized CdS colloid solution (d — sample 3)

the conversion degree of HQ to quinone after 8 hours of irradiation. The conversion degree represents the ratio of residual HQ concentration to the initial one. It is seen that the HQ oxidation rate increases in the series of reactions: solution without and in presence of ZnO NRs / CdS NPs composites. The highest rate and conversion degree of oxidation reaction is observed for sample 1.

Comparing the results for samples 1–3 obtained from XRD, optical and photocatalytic data, we suggest that the higher photocatalytic activity of the sample 1 in comparison with samples 2 and 3 (Fig. 4) is due to the higher content of CdS NPs in semiconductor composite (Table 1) and not to smaller particle size.

4. Conclusion

Semiconductor composite materials, consisting of CdS NPs embedded in a ZnO NRs, have been successfully produced by two step deposition process at relatively low temperatures. The ZnO NRs grown by solvothermal process were coupled by CdS NPs at 50 °C using *in-situ* and *ex-situ* routes in aqueous solutions. *In-situ* deposition of CdS NPs was carried out by CBD from solutions both supersaturated and unsaturated with respect to $Cd(OH)_2$ crystal phase. *Ex-situ* coupling ZnO NRs was held in pre-synthesized colloid solution of CdS NPs. Optical absorbance measurements show a blue shift of the Eg of CdS NPs due to the quantum

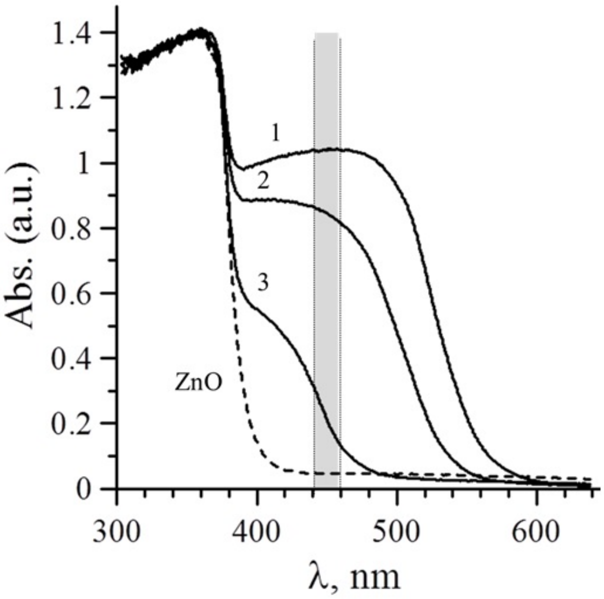

FIG. 3. Optical absorption spectra of uncoupled ZnO (experimental $E_g = 3.23$ eV) and ZnO NRs / CdS NPs composites (samples 1–3) obtained in UV and visible regions at room temperature. Visible light irradiation range while photocatalyzing HQ oxidation is highlighted by a gray bar

TABLE 1. Structural and optical characterization of CdS NPs in ZnO NRs / CdS NPs composites in dependence of coupling route. Experimental values of HQ conversion degree after oxidation in air in the presence of ZnO NRs / CdS NPs composites under irradiation at 440–460 nm for 12 h

Sample	Coupling route	Phase composition, ZnO:CdS:Cd(OH)$_2$	Characterization of CdS NPs in ZnO NRs / CdS NPs composites			Conversion degree of HQ, %
			Particle size $< D >$*, nm	Crystal structure	E_g, eV	
1	*in-situ* CBD at pH = 12.5	17 : 52 : 31	7	random close-packed	2.3	85
2	*in-situ* CBD at pH = 13.7	81 : 19 : 0	5	hexagonal close packed	2.4	79
3	*ex-situ* from pre-synthesized colloid solution of CdS NPs	99 : 1 : 0	< 2	amorphous	2.7	83

*The average particle size <D> was determined from XRD data using Debye-Scherrer formular [44].

confinement effect in the CdS NPs. The mean size of the CdS NPs in composites was observed to range from 2–7 nm. All synthesized ZnO NRs / CdS NPs composites show photocatalytic activity in the photooxidation of HQ in aqueous solution.

The most uniform fiber like morphology is observed for ZnO NRs / CdS NPs composite synthesized using *ex-situ* coupling (sample 3), but the CdS quantity (about 1 at.%) on ZnO NRs

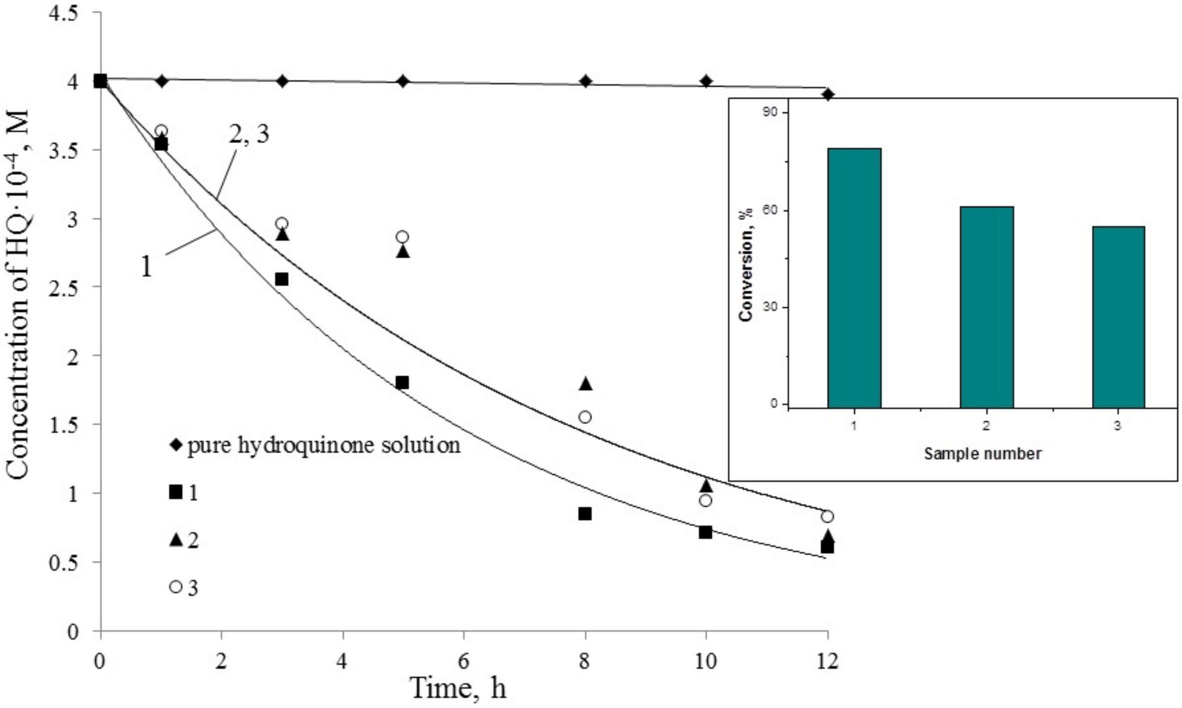

Fig. 4. The kinetics of catalytic oxidation of HQ aqueous solutions under visible light irradiation (440–460 nm) without and in presence of ZnO NRs / CdS NPs semiconductor composites (samples 1–3). The inset shows the conversion degree of hydroquinone to quinone via reaction $C_6H_4(OH)_2 + 0.5\ O_2 \Longleftrightarrow C_6H_4O_2 + H_2O$ after 8 hours of irradiation

is the smallest of three samples. The highest absorption intensity, rate and conversion degree in the photooxidation of HQ was observed for sample 1, obtained by CBD route and containing essential amount of $Cd(OH)_2$. The quantity of CdS NPs coupled with ZnO NRs in sample 1 is also the highest. On the one hand, $Cd(OH)_2$ forms one more crystal phase and violates the uniformity of composite microstructure. On the other, due to hydroxyl group it seems to play a role of bifunctional linker between ZnO and CdS and makes unnecessary additional surface treatment of ZnO NRs. This is important because despite of the porous structure of ZnO NRs, which helps in the coupling of CdS NPs, the number of CdS NPs reaches its maximum in the presence of $Cd(OH)_2$.

The chemical bath deposition technique of coupling ZnO NRs to CdS NPs presented in this work is advantageous, as it is a simple and efficient way to produce nanocrystalline semiconductor composites with controllable quantity and size of the nanoparticles, which could find use in large area surface coatings for advanced photocatalytic and solar cell materials.

Acknowledgements

This work is partially financially supported by RFBR (Project No. 12-03-00453-a).

References

[1] Hu L., Yan J., et al. An optimized ultraviolet -A light photodetector with wide range photoresponse based on ZnS/ZnO biaxial nanobelt. *Adv. Mater.*, **24** (17), P. 2305–2309 (2012).

[2] Panda S.K., Chakrabarti S., et al. Optical and microstructural characterization of CdS-ZnO nanocomposite thin films prepared by sol-gel technique. *J. Phys. D: Appl. Phys.*, **37** (4), P. 628–633 (2004).

[3] Fang X., Bando Y., et al. Inorganic semiconductor nanostructures and their field-emission applications. *J. Mater. Chem.*, **18** (5), P. 509–522 (2008).

[4] Hoffmann M. R., Martin S. T., Choi W., Bahnmann D. W. Environmental applications of semiconductor photocatalysis. *Chem. Rev.*, **95** (1), P. 69–96 (1995).

[5] Fang X., Wu L., Hu L. ZnS nanostructure arrays: a developing material star. *Adv. Mater.*, **23** (5), P. 585–598 (2011).

[6] Liu H., Hu L., et al. Cathodoluminescence modulation of ZnS nanostructures by morphology, doping and temperature. *Adv. Funct. Mater.*, **23** (29), P. 3701–3709 (2013).

[7] Jiang C.Y., Sun X.W., et al. Improved dye-sensitized solar cells with a ZnO-nanoflower photoanode. *Appl. Phys. Lett.*, **90** (26), P. 263501 (2007).

[8] Pan Z.W., Dai Z.R., Wang Z.L. Growth and structure evolution of novel tin oxide diskettes. *J. Am. Chem. Soc.*, **124** (29), P. 8673–8680 (2002).

[9] Pan Z.W., Dai Z.R., Wang Z.L. Nanobelts of semiconducting oxides. *Science*, **291** (5510), P. 1947–1949 (2001).

[10] Aroutiounian V. M., Arakelyan V. M., Shahnazaryan G. E. Metal oxide photoelectrodes for hydrogen generation using solar radiation-driven water splitting. *Sol. Energy*, **78** (5), P. 581–592 (2005).

[11] Jana T.K., Pal A., Chatterjee K. Self-assembled flower like CdS-ZnO nanocomposite and its photocatalytic activity. *J. Alloys and Compounds*, **583**, P. 510–515 (2014).

[12] Khanchandani S., Kundu S., Patra A., Ganguli A.K. Band gap tuning of ZnO/In_2S_3 core/shell nanorod arrays for enhanced visible-light-driven photocatalysis. *J. Phys. Chem. C*, **117** (11), P. 5558–5567 (2013).

[13] Balachandran S., Swaminathan M. Facile fabrication of heterostructured Bi_2O_3–ZnO photocatalyst and its enhanced photocatalytic activity. *J. Phys. Chem. C*, **116** (50), P. 26306–26312 (2012).

[14] Khanchandani S., Kundu S., Patra A., Ganguli A.K. Shell thickness dependent photocatalytic properties of ZnO/CdS core-shell nanorods. *J. Phys. Chem. C*, **116** (44), P. 23653–23662 (2012).

[15] Wang L., Wei H., et al. Synthesis, optical properties and photocatalytic activity of one-dimensional CdS@ZnS core-shell nanocomposites. *Nanoscale Res. Lett.*, **4** (6), P. 558–564 (2009).

[16] Barpuzary D., Khan Z., et al. Hierarchically grown urchinlike CdS@ZnO and CdS@Al_2O_3 heteroarrays for efficient visible light-driven photocatalytic hydrogen generation. *J. Phys. Chem. C*, **116** (1), P. 150–156 (2012).

[17] Fujii H., Ohtaki M., Eguchi K., Arai H. Preparation and photocatalytic activities of a semiconductor composite of CdS embedded in a TiO_2 gel as a stable oxide semiconducting matrix. *J. Mol. Catal. A: Chem.*, **129** (1), P. 61–68 (1998).

[18] Kamat P.V. Photochemistry on nonreactive and reactive (semiconductor) surfaces. *Chem. Rev.*, **93** (1), P. 267–300 (1993).

[19] Gopidas K.R., Bohorquez M., Kamat P.V. Photophysical and photochemical aspects of coupled semiconductors: charge-transfer processes in colloidal cadmium sulfide-titania and cadmium sulfide-silver(I) iodide systems. *J. Phys. Chem.*, **94** (16), P. 6435–6440 (1990).

[20] Evans J.E., Springer K.W., Zhang J.Z. Femtosecond studies of interparticle electron transfer in a coupled CdS-TiO2 colloidal system. *J. Chem. Phys.*, **101** (7), P. 6222–6225 (1994).

[21] Sudhagar P., Chandramohan S., et al. Fabrication and charge-transfer characteristics of CdS QDs sensitized vertically grown flower-like ZnO solar cells with CdSe cosensitizers. *Phys. Stat. Sol. A*, **208** (2), P. 474–479 (2011).

[22] Jun H.K., Careem M.A., Arof A.K. Quantum dot-sensitized solar cells — perspective and recent developments: A review of Cd chalcogenide quantum dots as sensitizers. *Renewable and Sustainable Energy Reviews*, **22**, P. 148–167 (2013).

[23] Qi X., She G., et al. Electrochemical synthesis of CdS/ZnO nanotube arrays with excellent photoelectrochemical properties. *Chem. Commun.*, **48** (2), P. 242–244 (2012).

[24] Kundu P., Deshpande P.A., Madras G., Ravishankar N. Nanoscale ZnO/CdS heterostructures with engineered interfaces for high photocatalytic activity under solar radiation. *J. Mater. Chem.*, **21** (12), P. 4209–4216 (2011).

[25] Tak Y., Hong S.J., Lee J.S., Yong K. Solution-based synthesis of a CdS nanoparticle/ZnO nanowire heterostructure array. *Cryst. Growth Des.*, **9** (6), P. 2627–2632 (2009).

[26] Tak Y., Kim H., Lee D., Yong K. Type-II CdS nanoparticle-ZnO nanowire heterostructure arrays fabricated by a solution process: enhanced photocatalytic activity. *Chem. Commun.*, **38**, P. 4585–4587 (2008).

[27] Hodes G. Comparison of dye- and semiconductor-sensitized porous nanocrystalline liquid junction solar cells. *J. Phys. Chem. C*, **112** (46), P. 17778–17787 (2008).

[28] Niitsoo O., Sarkar S.K., et al. Chemical bath deposited CdS/CdSe-sensitized porous TiO_2 solar cells. *J. Photochem. Photobiol. A*, **181** (2–3), P. 306–313 (2006).

[29] Nicolau Y.F., Dupuy M., Brunel M. ZnS, CdS and $Zn_{1-x}Cd_xS$ thin films deposited by the successive ionic layer adsorption and reaction process. *J. Electrochem. Soc.*, **137** (9), P. 2915–2924 (1990).

[30] Robel I., Subramanian V., Kuno M., Kamat P.V. Quantum dot solar cells. Harvesting light energy with CdSe nanocrystals molecularly linked to mesoscopic TiO_2 films. *J. Am. Chem. Soc.*, **128** (7), P. 2385–2393 (2006).

[31] Gyrdasova O.I., Krasil'nikov V.N., et al. Synthesis, microstructure, and photocatalytic characteristics of quasi-one-dimensional zinc oxide doped with d elements. *Doklady Chemistry*, **434** (1), P. 211–213 (2010).

[32] Melkozerova M.A., Krasil'nikov V.N., et al. Effect of doping with 3d elements (Co, Ni, Cu) on the intrinsic defect structure and photocatalytic properties of nanostructured ZnO with tubular morphology of aggregates. *Physics of the Solid State*, **55** (12), P. 2459–2465 (2013).

[33] Shalaeva E.V., Gyrdasova O.I., et al. Structural, optical, and photocatalytic properties of quasi-one-dimensional nanocrystalline ZnO, ZnOC:nC composites, and C-doped ZnO. In: Nanocomposites, Nanophotonics, Nanobiotechnology, and Applications. Springer Proceedings in Physics, **156**, (26), DOI 10.1007/978-3-319-06611-0_26 (2014) (in press).

[34] Kozhevnikova N.S., Vorokh A.S., Rempel A.A. Preparation of stable colloidal solution of cadmium sulfide CdS using ethylenediaminetetraacetic acid. *Russ. J. General Chem.*, **80** (3), P. 391–394 (2010).

[35] Rempel A.A., Kozhevnikova N.S., Rempel S.V. Structure of cadmium sulfide nanoparticle micelle in aqueous solutions. *Russ. Chem. Bulletin*, **62** (2), P. 398–402 (2013).

[36] Kitaev G.A., Morkrushin S.G., Uritskarya A.A. Chemical bath deposition conditions of CdS thin films on solid surface. *Russ. J. Phys. Chem.*, **39** (8), P. 2065–2066 (1965).

[37] Ortega-Borges R., Lincot D. Mechanism of chemical bath deposition od cadmium sulfide thin films in ammoni-thiourea system. *J. Electrochem. Soc.*, **140** (12), P. 3464–3473 (1993).

[38] Chapman A.J., Lane D.W., Rogers K.D., Özsan M.E. Microstructural changes of CdTe during the annealing process. *Thin Solid Films*, **403–404**, P. 522–525 (2002).

[39] Yan Y., Albin D., Al-Jassim M.M. Do grain boundaries assist S diffusion in polycrystalline CdS/CdTe heterojunctions? *Appl. Phys. Lett.*, **78** (2), P. 171–173 (2001).

[40] O'Brien P., Saeed T.J. Deposition and characterization of cadmium sulfide thin films by chemical bath deposition. *J. Cryst. Growth*, **158** (4) P. 497–504 (1996).

[41] Thavasi V., Renugopalakrishnan V., Jose R., Ramakrishna S. Controlled electron injection and transport at materials interfaces in dye sensitized solar cells. *Mater. Sci. Eng. R*, **63** (3), P. 81–99 (2008).

[42] Vorokh A.S., Rempel A.A. Direct-space visualization of the short and 'average' long-range orders in the noncrystalline structure of a single cadmium sulfide nanoparticle. *JETF Letters*, **91** (2), P. 100–104 (2010).

[43] Ukhanov Yu.I. *Optical Properties of Semiconductors*. Nauka, Moscow, 1977, 366 p. (in Russian).

[44] Vorokh A.S., Rempel A.A. Atomic structure of cadmium sulfide nanoparticles. *Phys. Solid State*, **49** (1), P. 148–153 (2007).

NANOSYSTEMS: PHYSICS, CHEMISTRY, MATHEMATICS, 2014, 5 (4), P. 590–596

SYNTHESIS AND STUDY OF NANOSIZED BIOMATERIALS BASED ON HYDROXYAPATITE

E. A. Bogdanova, N. A. Sabirzyanov
Institute of Solid State Chemistry, Ural Branch of the Russian Academy of Science,
Ekaterinburg, Russia
chemi4@rambler.ru, sabirzyanov@ihim.uran.ru

PACS 82.70.Kj

Directed synthesis of fluorine- and silicon-containing apatites was carried out. The limiting degrees of substitution of silicate groups for phosphate groups were proposed. The physico-chemical properties of the produced materials were investigated.

Keywords: biomaterials, fluorine-substituted hydroxyapatite, silicon-substituted hydroxyapatite.

Received: 16 June 2014
Revised: 30 June 2014

1. Introduction

Recent progress in the field of biomaterials intended to replace and reconstruct bone tissue is due to the application of hydroxyapatite (HAp) as bone implants. Numerous HAp-based biocomposite materials containing antioxidants, antibiotics, regenerating and anti-inflammatory agents have been designed and implemented in clinical practice.

However, in spite of attractive biological properties Hap, materials based thereon have some drawbacks, such as low bioresorption rate *in vivo*, poor stimulating effect on the growth of new bone tissues, low crack resistance and small fatigue durability in the physiological environment.

Chemical modification of HAp allows one to vary the characteristics of the materials over a wide range. The application of modified HAp opens up the opportunities for the preparation of artificial bone substances for implants and a large variety of drugs for curing different lesions of bone, soft and mucous tissues of the individual.

A promising method of modification is the introduction of fluorine or silicon into the primary structure with the formation of fluorine- or silicon-substituted HAp. The introduction of fluorine increases the resistance to biodegradation [1-3] and improves the adsorption of proteins [4] and adhesion of the coating to the metal substrate [5, 6]. Besides, fluorine is necessary for the growth and strength of bones and is a natural stimulator of bone tissue, tooth enamel and dentin formation. The application of fluorine-substituted HAp as a component of pharmaceutical compositions is thought to improve their stability in the reactive environment of the human body and to enhance the therapeutic effect.

Silicon-substituted HAp is of particular interest because of requirements to the implant to grow actively together with the bone tissue forming an intermediate area consisting of biogenic nanocrystalline HAp [7, 8]. Silanol (Si–O–H) bonds on its surface promote the formation of a new phosphate layer accelerating the implant adnation with the bone (osseointegration) [7-9]. Moreover, silicon is also necessary for formation of all body tissues including the basic substances of bone and cartilage tissues, since its physiological role is generally connected with synthesis of glycosaminoglycans and collagen.

To obtain new composite HAp-based materials combining biocompatibility with enhanced strength properties, the authors synthesized silicon-substituted HAp with different degrees of dispersion and a predetermined content of substituting anion while examining the physical and chemical properties of the obtained material.

2. Methods and materials

The monophasic samples were produced by the standard method of chemical condensation using additional silicon- and fluorine-containing reagents:

$$10\mathrm{Ca(OH)_2} + 6\mathrm{H_3PO_4} \rightarrow \mathrm{Ca_{10}(PO_4)_6(OH)_2} + 18\mathrm{H_2O}$$

$$\mathrm{Ca_{10}(PO_4)_6(OH)_2} + x\mathrm{F^-} \rightarrow \mathrm{Ca_{10}(PO_4)_6(OH)_{2-x}F_x} + x\mathrm{OH^-}$$

$$(x = 1;\ 1.5;\ 2)$$

$$10\mathrm{Ca(OH)_2} + (6\text{-}x)\mathrm{H_3PO_4} + x\mathrm{Si(OR)_4} \rightarrow$$

$$\mathrm{Ca_{10}(PO_4)_{6-x}(SiO_4)_x(OH)_{2-x}} + 4x\mathrm{ROH} + (18\text{-}3x)\mathrm{H_2O}$$

$$(\mathrm{R} = \mathrm{Et};\ x = 0.5;\ 1)$$

The phase composition of the synthesized samples was studied by X-ray phase analysis (Shimadzu XRD 700 $\mathrm{Cu}_{k\alpha}$-radiation) and infrared spectroscopy (Spectrum One; Nicolet 6700, FT-IR). The morphological peculiarities of the obtained specimens were examined using scanning electron microscopy (JEOL JSM 6390 LA with an energy-dispersion analyzer). The thermal stability was studied by differential thermal analysis and thermogravimetry with a TG-DTA-92 device (Setaram). The lattice constants were calculated on the basis of powder patterns using the Celref software.

3. Results and discussion

Examination of the microstructure of the samples by scanning electron microscopy showed that the synthesis products are poorly crystallized and consist of nanosized particles integrated in agglomerates (Fig. 1), which can be destroyed by grinding the dried product in ball mills.

The X-ray data reveal that the powder patterns of the obtained compounds are identical to those of HAp. Since different minerals known as apatites give similar powder patterns with minor variations, and the considerable width of the scattering peaks caused by small sizes of crystals reduces the accuracy of comparative analysis of powder patterns, we used infrared spectroscopy method to confirm the presence of fluorine in Hap and identify the chemical bonds of the phosphate and silicate groups emerging with the introduction of silicon into the HAp structure.

The IR spectra of the fluorine-substituted (Fig. 2.1) and silicon-substituted HAp (Fig. 2.2) samples with different substituting ion content indicate the presence of valence and deformation oscillations of the main groups and bonds typical of these compounds: absorption bands of P–O groups at 1053, 1021 and 950 cm^{-1} (asymmetric ν_3 and symmetric ν_1 valence oscillations of bonds in phosphate tetrahedron $\mathrm{PO_4^{3-}}$), doublets at 601 and 569 cm^{-1}(asymmetric deformation ν_4 oscillations of P–O bonds) and valence oscillations of O–H bonds at 3570 cm^{-1}, deformation oscillations at 1646 cm^{-1} and valence oscillations of water absorbed during synthesis at 3435 cm^{-1}.

The substitution of fluorine for hydroxyl groups reduces the resolution of the oscillation bands of O–H bonds at 3570 cm^{-1} owing to partial loss of O–H groups, which indirectly confirms the expected mechanism of substitution.

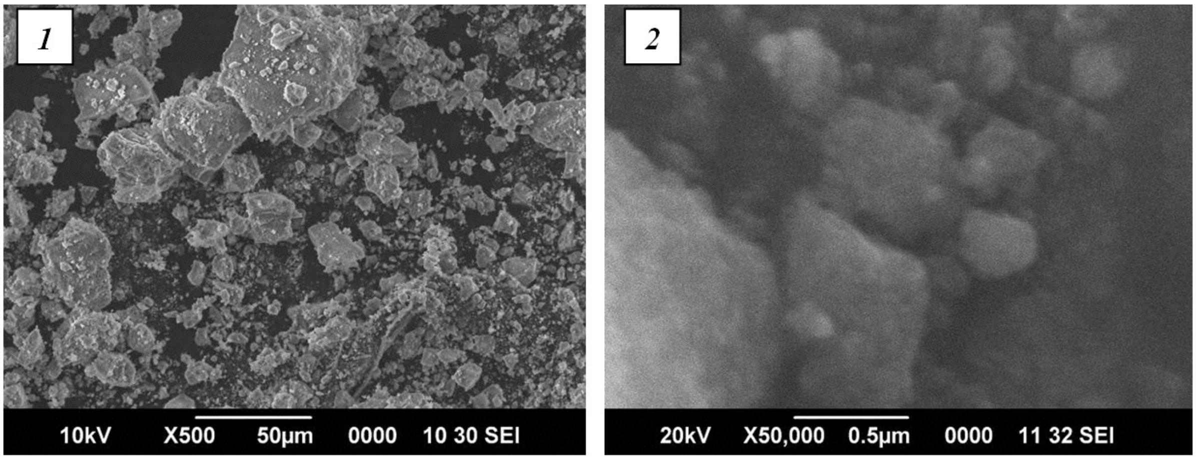

FIG. 1. Micrographs of crystalline fluorine-substituted HAp of the composition $Ca_{10}(PO_4)_6F_2$, magnification: ×500 ***(1)***, ×50000 ***(2)***

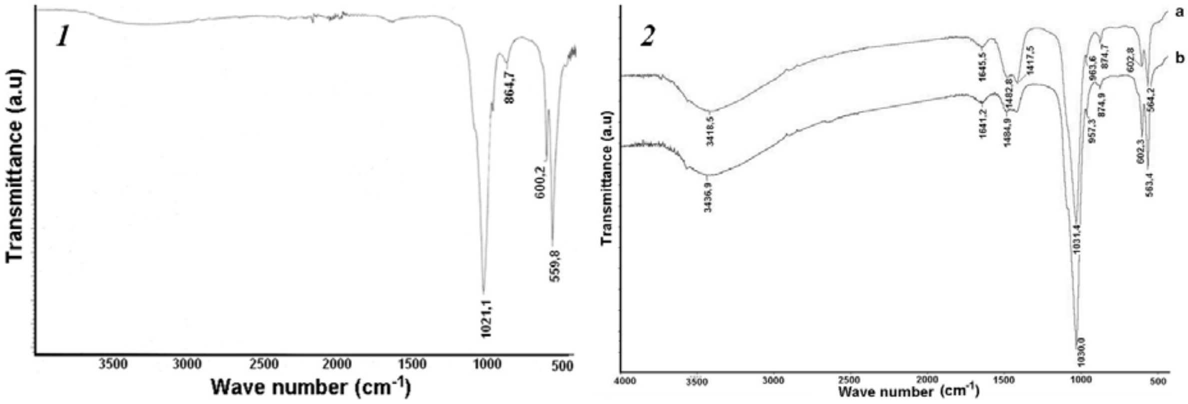

FIG. 2. IR spectra of $Ca_{10}(PO_4)_6(OH)_{2-x}F_x$ for x = 1; 1.5; 2 ***(1),*** $Ca_{10}(PO_4)_5(SiO_4)(OH)$ ***(2a)*** and $Ca_{10}(PO_4)_{5.5}(SiO_4)_{0.5}(OH)_{1.5}$ ***(2b)***

The absence of hydroxyl vibration oscillations at 630 cm^{-1} near the low-frequency band typical of P–O oscillations (601 cm^{-1}) is due to the reduction of the number of OH^- ions in the compound to compensate the extra charge emerging with the introduction of silicate groups into the HAp lattice. The absorption bands typical of oscillations of Si–O bonds are also present: absorption band with a frequency of 500 – 520 cm^{-1}, typical of oscillations of the silicate group bonds in the apatite structure, is due to the deformation oscillations of Si–O bonds; the valence oscillations bands of these bonds at 945 cm^{-1} overlap with the intense absorption bands of the phosphate group in the 900 – 1200 cm^{-1} range. The intensity of the PO_4^{3-} bands for the silicon-substituted HAp samples decreases with an increase in the substitution degree. The presence of oscillations of the CO_3^{2-} group at 1420 – 1480 cm^{-1} in the IR spectra is explained by a considerable affinity of the silicon-substituted HAp to the carbonate-anion, which, being located in the phosphate ion position [10], compensates for the silicate anion charge. The substitution degree of CO_3^{2-} increases with the content of silicon in the sample, which is confirmed by an increase in the band intensity of this group on the IR spectra.

The energy dispersive X-ray analysis – EDAX confirmed that the composition of the synthesized samples corresponds to pre-assigned stoichiometry (Fig. 3). Analysis performed through 20 points in different parts of the samples gave an insignificant scatter of results.

No fluorine-free points were found in the fluorine-substituted and silicon-free points in the silicon-substituted HAp samples confirming the formation of solid solutions in these systems.

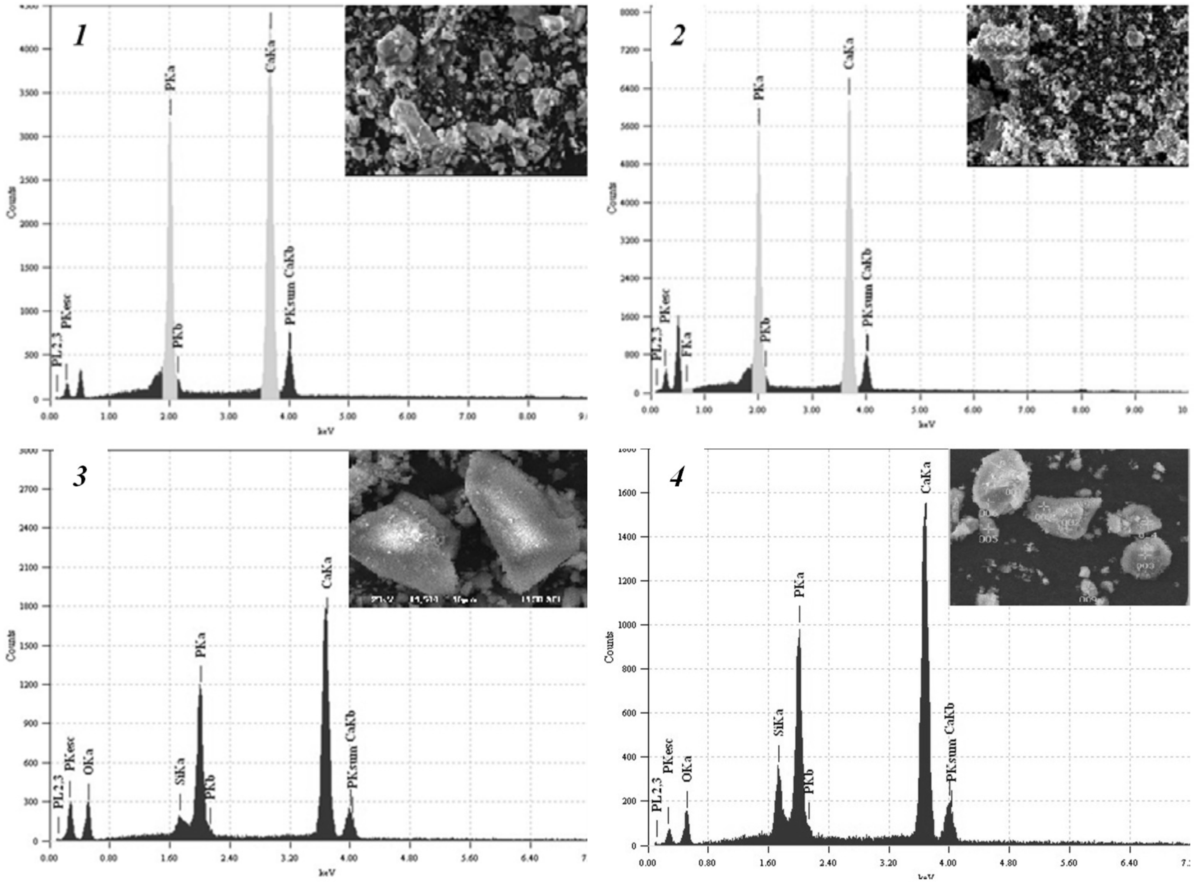

FIG. 3. EDAX-spectra of HAp ***(1)*** and anion-substituted HAp with the formula $Ca_{10}(PO_4)_6F_2$ ***(2)***, $Ca_{10}(PO_4)_{6-x}(SiO_4)_x(OH)_{2-x}$ for x = 0.5 ***(3)*** and x = 1 ***(4)***

Thus, the assumption that fluorine or silicon can be embedded into the HAp lattice is confirmed by the experimentally established facts: the absence of phases of other calcium phosphates or anion-containing compounds in the powder patterns; the change in the spectral pattern in the characteristic fields as well as by the EDAX data.

The introduction of fluorine or silicate ions into the initial HAp structure should change the lattice constants. The lattice constants of the synthesized samples of anion-substituted HAp were calculated on the basis of the powder patterns using the Celref software. The calculated results reveal (Tabl. 1) that the lattice constants of the synthesized samples of fluorine- and silicon-substituted HAp different from the stoichiometric HAp, which indirectly confirms anionic substitution. In the literature, there are different values of the lattice constants of silicon-substituted Hap obtained by different methods. For example, in [11] the lattice constants of silicon-substituted HAp were found to increase with the silicon content. At the same time, reduction of the lattice constants for silicon-substituted HAp was reported in [12]. Analysis of the obtained data correlates with the data [7] showing that the introduction of silicon into the HAp lattice decreases the parameter a and increases the parameter c. The introduction of fluorine into the initial HAp structure also decreases the lattice constants.

TABLE 1. The lattice constants of HAp and anion-substituted forms

Compound	a, Å	c, Å	Volume of crystal unit, Å^3
$Ca_{10}(PO_4)_6(OH)_2$	9.418	6.884	528.80
$Ca_{10}(PO_4)_{5.5}(SiO_4)_{0.5}(OH)_{1.5}$	9.389+0.027	6.893 ± 0.002	526.21 ± 2.28
$Ca_{10}(PO_4)_5(SiO_4)(OH)$	9.246+0.017	6.885 ± 0.001	509.69 ± 0.92
$Ca_{10}(PO_4)_6(OH)F$	9.375± 0.015	6.887± 0.001	524.19± 0.85
$Ca_{10}(PO_4)_6(OH)_{0.5}F_{1.5}$	9.376± 0.030	6.883± 0.001	524.09± 1.68
$Ca_{10}(PO_4)_6F_2$	9.383± 0.033	6.881± 0.001	524.70± 1.88

The results of thermogravimetric analysis (Fig. 4) reveal the following stages of thermal decomposition accompanied by weight loss of the samples: the loss of bound water and some amount of carbonate ions in the 200 – 600°C interval and considerable loss of carbonate ions in the interval from 600 to 1000°.

The $Ca_{10}(PO_4)_5(SiO_4)(OH)$ sample loses weight (16.8 wt.%) more readily than the other samples since it contains, along with bound water, carbonate ions, to which silicon-substituted HAp shows considerable affinity. For silicon-substituted HAp $Ca_{10}(PO_4)_{5.5}$ $(SiO_4)_{0.5}(OH)_{1.5}$, the weight loss is 9.95 wt.%, which is explained by a lower carbonate ion content in this sample.

The fluorine-substituted forms have greater thermal stability increasing with the degree of substitution. The weight loss of fluorine-substituted Hap was: $Ca_{10}(PO_4)_6(OH)F$ – 12.3 wt.%; $Ca_{10}(PO_4)_6(OH)_{0.5}F_{1.5}$ – 10.2 wt.%; $Ca_{10}(PO_4)_6F_2$ – 9.7 wt.%.

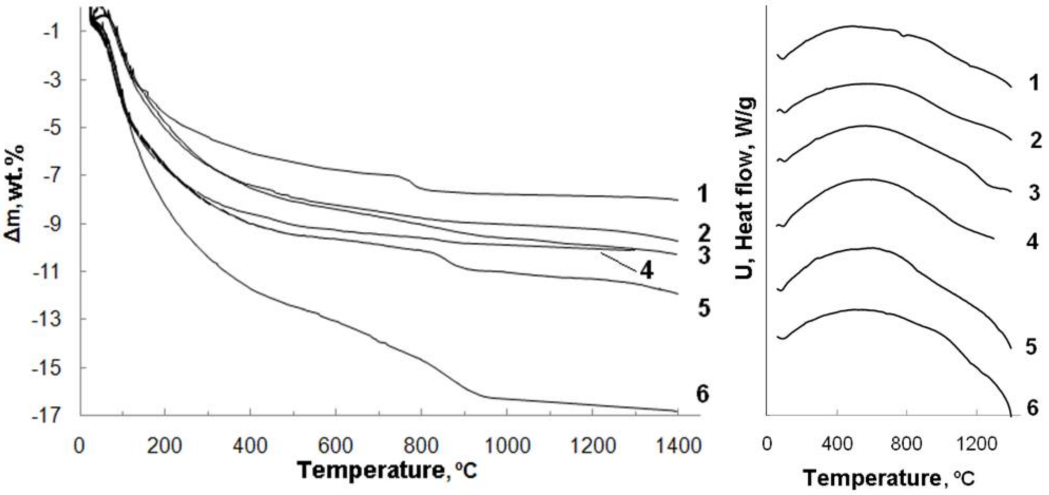

FIG. 4. DTG and DTA curves for: ***1*** – $Ca_{10}(PO_4)_6(OH)_2$, ***2*** – $Ca_{10}(PO_4)_6F_2$, ***3*** – $Ca_{10}(PO_4)_{5.5}(SiO_4)_{0.5}(OH)_{1.5}$, ***4*** – $Ca_{10}(PO_4)_6(OH)_{0.5}F_{1.5}$, ***5*** – $Ca_{10}(PO_4)_6(OH)F$, ***6*** – $Ca_{10}(PO_4)_5(SiO_4)(OH)$ samples

Pure HAp loses 8 wt.%, but this sample is unstable. The endothermic effect at 800°C on the DTA curves (Fig. 5) is attributed to partial decomposition of HAp and to the formation of tricalcium phosphate, which is typical of HAp obtained by precipitation. The occurrence of the tricalcium phosphate impurity phase was confirmed by X-ray, while the powder patterns of anion-substituted HAp samples with varying degrees of substitution annealed at 800 and 1000°C are monophasic and correspond to those of HAp. EDX confirmed that composition of the annealed samples corresponds to the initial compositions with predetermined degrees of substitution.

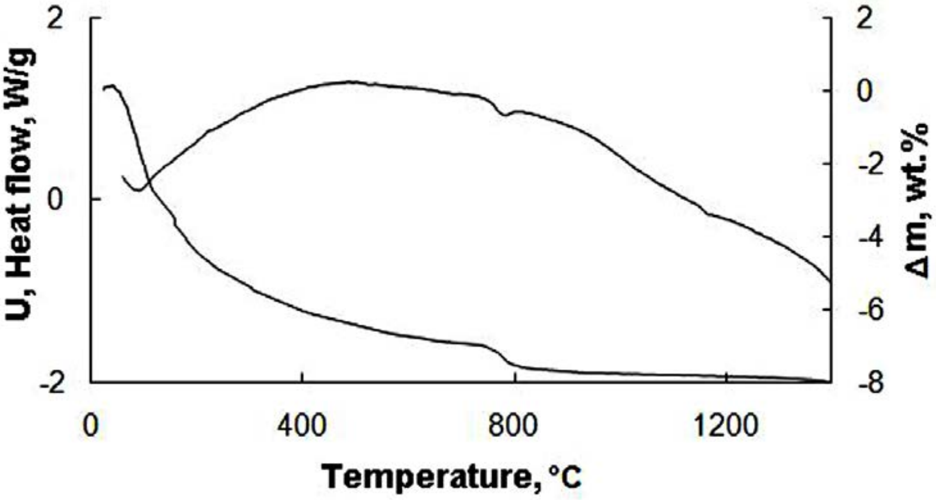

Fig. 5. DTA curves of pure Hap

Thus, the study of the influence of anionic substitution on the thermal stability of HAp showed that in comparison with pure HAp the anion-substituted forms have greater thermal stability. The most thermally stable sample is $Ca_{10}(PO_4)_6F_2$. The thermal stability of fluorine-substituted HAp can be explained by the difference in the energies of chemical bonds of $F^-$and OH^- ions with calcium ions in Ca-channels and by structural stabilization.

Inasmuch as one of the crucial requirements to modern materials for biomedical applications is high bioactivity allowing not only for biological processes of cell growth and differentiation but also for the rate of material dissolution, we have studied the behavior of the synthesized samples in a sub acid medium (acetate buffer solution with pH = 4). It was established that in comparison with pure HAp, silicon-substituted HAp has a higher solubility, increasing with the degree of substitution of silicate ions for phosphate ions (Fig. 6).

The solubility study shows that the introduction of fluorine into the structure, be it complete or partial replacement of OH^- groups, exerts a stabilizing effect and promotes production of a material with improved strength properties, because it increases the resistance to biodegradation and to the action of acids.

4. Conclusions

Thus, a method for changing the physicochemical properties of HAp by partial anionic substitution has been proposed. Directed synthesis of silicon-containing apatites was carried out, which is a complex physicochemical problem. The limiting degrees of substitution of silicate groups for phosphate groups were proposed.

The thermal stability study showed that the introduction of fluorine or silicon stabilizes the apatite structure. Examination of the behavior of the produced materials in the model solution revealed a greater resorbing ability and consequently, greater bioactivity for the silicon-modified samples in comparison with pure HAp. The application of these materials for medical purposes is very promising.

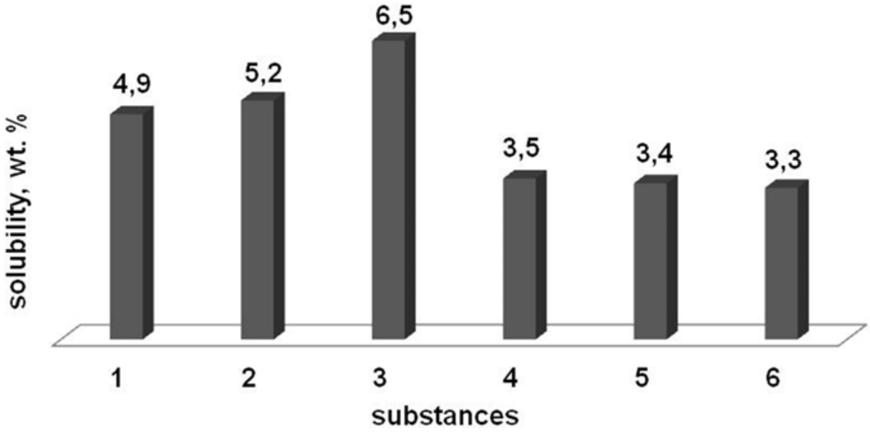

FIG. 6. The solubility for: ***1*** – $Ca_{10}(PO_4)_6(OH)_2$, ***2*** – $Ca_{10}(PO_4)_{5.5}(SiO_4)_{0.5}(OH)_{1.5}$, ***3*** – $Ca_{10}(PO_4)_5(SiO_4)(OH)$, ***4*** – $Ca_{10}(PO_4)_6(OH)F$, ***5*** – $Ca_{10}(PO_4)_6(OH)_{0.5}F_{1.5}$, ***6*** – $Ca_{10}(PO_4)_6F_2$ samples

Acknowledgments

This work was supported by the Presidium of the Ural Branch of RAS (program No. 12-P-3-1003).

References

[1] Guelcher S.A., Hollinger J.O. *An introduction to biomaterials.* New York: CRC Press, 2006.

[2] Darimont G.L., Gilbert B., Cloots R. Non-destructive evaluation of crystallinity and chemical composition by raman spectroscopy in hydroxyapatite-coated implants. *Mater Lett.*, **58**, P. 71–73 (2003).

[3] Cheng K., Weng W., Qu H., Du P., Shen G., Han G., Yang J., Ferreira J.M.F. J. Biomed. Matter. Res. Part B, *Appl. Biomater.*, **B.69**, P. 33 (2004).

[4] Zeng H., Chittur K.K., Lacefield W.R. *Biomaterials*, **20**, P. 377 (1999).

[5] Zhang S., Zeng X.T., Wang Y.S., Cheng K., Weng W. Adhesion strength of sol-gel derived fluoridated hydroxyapatite coatings. *Surf Coat Technol.*, **200**, P. 6350–6354 (2006).

[6] Lee E.J., Lee S.H., Kim H.W., Kong Y.M., Kim H.E. Fluoridated apatite coatings on titanium obtained by electron-beam deposition. *Biomaterials*, **26**, P. 3843–3851 (2005).

[7] Gibson I. R., Bests. M., Bonfield W. Chemical characterization of silicon-substituted hydroxyapatite. *J. Biomed. Mater. Res.*, **44**, P. 422 (1999).

[8] Patel N., Best S.M., Bonfield W. *J. Mater. Sci. Mater. Med.*, **13**, P. 1199–1206 (2002).

[9] Kim S.R., Lee J.H., Kim Y.T., Riu D.H., Jung S.J., Lee Y.J., Chung S.C., Kim Y.H. Synthesis of Si, Mg substituted hydroxyapatites and their sintering behaviors. *Biomaterials*, **24**(8), P. 1389–1398 (2003).

[10] Bonel G. Contribution al etude de la carbonation des apatites. *Ann.Chim.*, **7**(3), P. 127–144 (1972).

[11] Putlayev V., Veresov A., Pulkin M., Soin A., Kuznetsov V. Silicon-substituted hydroxyapatite ceramics (Si-HAp): densification and grain growth through the prism of sintering theories. *Mat.-Wiss. Werkstofftech.*, **37**(6), P. 416–421 (2006).

[12] Pietak A.M., Reid J.W., Stott M.J., Sayer M. Silicon substitution in the calcium phosphate bioceramics. *Biomaterials*, **28**, P. 4023–4032 (2007).

NANOSYSTEMS: PHYSICS, CHEMISTRY, MATHEMATICS, 2014, 5 (4), P. 597–602

ADSORPTION CAPACITY OF WATER-OXIDIZED LANTHANUM-DOPED ALUMINUM ALLOY POWDER

A. Ryabina, V. Shevchenko, D. Eselevich

Institute of Solid State Chemistry of the Ural Branch of the Russian Academy of Sciences,
Ekaterinburg, Russia

anna-ryabina@yandex.ru

PACS 68.43.-h; 68.43.Bc; 73.20.Hb; 82.65.+r; 81.07.Bc; 68.47.De; 68.37.Xy; 61.10.Nz

The adsorption of nitrogen onto the surface of lanthanum-doped ultrafine aluminum (UFA) powder was studied before and after aqueous oxidation under relative adsorbate (Pa/Po) pressures from 0 to 1 using low-temperature nitrogen adsorption method in a volumetric static vacuum facility. The adsorption isotherms are considered for their compliance with the isotherms in the classification of S. Brunauer, L. Deming, U. Deming and E. Teller. The obtained results confirm that treatment of REM-containing powders with water leads already at room temperature to the formation of new phases and affects their morphology. It is shown that a large role in the properties of water-treated powders belongs to the nanopores formed between crystallites on the surface of particles in the process of oxidation with water and during subsequent thermal dehydration. The adsorption properties of Al – 3% La sample were examined by the following methods: analysis of adsorption-desorption isotherms of vapors (statistical volumetric method) based on nitrogen adsorption at 78 K, electron microscopic technique, and X-ray analysis. The specific surface area and porosity of the powders were calculated.

Keywords: adsorption, ultrafine powders, pores, specific surface area.

Received: 16 June 2014
Revised: 30 June 2014

1. Introduction

Hydrothermal synthesis is an effective method for producing porous aluminum hydroxides used as adsorbents, catalysts and catalytic materials carriers [1,2]. Comprehensive information about the interaction of aluminum powders of different dispersion with water is presented in Ref. [2]. In this study, we show that the interaction is suppressed by high protective properties of the oxide film on the surface of particles. One of the promising methods for destruction of the barrier layer is alloying of aluminum with active metals. So, the interaction of aluminum-gallium and thallium-tin alloys with water was examined in Refs. [3–7]. The distribution of alloying elements on the grain boundaries leads to active intergranular corrosion and to destruction of metal to an ultrafine and nanosized state, complete transformation into aluminum hydroxide taking place for a shorter period of time than for pure aluminum. Later it was found that the presence of gallium can be used to advantage for the production of hydrogen [8]. At the same time, the use of alloy powders makes it possible to affect the physicochemical and mechanical properties of materials synthesized by hydrothermal synthesis, as well as their adsorption capacity.

This paper deals with the adsorption capacity of aluminum lanthanum alloy powders and the products of interaction with water obtained at room temperature.

2. Methods, results and discussion

The alloy synthesis, powder production and experiment procedures were the same as described previously [9, 10].

The objects of this study were prepared by spraying the melts with nitrogen followed by recondensation of gas plasma under low-temperature plasma conditions on GNIICHTEOS plants [11].

Before and after the experiment, the samples were weighed on a Shimadzu AUW 120D high-accuracy electronic balance.

The content of active aluminum powders during hydrotreatment was determined by the volumetric method – from the volume of evolved hydrogen. The adsorption properties were studied on a Sorptomatic plant from nitrogen adsorption on the particle surface. The specific surface area and porosity were calculated by the BET and Barrett, Joyner and Halenda (BJH) methods [12].

Surface oxidation of aluminum powder with water leads to a dramatic increase in the specific surface area. UFA can be classified with non-porous materials. Its specific surface area was 7 m^2/g before and 30 m^2/g after hydrotreatment. UFA powder was stored in a conditionally sealed package and interacted with atmospheric moisture during storage, therefore it already contained oxide phases because the active aluminum content was $\sim 80\%$. The electron micrographs of the UFA sample before and after water treatment are presented in Fig. 1. The UFA powder particles before aqueous oxidation had a spherical form of about 5–10 microns in diameter, which were coated with smaller particles formed when the initial ASD–4 type alloy powder passed through a plasmatron. After interaction with water, the particles were bound agglomerates differing greatly in size. As is seen, they were the same spherical particles coated with a fine fraction of aluminum oxide hydroxide AlOOH. Analysis of the phase composition of the samples after water oxidation was carried out on a Shimadzu diffractometer (Cukα radiation) using the JCPDS standard database. The content of active aluminum decreased by 14%.

The Al – 3% La powder before interaction with water was a non-porous sample corresponding to the isotherm of type 2. After water treatment, the Al – 3% La sample belongs to mesoporous materials and corresponds to the isotherm of type 4, according to the recommendations of the International Union of Pure and Applied Chemistry (IUPAC) [12].

The adsorption isotherm of Al – 3% La has a hysteresis loop, Fig. 2. According to the IUPAC classification, hysteresis for Al – 3% La is of H3 type, i.e. this material has near-slit-like pores. The isotherm of Al – 3% La after water oxidation is typical of porous aggregates with a developed network of intersecting pores [13].

The structure of porous carriers is generally characterized not only by the specific surface area, but also by the pore volume and pore size distribution [12, 14].

The porous structure of Al – 3% La sample obtained in the aqueous process was calculated using the Barrett, Joyner and Halenda theory (BJH method) [12, 15]. It was found to be of polydisperse nature with mesopores with a narrow size distribution of in the range from 30 to 40 Å, Fig. 3. The total pore surface area was 45 m^2/g. The total pore volume was 0.058 cm^3/g. The specific surface area of the sample before and after interaction with water was respectively 20 and 60 m^2/g.

Although lanthanum is not registered in any form by XRD, the presence of lanthanum had an influence not only on the reaction between aluminum and liquid water stimulating oxide hydroxide formation, but also on the structural characteristics of the synthesized product

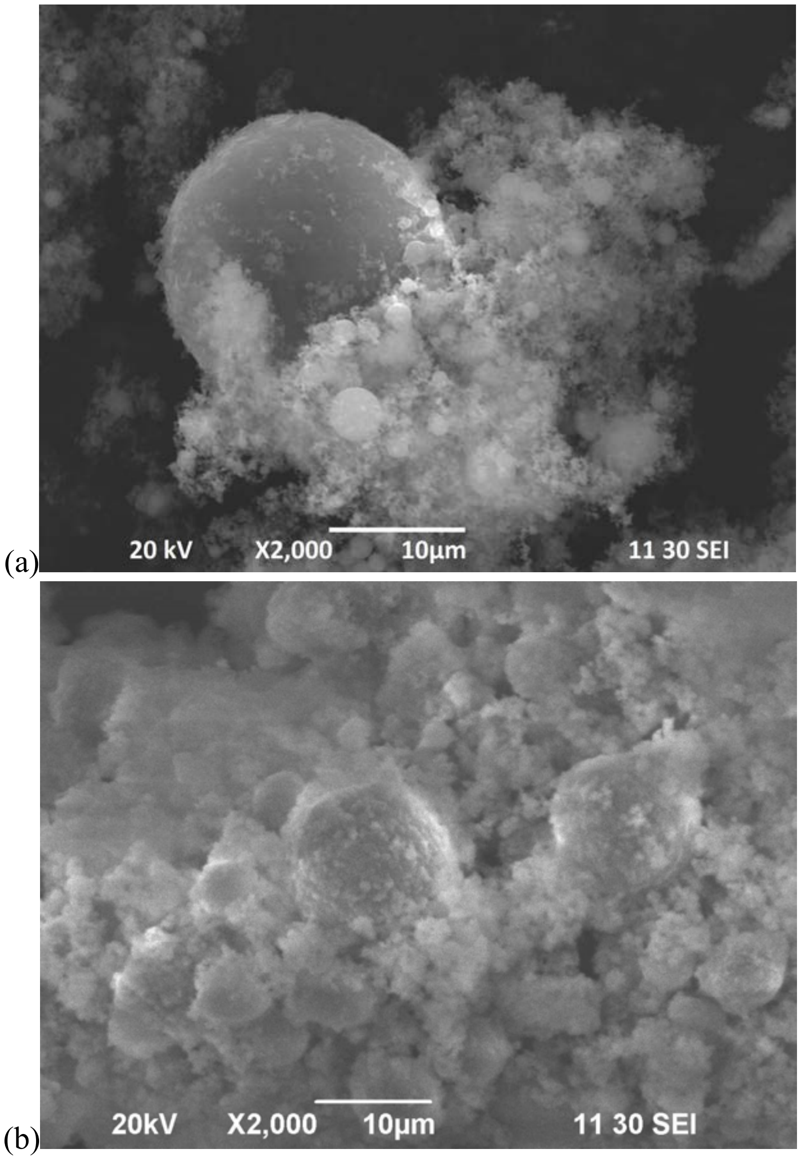

FIG. 1. Micrographs of alloy powders: (a) initial UFA, (b) UFA after interaction with water (48 h)

increasing the degree of its amorphism. The amorphism of Al – 3% La powder after hydrotreating is also attested to by the presence of a wide band (halo) inherent in the amorphous phase corresponding to boehmite AlOOH, Fig. 4.

According to electron microscopic examination of the Al – 3% La sample after water oxidation, the powder has a loose structure (loose agglomerates of amorphous particles) where plates with slit-like pores are observed, Fig. 5. Thus, the pseudoboehmite precipitate produced at a temperature not higher than 30 °C consists of fine crystal grains forming the porous structure of slit-like pores with the average pore diameter of 3–4 nm that are combined into secondary particles (flakes) containing a large amount of colloidal-bound water. This water is held by the hydrate very firmly and can be removed only by drying at 110–130 °C. The entire sample reacted with water completely, as evidenced by phase and volumetric analysis. The specific surface area increased up to 60 m^2/g.

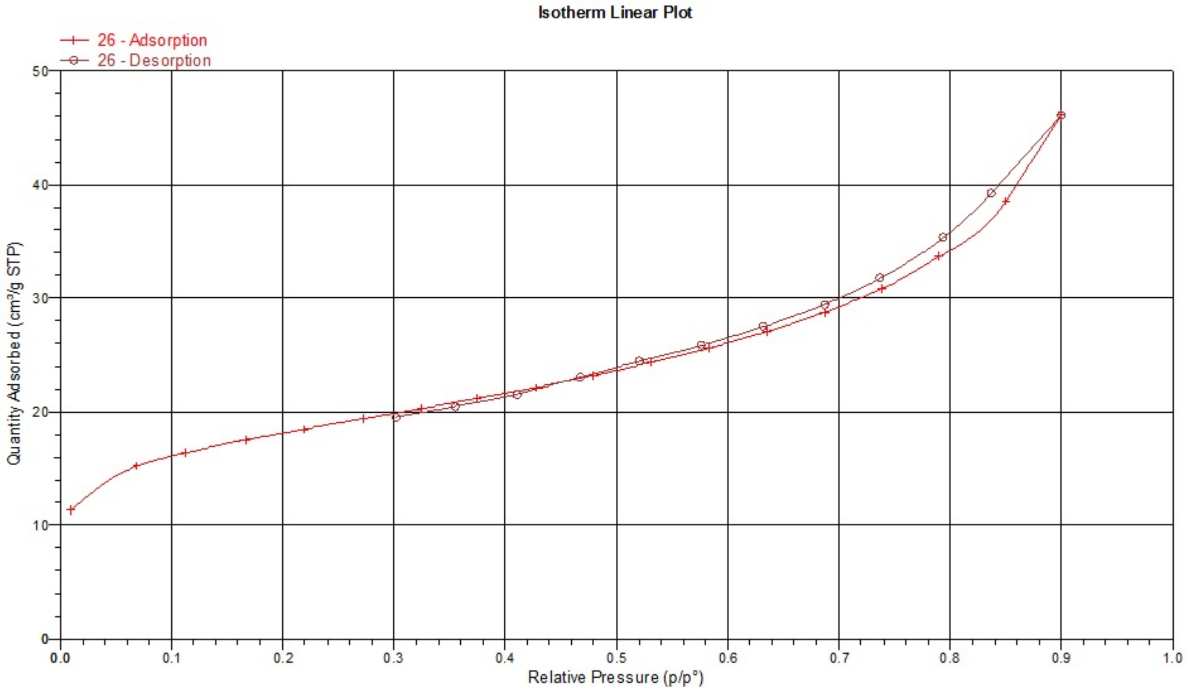

FIG. 2. Nitrogen adsorption isotherm on the surface of Al – 3% La powder after interaction with water

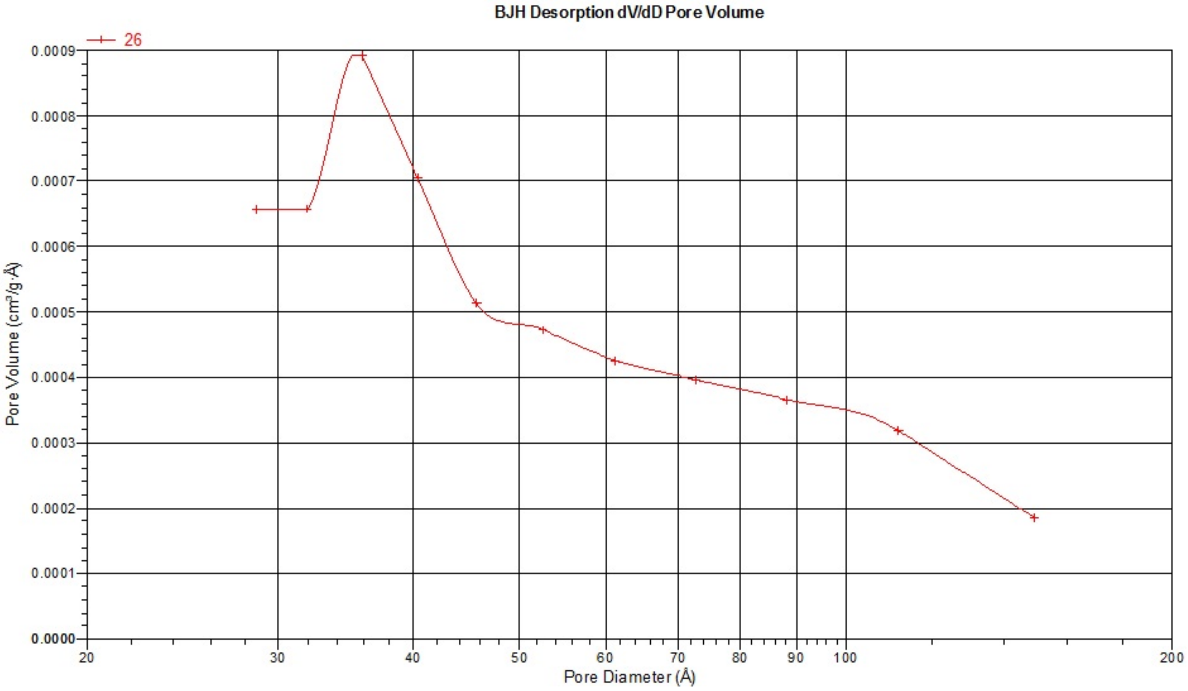

FIG. 3. The pore diameter distribution curve for the Al – 3% La composition

The results obtained showed that at room temperature the process of interaction of Al – 3% La with water is most likely to flow the scheme: amorphous phase – pseudo-boehmite (AlOON) – boehmite (γ–AlOOH) – bayerite $Al(OH)_3$ – gibbsite $Al(OH)_3$ [16].

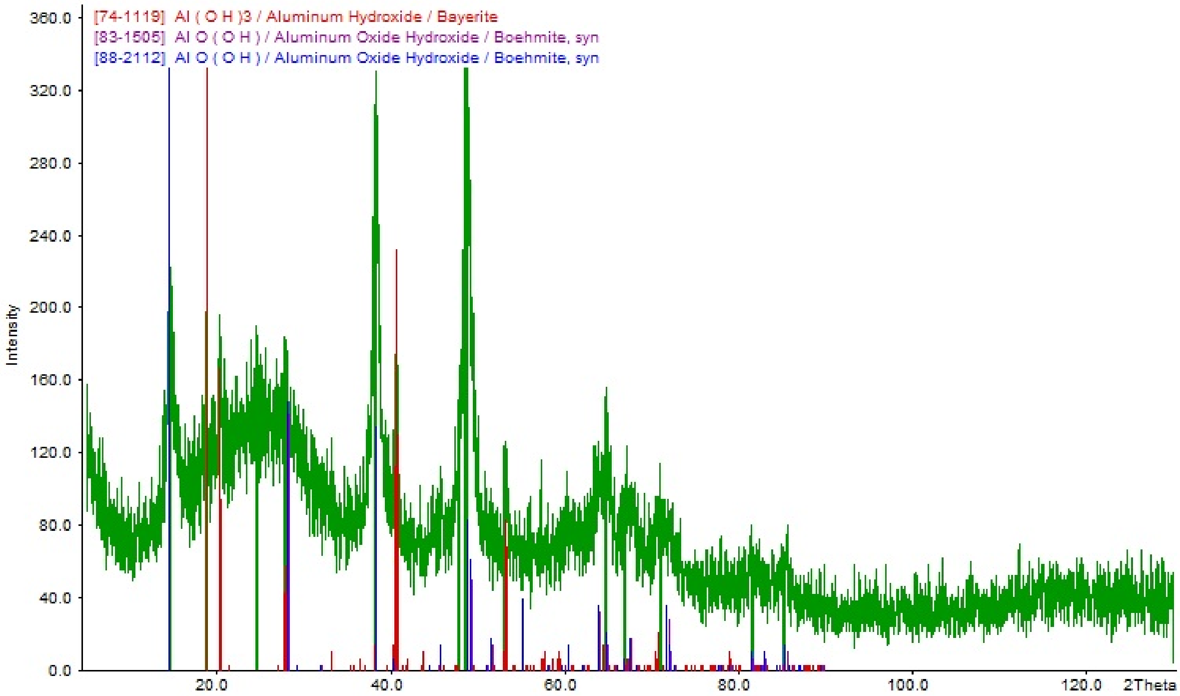

FIG. 4. The diffractogram of water-treated Al – 3% La powder

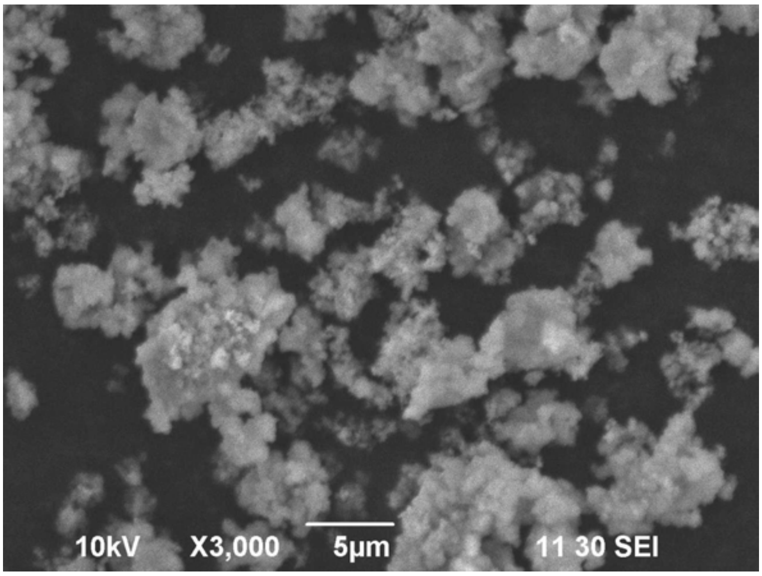

FIG. 5. Microphotograph of Al – 3% La alloy powder after interaction with water (48 h)

3. Conclusions

The interaction of Al – 3% La alloy powder with water at room temperature has been studied for the first time. During 48 h the sample completely reacted with water to form AlOOH and $Al(OH)_3$.

Alloying aluminum with lanthanum activates the interaction process and leads to the formation of nanoscale products with a specific surface area of 60 m^2/g and a narrow size distribution for mesopores, ranging from 30 to 40 Å.

References

[1] Kudryashov A.V., Dyagilets S.M., Andrianov N.T. Optimization of synthesis conditions of hydroxides and superfine alumina. *Steklo i keramika*, **4**, P. 22–24 (2002). [in Russian]

[2] Tikhov S.F., Romanenkov V.E., et al. *Porous composites based on aluminum oxide cermets (synthesis and properties)*. Novosibirsk: Geo, 2004, 205 p. [in Russian]

[3] Kozin L.F., Sakharenko V.A., Budarina A.N. Kinetics and mechanism of interaction of activated aluminum with water. *Ukr. khim. zhurn.*, **50** (21), P. 161–169 (1984). [in Russian]

[4] Kozin L.F., Sakharenko V.A. Kinetics and mechanism of interaction of aluminum, gallium and thallium based alloys with water. *Ukr. khim. zhurn.*, **50**, (1), P. 9–15 (1984).[in Russian]

[5] Kozin L.F., Sarmurzina R.G. Study of the rate of interaction with water and the microstructure of aluminum gallium alloys. *Zhurn. prikl. khim.*, **54** (310), P. 2176–2180 (1981). [in Russian]

[6] Sarmurzina R.G., Sokolsky D.V., Kuralov G.G., Vozdvizhensky V.F. Physicochemical foundation of activation of aluminum for production of hydrogen fuel. *Vopr. atomnoi nauki i tekhniki, ser. Atomnovodorodnaya energetika i technologiay*, **2**, P. 28–32 (1985). [in Russian]

[7] Sarmurzina R.G. The kinetics of interaction of activated aluminum with water. *Proc. of the Ist All-Union Symposium on microsc. kinetics and chem. gas dynamics*. Alma-Ata, Chernogolovka, **1** (2), P. 24–25, 19–22 (1984). [in Russian]

[8] Yatsenko S.P., Skachkov V.M., Shevchenko V.G. Production of hydrogen by decomposition of water with activated aluminum. *Zh. prikl. khim.*, **84** (1), P. 35–38 (2011). [in Russian]

[9] Ryabina A.V., Kononenko V.I., Razhabov A.A. Electrode-free method for measuring the electrical resistance of metals in solid and liquid states and an installation for its implementation. *Rasplavy*, **1**, P. 36–42 (2009). [in Russian]

[10] Ryabina A.V., Kononenko V.I., Seleznev A.S., Petrov L.A. Nitrogen adsorption on aluminum powders Al_2O_3 and AlN at 78 K. *Zhurn. fizich. khimii*, **88** (1), P. 134–137 (2014). [in Russian]

[11] Shevchenko V.G., Malashin S.I. et al. The properties of finely dispersed Al-REM alloys produced by plasma recondensation. *Perspektivnye materialy*, **1**, P. 68–75 (2010). [in Russian]

[12] Greg S., Sing K. *Adsorption. Specific surface. Porosity.* Transl. from English. 2nd ed. Moscow: Mir, 1984. 306 pp. [in Russian]

[13] Zhdanov V.P., Fenelonov V.B., Efremov D.K. *J. Colloid Interface Sci.*, **120** (1). . 218 (1987).

[14] Belyi A., Smolikov M.D., et al. The distribution of active componenet in the pores of different sizes in the structure of oxide carriers. *Kinetika i kataliz*, **27** (3), (1986). [in Russian]

[15] Tolmachev A.M. Physico-chemical processes on interfaces. Adsorption of gases, vapors and solutions. II description and a priori calculations of adsorption equilibria. *Fizikokhimiya poverkhnosti i zashchita materialov*, **46** (3), P. 242–260 (2010). [in Russian]

[16] Chalyi V.P. *Metal hydroxides (Regularities of formation, composition, structure and properties)*. Naukova Dumka, Kiev, 1972. [in Russian]

NANOSYSTEMS: PHYSICS, CHEMISTRY, MATHEMATICS, 2014, 5 (4), P. 603–612

INTRODUCTION OF SCANDIUM, ZIRCONIUM AND HAFNIUM INTO ALUMINUM ALLOYS. DISPERSION HARDENING OF INTERMETALLIC COMPOUNDS WITH NANODIMENSIONAL PARTICLES

V. M. Skachkov, L. A. Pasechnik, S. P. Yatsenko

Institute of Solid State Chemistry, Ural Branch of the Russian Academy of Science,
Ekaterinburg, Russia

Yatsenko@ihim.uran.ru

PACS 61.66.Dk

The state of intermetallic compounds Al_3Sc, Al_3Zr, Al_3Hf and slag shots introduced by high-temperature exchange reactions of corresponding fluoride-chloride salts with liquid aluminum has been studied. The particle size and segregation direction during centrifugation and filtration of melt have been examined by microscopy and local X-ray analysis methods. The dispersoids formed during decomposition of solid solution are strong phase reinforcers.

Keywords: Aluminum, scandium, zirconium, hafnium, alloy, intermetallic compounds (IMC), slag, inclusions, microstructure.

Received: 16 June 2014
Revised: 30 June 2014

1. Introduction

Small additions of scandium, as well as zirconium and hafnium to aluminum and aluminum-based alloys abruptly increase their strength characteristics. For example, introduction of 0.3%Sc into AMg5 alloy (Al–5%Mg) increases the tensile strength of annealed sheets from 260 to 400 MPa. The structure of scandium-free alloy remains completely recrystallized, while that of scandium-containing alloy is nonrecrystallized [1]. In the presence of zirconium, the modifying effect of master alloy manifests itself at lower scandium concentrations. Aluminum grain nuclei in the presence of zirconium are $Al_3(Sc_xZr_{1-x})$ particles, in which zirconium substitutes for 50% scandium, the lattice type (LI_2) remaining the same [2,3]. Modification of cast alloy Al–Zn–Cu–Mg with a master alloy (0.48%Sc+Zr) leads to grain size refinement to 23 μm [4]. At the same time, the dendritic grain structure disappears. Al_3Sc, Al_3Zr and $Al_3(Sc_{1-x}Zr_x)$ dispersoids formed by secondary segregation have dispersity of <10 nm and are coherent with the aluminum matrix. Hafnium in aluminum alloys has a stronger refining effect than zirconium, which is explained by its more pronounced metallic properties; additionally, hafnium is a good absorber of thermal neutrons. Addition of 1% hafnium in aluminum leads to the production of aluminum superalloys with metal grain size of 40–50 nm. Here, not only alloy reinforcement, but also considerable relative elongation is achieved, the shear and torsional strength is increased and the vibration resistance is improved [5].

Production of light alloys containing expensive rare metals is economically more sound by their synthesis using high-temperature exchange reactions between fluoride-chloride salt melts containing one or several compounds of rare metals and liquid aluminum or its alloys with magnesium [6–8]. With this method of alloy production, liquid aluminum was found to contain inclusions of intermetallic compounds (IMC) and slag shots. Usually, the methods for removal of inclusions include kiln deposition followed by filtration through glass net with a high content of alumina or passing through a layer of coke, carbon, flux etc. The materials used for such refining of melts often become clogged up and are washed out by metal, whereas the inclusions pass through the partitions. Some refractory materials are able to contaminate the filtered metal. The presence of large inclusions leads to sheet stock and stamping rejects, as well as to reduction of the durability of articles because of crack formation and failures, especially under vibrational loads. In this work, we examine the behavior of some solid inclusions during centrifugation.

The performed laboratory-scale experimental studies allowed us to establish that aluminum alloys with required content of alloying additions (scandium, zirconium, hafnium), taken in different ratios, can be produced by the injection method. This method provides uniform distribution of doping metals in the whole bulk of the alloy, the duration of the operation decreases in comparison with other methods of alloying, small amounts of available salts are used, and some impurities are removed into the slag.

2. Analysis of inclusions in aluminum alloys

2.1. Sedimentation theory

In accordance with the Stokes law, during centrifugation of aluminum melt with rotating velocity f until its hardening, the IMC and slag particles move to the bottom or to the top of the crucible with rate υ determined by equation:

$$\upsilon = \frac{2\pi^2}{9} \cdot \frac{d^2 f^2 (\rho_{Al} - \rho_p)\alpha r}{\eta} \tag{1}$$

where η is the aluminum viscosity coefficient; d is the spherical diameter; r is the distance between the rotation axis and particle; ρ_{Al} and ρ_p are the densities of Al and particle; and α is the relative velocity of particle with respect to the velocity of spherical particle of equal volume (α is a constant value depending on the particle profile; for round particles including disk-shaped and rod-like forms, the values of α lie within 0.8–1.0; for film forms, for example, thin oxide films, the values of α can range in the region of 0.25–0.35 depending on the film orientation).

The spherical diameter d of finest inclusions moving to the bottom of the crucible in the melt is determined by equation [9]:

$$d = \left[\frac{45\eta \cdot \ln\left(R_b/R_g\right)}{8\pi^2 \alpha \cdot f^2 \left(\rho_{Al} - \rho_p\right)\left(t - \frac{7}{12} t_1\right)} \right]^{1/2} , \tag{2}$$

where f is the rotating velocity; t is the period of time when the melt is in the liquid state during centrifugation; R_b is the distance from the rotation axis to the top of the melt in the crucible; R_g is the distance from the rotation axis to the bottom of the melt in the crucible; η is the viscosity coefficient of liquid at starting temperature; and $t = t_1$.

2.2. Experiment conditions

Aluminum alloy ingots were melted, heated to 850°C and centrifuged in cylindrical alundum crucibles with chamotte thermal isolation using an S–6UHL4.2 centrifuge. Centrifugation was carried out with rotating velocity from 600 to 3000 rev/min until hardening of metal. Depending on the alloy mass, the time before crystallization varied from 6 to 10 min (Fig. 1).

The duration of crystallization of samples until complete hardening was 5–8 min. The samples' liquid state time was enough for large particles to settle on the crucible bottom (Fig. 2).

The oxide agglomerates, of lower density than that of the melt, move towards the rotation axis. The samples were divided along the cylindrical axis. The inclusions were analyzed using microscopic, chemical and X-ray phase methods. The centrifuge and samples parameters are as follows: the distance from the rotation axis to the melt upper level in the crucible is R_b=120–150 mm, the same to the crucible bottom is $R_g = 200$ mm, the crucible diameter is $\emptyset_{id} = 40$ mm and the viscosity of aluminum is $\eta_{Al} = 3 \div 5$ Poise.

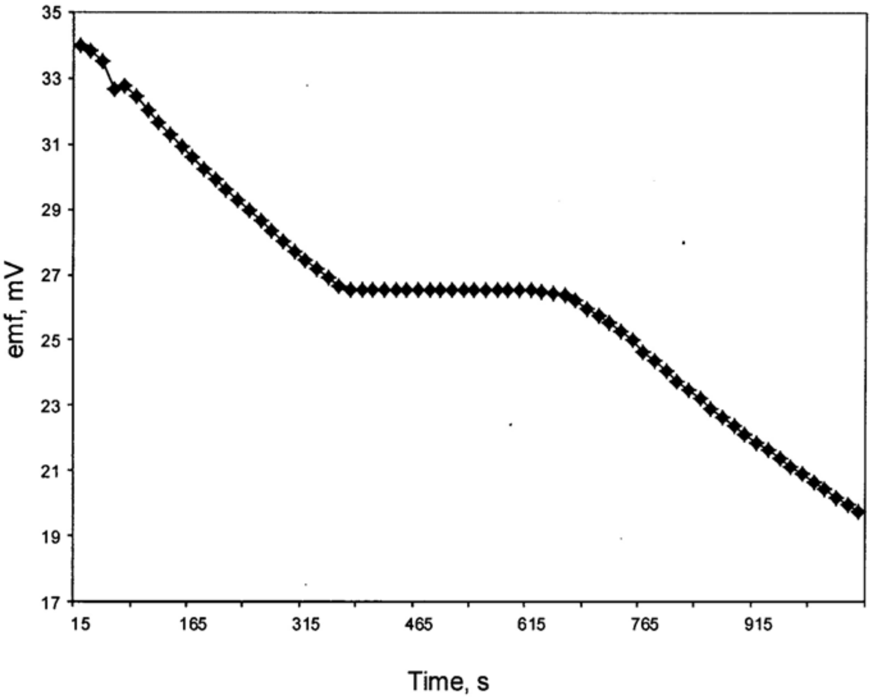

Fig. 1. Crystallization diagram

2.3. Results and discussion

The Al_3Sc phase in aluminum is formed by a peritectic reaction at 1427°C. It has a cubic lattice with four atoms in the cell and the parameter $a = 4.106 \times 10^{-10}$ m and is isomorphous with aluminum with $a = 4.100 \times 10^{-10}$ m [10]. The density of isolated crystals determined by the bottle method is 3.00 g/cm^3.

The compound Al_3Zr in aluminum is melted congruently at 1577°C. At 660.3°C, in the aluminum-rich region, a peritectic reaction takes place, during which Al_3Zr interacts with the melt containing 0.03 at.% Zr and forms an α_{Al}-solid solution. The metastable modification

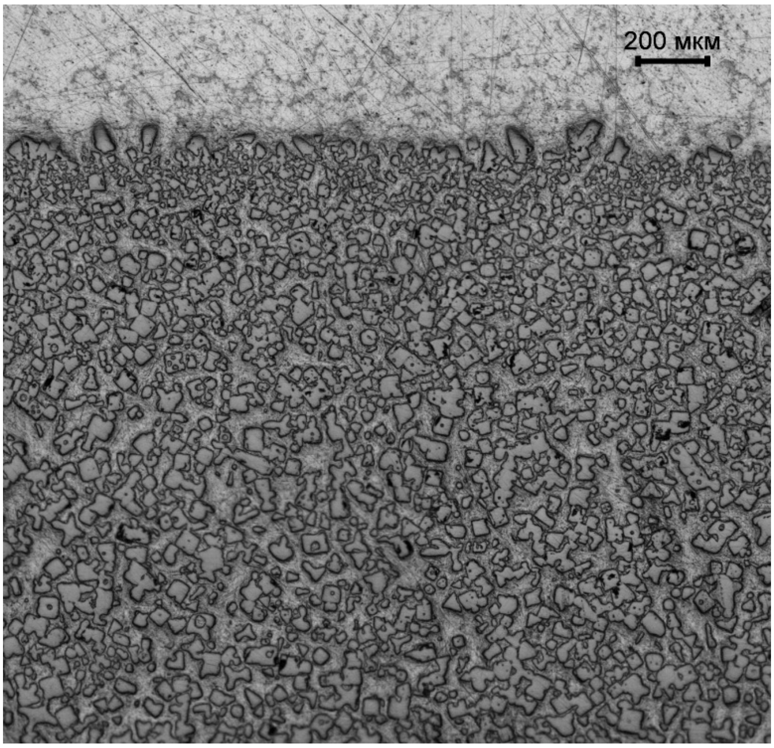

FIG. 2. Large-size IMC particles on the boundary of bottom sediment

of the phase, formed by annealing from supersaturated aluminum solid solution, has a cubic Cu_2Au-type crystal structure with lattice parameters $a = 4.050 \times 10^{-10}$ m [10]. The density of isolated crystals was also determined by the bottle method to be 4.10 g/cm^3.

The compound Al_3Hf is melted congruently at 1590°C, and at 662°C, as a result of a peritectic reaction with the melt containing 0.073 at.% Hf, it forms an α_{Al}-solid solution having the maximum solubility at this temperature, 1.2 mass %. The lattice parameter increases to the maximum, $a = 4.051 \times 10^{-10}$ m [11, 12]. The density of these crystals determined by the bottle method is 6.18 g/cm^3.

Additions of transition metals to the binary alloy Al–2%Sc appreciably affect the strengthening value. The best strengthening during decomposition of the solid solution in the experimental alloy is achieved when the Sc and Zr contents are equal. Additions of Hf produce an analogous effect in character, but of slightly lower magnitude [13].

Depending on the initial content of metals introduced into aluminum and on the alloy cooling rates, the Al_3Me crystals have different sizes and shapes. Without centrifugation (settling) of the alloy containing 10 mass% Sc, the microstructure of the sediment is characterized by round 10–140 μm particles and needles of size to several millimeters. The inclusions of Al_3Sc particles in the ingot volume without centrifugation are predominately 5 μm in size. Large needles are not observed over the sediment from the melt containing 4–5% Sc. In the ingot volume, the particles are under 5 μm in size. At the initial Sc concentration of 2.0%, the major part of the particles in the ingot volume have a rectangular shape and a size of less than 4 μm, while 5–7 μm particles are not more than 10%. Centrifugation of Al–2%Sc master alloy at a rate of 1000 rev/min results in deposition of large IMC particles on the bottom, whereas the nanoparticles of size < 400 nm remain in the bulk. The microstructure of 1.8–2.0% Sc-containing alloy ingots, with crystallization in cast-iron molds and a melt cooling rate from 800°C of minimum 100°C/s, is represented by crystals and plates under 5 μm in size. The composition of α_{Al}-solid solution and IMC particle inclusions was examined with the use of quantitative MS analysis. The content of elements (mass %) was determined for the upper boundary of the bottom layer particles: Al–62.57 and Sc–32.43 (Al_3Sc), and a lower content of scandium was found for the dark particles and for the center of the particles: 16.62–17.78 and 20.77–24.05, respectively. Depending on the temperature, the scandium content of scandium (mass %) in the α_{Al}-solid solution is 0.38 (660°C), 0.22 (600°C), 0.07 (500°C) and 0.03 (400°C).

As a result of centrifugation of zirconium-rich (10 mass %) aluminum alloy, 50 μm and smaller particles are observed in the microstructure of the bottom phase, and on the boundary with the bottom phase also needles of 200 μm and less in length are found. As distinct from Al–Sc ingots, slag inclusions in the form of black shots are seen in the bottom sediment layer. Without centrifugation, the IMC particles in the ingot volume are chiefly 5–15 μm in size. Depending on the initial content of zirconium in the aluminum melt, the dissolution of large-sized particles at 750°C is slow. At 0.3 mass % Zr content, at least 30 min are required for their dissolution at this temperature. After centrifugation of the melt, the content of zirconium in the α_{Al}-solid solution was found to be 0.28–0.30 mass %. The intermetallic particles contain 36.18–56.38 mass % of Zr. Iron (0.07–0.08) and silicon impurities (0.55–1.63), as well as an enhanced zirconium content (0.33 mass %) are found in some samples of α_{Al}-solid solution of the master alloy. In the aluminum angle of the phase diagram Al–Zr–Sc, the only nonvariant peritectic transformation is found at a temperature of 659°C, $L + Al_3Zr \rightarrow (Al) + Al_3Sc$ [9].

For the initial concentration of 12 mass % Hf in aluminum, round particles of a maximum 60 μm in size are deposited on the bottom during centrifugation. At the initial concentration of 5 mass % Hf in the melt, no needle-shaped inclusions are found over the sediment. The size of IMC particles in the ingot volume did not exceed 2 μm. The bottom sediment, like for the alloys with zirconium, is found to contain round slag inclusions.

Thus, it was shown that depending on the initial concentration of alloying component (Sc, Zr, Hf), crystallization conditions and the presence of other alloying components, IMC of different forms are obtained and large IMC particles can be formed, which slowly dissolve at the temperature of master alloy introduction into the alloy.

3. Chemical alloying of aluminum and alloys based thereon

In the light of the above discussion, alloying of aluminum and aluminum-based alloys (both cast alloys and wrought alloys) using aluminothermic methods holds much promise. These methods can be used for introduction of refractory, scattered and rare metals into alloy and for improvement of properties (such as heat resistance, corrosion resistance, weldability, mechanical strength etc.). In particular, the case in point is alloying of aluminum with small additions of scandium, zirconium and hafnium. The application of aluminothermic methods for the production of master alloys and alloys by blowing (injection) through aluminum melt using a gas-powder suspension consisting of inert gas (argon Ar or carbon dioxide CO_2) and a ground salt mixture of sodium fluoride and potassium chloride with aluminum fluoride that contains oxides and fluorides of metals introduced into the alloy at 700–900°C is described in detail in Ref. [14]. Production of aluminum-scandium alloys in industrial kilns of KUMZ OJSC is described elsewhere [15].

The new method, developed by the authors, allows alloying of aluminum and aluminum-based alloys with scandium, zirconium and hafnium with the use of a salt composition consisting of a mixture of potassium chloride and potassium and aluminum fluorides (or only potassium, sodium and aluminum fluorides), which contains oxides of the corresponding metals introduced by injection into melted aluminum. During melting, the ground mixtures of these salts dissolve the oxides forming complex compounds, which easily interact with melted aluminum; for example, the application of a mixture of sodium and potassium fluorides can hold promise for dissolution of scandium oxide (Fig. 3).

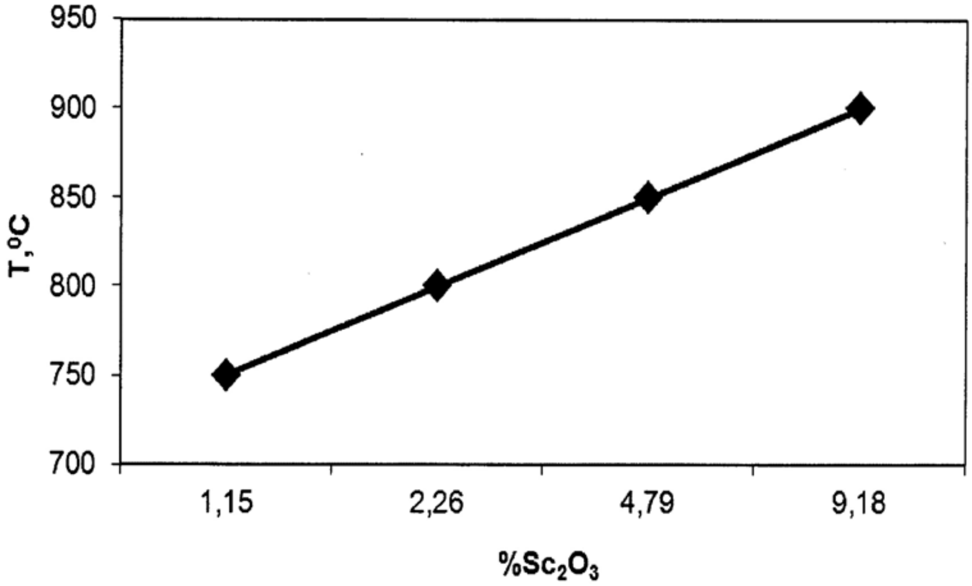

FIG. 3. The liquidus curve piece of a salt system with scandium oxide (0.4NaF + 0.6KF) – Sc_2O_3

From the X-ray phase analysis data presented in Fig. 4 it was established that during melting with sodium and potassium fluorides, scandium oxide is dissolved forming sodium dipotassium hexafluoroscandiate (scandium cryolite-elpasolite) K_2NaScF_6.

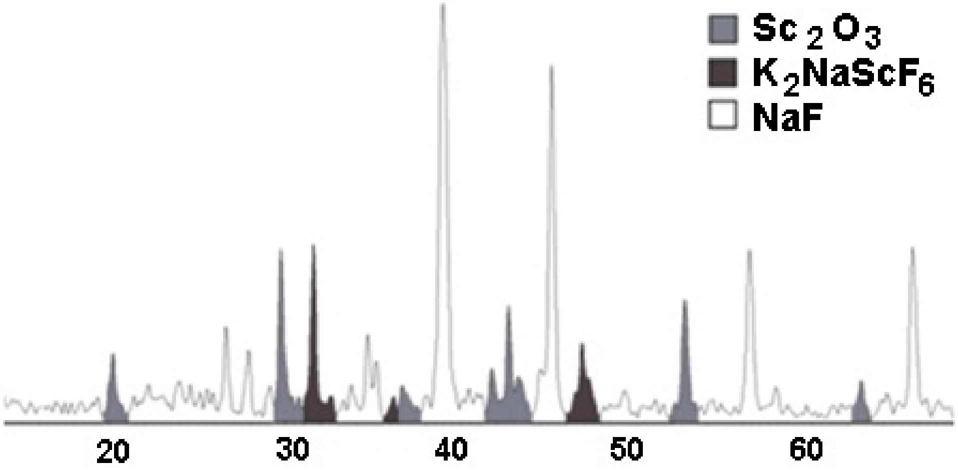

FIG. 4. The X-ray diffraction pattern of a salt system with scandium oxide (0.4NaF + 0.6KF) – Sc_2O_3

Alloying of aluminum with scandium, zirconium and hafnium allows new-generation alloys to be produced (for example, 1570, 1975 etc.). After blowing of aluminum melt with a gas-powder suspension, the slag is easily removed and the finished product can be poured into moulds if other alloying additions, for example lithium, are not introduced. The laboratory-scale experimental studies performed showed that the injection method can be used for obtaining aluminum alloys with required content of alloying additions (scandium, zirconium, hafnium) taken in different ratios. This method provides uniform distribution of doping metals in the whole bulk of the alloy, the duration of the operation decreases in comparison with other methods of alloying, small amounts of available salts are used, and some impurities are removed into slag. So, it is established experimentally that the content of sodium decreases by 15% (if a salt mixture without sodium fluoride is used), silicon – by 25% and copper – by almost 80%. In order to obtain a satisfactory ratio of dopants during complex alloying of aluminum, the concentrations of the compounds of introduced metals in the salt mixture should be maintained with allowance for the yield of alloying metals into the alloy at the temperature of the process. In case of deviation from the necessary concentration of salts of metals reduced by the aluminothermic method, the required ratios in the alloy cannot be attained.

The injection method is carried out in the following way:

– Preliminarily preparation of the salt mixture (50–60% KCl, 30-45% KF, 5–10% AlF_3): drying at 150°C, mixing, introduction of the calculated amount of compounds (oxides) of alloying addition (not more than 25% of the total mass of the mixture), grinding with simultaneous mixing and loading into the injection plant (Fig. 5). The reagents are taken in 5–20% excess.

– The necessary amount of alloying aluminum (or aluminum-based alloy) is melted in an L–9/11/B180 Nobertherm furnace to the temperature specified in the process instruction for a particular alloy, for example 750–800°C for pure aluminum.

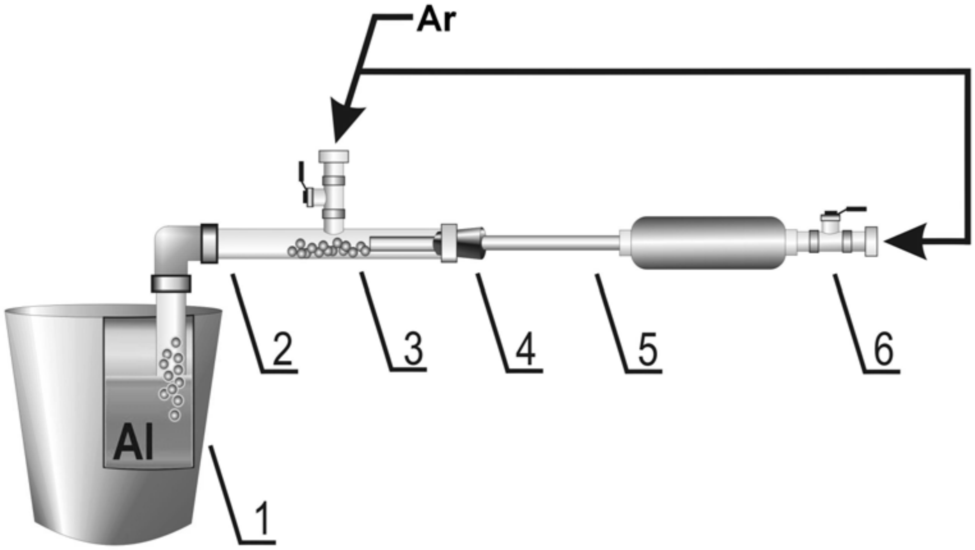

Fig. 5. The diagram of a plant for injection of powdered salts into liquid aluminum. 1 – crucible for aluminum; 2 – single-jet tuyere; 3 – powdered salts; 4 – plug; 5 – accelerating jet; 6 – pulse gate; CO_2 – shielding gas; Al – liquid aluminum

– The powder is injected into aluminum melt with the use of carbon dioxide until all salt mixture is consumed. Gas blowing is carried out for as many again as 1–5 min, after that, the slag is discharged and the metal is poured into a cast-iron mold.
– The content of alloying additions in aluminum is refined analytically in the Laboratory of physicochemical methods of analysis at the ISSC UB RAS using the atomic absorption spectroscopy method (plasma version) on a Perkin Elmer-503 Atomic absorption spectrometer.

The alloying component in the composition of powder mixture is introduced into the melt by blowing the mixture in the carrier gas jet through aluminum melt. The powdered mixture is composed of potassium fluoride, potassium chloride and aluminum fluoride, and the alloying elements are oxides of the corresponding metals taken in the ratio, mass %:
– potassium fluoride (KCl) – 50-60%,
– potassium chloride (KF) – 15-35%,
– aluminum fluoride (AlF_3) – 5-10%,
– oxide of introduced metal (a mixture of metal oxides) – 10-25%.

Carbon dioxide (CO_2) is used as a carrier gas; it is fed with a rate of 0.2–20 ndm^3/min under a pressure of 0.1 atm. The direct metallurgical yield of alloying components, both at individual and joint introduction of dopants, is more than 90%. Alloys with estimated content of alloying elements, from 0.3 to 0.6 mass %, are produced.

The decomposition of solid solutions with the formation of secondary dispersoids begins below 500°C. The eutectic temperature of the Al–Sc alloy is only 1°C lower than the melting point of aluminum and has a composition of 0.47% Sc (0.38 at.% Sc). The solubility of Sc in solid Al at the eutectic temperature is 0.34%, and at 600°C, it decreases to 0.23% [10]. The size of nucleus in the form of Al_3Sc particle is smaller than 1.8 μm, and Al_3Sc dispersoid formed by secondary segregation, as was already mentioned above, is < 10 nm in size and is completely coherent with the aluminum matrix, which further improves the mechanical properties.

When, besides scandium, cheaper modifying agents (zirconium and hafnium) are introduced into aluminum alloy, the structure of the formed IMC becomes more complicated, which appreciably affects the strength and other properties. According to the dependence proposed by Darken and Gurry [16] that the proximity of atomic radii and electronegativities of melted components promotes the formation of vast regions of solid solutions, it can be suggested that the mechanical properties (hardness) of light aluminum alloys are strengthened.

Examination of alloys containing individually Sc, Zr, Y and Hf or their mixtures and having different compositions shows that the microhardness of the produced materials increases when the element's atomic number and the complexity of the component composition lower (Fig. 6).

The results obtained can be used for predicting the properties after introduction of modifying agents into aluminum alloys. The microhardness of alloys containing Sc, Zr, Y and Hf increases as the element atomic number and the composition complexity lower.

4. Conclusions

The studies performed showed that depending upon the initial concentration of alloying component (Sc, Zr, Hf) and other conditions, IMC crystals of different shape are produced and large IMC particles can be formed, which dissolve slowly at the temperatures of master alloy introduction into the alloy. Segregation of inclusions into a small region of sediment is possible already at a centrifuge rotating velocity of 1000 rev/min. When zirconium and hafnium are introduced by high-temperature exchange reactions into the salt

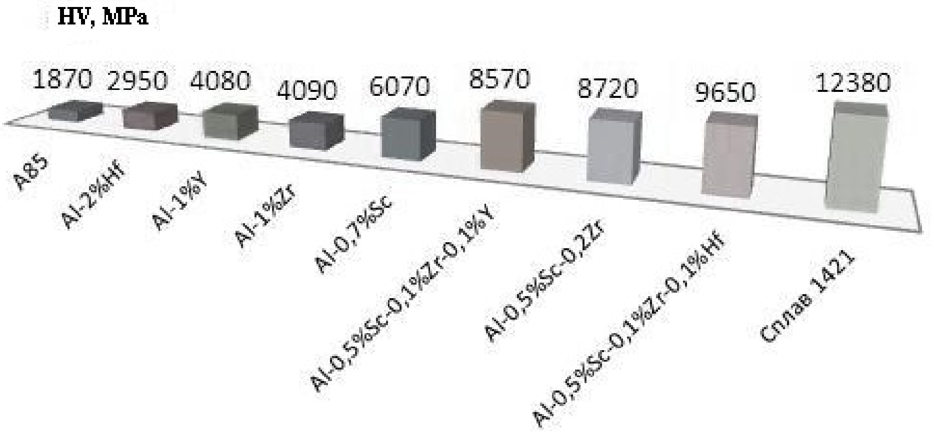

FIG. 6. The microhardness of alloys versus their composition

melts based on fluorides and chlorides of alkaline metals and the corresponding rare metal with aluminum, “heavy” slag shots can also deposit on the bottom. Primary removal of suspended impurities from aluminum alloy can be carried out in settling centrifuges; the diameter of finest inclusion particles removed from the solution is 400–500 nm. The centrifugation method can be used to analyze the particles in the melt and to determine the solubility of phases and the kinetics of particle size as functions of the melt temperature.

The introduction of alloying additions (scandium, zirconium, hafnium) into aluminum and aluminum-based alloys by injecting process powders into aluminum melt has the following advantages over other methods:

1. Cheap compounds (oxides) of alloying metals are used.
2. Low process temperatures.
3. Uniform distribution of dopants in the volume.
4. Easily accessible carbon dioxide is used for injection.
5. Complex alloying is possible.

Owing to segregation of secondary nano-sized IMC located on the grain boundary, at comparable concentrations, dispersion hardening of alloys is superior to solid-solution strengthening.

References

[1] Zakharov V.V. Effect of scandium on the structure and properties of aluminum alloys. *Metallovedeniye i termicheskaya obrabotka metallov*, **7**, P. 7–15 (2003). [in Russian]

[2] Belov N.A., Alabin A.N. Promising aluminum alloys with zirconium and scandium additions. *Tsvetnye metally*, **2**, P. 99–106 (2007). [in Russian]

[3] Fanhao Zeng, Changging Xia, Yi Gu. The 430°C isothermal section of the Al-4Mg-Sc-Zr quaternary system in the Al-rich range. *J. Alloys and Compounds*, **363**, P. 175–181 (2004).

[4] Popova E.A., Shubin A.B., Kotenkov P.V., Brodova L.E. et al. Al-Sc-Zr master alloy and estimation of its modifying ability. *Rasplavy*, **1**, P. 12–15 (2011). [in Russian]

[5] Kubaschewski O., Von Galdbeck. Phase diagram Hf-Al. In book: Hafnium: Physico-chemical Properties of its compounds and alloys. *Atomic Energy Review*, Special issue No. **8**, IAEA, Vienna., P. 58–60 (1981).

[6] Yatsenko S.P., Khokhlova N.A., Pasechnik L.A., Sabirzyanov N.A. Production of aluminum-based master alloys by high-temperature exchange reactions in salt melt. III. Multicomponent modifying a;uminum master alloys with scandium, zirconium and hafnium. *Rasplavy*, **2**, P. 89–93 (2010). [in Russian]

[7] RF patent No. 2421537. Method for production of aluminum-containing master alloy and charge for obtaining of aluminum-scandium-containing master alloy. Yatsenko S.P., Ovsyannikov B.V.,

Varchenya P.A. Patent holders: ISSC UB RAS and OJSC KUMZ. Published 2010, Bull. No. 22. [in Russian]

[8] RF patent No. 2361941. Method for production of aluminum-scandium master alloy, flux for obtaining of master alloy and a device for implementation of the method. Yatsenko S.P., Sabirzyanov N.A., Yatsenko A.S. Published 2009, Bull. No. 20. [in Russian]

[9] Simensen Chr.J. Sedimentation Analysis of Inclusions in Aluminium and Magnesium. *Metallurgical Trans. B*, **12B**, P. 733–743 (1981).

[10] Belov N.A. *Phase composition of commercial and prospective alloys.* Moscow: MISiS, 511 p. (2010). [in Russian]

[11] Mandolfo L.F. *Aluminum alloys: Structure and Properties.* Butterworths, London, 312 p. (1976).

[12] Kubaschewski O., Von Goldbeck. Hafnium: Physico-chemical Properties of its compounds and alloys. *Atomic Energy Review.* Special issue No. **8**. IAEA. Vienna, 60 p. (1981).

[13] Zakharova V.V., Rostova T.D. Effect of scandium, transitions metals and impurities on strengthening of aluminum alloys during decomposition of solid solution. *Metallovedeniye i termicheskaya obrabotka metallov*, **9**(627), P. 12–19 (2007). [in Russian]

[14] Skachkov V.M., Yatsenko S.P. Production of aluminum-based Sc, Zr, Hf, Y master alloys by high-temperature exchange reactions in salt melts. *Tsvetnye metally*, **3**, P. 22–26 (2014). [in Russian]

[15] Skachkov V.M., Varchenya P.A., Ovsyannikov B.V., Yatsenko S.P. Injection of scandium-containing process powders into aluminum alloys. *Tsvetnye metally*, **12**, P. 81–86 (2013). [in Russian]

[16] Darken L.S., and Gurry R.W. *Physical chemistry of metals.* McGraw Hill, New York, 535 p. (1953).

N A N O
Ф&Х&М

NANOSYSTEMS:

PHYSICS, CHEMISTRY, MATHEMATICS

Журнал зарегистрирован
Федеральной службой по надзору в сфере связи, информационных технологий и массовых коммуникаций
(свидетельство ПИ № ФС 77 - 49048 от 22.03.2012 г.)
ISSN 2220-8054

Учредитель: федеральное государственное автономное образовательное учреждение высшего образования
«Санкт-Петербургский национальный исследовательский университет информационных технологий, механики и оптики»

Издатель: федеральное государственное автономное образовательное учреждение высшего образования
«Санкт-Петербургский национальный исследовательский университет информационных технологий, механики и оптики»

Отпечатано в Учреждении «Университетские телекоммуникации»
Адрес: 197101, Санкт-Петербург, Кронверкский пр., 49

Подписка на журнал НФХМ
На первое полугодие 2015 года подписка осуществляется через
ОАО Агентство «Роспечать»
Подписной индекс 57385 в каталоге «Издания органов научно-технической информации»